The Interaction of Chiral Nanoparticles with Biological Objects

A thesis submitted to the School of Chemistry,

Trinity College, the University of Dublin,

for the degree of Doctor of Philosophy

Vera Kuznetsova

Under the supervision of Professor Iouri Gounko

July 2021

Summary

The main goal of this research is to investigate how different factors influence the induced optical activity of semiconductor nanoparticles (NPs) of various shapes and test the biological activity of NPs capped with chiral molecules on living cells. We also plan to study the influence of quantum dots (QDs) on the optical activity of a chiral molecule using the example of the photosensitizer chlorin e6 and to investigate the photodynamic efficiency of QD complexes with chlorin e6.

Chapter 1 of the thesis provides the introduction and describes the background theories and presents the literature review on QDs and chirality, including chirality at the nanoscale.

Chapter 2 provides experimental details for all procedures: the protocols of the synthesis and modifications of the quantum nanostructures; characterisation techniques used and the main principles of their functioning; as well as details of cell culturing and biological studies.

Chapter 3 is dedicated to the investigation of the dependence of optical activity and PL upon CdS shell thickness in a range of core-shell structured CdSe/CdS QDs capped with chiral ligands. For our study, five samples of CdSe/CdS were synthesised utilizing successive ion layer adsorption and reaction (SILAR) to vary the thickness of the CdS shell from 0.5 nm to 2 nm, upon a 2.8 nm diameter CdSe core. Following this, a ligand exchange of the original aliphatic ligands with L- and D-cysteine was carried out, inducing a chiroptical response in these nanostructures. The samples were then characterized using CD, UV-Vis, PL spectroscopy and PL lifetime spectroscopy. It has been found that the induced chiroptical response was inversely proportional to the CdS shell thickness and showed a distinct evolution in signal, while the photoluminescence of our samples showed a direct relationship to shell thickness. In addition, a detailed study of the influence of annealing time on the optical activity and PL quantum yield was performed.

Chapter 4 presents the study of the influence of chiral cysteine molecule concentration and cysteine binding mode on the intensity of QD CD signal. It was revealed that initially, by increasing the cysteine concentration, the QD CD intensity increased, but

after reaching a certain critical point, it started to reduce. Remarkably, the intensity of CD signal varied by almost 10 times. NMR and FTIR analysis as well as DFT calculations showed that at low concentrations cysteine bound to QD surface with all three functional groups, while at high concentrations it coordinated only by SH and NH_2 groups. These tri- and bidentate forms of bound cysteine appeared to be near stereoisomeric configurations, which can result in general CD signal reduction. In this chapter we also highlight the factors that must be taken into account when designing optically active nanoparticles.

Chapter 5 describes the investigation of enantioselective interactions of fluorescent NPs capped with chiral molecules with A549 cells. These NPs were stabilized with D- and L-cysteine using a ligand exchange technique. It was found that NPs stabilized by opposite ligand enantiomers, had identical PL and UV–Vis spectra and mirror-imaged CD spectra, but displayed different cell accumulation and cytotoxicity: NPs capped with D-cysteine had greater cytotoxicity than L-cysteine capped NPs.

Chapter 6 is devoted to the study of the optical properties of complexes of CdSe/ZnS as well as Cd-free ZnSe/ZnS QDs and the photosensitizer chlorin e6 (Ce6), which are widely used for photodynamic therapy. CdSe/ZnS QDs were bound to Ce6 using bovine serum albumin (BSA) as a linker and ZnSe/ZnS QDs created with Ce6 electrostatic complexes. The photodynamic therapy (PDT) test of the electrostatic complexes against the Erlich acsite carcinoma cell culture demonstrated a twofold enhancement of the cancer cell photodynamic destruction compared to that of free chlorin e6 molecules. It was shown that the PDT effect was significantly increased due to two factors: the efficient QD–chlorin e6 photoexcitation energy transfer and the improvement of cellular uptake of the photosensitizer in the presence of ZnSe/ZnS QDs.

Finally, chapter 7 presents the conclusions and summarizes main outcomes of this research. It also discusses the future research that would follow on from this work.

In overall, in these studies, we have been able to clearly illustrate the approach and strategies that should be used for designing optimal luminescent optically active QDs for potential biomedical applications. We believe that our findings may lay the groundwork

for new approaches to control the biological properties and behaviour of QDs capped with chiral molecules in living cells, including PDT properties of QDs complexes with appropriate photosensitizers (e.g. chlorin e6).

Declaration

This thesis is submitted for the degree of Doctor of Philosophy to the University of Dublin, Trinity College and has not been submitted before for any degree or examination to this or any other university. Other than where acknowledged, all work described herein is original and carried out by the author alone. Permission is granted so that the Library may lend or copy this thesis upon request. This permission covers only single copies made for study purposes, subject to normal conditions of acknowledgement.

Vera Kuznetsova

Acknowledgements

First of all, I would like to thank my supervisor Prof. Yurii Gun'ko for the opportunity to work in his group and for his invaluable contribution to my professional progress, his willingness to help with advice, consultations and to thoughtfully discuss the results of my work.

I would also like to express my gratitude to Prof. Yuri Volkov, Dr. Adriele Prina-Mello and Dr. Ciaran Maguire for the opportunity to carry out biological research on the basis of their laboratory, and also for introducing me to a whole new area of research, for their expert advice and discussion and for their assistance in writing articles and theses.

My gratitude is extended to my colleagues Dr. Anastasia Visheratina, Dr. Finn Purcell-Milton, Dr. Alex Loudon, Dr. Marina Carmona and Dr. Yulia Gromova for their great help in my experimental work, for their skills, their help in editing my articles and abstracts, consultations and interest, as well as for the friendly atmosphere they created in the group and their kind attitude. I'd like to give special thanks to Dr. Finn Purcell-Milton and Alex Loudon for performing synthesis of Nanoparticles for my work and for introducing me to the nanoparticle synthetic procedures. I would like to thatk prof. Max García-Melchor Eric Mates-Torres for DFT calculation and frutefull caloboration. I am grateful to my many students; Nadezda Prochukhan, Aisling Rayn, Madeline Marcastel, Benjamin Sgro, Matthias Schmitt and Natalia Garcia Domenech, who worked with me, for the experiments they performed and the results we obtained.I would like to thank once again all of Prof. Gun'ko's group for their support, advice and their help in the organization of my experiments.I would also like to express my gratitude to my colleagues at ITMO University, St. Petersburg, Dr. Anna Orlova and Dr. Irina Martynenko for their expert consultations and their help in writing my work.

I am also profoundly thankful to IRC for providing me with funds to pursue my academic interest.

Contents

List of Figures

List of Abbreviations

1-D – 1- Dimensional

2-D – 2 – Dimensional

BSA – Bovine serum albumen

CD – Circular dichroism

Cys -Cysteine

DBA – Dibenzylamine

DDT - Dodecanethiol

DiR – Dot in Rod

DLS – Dynamic Light Scattering

DMEM – Dulbecco's Modified Eagle's Medium

DMSO – Dimethyl Sulfoxide

FBS – Fetal bovine serum

GSH – Glutathione

HPLC – High Performance Liquid Chromatography

LED – Light emitting diode

MEH - poly(2-methoxy-5-(2'-ethyl-hexyloxy)-1,4-phenylene vinylene)

MPA – mercaptopropionic acid

NC – Nanocrystal

NIR- Near Infra-red

NP – Nanoparticle

ODE – 1-octadecene

PBS – phosphate buffered saline

Pen – Penicillamine

PL- Photoluminescence

PL QY – Photoluminescence Quantum Yield

QD – Quantum Dot

SEM – Scanning electron microscope

TEM – Transmission electron microscope

TGA – Thermogravimetric analysis

TOP – Trioctylphosphine

TOPO – Trioctylphosphine oxide

TP – Tetrapod

UV-Vis – Ultraviolet-Visible

XRD – X ray diffraction

1   Chapter 1. INTRODUCTION

1.1   Quantum Dots

There is a wide variety of nanomaterials, which are very promising for a range of biomedical applications[1]. In particular, quantum dots (QDs) are of great interest[2]. QDs are semiconductor NPs that possess unique optical properties, such as size-dependent photoluminescence (PL) with high PL quantum yield (QY) (up to 100%); large absorption coefficients continuous across a wide spectral range, excellent photo- and chemical stability[3,4]. Due to these properties QDs have been successfully used in a variety of biological applications, such as biological imaging, bio sensing and others[2–6].

1.1.1   Band structure and photoluminescence of QDs

Atoms have discrete electronic energy levels which are called atomic orbitals. In molecules each energy level of individual atoms is hybridized with orbitals of other atoms to form the molecular orbitals. As a result, the general energy of the system becomes lower. This approach is known as the linear combination of atomic orbitals. The more atoms are in the molecule the more molecular orbitals are formed. In the crystals where the amount of atoms can be considered as infinite, combined molecular orbitals are merged in crystal bands: a continuous range of energies that an electron within the solid may have (Figure 1-1).
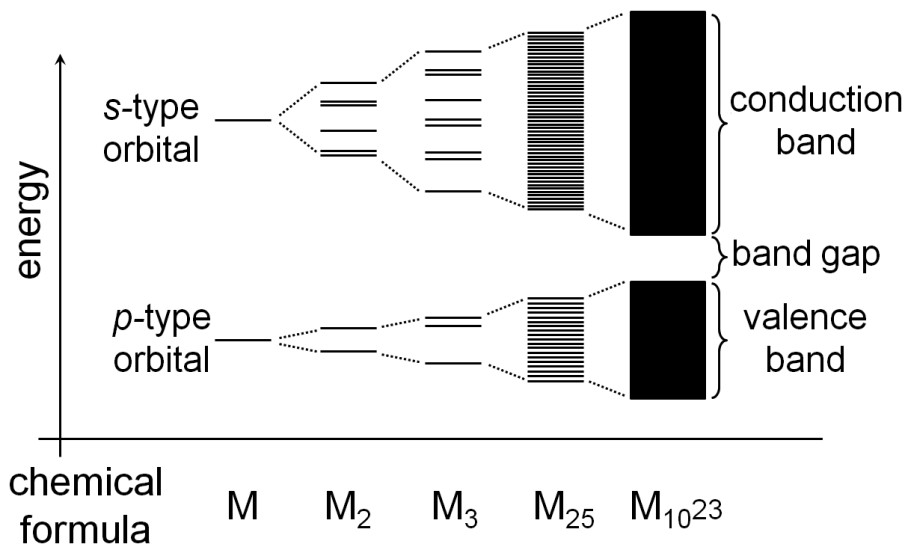
Figure 1-1:The conversion of orbitals into bands for bulk materials. Reproduced from https://www.cambridge.org/core/books/colloidal-quantum-dot-optoelectronics-and-photovoltaics/electronic-structure-and-optical-transitions-in-colloidal-semiconductor-nanocrystals

Metals have overlapping lowest energy unoccupied band (conduction band) and highest energy occupied band (valence band), that allow the electron to move freely through the material. Semiconductor materials have a relatively small energy band gap (up to 4eV) between valence band and conduction band and the insulators have a large band gap. Electrons in semiconductors can be promoted from the valence band to the conduction band by light excitation. Exited electrons can relax and go back to the valence band. This leads to the emission of photons. The energy of the photons corresponds to band gap energy. When an electron is excited, it creates a positive hole in its absence. The electron and hole are bound by Coulomb interaction and are known as an exciton. The distance between an excited electron and the positive hole it generates is known as the Bohr exciton radius of the semiconductor. The Bohr exciton radius of a material is given below in Equation 1-1:

$$r_B = \frac{\hbar^2 \varepsilon}{e^2}\left(\frac{1}{m_e^*} + \frac{1}{m_h^*}\right)$$

Equation 1-1. Bohr Exciton radius, where e is the charge of the electron, m_e and m_h are the effective masses of the electron and hole respectively, and ε is the dielectric constant of the material.

When the size of the semiconductor is smaller than the Bohr exciton radius of the material, the exciton undergoes quantum confinement effect, which is theoretically described by theparticle in a box model, resulting in dependence of the band gap on a particle size (*Figure 1-2*)[7]. The dependence of the band gap energy on particle radius was firstly quantified by Brus et al[7] in 1984 with the well-known Brus equation seen below (Equation 1-2):

$$\Delta E(r) = E_{gap} + \frac{h^2}{8R^2}\left(\frac{1}{m_e^*} + \frac{1}{m_h^*}\right)$$

Equation 1-2. Brus equation, where ΔE(r) is the observed exciton energy, E_{gap} is the band gap energy of the bulk material, R is the QDs radius and m_e* and m_h* are the effective masses of the electron and hole respectively.
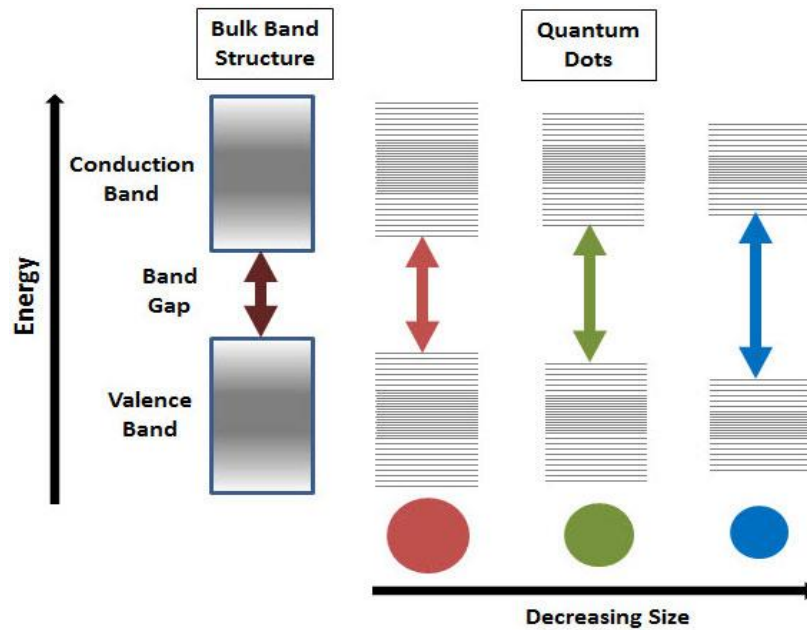
Figure 1-2. Demonstration of band gap increase due to quantum confinement effect; Reproduced from https://www.sigmaaldrich.com/technical-documents/articles/materials-science/nanomaterials/quantum-dots.html

When the particle is smaller than the Bohr radius, the probability of radiative exciton recombination is much higher than in the bulk material. It happens because the electron and hole wave functions have a larger overlap due to the confinement.

As a result, the optical properties such as PL and UV-Vis spectra depends on QD size. The smaller the particle, the larger is the band gap and the deeper is the blue shift of PL, and vice versa[8] (Figure 1-3). This gives a possibility to control the PL wavelength on the QDs, which is widely used in practice.
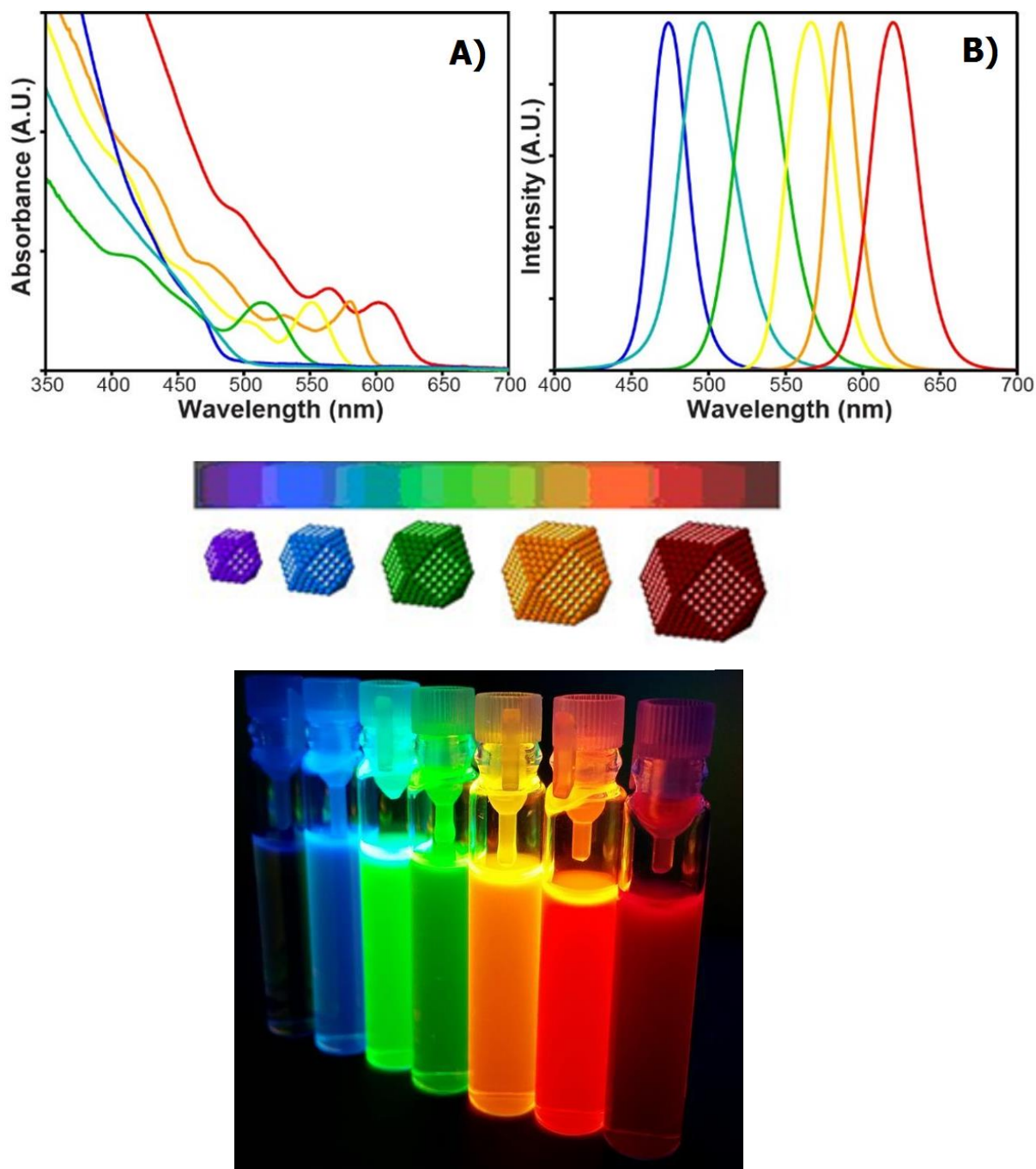
Figure 1-3. Representation of the size-tunable A) UV-Vis and B) PL spectra of CdSe QDs. C) representation of QDs with different PL colours. Reproduced from ref.[9].

UV-Vis spectra of QDs have a characteristic peak corresponding to exciton absorption, the position of which depends on QD size, and then the absorption continuously rises with decreasing the wavelength (Figure 1-3). Thus, QDs absorb light in a very broad region which is useful for many applications.

As QDs emit light when the electrons are transferred from the bottom of the conduction band to the top of the valence band, the QD PL spectrum usually has a single peak with the wavelength corresponding the band gap energy (Figure 1-3). The PL spectrum may also sometimes have peaks related to trap states, which produce a broad, strongly red shifted luminescence.

The PL efficiency is defined by Quantum Yield (QY), which represent a percentage of emitted photons divided by the total absorbed photons. Surface or crystal defects, as well as impurities strongly decrease PL QY, because they form the inter-bandgap energy states increasing the probability of the non-radiative relaxation.

As QDs have a very small size, a large amount of the atoms is located on the surface. This can be quickly estimated to be equal to 24% of the atoms for a 6 nm CdSe QD are upon the QD surface which rises to 35% for a 4 nm CdSe QD, and further to 60% for a 2 nm CdSe QD. The surface interactions strongly influence the electronic states of QDs. Due to this QDs are very sensitive to the interaction with capping ligands, surface oxidation and surface defects formation, especially under illumination.

1.1.2   Synthesis of QDs

Colloidal NPs can be synthesised by different methods including solvothermal[9–11], microwave synthesis[12], and electron beam irradiation[13,14]. However, the most common approach to produce colloidal quantum dots do date is the "hot injection" which was first published in 1993[15].

For the "hot injection" synthesis, the reaction vessel is filled with an appropriate high temperature boiling solvent, ligands and one of the QD precursors (Figure 1-4, A). It is very important to remove all the oxygen and water from the reaction medium to obtain high quality QDs. Then vessel is filled with argon and heated to the certain temperature. At the same time the second precursor in a different flask is dissolved in the solvent and degassed, and then is quickly injected to the reaction vessel with the syringe.
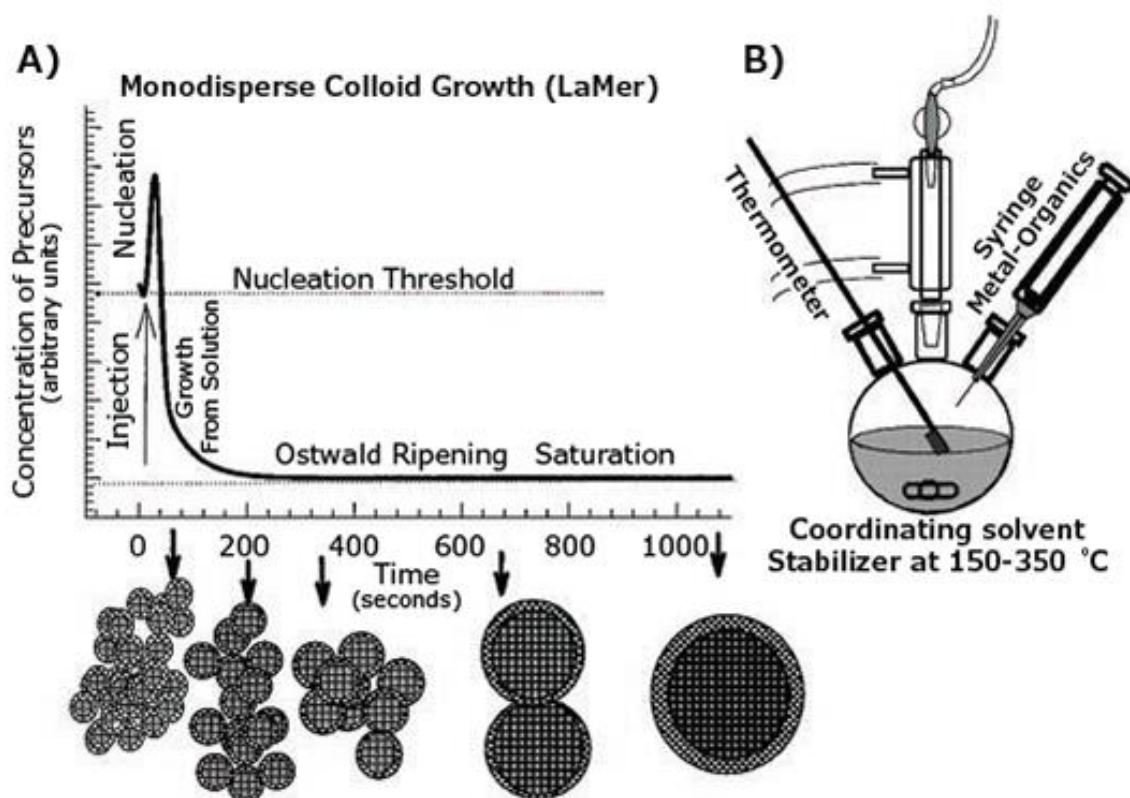
Figure 1-4. A) Schematic of the nucleation and growth stage for the preparation of monodisperse nanocrystals in the framework of the La Mer model. B) Representation of the simple synthetic apparatus employed to prepare monodisperse nanocrystals. Reproduced from ref [16].

Fast injection of precursors creates the supersaturated solution, resulting in the nucleation and crystal growth, which can be described by the LaMermodelforcolloidalgrowth[17] (Figure 1-4, B). The crystal grow rate depends on the crystal size. Sugimoto *et al*.[17] have reported the plot of the growth rate of nanocrystals as a function r/r* and described how crystals above or below this critical size behave (Figure 1-5), where r* is the zero-growth rate nanocrystal radius for a given monomer concentration, otherwise known as the critical size, and r is a crystal radius.
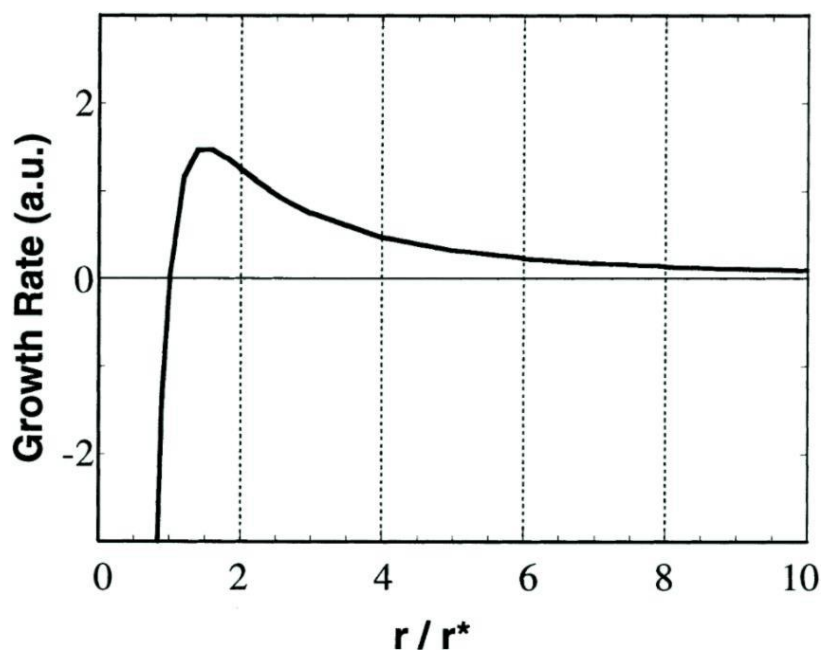
Figure 1-5. Effect of nanocrystal size on growth rate (reproduced from ref [17])

From this model, crystals smaller than r* dissolve, while bigger crystals grow. Besides, maximal rate of growth is achieved when the crystal size is approximately 1.5 times larger than r*; bigger particles have lower growing rate. Normally, in order to obtain the narrow size distribution, QD crystals must be slightly bigger than r*. In this case, small particles grow faster than bigger ones, narrowing the size distribution.

Critical radius r* also depends on the precursor concentration. When concentration become low, r* increases, and smallest particles start to dissolve, while large crystals continue to grow. This process is called Ostwald ripening. To avoid this, the reaction mixture must be cooled down before this starts to happen.

1.1.3   QD properties and their applications in biochemistry and biology

Organic fluorophores and fluorescent dyes are traditionally used for biological imaging[3]. However, the main disadvantage of organic fluorescent probes is their very low photo-stability. By contrast, QDs are resistant to photo-bleaching when compared to traditional dyes, this makes them very attractive candidates for biological imaging. Organic fluorophores mostly undergo photo-degradation after 10-15 minutes, whereas

the QDs can be stable for 5-10 hours under irradiation[3]. Secondly, the size dependent band gap allows the tuning of the optical properties of the QD by controlling the size. Another advantage of QDs is their wide absorption, ranging from UV to near infrared region, thus any laser can be used to excite them. Organic fluorophores have UV-Vis spectra that are generally asymmetric and resonate across a range of frequencies that are considerably narrow[3].

Conversely, the inorganic composition of QDs deems them to be very stable and robust light emitters that makes them attractive fluorophores for sensing and long-lasting bio-labelling applications.

1.1.4 QD composition

Normally II-VI type QDs are made of Cd-containing materials, such as CdTe, CdSe, CdS. These QDs possess a number of advantages: high PL QY and narrow PL spectra, UV-Vis and PL spectra in the visible range, relatively easy synthesis procedure[4,5,18]. However, the cytotoxicity of Cd-containing QDs is the main problem limiting their *in-vivo* application[19,20].

One of the alternative to the Cd-containing QDs are the QDs based on Zn chalcogenides, such as ZnSe or ZnS QDs. These QDs don't display heavy-metal-associated toxicity within living cells and organisms[21,22]. However, these materials have larger band gaps than Cd-based ones and, consequently, they absorb and emit light only in UV and near UV region. It limits their utilization in biology and medicine, because biological tissue has a strong adsorption and auto luminescence in the same region. This problem can be partly solved by doping Zn chalcogenides based materials with transition metal ions, such as Cu or Mn[21,23]. Doping is the adding of very small amounts of a dopant (around 1%). It can dramatically change the optical properties of the QDs. As a result, the PL of doped QDs shifts to a visible spectral region. The mechanism of the PL is shown in Figure 1-6.
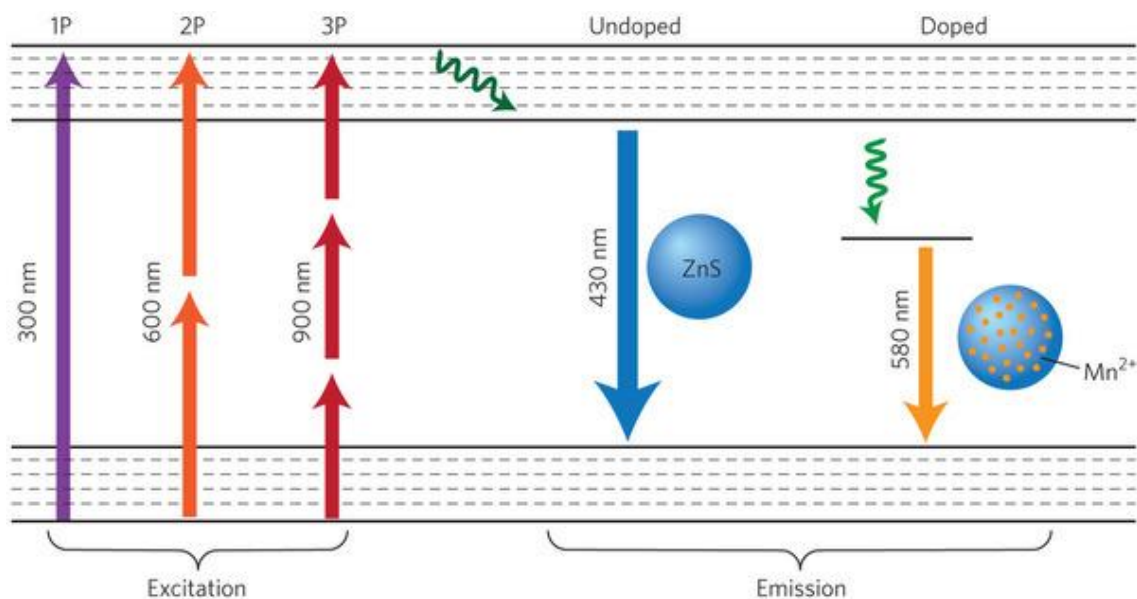
Figure 1-6. Diagram explaining Mn(II) doping effect on ZnS quantum dots. Reproduced from ref. [23].

It wasdemonstrated that doping ZnS QDs with manganese (II) provides an alternative phosphorescent decay pathway through the manganese ions, leading to the very large red-shift compared to the undoped ZnS QDs emission. The phosphorescence of ZnS:Mn QDs occurs as a result of energy transfer from the ZnS to dopant Mn^{2+} ions[23]. As depicted in Figure 1-6, excited electrons jump to the ZnS conduction band as usual, but on relaxation they take a lower energy-requiring pathway via the Mn orbital, that results in the characteristic orange emission of manganese at 585 nm, where biological tissue auto fluorescence is negligible, meaning these QDs are appropriate labels for bio imaging. Because the wavelength of light emitted from such QDs is determined by the presence of the Mn^{2+} dopant, changing the size of these specific QDs will not affect the color of emitted light.

Another problem of ZnS and ZnSe materials is the light absorption is only in the UV and near UV region. The excitation on these wavelengths cannot be used in biology because it is damaging to live cells. This problem can be solved by using the two- or three-photon excitation via a pulse laser. In this case two or three photon can be combine providing double and triple energy respectively. Thus, ZnS:Mn QDs can be excited by three-photon excitation using 920 nm light source within the near-infrared window of biological tissue[23]. An additional advantage of doped Zn-based QDs is phosphorescence

10

has much longer lifetime and can be separated from background auto fluorescence of the biological tissue.

Another alternative to Cd-containing QDs is In-based QDs, such as indium phosphide (InP), copper indium sulphide ($CuInS_2$), silver indium sulphide ($AgInS_2$), etc. However, this type QDs were not used in this work.

1.1.5 Core-Shell QDs

The Physical and chemical properties of semiconductor QDs can be modified by growing shell of another semiconductor material[24]. There are three general types of semiconductor core-shell QD structures depending on band gap size and electron-hole distribution between core and shell (*Figure 1-7*).
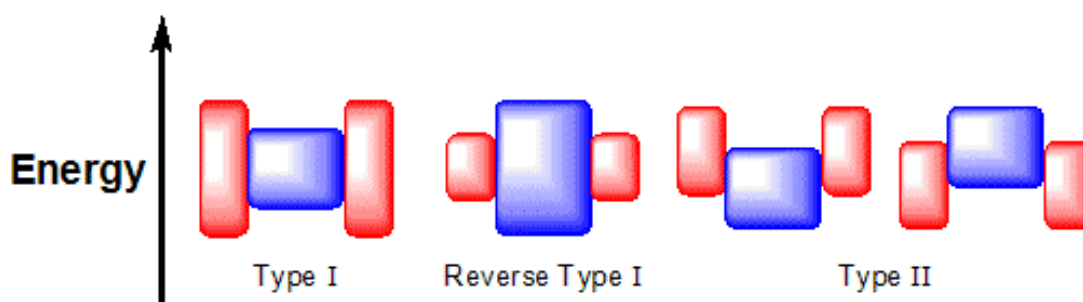
Figure 1-7. Schematic presentation of the three types of core–shell nanocrystals. The upper and lower edges represent the upper and lower energy edges of the core (blue) and the shell (red). Reproduced from https://en.wikipedia.org/wiki/Core– shell_semiconductor_nanocrystal

Type I

QDs of the Type I have the shell made of the material with larger band gap energy than core (*Figure 1-7*). Thus the exciton is confined to the core and have much less contact with environment. The probability of electron transfers and other non-radiative processes become much lower, so PL QY of QDs and stability against photobleaching increase. The growing of the shell thickness results in a red shifting in exciton absorption due to the lattice strain. Examples include CdSe/CdS[25,26], CdS/ZnS[27], ZnSe/ZnS[28] and InP/ZnS[29].

Reverse Type I

QDs of the Reverse Type I have core material with larger band gap energy covered with the shell made of the material with lower band gap energy. This type results in partial exciton delocalisation in the shell. Because the electron is located closer to the surface and interacts easier with the environment, PL QY of these QDs is much lower than Type I QDs. As the exciton is transferred to the lower energy level of the shell, the absorption shifts to the red spectrum region with the shell growth.Examples of QDs of Reverse Type I includeCdS/CdSe[30]andZnSe/CdSe[31].

Type II

The type II QDs have a staggered band alignment, i.e. it is a conductive band or a valence band of the shell material in the band gap of the core material. As a result, the electron and hole are separated. One of the charge carrier is located in the shell and another one in the core material depending on the correlation between energy levels. A bandgap of these QDs is smallerthaneithertheshellorcorematerial, therefore both absorption and emission are strongly red shifted. Examples include CdSe/CdTe[32,33] and ZnSe/ZnTe[34].

Multiple shelled QDs

It is also possible to synthesise QDs with several shell layers consisting of different semiconductor materials. It allows one to obtain the QDs with a thicker shell, with a lower lattice strength and with a range of interactions to take place between the shells. Examples include CdSe/CdS/ZnS[35] and CdTe/CdS/ZnS[36].

1.1.6 Synthesis of core-shell QDs

As for the semiconductor QDs in general, the most commonly used method of QD shell growing is a hot injection colloidal synthesis. During the shell growing it is very important to provide the conditions, at which new homogenous nucleation does not happen and crystal growth occurs only around the cores. For this purpose, the temperature is adjusted to be lower than for core growth and the precursors are added very slowly, dropwise.

It is worth to mention the successiveionlayeradsorptionandreaction (SILAR) approach to grow the shell[37]. In this method anionic and cationic shell layers are grown

by turn due to anionic and cationic precursors, which are added to the reaction vessel separately portion by portion. The amount of precursor in the portion is precisely calculated for one shell monolayer. It allows one to control accurately the shell thickness.

Usually, core and core-shell QDs are spherical, but also it is possible to obtain anisotropic shape of the shell. For this purpose, it is necessary to add the ligand, which binds more strongly to certain crystal faces limiting growth in those directions, for example, hexyl-phosphonic acid[38]. The shell grows only in the direction of the one crystal face and rod-shape structure is obtained[38] (*Figure 1-8*, A). Temperature has a significant impact on the shape control in the synthesis. At high temperature the preferential shell growth along one axis is overcome thermodynamically, leading to spherical shell formation.

It is possible to grow an even more complex shape of the shell, such as a tetrapod-shape[38] (*Figure 1-8*, B). If the shell is forming on the core with cubic structure in presence of limiting ligands, the crystal growth will be preferential upon four faces of the QD, resulting in dot-in tetrapod.
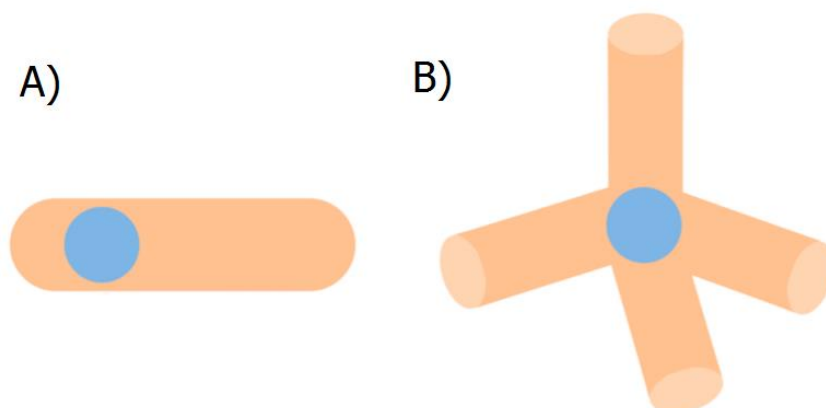
Figure 1-8. A) Dot-in-Rods and B) Dot-in tetrapods was used in the present study to investigate the influence of the shape of the particles on their optical activity and interaction with living cells. Reproduced from ref.[39]

1.2 Chirality

A chiral molecule has two mirror-image forms, known as enantiomers, which are not superimposable in three dimensions. Enantiomers have identical physical properties, and differ only in how they rotate the polarization vector of circular polarized light. Therefore, an enantiomer can be either levorotatory (L) or dextrorotatory (D). This phenomenon of rotating polarized light is specifically known as optical activity and can be directly studied using circular dichroism (CD) spectroscopy[40].

Chirality plays a very important role in biological systems, since most of organic molecules in living organisms are chiral, including amino acids, carbohydrates, proteins and DNA[40]. Chirality strongly influences many biological properties of materials, such as intracellular accumulation, enzymatic activity and toxicity. Also, more than 80% of new drugs are chiral and hence drug enantiomers can influence organisms in significantly different ways. One of the most famous examples of when chirality played a vital role is Thalidomide, which used to alleviate morning sickness in pregnant women. It has two enantiomeric forms (Figure 1-9).

R-(+)-Thalidomide   *S*-(–)-Thalidomide
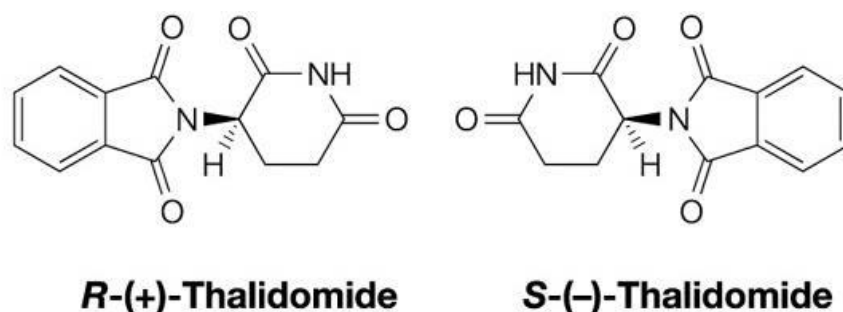
Figure 1-9. The two enantiomeric forms of Thalidomide.

After several years of usage of thalidomide for clinical purposes it appeared to be that one of the enantiomers led to irreparable birth defects. This very clear example of importance of knowledge about chirality and the use of chiral substances. Therefore, the ability to analyse, interpret and apply the properties of chirality is highly important in the fields of chemistry, pharmacology, biology and medicine.

1.3   Chirality and optical activity of NPs

The area of chirality-related research in nanoscience is relatively new but it is rapidly expanding (Figure 1-10), due to the numerous potential applications of chiral NPs, such as catalysis and sensing[41–44].
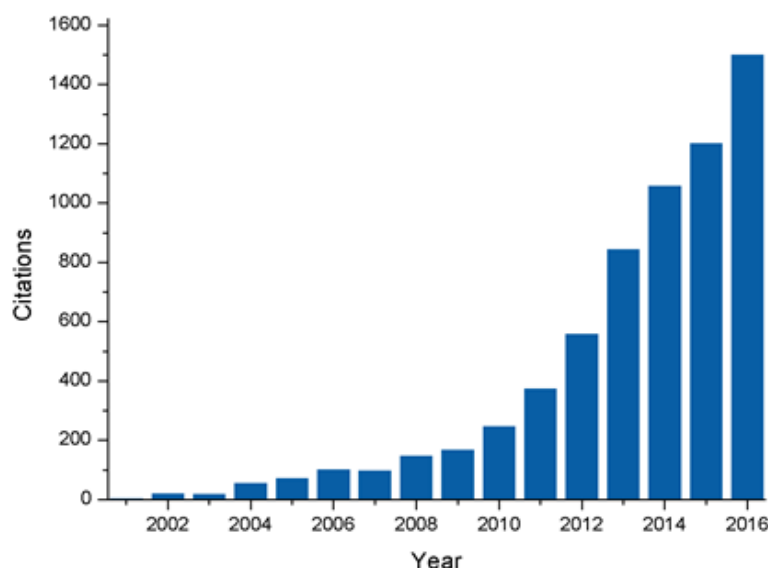
Figure 1-10. Number of citations for publications about chiral nanomaterials by year.

Chirality may be induced in nanomaterials by the variety of ways. Firstly, nanomaterials may be grown to be structurally chiral, such as the growth of chiral CdTe nanoribbons[45]. Secondly, inorganic materials may be combined with an organic chiral scaffold, such as DNA, in order to create chiral NP assemblies as has been shown for a variety of NPs including gold and silver[46]. Thirdly, the use of chiral ligands in the aqueous synthesis of NPs has been shown to produce NPs which demonstrate optical activity, such as penicillamine capped CdS QDs[47]. Finally, optical activity may be induced in colloidal NPs through the exchange of the original achiral ligands with chiral ligands, such as cysteine or penicillamine[41,48]. Such NPs enantiomers display mirror image CD signals in the exciton region, where chiral ligands don't absorb light. Induction of optical activity in the spectral region of QD exciton absorption after the ligand exchange can be attributed to the hybridization of QD valence band states with the HOMO/LUMO orbitals of the chiral D- and L-Cys ligands[49,50]. All these approaches are discussed in details bellow.

1.3.1 Chiral structures and chiral assemblies of NPs

NPs can be synthesised as chiral structures, such as single helixes. For example, nano-helices were made out of silica and titania[51–56]. Besides, achiral NPs can be arranged in chiral structures by macro-assemblies, such as helices. It can be chiral self-assembly or binding of NPs to the chiral scaffold such as DNA or RNA.

An Interesting example of self-assembly was published by Kotov et al.[45], where achiral CdTe QDs capped with mercaptopropionic acid, when interacted with circularly polarised light, resulted in either left or right handed twisted ribbons demonstrating high degrees of optical activity (Figure 1-11).
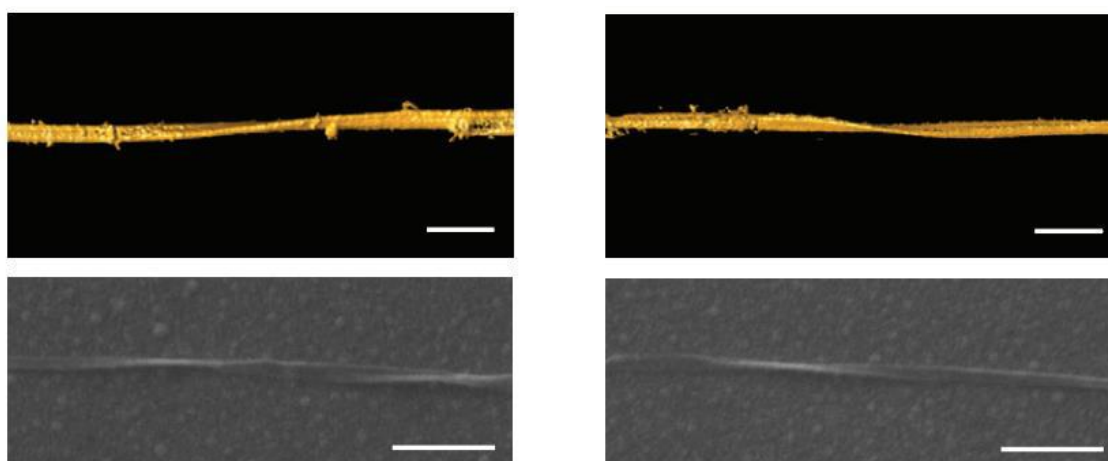
Figure 1-11. Left and right-handed CdTe nanoribbons (reproduced from ref.[45])

The large optical activity of these structures is explained by the long-range order of NPs in a chiral arrangement. The magnitude of the CD response is proportional to the size of the structure, and thus these assemblies exhibit much stronger CD and CPL signals compared to single chiral nanoparticles.

1.3.2 Intrinsic chirality of NPs

Intrinsic crystal chirality

NPs can have a chiral surface or an entire structure and demonstrate optical activity without any external influences of chiral ligands or scaffolding. For example, quartz, β-AgSe, α-HgS, selenium, and tellurium crystals have chiral lattice structure and synthesized NPs have 2 enantiomers. To obtain a pure enantiomeric form of the NPs, enantiomers can be separated after synthesis using thiolated chiral biomolecules[57], or chiral molecules can be added during synthesis to initiate the formation of the certain enantiomeric crystal lattice[58].

Some materials have chiral surfaces. For example, it was shown that kinked-stepped, high miller index surfaces on copper are chiral and therefore display enantioselective properties[59] (Figure 1-12).
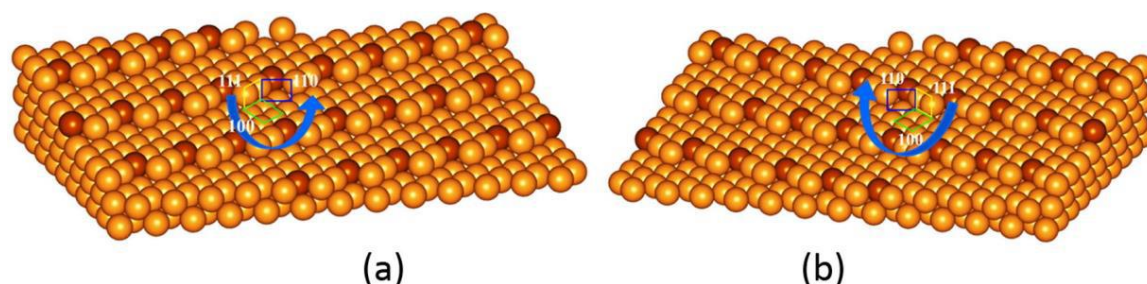
Figure 1-12. Chiral (a) Cu(3,1,17)S and (b) Cu (3,1,17)R surfaces (reproduced from ref. [60])

Chiral defects (screw dislocation)

QDs obtained by traditional hot injection synthesis without any chiral ligands can have chiral defects in their crystal structure, such as screw dislocation[48] (*Figure 1-13*). The post-synthesis QD solution is a racemic mixture of QDs with left- and right-hand chiral dislocations and does not demonstrate any CD signal. The mixture can be enantioselectivelly enriched using BSA[45] or L- and D-cysteine[61] since chiral molecules have different binding affinity to QDs with left- and right-hand chiral defects. The Enriched solution has optical activity even after removing the chiral ligands.
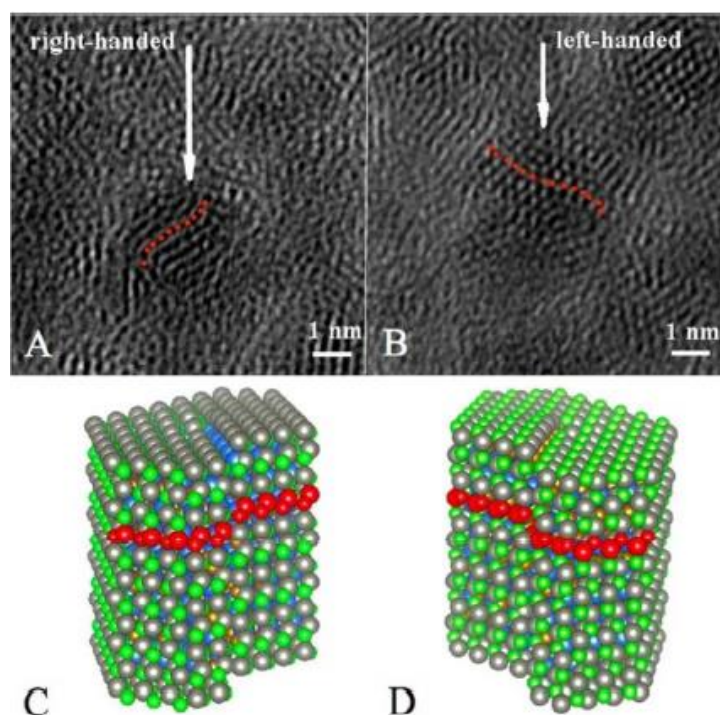
Figure 1-13. (A, B) TEM images of the CdSe/ZnS QDs. The arrows indicate possible screw dislocations. (C, D) Atomistic models of CdSe/ZnS QDs with right (C) and left (D) screw dislocations. Dislocations are set in the (010) plane of CdSe core of nanocrystals with (-) Burgers vector (C) and (+) Burgers vector (D). Red dotted lines indicate the direction of the dislocations. Reproduced from ref. [48].

Chiralimprinting

Surface chirality can be formed on QDs by chiral imprinting[62]. When QDs are synthesised in the present of chiral substances such as cysteine or penicillamine, the chiral molecule bound to the growing crystal contribute to the formation of chiral defect of the crystal surface. In this case QDs demonstrate the optical activity even after removing the organic ligands[63]. Moloney was the first to synthesis chiral QDs using this method[47]. Chiral CdS QDs were obtained by aqueous microwave synthesis in the presence of D- or L-penicillamine. Gallagher *et al*. used a similar microwave synthesis techniques to obtain chiral CdSe QDs stabilised with D- and L- penicillamine[18]. Semiconductor NPs with chiral surface can be produced without using microwave treatment as well. Chiral CdTe QDs[64] and CdS tetrapods[65]were also produced using reflux heating methods in the presence of chiral molecules.

1.3.3 Ligand-induced optical activity in NPs

NPs can obtain optical activity due to interaction with chiral organic ligand. Firstly, the effect was demonstrated for metallic nanoparticles such as gold and silver nanoparticles. But it has been found as a common effect for many kinds of NPs.

In 2000 by Schaff et al. reported that L-glutathione capped gold nanoparticles demonstrated optical activity[66]. Similarly, Yao et al. showed in 2005 that gold NPs covered with D- and L-penicillamine possessed mirror image CD spectra[67]. After that the effect of ligand induced optical activity was widely investigated on plasmonic NPs[68–70].

Govorov et al. has reported the theoretical analysis of chiral ligand interaction with gold NPs and developed a model for ligand induced optical activity[71,72]. The researchers have shown thatCD signal of the chiral ligands is enhanced by Coulombic coupling with the plasmonic resonance of the metal nanoparticle and at the same time the plasmonic absorption of the nanoparticle was influenced due to the dipole-dipole interaction with the chiral surface ligand. The induced optical activity is originating mostly from the second effect. NPs obtained the CD signal in the intrinsic absorption region where ligands do not absorb the light[71,72].

Capping semiconductor QDs with chiral ligands can induce the optical activity in them as well, but the mechanism is different, which will be discussed below.

1.3.4 Ligand-induced optical activity in QDs

Optically active QDs can be produced by post-synthesis phase transfer technique, by which QDs synthesised in organic phase by hot-injection method are covered by hydrophilic chiral molecules and transferred to aqueous phase. Hot- injection synthesis has many advantages comparing to aqueous: high crystallinity of QDs, high PL quantum yield, more approaches and possibilities to influence the size and shape of NPs.

Ligand exchange technique was pioneered by M. Balaz *et al*[49]. They transferred trioctylphosphine oxide covered CdSe QDs from toluene into the aqueous phase using

chiral ligands. As the result, QDs obtained CD signal. The authors have explained the origin of the induced CD in QDs by the hybridisation of the chiral ligand's HOMOs with the CdSe hole level orbitals.

Normally, QDs are spherical in shape, however by adjusting the reaction conditions a variety of different nanostructures may be formed, including dot in rods (DiRs) or dot in tetrapods (TPs)[38,65,73]. Anisotropic DiR and TPs nanostructures have a high aspect ratio and are expected to interact differently with chiral molecules during ligand exchange and, consequently, NPs with unusual shape might have stronger chiral response than spherical QDs and can potentially demonstrate circularly polarized emission[44,48,74].

1.4 Chiral and optically active QDs in biology, biochemistry and medicine

1.4.1 Biological applications of QDs

The QDs have potential application in biology and medicine for bio sensing, cell imaging, fluorescent assays, photodynamic therapy and many others (Figure 1-14)[75].

As it was mentioned above, QDs have much higher photo stability than organic fluorescence dyes. Therefore, QDs are a very good fluorescent labels for long-term biological processes. Besides, QDs have other advantages: a tuneable PL, which give a possibility to make the labels with different colours from the same material; and wide range of absorption, allowing the use of different lasers.

PL of QDs can be quenched by different factors, such as FRET, electron transfer and other non-radiative processes[50,76]. This can happen, for example, when some molecule binds to QDs or is located very close to it, as well as when pH or other solution properties change[6,77,78]. Thus, QDs can be used as sensors for the specific chemical substances or media states. For these purposes, QDs can be functionalised with substrate-specific ligands or receptor units, appropriate for sensing.
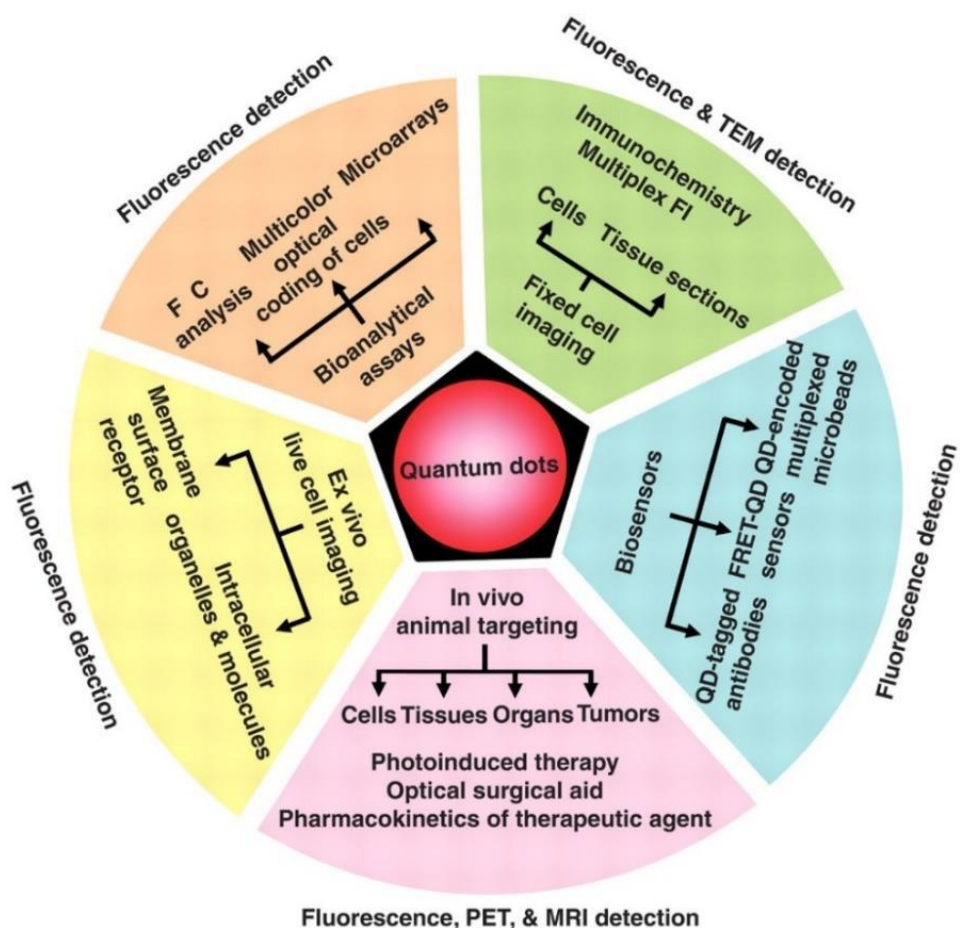
Figure 1-14. The numerous uses for quantum dots in biomedical applications.

Reproduced from ref. [75]

1.4.2 Chiral QDs for enantioselective sensing

One of the main potential applications of the chiral and optically active QDs is chiral molecule sensing. For example, chiral CdSe-ZnS core-shell QDs were used for enantioselective sensing of drugs such as naproxen and ibuprofen. It was shown that the chiral molecules quenched the QD PL enantioselectively and with linear dependence on concentration[79]. Another example of chiral sensing is selective quenching of CdSe/ZnS QDs covered with a thiolated β- cyclodextrin by D- and L- penicillamine[80].

1.4.3 The interaction of chiral QDs with living cells

An acquisition by nanostructure chiral properties should lead to significant changing in their interactions with biomolecules and biological behavior[44]. It opens up new possibilities to realize stereospecific interactions of nanostructures with biological objects. These chiral QDs could find potential applications in biomedical research, therapy and diagnostics. Consequently, it is very important to investigate the interaction of chiral QDs with living cells.

It has been recently shown that NPs capped with opposite enantiomers of chiral ligands demonstrate different biological activity, including cellular accumulation and cytotoxicity within living cells[41,43,81]. Despite the fact that chiral NPs are widely investigated, there are only a few reports devoted to their interaction with living cells and therefore this research area is still unexplored.

1.5 Influence of QDs on optical activity of chiral molecule

Since the first observation of induced chirality in CdS quantum dots (QDs) capped with a chiral penicillamine ligand[47], a lot of effort has been made to investigate the ligand induced chirality in QDs. At the same time, there are no systematic studies of the opposite effects: the influence of semiconductor nanocrystals on optical activity of surface molecules, nevertheless such studies are crucial since chiroptical properties of molecules can be significantly changed near a NC's.

As it was mentioned above, the Balaz et al[49] experiment demonstrated that a QD's optical activity can be acquired as a result of hybridization of the ligand HOMO with the QD valence band states. This interaction must influence not only NP chiral properties, but also chiral molecule itself. Indeed, it was shown that the optical activity of chiral molecules can be altered in the presence of achiral CdSe/ZnS QDs[82]. Moreover, penicillamine molecules attached to the surface of CdS QDs, display a reversed circular dichroism (CD) signal compared to that of free molecules[43]. Such reversal of CD signals after molecule

adsorption onto the QD surface has been also reported for glutathione molecules and CdTe QDs[83].

Potentially the change in optical activity of a molecule can be accompanied by a transformation of its spatial configuration and functional properties. Therefore, studying of NP influence on the chiral properties of organic molecules is of great interest from a fundamental and applied point of view.

1.6   Photodynamic therapy

Photodynamic therapy (PDT) is cancer treatment is based on the ability of photosensitizer to selectively accumulate in the cancer cells and to generate singlet oxygen under an appropriate light irradiation, which destroys the cancer cells[84–86]. Photosensitizers usually have narrow UV-Vis absorption bands, while QDs absorb the light at a very broad wavelengths region and have much higher extinction coefficient. QDs can transfer energy to photosensitizers by FRET mechanism, so they can be used as an effective energy donor for photodynamic therapy[87,88]. It was shown that QDs increased the efficiency of singlet oxygen generation by photosensitizers[89–92]. Experiments on cells revealed that using complexes of QDs with photosensitizers increase the PDT occasioned cell destruction ability comparing to pure photosensitizers[93–95].

Chlorin e6 is one of the photosensitises used nowadays in medical practise[96]. It is a porphyrin with the formula represented in Figure 1-15. It was shown in many studies that QDs are able to effectively transfer excitation energy to Chlorin e6 by FRET mechanism[87,97–99] and such complexes can increase the generation of singlet oxygen[89–92].
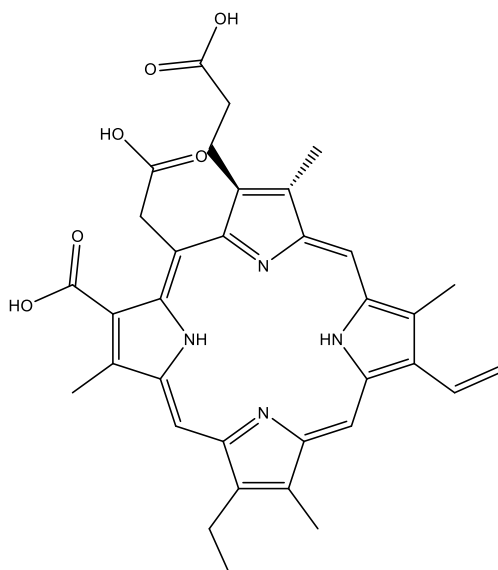
Figure 1-15. Formula of Chlorin e6.

1.7 Aims of the project

The main aim of our studies is to develop new chiral quantum dot based nanomaterials of different shapes and investigate their biological behavior and interactions with living cells, varying the NP shape and composition.

Our technical objectives include the development of optimal CdSe/CdS QD nanostructures for investigation of interaction with biological objects, where QDs must display a chiral response as well as high PL quantum yield. For this purpose, the influence of CdS shell thickness, synthesis duration and ligand concentration on QD CD and PL intensity are to be determined. We also aim to investigate optical properties of NPs with different shape and composition (CdSe/CdS DiRs and TPs and spherical ZnS:Mn QDs) for further intracellular assays.

Since the interaction of chiral NPs with living cells occur in specific biological medium, which contains a lot of chiral molecules, we also will investigate the influence of biological cell culture medium on NP properties, including NP induced chirality. We aim to perform a number of *in vitro* studies focusing on the chiral NPs cellular uptake and cytotoxicity within a selected cancer cell line, A549 cells.

24

And finally, we plan to investigate how QDs influence a chiral molecules optical activity using the example of the chiral photosensitizer Chlorin e6. We aim to study optical properties and FRET efficiency in the synthesised complexes of QDs with Chlorin e6 and test them for PDT on living cells.

We expect that these studies of QD nanomaterials will find important biomedical applications including the development of new chiral imaging probes for various chemical and biological systems and PDT agents.

2 Chapter 2. Experimental

2.1 Starting materials and general procedures

All starting materials were supplied by Fischer Scientific and Sigma Aldrich unless stated otherwise, Solvents (HPLC grade) were obtained from the solvents stores in Trinity College and used without purification unless stated otherwise. Millipore water was prepared by filtering water through a MilliQ 18MΩ system.

Materials for biological experiments were purchased from Invitrogen. Glass-bottomed Petri dishes and μ-slides were supplied by Ibidi.

A Hettich Zentrifugen Universal 32 was used for centrifugation of large volumes, namely for fractioning and cleaning of QDs. For small volumes and higher speed required to wash and phase transfer of nanoparticles, a Hermle Z233 M-2 was used.

For ultrasonic agitation, a Grant XB6 ultrasonic bath was used.

2.2 Cell culturing and cell viability testing.

Two cell lines were used in this research: the human lung derived A549 cancer line and The Ehrlich ascites carcinoma (EAC) cell culture.

The A549 cancer cell line was purchased from ATCC (American Tissue Culture Collection, Rockville, MD). A549 were grown in supplemented DMEM medium (Gibco/Invitrogen, La Jolla, CA) containing 4.5 g L−1 glucose, 10% FBS, and 5 mg L−1 gentamicin in the incubator at 37 °C supplied with 5% CO2. The Ehrlich ascites carcinoma (EAC) cell culture was obtained from the Petrov Research Institute of Oncology from white laboratory mice with an average weight of 20 g after 8–9 days of ascite growth. The mice were killed by cervical dislocation. The cell suspension was purified from the erythrocytes by 5 min treatment with a lysis buffer (0.01 mol tris HCl, 0.87% NH_4Cl, pH=7.4). The cells were then washed twice with Hank's Balanced Salt Solution (HBSS) and resuspended in RPMI-1640 medium with 10% of bovine embryonic serum and 100 U ml^{-1} penicillin.

Cell concentration in media was determined *via* Countess Automated Cell Counter with Trypan Blue Stain.

Cell microscopy was performed *via* laser scanning confocal microscopy (LSCM) using ZEISS LSM 510 Meta confocal microscope equipped with a Zeiss Zen software.

Cell count and QD fluorescence inside cells was measured with BD Accuri C6 flow cytometer.

2.3   Experimental details for chapter 3 and 4

2.3.1   Synthesis of CdSe QDs

CdSe QDs have been prepared according to Chen et al.[100]using a scaled up and modified by us procedure. A 0.2 M Cd-oleate stock solution (in ODE) was prepared by adding 0.257 g of CdO to 2 mL of oleic acid in 8 mL of ODE, degassing it under reduced pressure, and then heating to 300 °C under argon, followed by cooling to 30 °C. A 1.5 M Se-TOP solution was prepared by dissolving 0.3553 g of Se in 3 mL of TOP using sonication under argon. Next, CdSe core nanocrystals were prepared by mixing 4.5 g of octadecylamine, 1.5 g of TOPO, 12 g of ODE, and 3 mL of Cd-oleate solution in a three-neck round-bottom flask. This mixture was then degassed at 90 °C for 30 min, flashed with argon, and then heated to 290 °C. Upon reaching this temperature, the Se-TOP solution above was injected and the reaction vessel was immediately removed from the heat. The solution was allowed to cool to room temperature, followed by the addition of 20 mL of acetone to the mixture to precipitate QDs and centrifugation for 5 min at 9 000 rpm.

2.3.2   Synthesis of CdSe/CdS core/shell QDs

This synthesis was carried out as per Mahler et al.[101]using a modified by us procedure. The volumes used were calculated using SILAR approach to control the thickness of CdS deposited precisely. Initially, a 0.1 M cadmium stock solution was prepared by adding 0.514 g (4 mmol) of CdO to 8 mL of oleic acid and 32 mL of ODE, which was degassed and then heated to 300 °C under argon, and then cooled to 30 °C. A 0.1 M sulphur stock solution was prepared by dissolving 0.128 g (4 mmol) of sulphur in 40 mL of ODE at 180 °C under argon (should appear as a yellow solution, changing from a very light straw colour at 120 °C). Next, 33.2 mL of oleylamine, 66.4 mL of ODE, and 2.24×10^{-6} mol of QDs were added to a 250 mL three-neck round-bottom flask (concentration of CdSe

QDs was calculated using well known method described by X. Peng and Co. in 2003[102] according to which the extinction coefficient and exciton peak wavelength of QDs are determined by QD size). This mixture was heated to 50 °C and degassed for 60 min, followed by injection of 4.6 mL of Cd stock solution and then heating to 230 °C. The calculation of the volume of the precursors added for each leayer can be found in Table 2-1.

Amount of QDs in sample, μmol	2.24
Density of CdS, g/ml	4.82
Molar mass of CdS, g/mol	144.46
Lattice parameter of CdS, nm	0.333

Number of layer	QD Radius, nm	Volume of layer of QD, nm^3	Volume of reaction mixture in flask	Amount of QDs left in flask, μmol	Amount of CdS in each layer of sample, μmol	Volume of 0.1M precursor (mL)
0	1.4	11.5	99.6	2.24		
1	1.7	21.8	108.9	2.24	464	**4.6**
2	2.1	36.9	94.4	1.73	525	**5.2**
3	2.4	57.8	83.2	1.65	691	**6.9**
4	2.7	85.4	71.6	1.21	669	**6.7**
5	3.1	120.5	61.7	1.07	757	**7.6**

Table 2-1. Summary of CdSe/CdS optical properties and morphology properties in the organic phase, where φ is the photoluminescent quantum yield, while <τ> is the average photoluminescence decay lifetime. The given diameters were determined by TEM, while the shell thickness was calculated from the original core diameter.

After 10 min at this temperature, 4.6 mL of sulphur solution was injected using a syringe, followed by a 10 min wait. The reaction was then heated to 250 °C for 1 h to fully allow the reaction to complete the growth of the first shell. At this time, 25 mL of the reaction solution was removed and allowed to cool under argon, producing the first sample. Then following the same procedure, 5.2 mL of 0.1 M Cd and S stock solution was

added to grow the second shell, removing 25 mL of reaction solution again to produce the second shell sample. This overall procedure was repeated three times further, injecting 6.9 mL for shell 3, 6.7 mL for shell 4, and 7.6 mL for shell 5, following which the solution was allowed to cool to room temperature, at which time 20 mL of acetone was added to precipitate the samples and isolate the precipitate using centrifugation. The precipitate was then redispersed in a minimum volume of hexane and precipitated again using acetone. This procedure was repeated twice to produce a cleaned sample.

2.3.3 Synthesis of Annealed CdSe/CdS QDs.

The synthesis was carried out as described above, but between each injection, the reaction was only heated to 230 °C for 10 min. In addition, aliquots were not removed from the reaction between shell growth. After the five-shell injection, an annealing step was included at the end of the experiment, heating to 250° C, for 4 h in total, and aliquots were taken out at a range of times, with each aliquot cleaned as described above and used for further studies.

2.3.4 Ligand Exchange of the CdSe/CdS Core/Shell Quantum Dots with Chiral Cysteine Molecules.

The cysteine ligand exchange was carried out using the previously reported method[103] with some modifications. Briefly, 750 μL of CdSe/CdS QDs in chloroform with the concentration of 12 μM was precipitated with methanol (1 mL). Centrifugation was used to separate precipitated QDs from solution, which were re-dissolved in chloroform (750 μL). Then 75 μL of a cysteine solution in methanol (0.27 M) was added to the QD chloroform solution, shaken, and left for 2 min. Next, 750 μL of an aqueous 0.01 M KOH solution was added, therefore adjusting the pH to 12 and forming a bilayer solution. The layers were then mixed by gentle inversions multiple times until the majority of the QDs were transferred to the aqueous layer, as indicated by colour change. The sample was then centrifuged in order to fully separate the layers and remove aggregates (15 000 rpm, 1 min). Finally, the aqueous layer was extracted using a pipet and stored in the fridge at the temperature between 2 and 5 °C.

2.4 Experimental details for chapter 5

CdSe/CdS core/shell QDs with 5 CdS monolayers were synthesized by the method described above.

2.4.1 Synthesis of ZnS:Mn quantum dots

ZnS:Mn quantum dots have been prepared by previously reported procedure[23].

0.4 g (2.9 mmol) of $ZnCl_2$ and 0.02 g (0.1 mmol) of $MnCl_2.4H_2O$ were dissolved in 54 mL of dibenzylamine and heated under vacuum at 120°C for 2 hours (named pot 1). A separate solution must be made up of 0.8 g (5.8 mmol) of $ZnCl_2$ in dibenzylamine and heated under vacuum at 120°C for 1 hour (named pot 2). The pot 1 solution was then cooled down to 50°C and removed from vacuum and 0.6 g (18.7 mmol) of sulphur powder was added. After that the solution was heated to 260°C under argon and held at this temperature for 15 minutes. The solution was then cooled to 160°. 5 mL of the pot 2 solution and heated again to 260°C and held at that temperature for a further 15 minutes. The solution was then cooled to around 160°C and ethanol was added to precipitate out the quantum dots. The quantum dots were then washed and centrifuged several times with ethanol in order remove excess of sulphur until the supernatant was no longer yellow. Once cleaned, the quantum dots were stored in chloroform (20 mL) and 100 µL of oleylamine was added for improved colloidal stability.

2.4.2 Dot in rod and Tetrapod synthesis.

The dot in rod and tetrapods used in this chapter were synthesized by first preparing either wurtzite (for DiRs) or zinc blende CdSe (for TPs) nanocrystals. These seeds were produced by hot injection into a solution of cadmium, octadecylphosphonic acid, propylphosphonic acid, trioctylphosphine and trioctylphosphine oxide according to published procedure[38]. The preparation of the seed solutions, the Cd/ODPA/PPA/TOP/TOPO solution, and the subsequent DiR and TP synthesis are described below.

Synthesis of wurtzite CdSe QDs

CdSe QDs have been prepared using previously reported procedure[38].

A solution of 25.9 mmol (10.g) of TOPO and 20.7 mmol (5.00 g) of hexadyclamine were mixed in a 50 mL three-neck flask and held at 110 °C for 50 minutes under vacuum. In an inert atmosphere under argon, 1.68 mmol (0.3 g) of octadecylphosphonic acid was added and the reaction mixture was degassed for 5 minutes under vacuum. The solution was then heated to 300 °C under argon, and a solution of 1 mmol of TOPSe and 1.64 mmol of CdMe$_2$ in 5 mL of TOP was rapidly injected into the mixture with constant stirring. The reaction mixture was held at 300 °C under argon overnight. The reaction vessel was then cooled to room temperature at which point the reaction mixture becomes solid and then dissolved in anhydrous toluene. Any remaining solids were centrifuged out and the resultant mixture was then precipitated using anhydrous ethanol and redissolved in toluene.

Synthesis of zinc blende CdSe QDs

CdSe QDs with zinc blende structure have been prepared using previously reported procedure[38].

0.6 mmol (0.34 g) of cadmium myristate was dissolved in 1-octadecene in a 100 mL 3-neck round bottomed flask. The mixture was then degassed by heating to 90 °C and holding it for 40 minutes under vacuum. The resultant solution was cooled to room temperature, at which point 0.3 mmol (0.024 g) of selenium powder (99.999%) is added. The solution was then degassed for 10 min at 50 °C. After that the solution was heated to 240 °C at a rate of 20 degrees per minute and held at this temperature for 3 minutes. At this point a solution of 0.1 mL of oleic acid and 1 mL of oleylamine in ODE (4 mL) was added dropwise. The reaction was then cooled to room temperature and the resultant QDs were precipitated with ethanol and redispersed in hexane.

Preparation of initial solutions for synthesis of CdSe/CdS DiRs and TPs

CdSe/CdS DiRs have been prepared according to previously published procedure[38].

A 25 mL three neck round bottomed flask was loaded with CdO (0.207 g, 1.61 mmol), n-octadecylphosphonic acid (1.08 g, 3.23 mmol), n-propylphosphonic acid (0.015 g, 0.12 mmol) and TOPO (3.35g, 9.18 mmol) and the mixture was degassed under vacuum

at 120 °C for 30 minutes. The mixture was then heated to 320 °C under argon until a clear solution was obtained. Once the CdO had dissolved completely the solutions was cooled to 120 °C and once again placed under vacuum for a further 2 hours. It was then heated to 340 °C (for dot in rods) or 300 °C (for tetrapods) under argon. TOP (1.5 g, 4.05 mmol) was then injected and the solution was allowed to heat up to either 340 °C or 300 °C for either rods or tetrapods respectively. For subsequent sections this solution will be known as solution **1**.

Separately, TOPS was prepared by reacting equimolar amounts of TOP and elemental sulphur at 50 °C under inert atmosphere.

Synthesis of CdSe/CdS dot in rods

CdSe/CdS tetrapods have been prepared according to previously published procedure[38].

TOPS (0.3 g, 1.61 mmol) was injected into solution **1** at 340 °C. After twenty seconds, ~10^{-8} mol of wurtzite CdSe seeds dissolved in TOP (0.5 g, 1.35 mmol) was injected. The wurtzite CdSe QD solution was prepared by taking 1 mL of the lower concentration stock solution and reducing it to approximately 50 µL and adding TOP (0.5 g). The temperature of the reaction was adjusted to 320 °C and was kept at that temperature for 10 minutes. Anhydrous toluene was then used to quench the reaction and it was removed from the heat. The room temperature crude solution was diluted with toluene and the dot-in-rods were precipitated using ethanol. After centrifugation the pellet was redispersed in 8:1 hexane/octylamine and precipitated again using ethanol. The DiRs were then stored in toluene.

Synthesis of CdSe/CdS tetrapods

CdSe/CdS tetrapods have been prepared according to previously published procedure[38].

TOPS (0.65 g) was injected into solution **1** at 300 °C. After forty seconds, ~10^{-8} mol of zinc blende CdSe seeds dissolved in TOP (0.5 g, 1.35 mmol) was injected. The temperature of the reaction was increased to 315 °C and was kept at that temperature

for 20 minutes. The solution was then cooled to room temperature. The room temperature crude solution was diluted with toluene and the tetrapods were precipitated using acetone. After centrifugation the pellet was redispersed in 8:1 hexane/octylamine and precipitated again using acetone. The tetrapods were then stored in toluene.

2.4.3 The investigation of the QDs aggregation in biological medium

The aggregation of QDs in biological medium was established using DLS. To stabilize QDs in biological medium, 0.3 mg mL−1 of bovine serum albumin (BSA) was added to the aqueous solutions of L- and D-cysteine stabilized QDs (L-Cys-QDs and D-Cys-QDs) at a concentration of 32 µM and incubated in darkness overnight at room temperature. The resulting L–/D-CysBSA-QDs and initial L–/ D-CysQDs were added to Dulbecco's modified Eagle medium (DMEM) containing 10% fetal bovine serum (FBS) (additions of QDs were 10% of volume). Samples were incubated overnight at room temperature and then DLS spectra were recorded.

2.4.4 Cell viability assessment by high content screening

For cytotoxicity assays, the A549 cells were seeded in 96-well plates in 100 µL supplement DMEM medium at 37 °C for 24 h. Cell density was 5×10^3 cells/well. L- and D-Cys-QDs were incubated overnight with 0.3 mg mL^{-1} of BSA. Then QDs mixed with DMEM containing 10% FBS were added to cells and incubated at 37 °C for 24 h. QDs concentration ranged from 4–32 µM, the volume of maximum addition was 10 µL per well (10% of medium volume). After fixation with 3.7% formaldehyde solution for 30 min the cellular nuclei were stained with Hoechst 33432 dye and a cell imaging and recording was carried out using Cytell Cell Imaging System (GE Healthcare, Buckinghamshire, UK). Cell viability was estimated by high content screening (HCS) analysis using the preinstalled GE Cell Viability BioApp 2-color protocol at 10x magnification. Ten random fields were imaged across the entire well area of each QDs concentration exposure point. Exposures were repeated three times. Average cell viability was calculated comparing data from experimental samples and negative control. Positive control was 100 µM Valinomycin as indicated.

33

2.4.5 Confocal imaging of living cells

Incubation of A549 or EAC cells with QDs was carried out in 6-well plates with cover slide glass bottom (ThermoFisher, USA) in DMEM and RPMI-1640 medium, respectively, containing 10% of bovine embryonic serum and 100 U ml−1 penicillin at 37 °C, 5% CO_2, 90% relative humidity. QD concentration was 1 µmol L^{-1}. After incubation the cells were washed 3 times with PBS and fixed. Confocal images were recorded with a LSM 710 (Zeiss) laser scanning confocal microscope. QDs were excited with a diode laser 405 nm line. The emission was measured in the spectral region 500–560 nm corresponding to the QD emission band of 530 nm. The mean fluorescence signal per cell was quantitatively estimated using 'ImageJ' software (Wayne Rasband). Five independent measurements were performed after which the average fluorescence signal per cell and the respective standard deviations (SDs) were calculated by selecting 100 cells randomly observed on the fluorescence images. Fluorescence spectra of L- or D-Cys QDs in living cells were obtained using standard operation modes of the LSM 710, which allows collection of the emission from the region of interest within the sample.

2.4.6 Fluorescence lifetime imaging studies

Fluorescence lifetime imaging was performed using a time correlated single photon counting (TCSPC) spectrometer (PicoQuant, Inc.) equipped with a ×40/0.65NA objective. A pulse laser radiation (405 nm) with an average power of 1 mW, pulse duration of 70 ps and repetition rate of 40 MHz was used for fluorescence excitation. A 500–560 nm band pass filter was used to collect the QD emission. The measurements of fluorescence lifetime for D-Cys, L-Cys and TOPO-QD solutions were made with the QD concentration of 0.5 µmol/L. Prior to obtaining fluorescence lifetime images of EAC cells with QDs, the EAC cells were incubated with D-Cys or L-Cys QDs for 3, 6, 24, 48 and 96 h under the previously described conditions. The concentration of QDs was equal to 10 µmol/L. The following protocol was used for image acquisition. Cells were washed 3 times, suspended in HBSS and loaded into the glass hemocytometer. Data acquisition was performed from a 75×75 µm^2 area with a 512×512 pixels spatial resolution with a collection time of 5 ms per pixel. Parameters were chosen so that unlabelled cell auto fluorescence did not yield a measurable signal. All experiments were carried out under

the same instrumental settings. The fluorescence lifetime image presents a 512×512 pixel 2D matrix with a measured FL lifetime value at each pixel. The QD PL lifetime was found to be well fitted by a multi-exponential decay model:

$$I(t) = \sum_n A_n \exp(-t/\tau_n)$$

Equation 2-1. Multi-exponential decay model QD PL lifetime, where A_n are the amplitudes and τ_n are the fluorescent lifetimes.

The fitting procedure was performed using the SymPhoTime 64 software (PicoQuant, Inc.).

2.4.7 PL imaging of cells

Incubation of A549 cells with NPs was carried out in 96-well plates in DMEM containing 10% of FBS and 5 µg/ml gentamicin at 37 °C, 5% CO_2, 90% relative humidity for 24 h. NPs concentration were 20 µg/ml. PL microscopic images of cells were recorded with a Nikon Eclipse TE300 microscope. QDs were excited with a 360±20 nm UV light. The emission was collected in the spectral region 600-750 nm corresponding to the NP emission bands.

2.4.8 Laser Scanning Confocal Microscopy studies

A549 cells stock concentration in media was counted *via* Countess software with Trypan Blue. The cells were seeded in 8-well plates with cellular concentration $5×10^4$ mL^{-1} in media in DMEM with 10 % FBS and 5 µg/mL gentamicin and incubated at 37°C overnight. After incubation, the media was removed and L- and D-Cys capped CdSe/CdS QD samples of $1×10^{-7}$ M concentration in 0.5 mg/mL BSA were added to wells in media in ratio 1:9 to amount to 400 µL total. The passive transport control was used where the QD/media solution contained an inhibitor of the cellular energy-dependent mechanisms of uptake (0.1% sodium azide [NaN_3]; 1.5 mM, 3 h pre-treatment). Media (400 µL) and media with 0.1% azide (400 µL) were used as negative controls. The plates were incubated at 1 hr, 2 hrs, 3 hrs and 24 hrs intervals. The cells were stained with LysoSensor Green DND-189 dye to colour lysosomes green. The cells were then fixed with 3.7%

formaldehyde solution and nuclei were stained blue with Hoechst 33432 dye. The slides were prepared and imaged with LSCM. An average fluorescence intensity of QDs was calculated from Z-stacks and compared with controls and L- and between D-Cys capped QDs. The QD fluorescence within cells was quantified from the LSCM images with background subtraction by the method described by McCloy et al[104] using ImageJ.

2.4.9 Flow Cytometry studies

The A549 cells were seeded in 6-well plates with cellular concentration of 1×10^6 per well in media and incubated overnight. L- and D-Cys capped 5 CdSe/CdS QDs in media and media with 0.1% azide were prepared in the same ratios as before with media and media with 0.1% azide as controls with total volumes of 1.5 mL. After incubation, the media was removed and L- and D-Cys capped CdSe/CdS QD samples of 1×10^{-7} M concentration in 0.5 mg/mL BSA were added to wells in media solutions in ratio 1:9 to amount to 1.9 mL total. Similar procedure was repeated for media with 0.1% azide (1.9 mL). The cells with QDs were incubated for 2.5 h, fixed with 3.7% formaldehyde/PBS solution (500 µL) and precipitated by centrifuging at 3,500 rpm for 3 min. The sample was resuspended in 1% BSA/PBS solution (200 µL) and flow cytometry studies were performed. The PBS/BSA scattering, cell fluorescence vs scattering and debris with cell doublets were gated or excluded from flow cytometry count vs fluorescence intensity graphs. The mean fluorescence signals per cell were calculated using Origin Pro 9.0 software.

2.5 Experimental details for chapter 6. Influence of QDs on Ce6 optical activity.

The synthesis of CdSe/CdS QDs with different shell thickness is described in sections 2.3.1 and 0.

Synthesis of CdSe/CdS DiRs is described in section 2.4.2.

2.5.1 Hybrid nanostructures (HyNSs) formation

Ce6/NC HyNSs were formed in chloroform. Ce6 stock solution in methanol was prepared (ca. 5 mg/2 mL). Then 100µL of Ce6 solution was added to 100µL stock solution of NPs (CdSe/CdS QDs and CdSe/CdS DiRs) in chloroform. Resulted mixture was vigorously stirred to complete the binding of chlorin e6 carboxyl groups to the NP surface. Then the

mixture was centrifuged (1 min/15000 rpm), and precipitate (NPs with Ce6 on the surface) was dissolved in chloroform. All studied HyNSs with low molar ratios of Ce6 and QDs ($n = C_{Ce6}/C_{NC} < 2$).

2.6 Experimental details for chapter 6. Complexes of QDs with Ce6 for PDT

2.6.1 QD–chlorin e6 complex formation

ZnSe/ZnS core/shell hydrophobic QDs were synthesized following the previously reported procedures[105]. In order to create a positive charge on the QD surface ZnSe/ZnS/TOP/HDA QDs were transferred into aqueous solution and stabilized using cysteamine. The cysteamine capped QD mixture was purified three times using 10 kDa Amicon Ultra centrifugal filter units to remove excess TOP and HDA molecules. Ce6-QD complexes were formed by electrostatic interaction between the positive QD surface groups and Ce6 carboxyl groups by simple mixing of equimolar concentrations (0.5 µmol L^{-1}) of Ce6 and ZnSe/ZnS QD aqueous solutions.

Time-resolved PL spectroscopy was performed using a time-correlated single photon counting spectrometer (PicoQuant). A pulse laser (405 nm) with an average power of 1 mW operating at 40 MHz with pulse duration of 70 ps was used for PL excitation. The QD and Ce6 PL decay curves were measured with 10 nm-band-pass filters, corresponding to positions of the PL maximum of QDs (430 nm) and Ce6 (660 nm).

2.6.2 Preparation of the cell culture

For the *in vitro* studies, the Ehrlich ascites carcinoma (EAC) cell culture was obtained from the Petrov Research Institute of Oncology. The 0.5 ml cell suspension was injected subcutaneously in to eight-week-old white laboratory mice of both genders having an average weight of 20 g. The ascite was allowed to grow for 8-9 days. The mice were then euthanized. Cell suspensions were extracted with a syringe and cannula from the abdominal cavity of a mouse on 8th to 10th day after injection. Erythrocytes were lysed in a lysis buffer (0.01 mol tris HCl, 0.87% NH_4Cl, pH = 7.4) for 5 min. The suspension was then washed two times with Hank's balanced salt solution (HBSS) (centrifuged for 5 min at 1500 RPM). The precipitate was resuspended in HBSS.

2.6.3 Photodynamic therapy study

In order to perform the photodynamic cancer cells destruction studies, as prepared EAC cells were re-suspended (1.5×10^6 cells per 1 ml of HBSS) and then added to aqueous solutions of pure ZnSe/ ZnS QDs, pure Ce6, or QD–Ce6 complexes. After incubation for 2 h at 37 °C in glass cuvettes, the cells were washed two times in HBSS (centrifuged for 5 min at 1500 RPM). This purification removes the excess QDs and Ce6 molecules. After that the cells were re-suspended to the initial concentration in HBSS and were irradiated by a 405 nm diode laser with a power of 40mWcm^{-2} for 10 min (light dose 24 J cm^{-2}). A comparative study was performed using 660 nm irradiation from an LED emitter for PDT LMT-15M (Light- MedTech) (power density 0.2Wcm^{-2} with time of exposure 7 min, light dose 85 J cm^{-2}). The cells were incubated with Ce6, QDs and QD–Ce6 as was previously described and were then divided into two glass vials and exposed separately to 405 nm and 660 nm irradiation, respectively. The control samples (EAC cells only) were incubated with the same cells concentration in the same volume of HBSS. The trypan blue assay was carried out to determine the cell viabilities. For this, cells were stained with 0.4% trypan blue solution for 5 min and cell viabilities were calculated using microscopic images of cells taken with a TC10 Automated Cell Counter (Bio-Rad). Transmitted light microscopy images of the cells were taken using a LSM 710 (Zeiss) laser scanning confocal microscope.

2.6.4 Cellular uptake assay

To study the influence of QDs on Ce6 cell uptake the suspension of EAC cells with a concentration of 1.5×10^6 cells per 1 ml of HBSS was incubated with free Ce6 and QD–Ce6 complexes with different initial concentrations of Ce6 (0.1, 0.25, 0.5, 1, 2 and 5 µmol L^{-1}) in glass vials for two hours. The QD concentration was kept the same for every sample and was equal to 0.5 µmol L^{-1}. The cells were then centrifuged as described above. The quantity of Ce6 in the cells was determined as the difference between the initial concentration of Ce6 and the concentration of Ce6 in the supernatant after the cells centrifugation. UV–vis absorption spectra of the supernatants were recorded to determine Ce6 concentrations using optical density at the absorption band 405 nm (ε_{405}

= 1.3×10^5 mol^{-1}L cm^{-1}) after subtracting absorbance contributions from QDs and EAC cells at the same wavelength.

To study the dependence of cellular uptake on the incubation time, extracted EAC cells were resuspended in glass vials (1.5×10^6 cells per 1 ml of HBSS). Aqueous solutions of free Ce6 or QD–Ce6 complexes with concentrations of 0.5 μmol L^{-1} each were added to each vial. The cells were incubated in the dark at 37 °C for different periods of time (0.5, 1, 2, 4 and 7 h). Cell viability studies were performed during the whole experiment and the percentage of the dead cells did not exceed 7%. The cells were then centrifuged and the Ce6 concentrations in the cells were determined as described previously.

2.6.5 Confocal PL imaging

EAC cells (1.5×10^6 per 1 ml of HBSS) with QD–Ce6 complexes, free Ce6 and free QDs with concentrations 0.5 μmol L^{-1} of each component were incubated in the dark at 37 °C for 1, 2, and 7 h. After washing the cells two times with HBSS, PL confocal images of cells were recorded under a LSM 710 (Zeiss) laser scanning confocal microscope with 405 nm laser excitation. The emission was recorded from two spectral regions corresponding to the QD emission band (410–460 nm) and the Ce6 emission band (630–730 nm).

2.6.6 BSA based QD-ce6 complexes

In order to investigate the influence of BSA on optical properties of QDs, Ce6 and their mixtures, aqueous solutions of BSA with concentrations from 2 to 60 μmol/L were prepared. Then consequential additions of stock solutions of QDs to each BSA solution were made to obtain the concentration of QDs 2 μmol/L. Mixtures were incubated during 12 hours at 4°C. After that solutions were mixed with 2 times more concentrated phosphate-buffered saline (2x PBS) solution in proportion 1:1, in order to obtain standard 1x concentration of PBS in working solutions. Further, small volume of Ce6 stock solutions were added to each mixture. The concentration of QDs and Ce6 in working solutions were 1 μmol/L, and concentration of BSA varied from 1 to 30 μmol/L.

Complexes of CdSe/ZnS quantum dots with chlorin e6 were formed using BSA as a linker. BSA adsorbed on the QD surface as result of hydrophobic and electrostatic

interaction and by coordination of BSA thiol groups to Zn atoms on QD surface. Ce6 was bound to BSA at the specific binding sites by hydrophobic and Van der Waals forces.

2.7 Characterisation techniques

2.7.1 Jablonski diagram

Jablonski diagram (*Figure 2-1*) describes the main principles of absorption and emission of light.
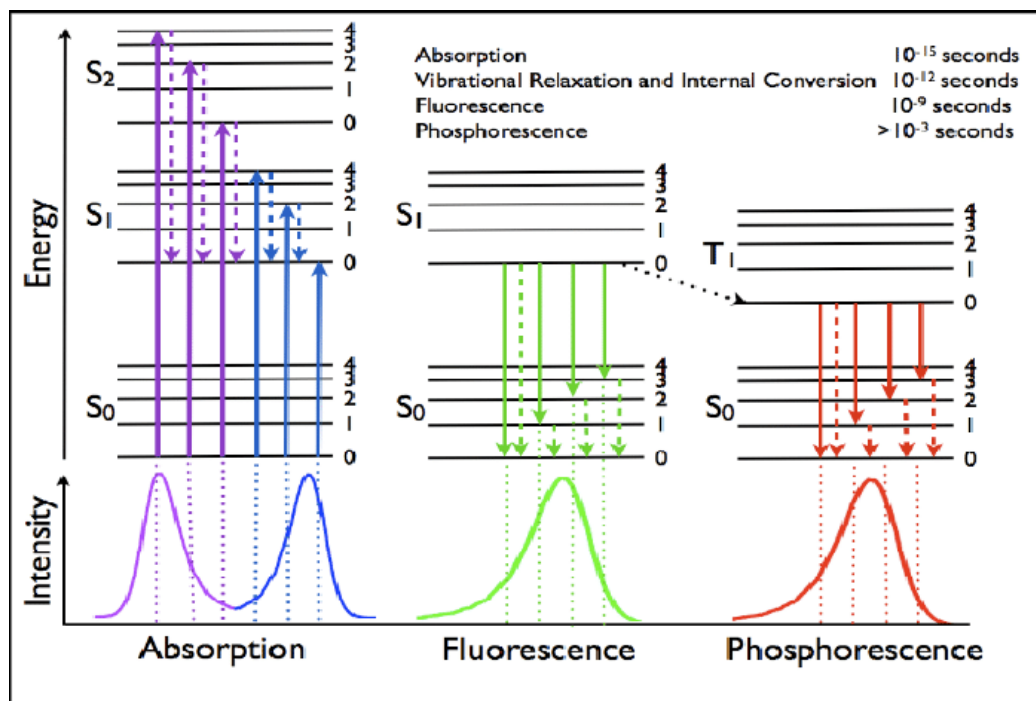
Figure 2-1. Jablonski diagram

Firstly, a photon of light is absorbed by the molecule or QD and electron is excited from S0 to a higher energy level such as S1 or S2, it depends on the energy of the photon. Thus, substances absorb only photons with energies equal to the distance between the levels. It reflexes in the maxima of UV-Vis absorption spectra. Then the excited electron undergoes vibrational relaxation to the vibrational level with the lowest energy within the excited state. After that internal conversion takes place, at which electron non-radiatively relaxes from a higher excitation state (S2) to a lower excited state (S1).

At this stage two radiative processes can happen: fluorescence of phosphorescence. During fluorescence electron relaxes from S1 to S0 directly emitting photon with corresponding energy. Phosphorescent take place, if the excited singlet state convert to an excited triplet state; and electron relaxes from excited triplet state to ground singlet state. The probability of this process is much lower than fluorescence one because phosphorescent transition is spin-forbidden. That is why phosphorescence is much slower than fluorescence, normally on the micro to millisecond timescale, comparing to nanosecond one.

2.7.2 UV-Vis spectroscopy

In this project UV-Vis spectra were recorded using a Varian/Cary 50 single beam spectrophotometer. All samples were analyzed using a 1 cm quartz fluorescence cuvette. If the solvent was volatile, a capped cuvette was used.

As it was described above, UV-Vis spectroscopy is based on a fact that substances absorb photons with the energy equal to transitions between electronic levels. By the Beer-Lambert law the absorbance A is proportional to the substance concentration (c) and the path length of the sample (l), and the proportional coefficient is ε, the extinction coefficient:

$$A = \varepsilon c l$$

Equation 2-2. Beer-Lambert law.

UV-Vis spectrometer run the light with all wavelengths through the sample and register the intensity of passing light as the function of wavelengths. The principle of work of UV-Vis spectrometer is shown in Figure 2-2: light from the source is going to entrance slit to monochromator, that transmits only the light with particular wavelengths, and then through sample to detector.

Conventional Spectrophotometer
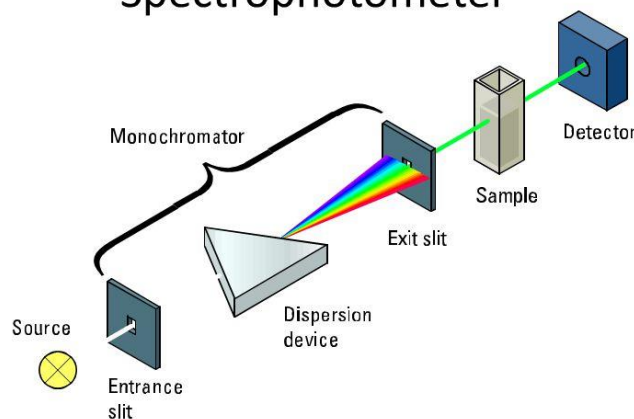
Schematic of a conventional single-beam spectrophotometer

Figure 2-2. The principle of work of UV-Vis spectrometer.

2.7.3 Photoluminescence Spectroscopy

PL spectroscopy studies were performed using a Cary Eclipse spectrometer and 1 cm quartz fluorescence cuvettes. Photoluminescent quantum yields were measured using the comparison approach using rhodamine 6G in ethanol (PL QY = 95%) as a standard.

$$Q_x = Q_{st} \frac{I_x}{I_{st}} \frac{A_{st}}{A_x} \frac{n_x^2}{n_{st}^2}$$

Equation 2-3. PL quantum yield calculation, where Q_x, I_x, A_x and n_x are PL QY, integrated PL intensity, absorbance and refractive index of solvent of the Sample and Q_{st}, I_{st}, A_{st} and n_{st} are the same characteristics of the standard (rhodamine 6G).

Photoluminescence lifetime measurements were performed using a time-correlated single-photon counting spectrometer equipped with a PCS900 plug-in PC card (Fluorolog-3 Horiba Jobin Yvon) and a semiconductor diode "NanoLED" excitation source (458 nm, Horiba Jobin Yvon) with pulse duration shorter than 1 ns. Lifetimes were obtained by a reconvolution fit using a solution of Ludox in water as the scatterer and the quality of fit judged by minimization of reduced χ^2 and the residuals.

There are two forms of photoluminescence: fluorescence and phosphorescence, both of which can be measured by PL spectrometer.

The scheme of working principle of PL spectrometer is represented in *Figure 2-3*. Similar to UV-Vis spectrometer, the light from source goes firstly to monochromator, which selects the light with particular wavelength (excitation wavelength), and then to the sample. Luminescent sample emits light to all the directions, that is why the PL is register in 90° angular to excitation beam. Then light goes to the emission monochromator and detector.
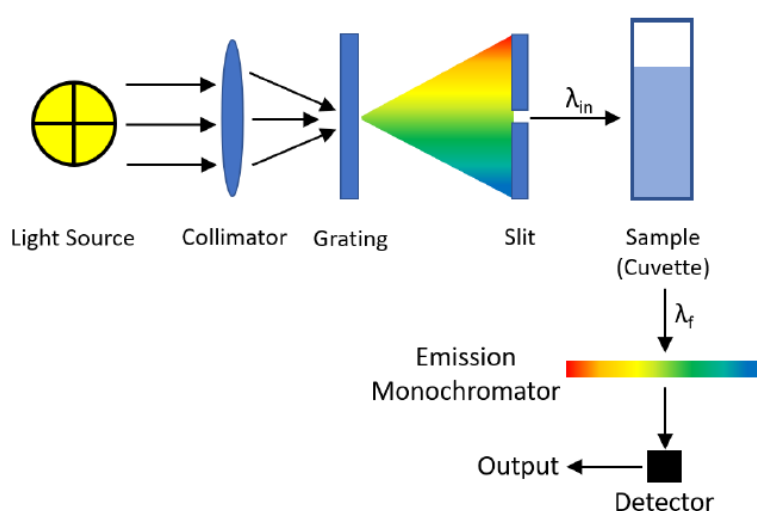
Figure 2-3. The principle of work of PL spectrometer.

Phosphorescence can be measured using the same equipment. But phosphorescence is much slower process that fluorescence, thus to separate them, the phosphorescence is registered with the time delay.

For fluorescence lifetime measurements the pulse laser is used and the PL intensity on the certain wavelength vs time is detected.

2.7.4 Circular Dichroism Spectroscopy

CD spectroscopy was carried out using a Jasco J-810 operating under a N_2 flow of 5-8 L/min. Samples were analyzed in 1 cm quartz fluorescence cuvettes. Samples were analyzed with a 100 nm / minute scan rate and a 1 second response time (9 accumulations).

Enantiomers of chiral substances preferentially absorb circularly polarized light (CPL) because dipole of one enantiomer overlaps better with the electric field of CPL of one handedness. CD spectrometer pass the left- and right-handed CPL and register the difference in their absorption:

$$CD\ (\Delta A) = A_L - A_R$$

Equation 2-4. Equation for circular dichroism.

CD intensity is usually recorded in ellipticity, θ in units of mDeg. To convert the CD into mDeg the following formula is used:

$$\theta\ (mDeg) = CD\ (\Delta A) \times 32980$$

Equation 2-5. Conversion of CD (ΔA) to CD (mDeg)

CD signal intensity is proportional to absorbance and consequently to concentration of the sample. To compare the chiroptical properties of the samples with different concentrations, G-factor was used instead of CD. The G-factor is defined as

$$G = (\varepsilon_L - \varepsilon_R)\ /\ \varepsilon,$$

Equation 2-6. G-factor calculation, where A_L and A_R are the absorbance of circularly polarized left-handed and right-handed light, respectively, and A is the absorbance of unpolarised light; ε is exctinction coefficient.

The G-factor depends on exctinction coefficients of the samples, and concentration does not influence on it.

2.7.5 Transmission Electron Microscopy

Our samples were imaged using a FEI Titan electron microscope operating at a beam voltage of 200 kV. Samples were diluted to approximately 1mg/10mL and allowed 53 to dry under vacuum for 12-24 hours depending on the solvent. The samples were deposited on lacey or holey carbon on copper grids.

Transmission Electron Microscopy (TEM) is based on the same principles that the light microscope, but instead of light it used the beam of accelerated electrons. As the wavelength of an electron can be up to 100,000 times shorter than that of visible light photons, electron microscopes have a higher resolution than light microscopes and can reveal the structure of nano objects. The working scheme of TEM is presented at Figure 2-4. Electron beam is generated and accelerated by the electron gun and go through the system of the condenser lenses and aperture to obtain monochromatic parallel beam. Lenses in TEM focus electron beam using magnetic field, manipulating electrons by left hand rule. Then electrons pass through the sample and the objective lens into a primary image. This image is then magnified as it passes through successive lenses and goes to the CCD detector.
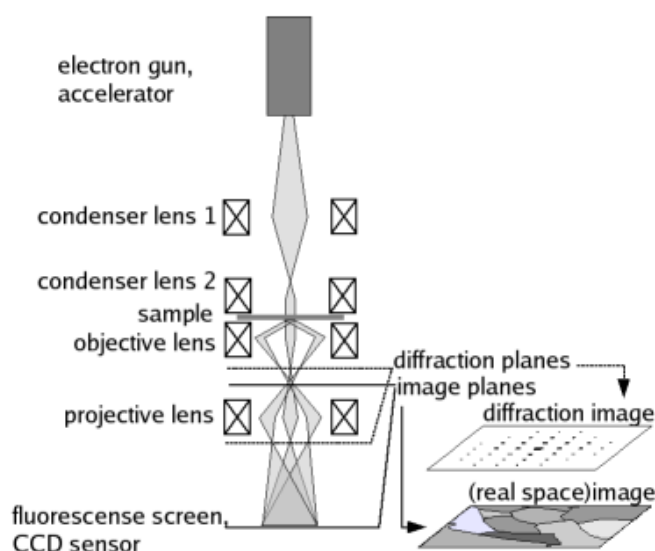
Figure 2-4. The principles of working of transmission electron microscope. From https://upload.wikimedia.org/wikipedia/commons/f/f6/TEM_ray_diag2.basic.en.png.

2.7.6 Nuclear Magnetic Resonance (NMR) spectroscopy

Solution NMR and MAS NMR in the present study were performed using Bruker Avance III 400 NMR and Bruker Avance HD-400 NMR respectively.

Nuclear Magnetic Resonance (NMR) spectroscopy is based on the principle that many nuclei have spin and this spin can orient in external magnetic field: parallel to and in the same direction as the external field or against the field i.e. antiparallel to the

external field (Figure 2-5). The spin can flip if nuclei absorb electromagnetic energy equal to the difference between parallel and antiparallel spin energy. This difference is dependent on the strength of the magnetic field and the type of the nuclei.
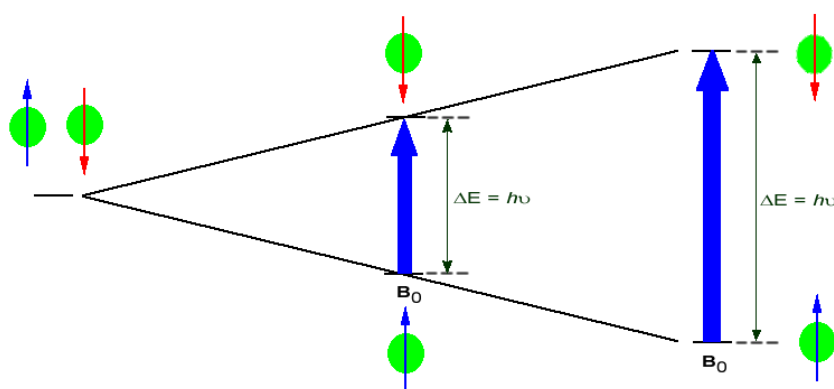
Figure 2-5. Orientation of the nuclei in external magnetic field. From https://chem.libretexts.org/Courses/Purdue/Purdue%3A_Chem_26505%3A_Organic_Ch emistry_I_(Lipton)/Chapter_5._Spectroscopy/5.3_Nuclear_Magnetic_Resonance_(NMR) _Spectroscopy.

The principle of working of NMR spectrometer is presented in Figure 2-6. A sample in a small glass tube is placed between the strong magnetic poles. Electromagnetic wave generator irradiates the sample and excites the nuclei, resulting in a spin-flip, which is detected by the detector and the signal sent to a computer as the spectra of the applied wave frequency *vs* the absorption. The position of peaks depends on many factor, such as nuclei nature, electric environment of nuclei, interaction of nuclei with each other (especially for ^{1}H NMR). Thus NMR give a lot of information about chemical structure of the materials. The most commonly analysed nuclei are ^{1}H and ^{13}C. NMR spectroscopy analysis of these nuclei was performed in this research as well.
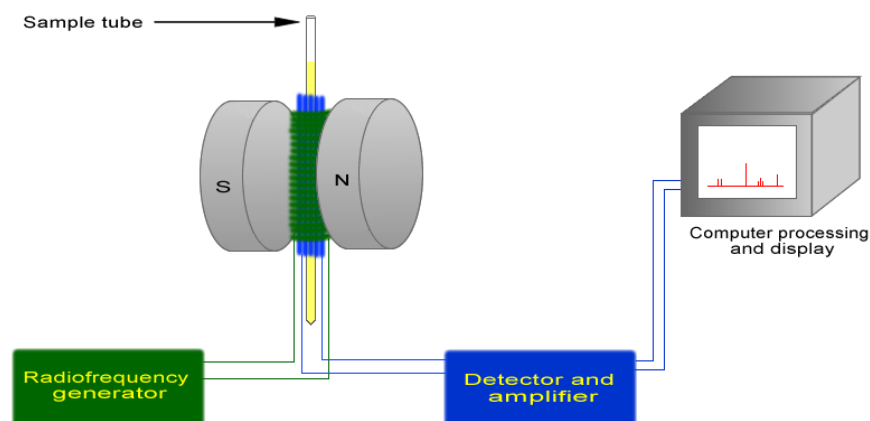
Figure 2-6. The principles of working of NMR spectrometer.

https://chem.libretexts.org/Courses/Purdue/Purdue%3A_Chem_26505%3A_Organic_Ch

emistry_I_(Lipton)/Chapter_5._Spectroscopy/5.3_Nuclear_Magnetic_Resonance_(NMR)

_Spectroscopy

2.7.7   Fourier-transform infrared spectroscopy (FTIR)

In the present research FTIR spectra were recorded on a Spectrum 100 instrument (PerkinElmer).

Fourier-transform infrared spectroscopy (FTIR) is based on the principle that molecules absorb the IR radiation with the frequencies corresponding to the vibration energies of bonds between the atoms in molecules.

Vibration energy depends on many factors, such as weight of the bound atoms, the type of bound and type of vibration modes (Figure 2-7). The heavier the bound atoms the lower the vibration frequency. Each bond has vibrational and rotational movement. Rotational movement gets less energy than vibrational move.
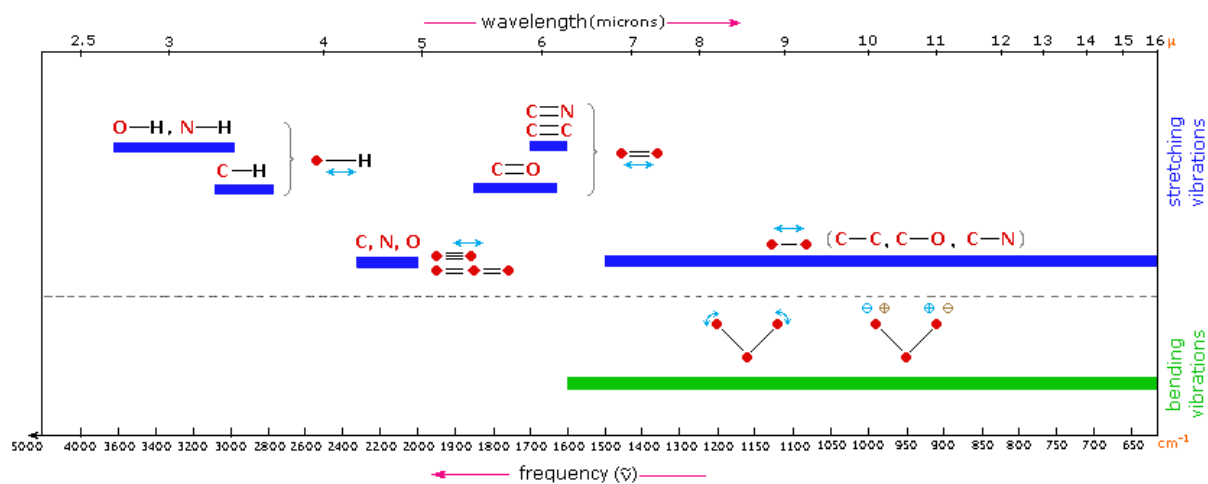
Figure 2-7. Positions of FTIR bands for different bound types and vibration modes. From

https://www2.chemistry.msu.edu/faculty/reusch/

VirtTxtJml/Spectrpy/InfraRed/infrared.htm

The interferometer working scheme is shown in the Figure 2-8. IR radiation from the source is going to beam splitter where light is divided into two beams, one of which travels by perpendicular direction towards the stationary mirror, another one follows the same direction and go to moving mirror. After reflection from the mirrors go back the beam splitter and then to sample compartment. As the result the interferogram of two beams is obtained and then is converted to a spectrum by Fourier transformation.
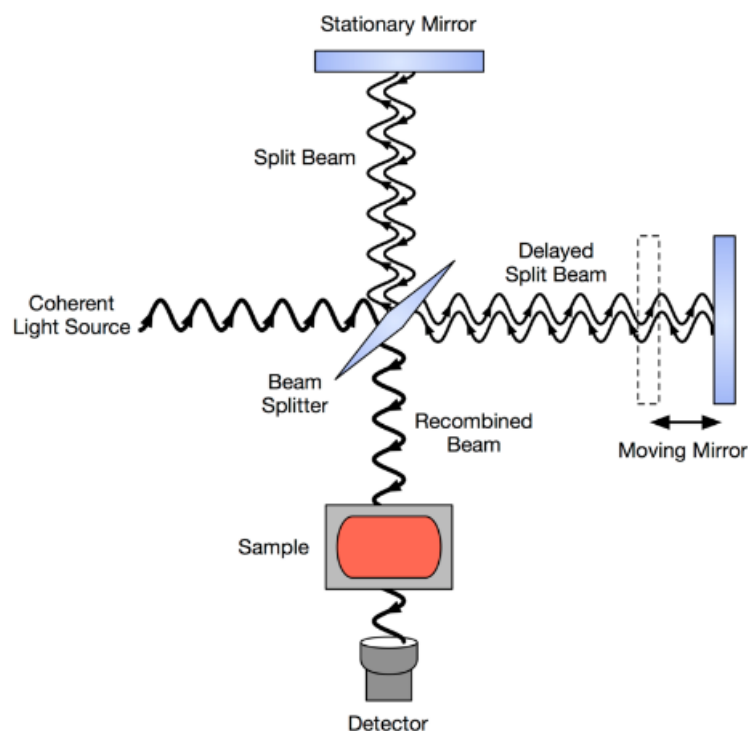
Figure 2-8. Schematic diagram of interferometer, configured for FTIR. From https://en.wikipedia.org/wiki/Fourier-transform_infrared_spectroscopy

2.7.8 Dynamic Light scattering

The hydrodynamic diameter of QDs in this work was collected by dynamic light scattering (DLS) using the Zetasizer Nano ZS system.

Dynamic Light scattering (DLS) uses two physical principles: 1) the Brownian motion speed of dispersed particles is proportional to size of the particle (more accurate, to the hydrodynamic radius of the particle), which is known as Stokes-Einstein equation:

$$D = \frac{k_B T}{6\pi\eta R_H}$$

Equation 2-7. Stokes-Einstein equation: where D isTranslational diffusion coefficient ("speed of the particles"); k_B is Boltzmann constant; T is Temperature; h is Viscosity and R_H is Hydrodynamic radius [m].

And second principle is that fluctuations in the intensity of the light scattered by the moving particles is proportional to speed of the Brownian motion. The working

principle of the DLS spectrometer is shown in Figure 2-9. Light from laser pass the sample and then scattered light goes to the detector.
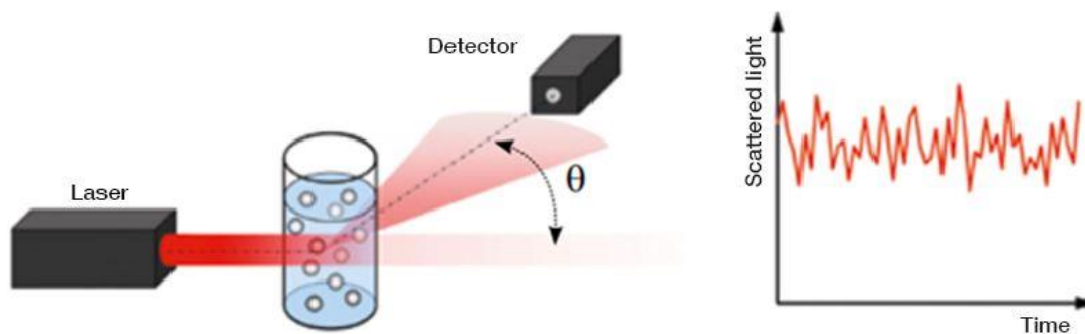
Figure 2-9. The principles of working of DLS spectrometer. From https://wiki.anton-paar.com/en/the-principles-of-dynamic-light-scattering/

2.7.9 Confocal Microscopy

In our work confocal images were recorded using LSM 710 (Zeiss) laser scanning confocal microscope. QDs were excited with a diode laser 405 nm line. The emission was measured in the spectral region 500–560 nm corresponding to the QD emission band of 530 nm.

Confocal microscope allows to obtain the image of very thin layer of the fluorescent material cutting the PL from layers above and below. Thus it gives the possibility to construct the 3D image of fluorescent sample. The principles of working of confocal microscope is shown in Figure 2-10: very small pinhole allow to pass through only the light from focal plane. As the result it is possible to obtain Z-stag image of the sample.
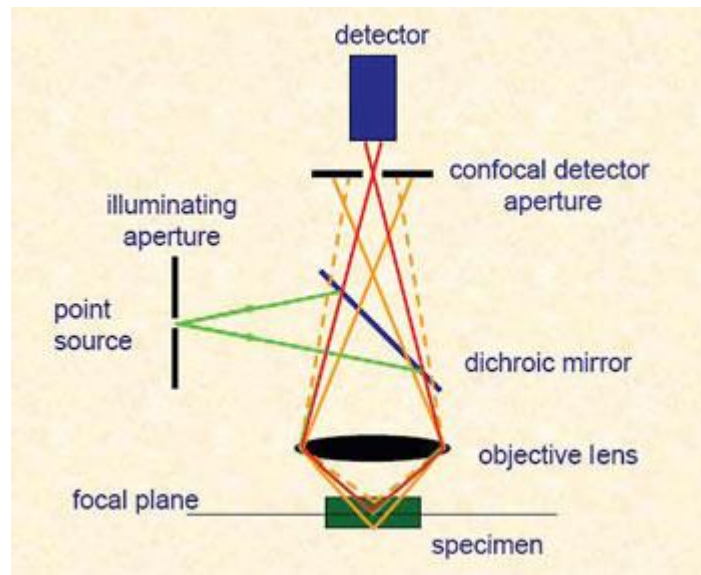
Figure 2-10. The principles of working of confocal microscope. From http://www.microscopist.co.uk/essential-techniques/confocal-microscopy/

2.7.10 Fluorescence Lifetime Imaging Microscopy

Fluorescence lifetime imaging in this study was performed using a time correlated single photon counting (TCSPC) spectrometer (PicoQuant, Inc.) equipped with a ×40/0.65 NA objective. A pulse laser radiation (405 nm) with an average power of 1 mW, pulse duration of 70 ps and repetition rate of 40 MHz was used for fluorescence excitation.

Fluorescence Lifetime Imaging Microscopy (FLIM) is based on the same main principle as the PL microscopy, with the difference that the sample is irradiated by pulse laser and signal is detected non depending on the PL intensity from the sample but depending on PL lifetime.

2.7.11 Flow cytometry

In the present study cell count and QD fluorescence inside cells was measured with BD Accuri C6 flow cytometer.

For flow cytometry analysis cell are passing through the very narrow tube and analysed one by one. Cells are irradiated by the light from lamps (mercury, xenon) in combination with blue, green and red lasers and forward-scattered light (FSC) and side-

51

scattered light (SSC) as well as dye-specific fluorescence signals are detected and convert to digital signal.
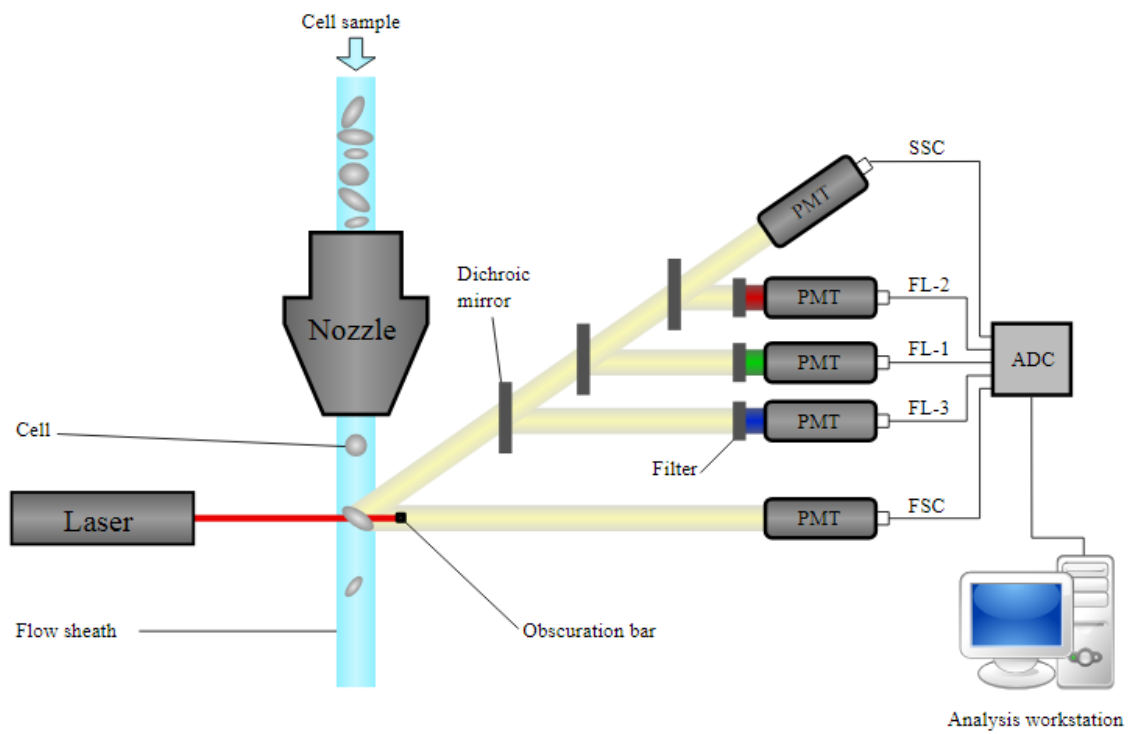
Figure 2-11. The principles of working of DLS spectrometer. From https://en.wikipedia.org/wiki/Flow_cytometry

3 Chapter 3: The influence of the CdS shell thickness on the CD intensity of CdSe/CdS QDs

3.1 Introduction

The development of core-shell QDs have been a significant advancement in the area of fluorescencent materials in particularly with a type I band alignment. In this structure, the core is coated in a shell of another semiconductor of a larger band gap, with a conduction band higher in energy and valence band lower in energy than that of the core, with common examples including (*e.g.* CdSe/CdS, CdSe/ZnS and InP/ZnS). This structure has the effect of confining the excited state to the core of the nanoparticle, which results in a number of favourable properties including a large increase in PL quantum yield (PL QY) and resistance to degradation. For these reasons and more, they have found a range of applications in the field of bio-imaging[77], bio-sensing[78], photovoltaics[106], LEDs[107], photodetectors[108], luminescent solar concentrators[109] and lasers[110].

Chiral semiconducting quantum dots are an emerging field in nanomaterials, showing potential in sensing[42,111,112], cell imaging[41], asymmetric catalysis[113], enantiomeric separation[114], spintronics[115] and as a novel circularly polarised light source[116,117]. This is due to the potential of PL and optical activity in a chiral quantum dot, which when combined with the intrinsic control of photo physical properties offered by QDs in general, creates a unique luminophore.

Chirality in QDs can be originated due to a range of mechanisms including chiral space groups[118], crystal dislocation induced[119], ligand-induced chiral surface[120,121], electronic coupling between chiral ligands and achiral QDs[122], or from a QD based chiral assembly[123,124]. The most common approaches to ligand induced chirality include techniques in which chiral ligands can be introduced to a quantum dot either by firstly synthesising the nanoparticles *in situ* with chiral capping ligands[18,47] or *via* a ligand exchange[125], in which the original achiral ligands are replaced with a chiral alternative. QD synthesis using *in situ* chiral ligands is an effective means to produce strongly chiral QDs in the aqueous phase, though samples produced using this approach have only been developed for a limited range of semiconductors and usually display low QY and broad PL

emission, assigned as surface trap state in origin[18,47,65,120,121,126]. Meanwhile, the ligand exchange method offers an opportunity to produce a range of various chiral QDs for study, since most of QDs are frequently produced in organic solvents at high temperatures by hot injection techniques.

This ligand exchange approach has been initially developed utilising QDs consisting of a single binary semiconductor (CdSe, CdS, CdTe)[50,125,127–129]. These studies have shown a complex evolution of the CD spectra as the size and composition of the QD is varied. A weak decreasing trend in CD signal was found to be dependent upon decreasing surface/volume ratio and therefore the size of the QDs[49,127]. In addition, the effective overlap of the ligand's electronic states and bands of the semiconductor play an important role[129]. The interplay between both of these trends gives rise to the complex development of the CD spectra found[49,130].

A common consequence of ligand exchanges is a strong reduction in QD PL, with samples reported to date showing a near quenched PL signal following ligand coordination[125]. This is due to the formation of surface trap states[5,131,132] and in the case of thiols is due to hole trapping of photo generated holes on the ligand[131]. At the same time, achiral core-shell QDs, of type I band alignment have been shown to be far more robust to the negative effects of ligand exchange[133], with studies showing a strong quantum yield dependency upon increased shell thickness, to a critical point[8]. This is due to increased exciton confinement to the core of the nanoparticle, avoiding possible non-emissive de-excitation routes present at the surface of the QD or through interaction with the environment.

A very interesting investigation of the evolving chiroptical properties of CdSe/CdS QDs depending on the CdS shell thickness has also been reported[129]. This study has shown that as the shell thickness of CdS is increased, the resulting chiral response of the sample is strongly reduced due to the increased distance of the hole present in the CdSe core from the coordinated chiral ligands on the surface of the QD. Though a more complex pattern emerged in the range of 0.5 – 2 nm shell thickness, which was explained to be due to the electronic effects that increased shell thickness has upon the valence band of the CdSe core.

This chapter is devoted to the comprehensive investigation of the combined effects involving chiral ligand exchange upon the induced chiral optical signal and PL, varying QDs shell thickness to produce an optimal QD nanostructure having both strong excitonic emission and a well expressed chiral ligand induced optical activity. In addition, we have performed a detailed study of the influence of annealing time on the optical activity and photoluminescence quantum yield. In our work, we have utilised the well-known SILAR[37,134] synthetic approach to vary the shell thickness of a CdSe/CdS QD sample, after which a cysteine based ligand exchange is applied[63], producing a range of optically active CdSe/CdS QDs. We believe that these investigations should contribute to the development and design of optimal chiral QD probes.

3.2 Results and Discussion

3.2.1 Preparation of optically active core/shell CdSe/CdS QDs

CdSe/CdS QDs were synthesised using a two-step procedure. Firstly, CdSe QDs were produced according to Chen et al[100] using a scaled up and modified by us procedure. Following this, the QDs were cleaned and then used in the second stage of synthesis in which a CdS shell of variable thickness was grown upon the core. This synthesis was carried out using previously reported by Mahler et al[101] procedure, which was scaled up and modified by us with the volumes of CdS precursor used calculated based upon the SILAR approach so as to control the thickness of CdS deposited precisely. Following the injection of equal moles of cadmium precursor and sulphur precursor, which were then allowed to react for 60 minutes, a 25-ml portion of the reaction mixture was removed and was allowed to cool under argon, producing the first CdSe/CdS sample. This procedure was repeated four times further to produce five samples of CdSe/CdS QDs in total. Following cleaning, a ligand exchange was then carried out upon each samples, using a cysteine as previously reported[63] with some modifications. Briefly this involved the dispersal of QDs into chloroform, to which a solution of cysteine was added in MeOH. To this was added deionised water, and the pH was adjusted to 12 using KOH solution. After this, shaking, the QDs changed phase to the aqueous layer, after which the layer was decanted and stored. The successful ligand exchange was confirmed by FTIR spectroscopy (Figure 3-1), showing complete replacement of the original achiral ligands.
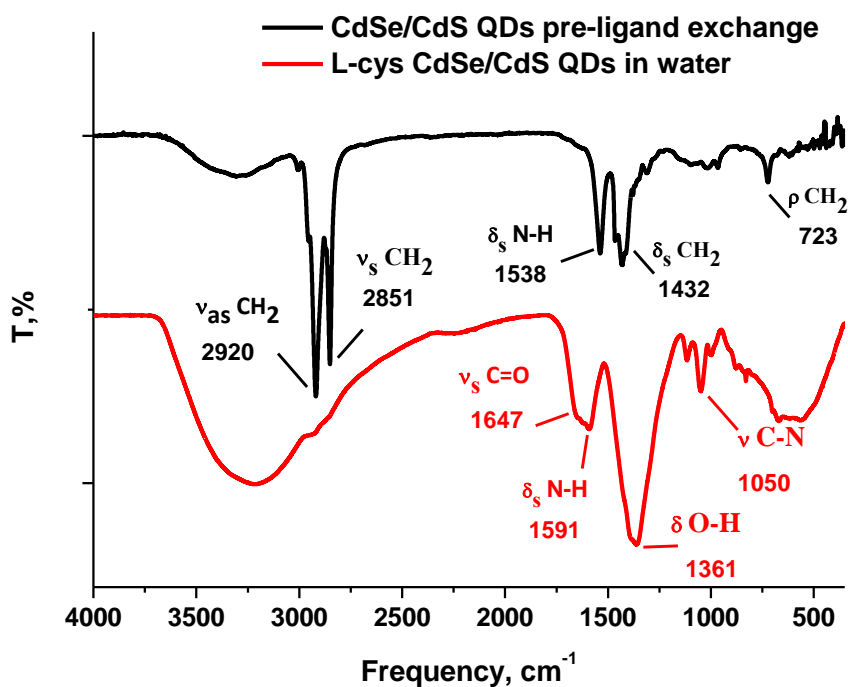
Figure 3-1. FTIR data of CdSe/CdS QDs prior and post cysteine ligand exchange, with peaks labelled showing the complete replacement of our original non-polar ligands with cysteine.

Next, we have carried out a detailed investigation of the resulting properties of these samples before and after chiral ligand exchange using UV-Vis, photo luminescent (PL), fluorescence lifetime and CD spectroscopy, and transmission electron microscopy (TEM).

3.2.2 QD characterization in organic phase

TEM analysis of each sample was carried out and is shown in Figure 3-2 with a summary of results presented in Table 3-1. Standart deviation was calculated using formula:

$$\text{SD} = \sqrt{\frac{\sum |x - \bar{x}|^2}{n}}$$

Equation 3-1. Standard Deviation calculation, where SD is standard deviation, x is a value in the data set, μ is the mean of the data set, and n is the number of data points in the population.

These show that the initial CdSe cores measured 2.8+/-0.4 nm in diameter [100,101] and were produced with a size distribution comparable with original synthesis, after which the diameter of the QDs was found to increase to 3.7 nm +/-0.4 value from the first CdS shell (S1) and then on average by 0.4 nm for each subsequent shell (S2-S5), finally obtaining a value of 5.2±0.8 nm after the fifth shell (S5), while maintaining a spherical morphology throughout. In addition, no CdS QDs were present in any portion, verifying the effective use of the SILAR approach so as to avoid CdS QD homonucleation[37].

	unit	Original QD	Shell 1	Shell 2	Shell 3	Shell 4	Shell 5
Measured size	nm	2.83	3.67	4.07	4.51	4.88	5.21
Measured shell thickness	nm	-	0.76	0.4	0.44	0.37	0.33
Standard deviation	nm	0.40	0.36	0.43	0.52	0.63	0.84

Table 3-1. Summarisation of size of CdSe and CdSe/CdS sample produced, determined using Transmission electron microscopy measurements from images.

CdSe
cores

1S

2S

3S

4S
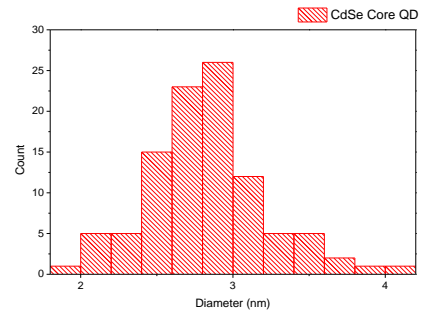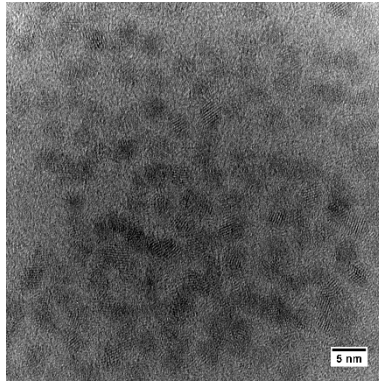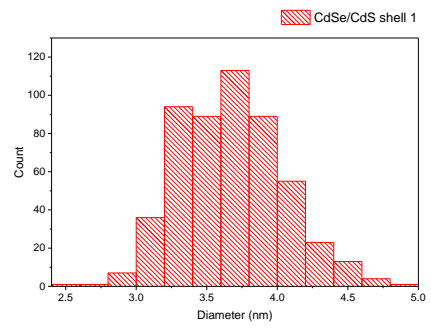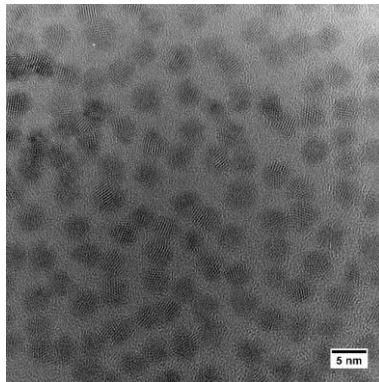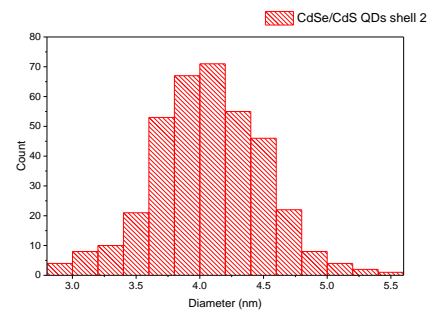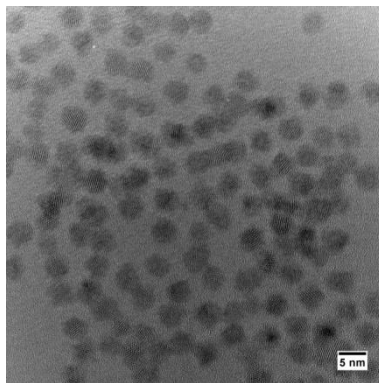
5S
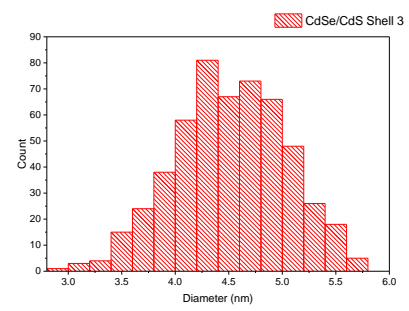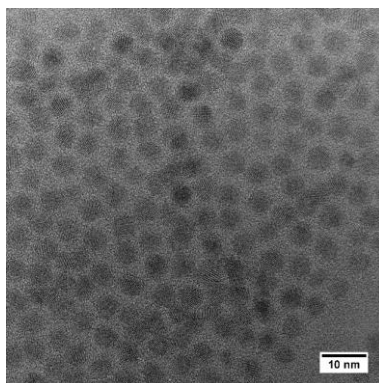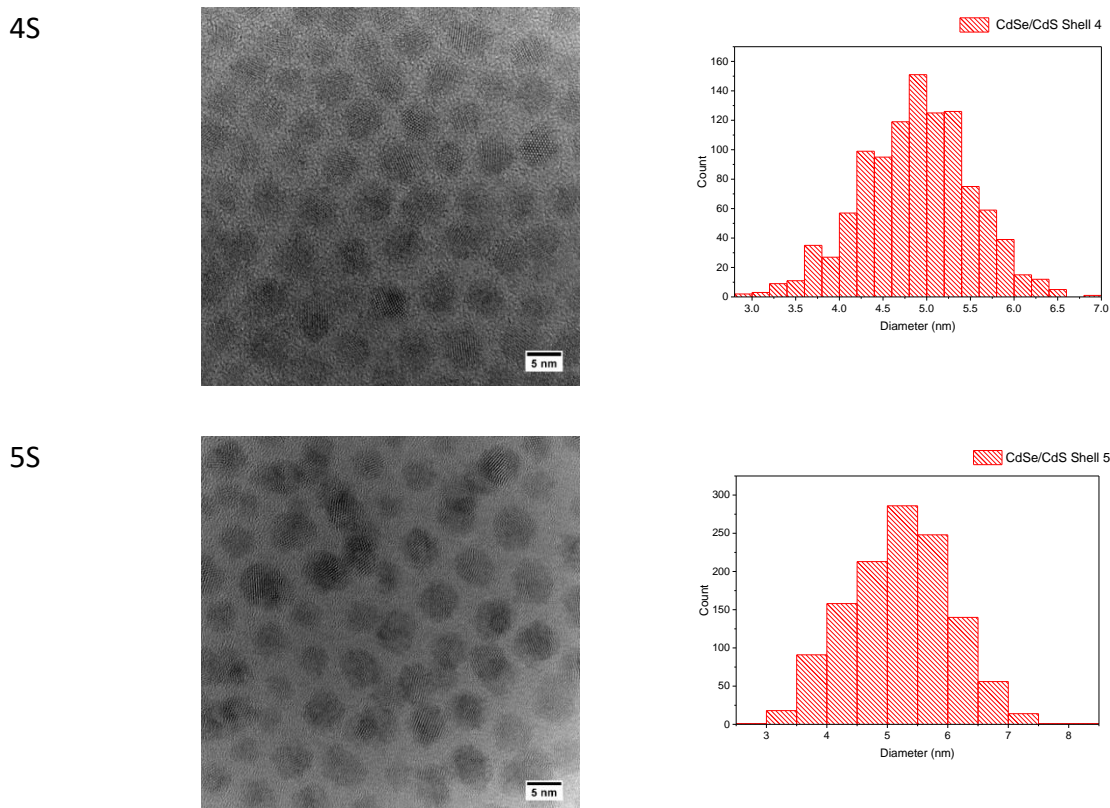
Figure 3-2. TEM images of CdSe/CdS QD with 0-5 shell monolayers (left) and histograms (right) of the resulting QD diameters

Initially, CdSe/CdS QDs in toluene with a number of CdS shells from S1 to S5 were characterized by optical spectroscopy. Figure.1 (a) shows the QD UV-Vis absorption spectra with strong increases in absorption below 500 nm with the growth of shell thickness. This is associated with CdS absorption onset, which also has the effectof significant red shifting in the first exciton peak of the CdSe core as the CdS shell thickness is increased. This shifting change the first exciton position from 549 nm (CdSe cores, S0) to 560 nm (S1) with further increases in shell thickness causing shifts up to 586 nm (S5). The same pattern as is expected is found in the PL spectra showing a gradual red-shifting in the luminescent peak emission as the shell thickness is increased as is shown in Figure *3-3* (b), shifting from 558 nm to 600 nm. The FWHM displayed a minor narrowing as shell thickness increased, indicating our CdSe size distribution was maintained during the shelling procedure. It was also found that the QD's PL quantum yield (PL QY) varied from

4.3+/-0.4 % to 19.2+/-1.9 % across the samples S1-S5 (Figure 3 (b)), with the PL QY initially increasing up to S3 and then showing a minor reduction as shell growth continued.

This behaviour is consistent with previously reported results demonstrating that a large increase will be initially observed which then reduces as the shell thickness increase due to the production of non-radiative relaxation roots. This due to either the introduction crystal defects into the shell via lattice mismatch between the CdSe core and CdS shell[24,135], or due the effects of a disordered structure present in the shell which has been shown to occur as shell thickness increases[100], in either case it has the overall effect of lowering the PL QY we observe.

a)   b)

(c)
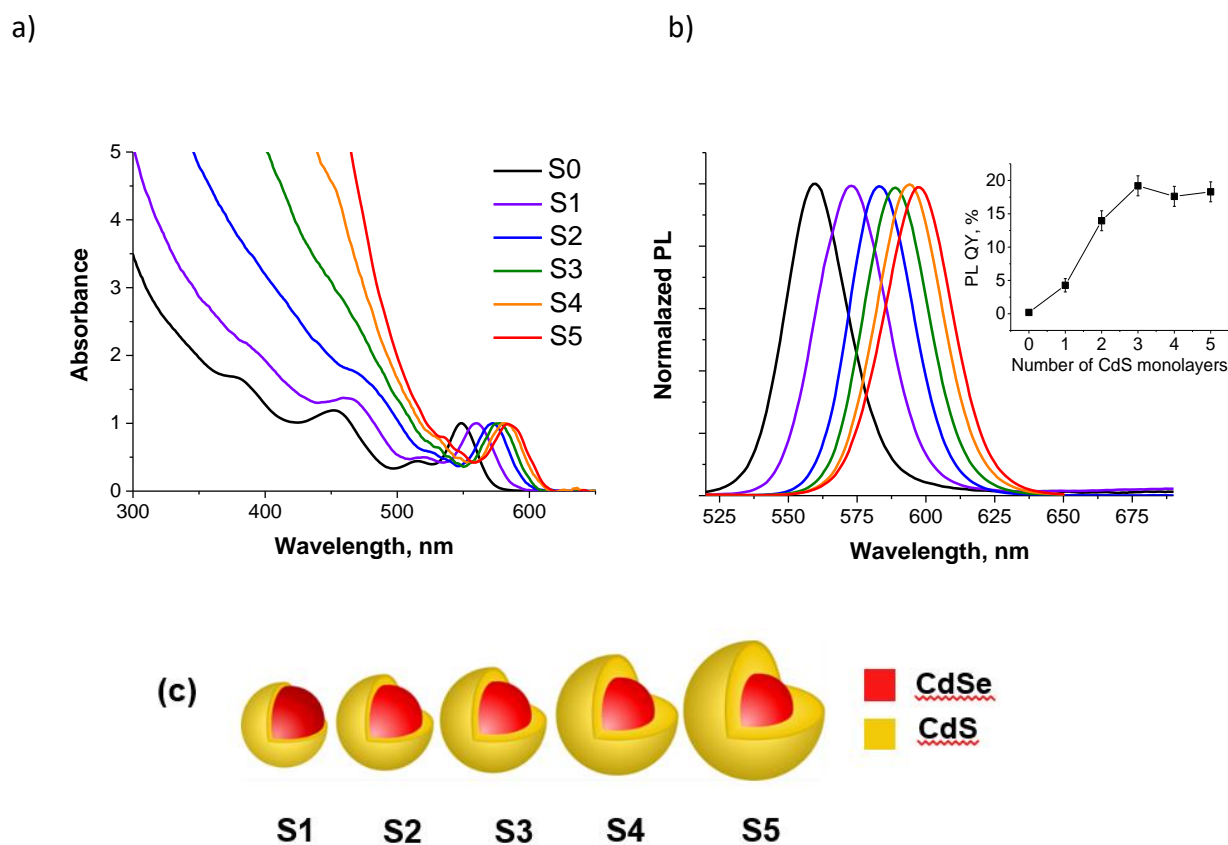
Figure 3-3. UV-Vis absorption (a), PL (b) spectra in toluene (λ exc = 350 nm) and (c) diagram of CdSe/CdS QDs. The dependence of PL QY of CdSe/CdS QDs in toluene on the number of CdS shells is shown in (b) inset.

We also examined the change in photoluminescent lifetimes, which is shown in Figure *3-4* and in Table 3-2 (further details given in Table 3-3). Lifetimes were obtained by a reconvolution fit using a solution of Ludox in water as the scatterer and the quality of fit

judged by minimization of reduced χ2 and the residuals. The QD FL lifetime was found to be well fitted by a multi-exponential decay model:

$$I(t) = \sum_n A_n \exp(-t/\tau_n)$$

Equation 3-2. QD PL lifetime fitting, where A_n are the amplitudes and τ_n are the fluorescent lifetimes.

Average lifetimes <τ> were determined as the average time for which the emitters (QDs) remain in their excited state after the onset of excitation:

$$\langle \tau \rangle = \frac{\sum_n A_n \cdot \tau_n{}^2}{\sum_n A_n \cdot \tau_n}$$

Equation 3-3. Average lifetimes <τ> calculation.

The fluorescence decay of the QDs shows three relaxation processes with slower and faster characteristic times that are usually observed for colloidal solutions of the QDs at room temperature[136]. The appearance of the third component in the fluorescence decays is a sign of dot-to-dot energy transfer[137].

Sample	λ_{abs}, nm	λ_{PL}, nm	FWHM, eV	Diameter, nm	Estimate of CdS thickness, nm	ϕ, %	$<\tau>$, ns
S0	548	560	0.10	2.8±0.4	-	0.2	-
S1	560	570	0.11	3.7±0.4	0.45	4.3±0.4	11.2
S2	572	584	0.09	4.1±0.4	0.65	14.0±1.4	14.2
S3	576	590	0.09	4.5±0.5	0.85	19.2±1.9	16.5
S4	581	596	0.09	4.9±0.6	1.05	17.6±1.8	19.2
S5	584	600	0.09	5.2±0.8	1.2	18.6±1.9	24.9

Table 3-2. Summary of CdSe/CdS optical properties and morphology properties in the organic phase, where φ is the photoluminescent quantum yield, while <τ> is the average photoluminescence decay lifetime. The given diameters were determined by TEM, while the shell thickness was calculated from the original core diameter.

This data shows a gradual increase in photoluminescent lifetime from an average time of 11.2 ns to 24.9 ns as the shell thickness increased. This can be attributed to greater exciton confinement from the surrounding environment, due to increased CdS shell thickness and is consistent with reported literature[101].
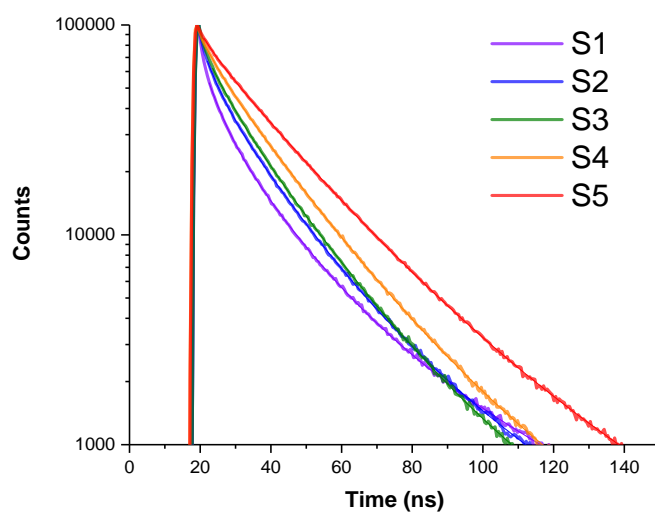
Figure 3-4. Photoluminescent lifetime measurements of CdSe/CdS QDs relative to CdS shell thickness ranging from S1-S5, the fitting of each spectrum indicated by a darker shade line.

In addition, a similar trend is found when examining the radiative de-excitation rate (see Table 3-3), showing an increase from 1.79×10^5 in shell 1 to 1.00×10^7 in shell 4, decreasing to 7.07×10^6 at shell 5.

Sample	t_1 (nsec)	Amplitude	t_2 (nsec)	Amplitude	t_3 (nsec)	Amplitude	QY, %	Average lifetime <t> (nsec)
shell 1	4.3	0.6211	15.1	0.2812	44.0	0.0977	0.2	11.2
shell 2	3.8	0.3781	15.2	0.4732	38.0	0.1487	4.3	14.3
shell 3	5.7	0.2647	16.9	0.6274	41.0	0.1079	14	16.5
shell 4	4.4	0.1171	17.1	0.7037	36.9	0.1792	19.2	19.2
shell 5	4.1	0.0272	20.1	0.711	40.2	0.2618	17.6	24.9

Table 3-3. Summarisation of CdSe/CdS QD prior to ligand exchange in toluene using 458 nm excitation fluorescence lifetime measurements relative to shell thickness. The spectra were measured using a 458 nm excitation source.

3.2.3 QD optical properties after the phase transfer

a) b)
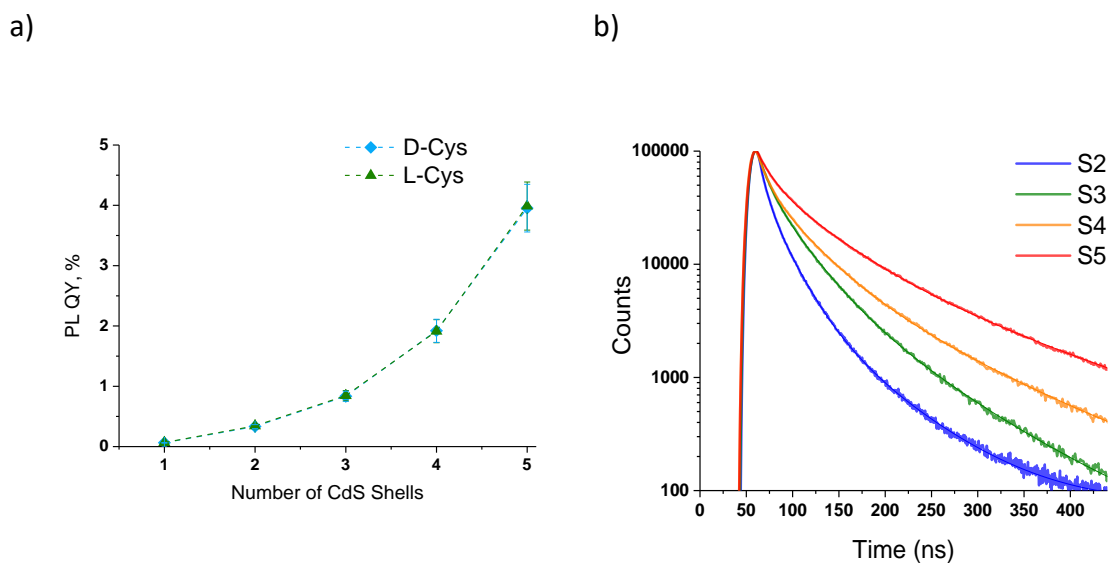
Figure 3-5. (a) The dependence of PLQY of L-/D-Cys CdSe/CdS QDs on the number of CdS monolayer shells. (b) The PL lifetime decays of D-Cys CdSe/CdS samples with varying thickness from S2-S5 with the fitting of each spectrum indicated by a darker shade line.

Following ligand exchange of the CdSe/CdS samples; transferring them into the aqueous phase using L- and D-cysteine ligands, the optical properties of the samples were examined by absorption dichroism, photoluminescent and fluorescent lifetime spectroscopy. The dependence of the PL intensity on shell monolayers can be seen in Figure *3-5* (a) (also see Table 3-4), which overall showed a significant reduction in photoluminescence due to the ligand exchange.

	PLQY (%)		
Sample	Toluene	L-Cysteine in water	D-cysteine in water
S1	2.3658	0.063	0.066
S2	20.4	0.332	0.342
S3	15.936	0.834	0.844
S4	18.517	1.92	1.913
S5	16.418	3.954	3.988

Table 3-4. Photoluminescent quantum yield (PLQY) measurements of CdSe/CdS QDs with variable shell thickness in toluene prior to ligand exchange and following L- and D cysteine ligand exchange in the aqueous phase.

We also found a gradual increase in PL QY with each additional CdS monolayer, with both the L- and D-cysteine 5 shell samples (S5) demonstrating the highest intensity PL after the fifth coating, giving a PLQY of 3.9 %. This is expected as the exciton is better confined to the core CdSe QD, and so less interaction takes place with the surface thiols. Fluorescence lifetime measurements were also carried out of the samples and is shown in Figure *3-5* (b), giving a trend of longer lifetimes that gradually increased as the shell thickness of the quantum dots increased. It is also worth noting, overall a significant reduction in photoluminescent lifetime has arisen due to the ligand exchange and is consistent with other findings regarding the photoluminescence of these CdSe/CDs QDs following ligand exchange[131]. The same pattern is found when we have evaluated the trend of the radiative decay as the shell increased (see *Table 3-5*), finding a strong increase from 1.08×10^6 to 4.65×10^6 as the CdS thickness increased.

Sample	t_1 (nsec)	Amplitude	t_2 (nsec)	Amplitude	t_3 (nsec)	Amplitude	QY, %	Average lifetime <t> (nsec)
shell 2	0.7	0.1934	2.3	0.5595	6.7	0.2471	0.3	3.1
shell 3	1.0	0.1934	3.3	0.5595	8.5	0.2471	0.8	4.1
shell 4	1.1	0.1608	3.9	0.4883	10.6	0.3509	1.9	5.8
shell 5	1.4	0.1205	5.2	0.465	14.3	0.4145	3.9	8.5

Table 3-5. Summarisation of D-cysteine capped CdSe/CdS QD post ligand exchange in water fluorescence lifetime measurements relative to shell thickness. The spectra were measured using a 458 nm excitation source.

3.2.4 QD CD spectroscopy studies

For CD measurements, CdSe/CdS QDs were stored in an excess of aqueous cysteine (0.08 mM) overnight prior to measurements, in order to ensure the QD's surface was completely coated. CD spectra of the S1-S5 CdSe/CdS samples exciton region is presented in Figure *3-6* (a). It can be observed that CD peaks corresponded to the excitonic bands of QDs, following the same red shift with the increase of shell thickness. In addition, it can be seen that the CD spectra splits at the absorption excitonic maxima, crossing zero and changing sign, the behaviour of which is described as the 'Cotton effect' in chiroptical spectra[129]. This can be assigned to the splitting of the excitonic hole level due to coupling interactions with the HOMO of the cysteine ligand producing two sub bands which are preferentially excited by alternating circular polarizations, though at present the precise mechanism of this coupling is unknown[129].

The dependence of the CD response on the number of CdS monolayers at the excitonic peak has been graphed independently and can be seen in the Figure *3-6* (b). This data utilises G-factor instead of CD signal and therefore avoids the influence of concentration

and oscillator strength when comparing the various samples. We see even a greater illustration of the lack of chiroptical signal inducement in the CdS shell in the region of CdS shell absorption onset (this can be seen in the Figure 3-7) as is to be expected.

a)   b)
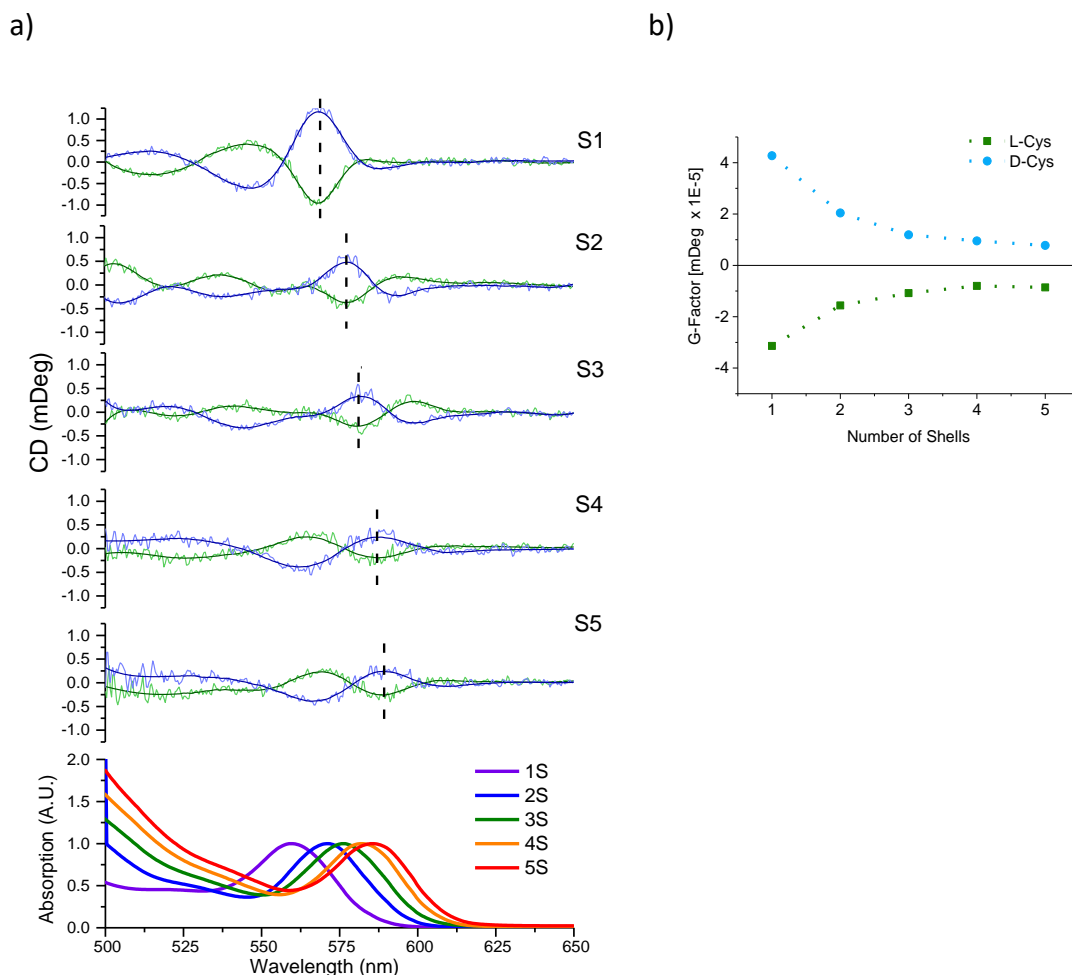
Figure 3-6. (a). CD spectra of L-/D-Cys CdSe/CdS QDs. (b). The dependence of the g-factor in the excitonic region of L-/D-Cys CdSe/CdS QDs on the number of CdS monolayer shells.

From this data, the chiral response intensity clearly illustrates an inverse relationship to the number of shell monolayers. This can be explained by the increase of distance from ligands to holes localized in the CdSe core and, consequently, the decrease of coupling between them and the chiral source. This explanation was also suggested in this work[129], though in contrast, this study shows a more complex dependence of QD chiral response. In this work, CdS shell thickness has the effect of CD signal enhancement for CdSe QDs with 1-3 CdS monolayers, and after which a decrease is found to take place as the

thickness increases to 4 and 5 monolayers of CdS. This was explained by the superposition of two opposing effects: signal reduction is due to the CD intensity decaying with the number of CdS monolayers, since the shell acts as an energy barrier for the holes. We believe that the same phenomena also contribute to our CD response, causing the reduction. But in their study, an additional effect is found that the CD signal increased with shell thickness, because the addition of CdS layers reduces the hole energy and shifts it closer to resonance with the ligand level. Interestingly we do not observe the same phenomenon in our system, while in our case the decrease of chiral response with shell thickness is unambiguous.
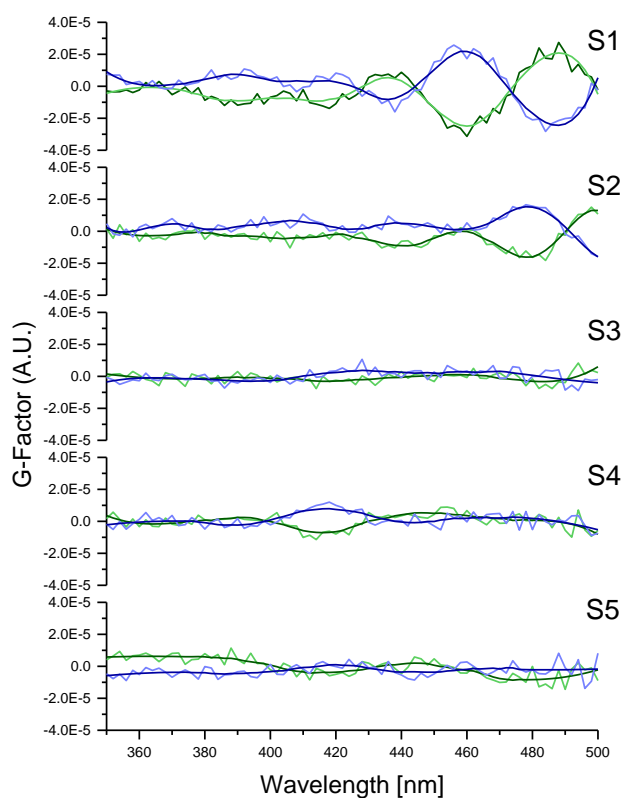
Figure 3-7. G-factor graphs of d-cysteine (blue) and L-cysteine (green) functionalised CdSe/CdS QDs with varying thickness of CdS shell, marked S1 –S5. The graphs also contain a smoothed function of the signals marked in the darker shade for each spectrum.

3.2.5   The Influence of Annealing on CD of QDs

A second goal of our research was to investigate the effects of shell annealing on the chiral properties of CdSe/CdS QDs in order to optimise the properties of the CdSe/CdS QDs. To investigate this, we heated samples of CdSe/CdS QDs with five shells at 250 ºC, and took aliquots at various times from 0, 15, 30, 60, 120 and 240 min. TEM images and size distribution data of the sample at 0 and 240 min of annealing are shown in Figure *3-8* and summarised in Table 3-6.

a)
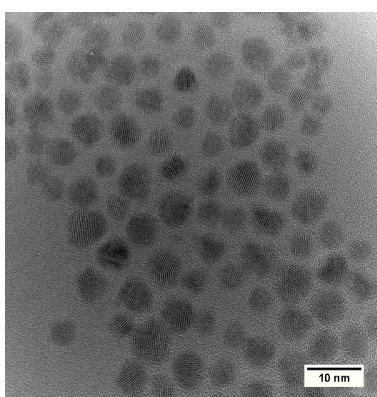
b)
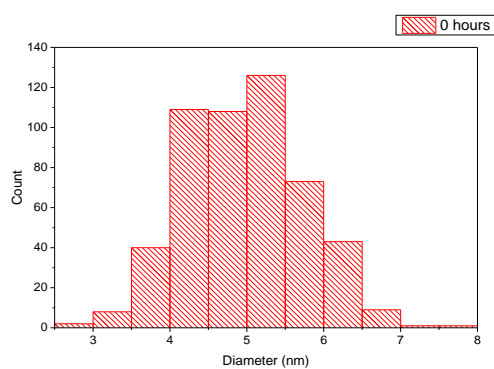
c)
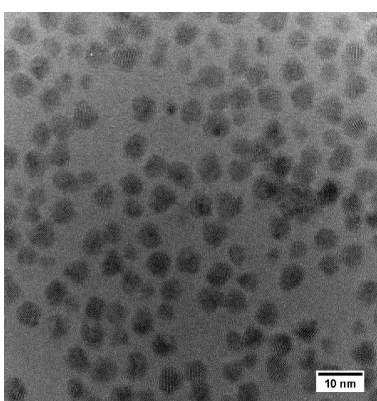
d)
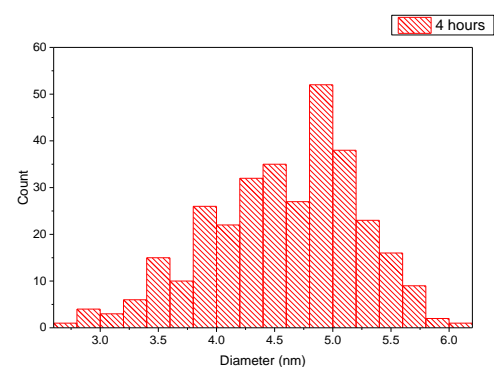
Figure 3-8. TEM image of 5 shell CdSe/CdS QDs, after 0 mins of annealing; B: Size distribution of 5 shell CdSe/CdS QDs, after 0 mins of annealing; C: TEM image of 5 shell CdSe/CdS QDs, after 4 hours of annealing; D: Size distribution of 5 shell CdSe/CdS QDs, after 4 hours of annealing.

Annealing time	N Total	Mean (nm)	Standard Deviation (nm)
0 min	520	4.96	0.77
250 min	322	4.58	0.65

Table 3-6. Size distribution data of annealing time dependence during CdSe/CdS QD synthesis derived from TEM analysis

It was observed that the annealing caused a very minor shape change in the CdSe/CdS QDs to occur, transitioning from a spherical to a slightly more angular shape. The diameters of the two forms of CdSe/CdS QDs were 5.0 nm ± 0.8 nm, and 4.6 nm ± 0.7 nm, for 0 min and 240 min, respectively. UV-Vis absorption spectra (see Figure 3-9) of the samples shows a gradual red shifting in exciton peak position from 587 nm to 593.6 nm from 0 min to 240 min.

a) b)
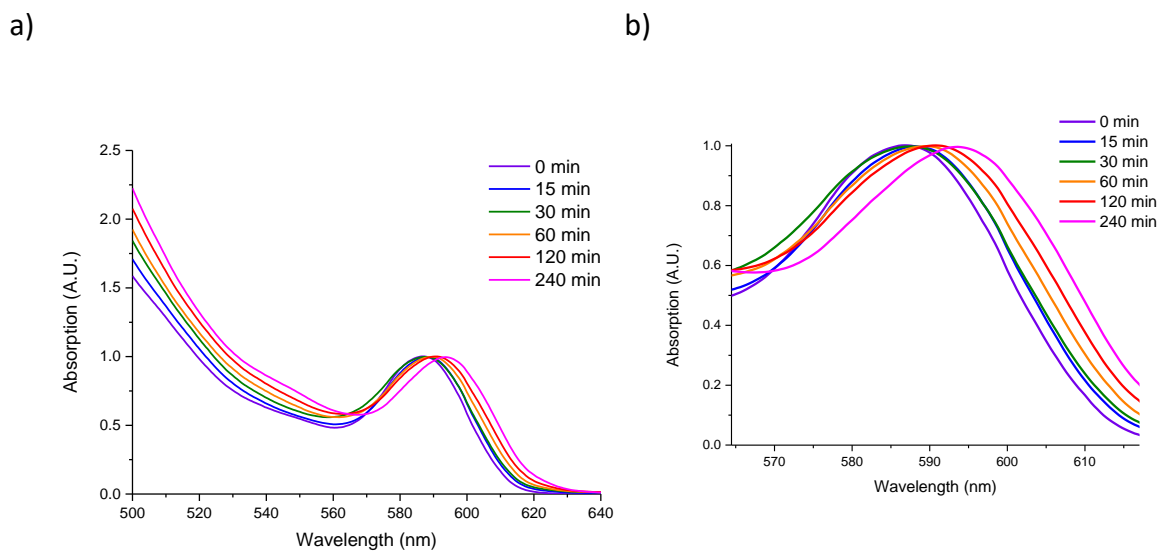
Figure 3-9. UV-Vis absorption spectra of 5 shell CdSe/CdS QDs with varying annealing time, marked 0 min to 240 min.

In addition, we find a red shifting in the photoluminescence from a peak emission of 599 nm to 606.5 nm (see Figure *3-10* A). Both of these effects are consistent with results found previously, with increased over coating, and is a consequence of the weak exciton confinement provided by the CdS shell[133-37].
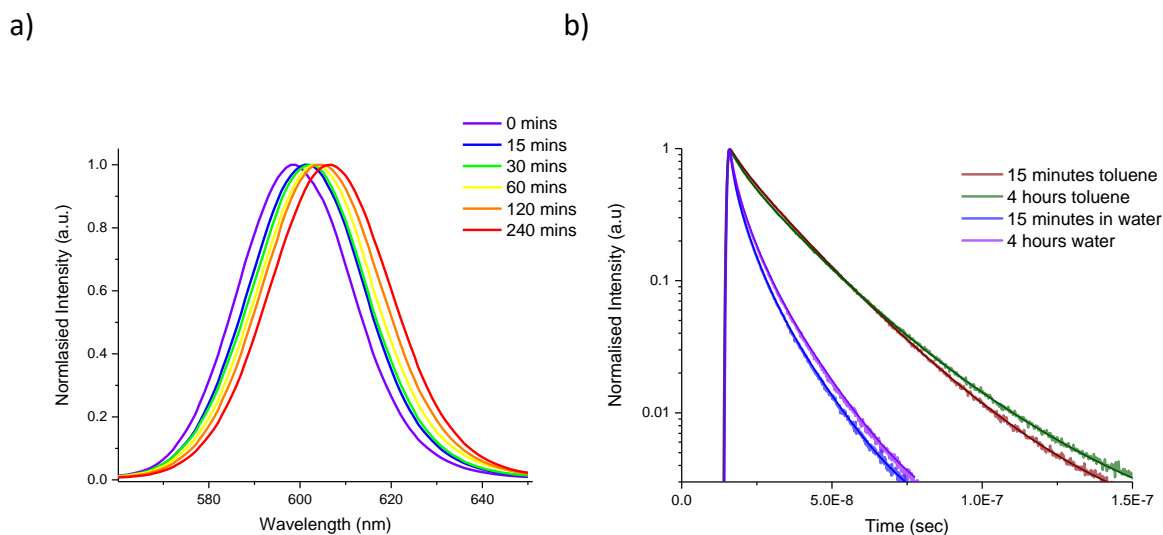
Figure 3-10. Pl emission spectra of 5 shell CdSe/CdS QDs is shown in (a) with varying annealing time, marked 0 min to 240 min measured in toluene, while figure (b) shows the fluorescence lifetime measurements made for two of these sample pre-and post-synthesis ligand exchange.

A ligand exchange was then carried out using L and D cysteine and the CD spectra was then measured of each aliquot. G-Factor spectra are represented in Figure *3-11*. The resulting G-factor signal of the exciton shows a gradual decrease in intensity as annealing occurs and is shown in Figure *3-12* A.
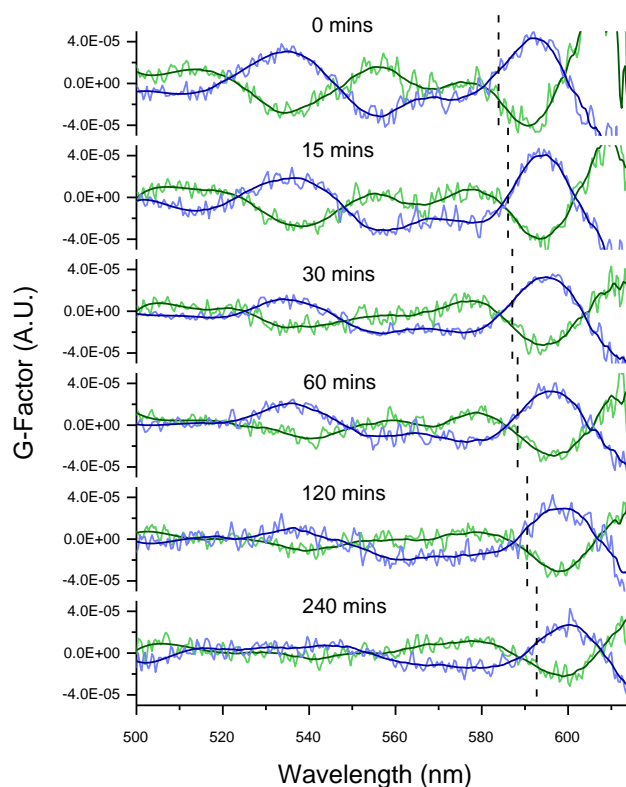
Figure 3-11. G-factor graphs of d-cysteine (blue) and L-cysteine (green) functionalised 5 shell CdSe/CdS QDs with varying annealing time, marked 0 min to 240 min. The graphs also contain a smoothed function of the signals marked in the darker shade for each spectrum

This result was unexpected since we had initially anticipated that annealing would improve the CD response, *via* an improved ligand inducement due to greater orbital overlap. Instead we have found that the presence of a defective surface in fact improves the CD response. This result has been reported previously[48,119,120] that *via* crystal defects, the resulting CD signal could be enhanced and so can explain the consequential trend.
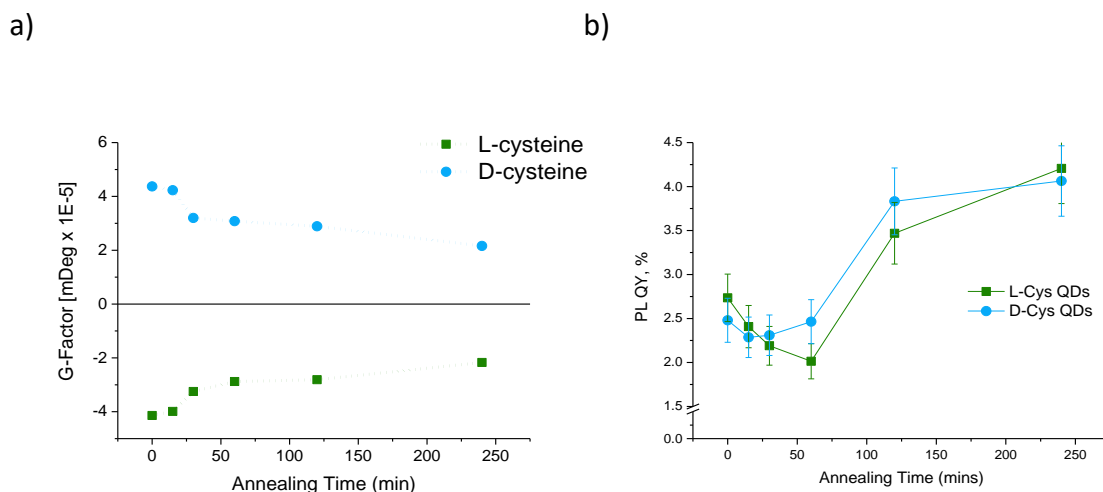
Figure 3-12. (a): The dependence of G-Value in excitonic region of L-/D-cysteine 5 shell CdSe/CdS QDs on heating duration of 5th monolayer shell during annealing time; (b): The dependence PL of L-/D-cysteine 5 shell CdSe/CdS QDs on heating duration of 5th monolayer shell during annealing time

The dependence of cysteine functionalised CdSe/CdS QDs PL QY is presented in Figure 5 B. In this case as opposed to CD, we find overall an increase in PL QY with annealingtimes, though a slight decrease is also evident from 0- 60 minutes. This overall increase can be related to the desired effect of crystal defect loss *via* the annealing effect. To further analysis this, fluorescence lifetime measurements were taken at the onset of annealing and following 4 hours of annealing. This was carried out prior and post cysteine ligand exchange, in both cases we find an increase in average fluorescence lifetime of the samples following annealing, further proving the heating process removed crystal defect sites.

Overall, we find opposing trends of increased annealing causing a loss in resulting CD signal intensity, while an increase in PL QY. From this data, it is clear precise synthetic control are vital to optimise core/shell QDs as chiroptical fluorescent QDs, since it is evident that annealing and therefore crystal defects also play an important role.

3.3   Conclusions

Thus, our investigations have shown the subtle relationship between PL and CD signals in ligand induced chiroptically active CdSe/CdS QDs. We have found that it is paramount

to optimise the thickness of the CdS layer on a CdSe/CdS QD so as to produce a luminophores with a strong CD response and effective PL following ligand exchange. We have observed the same trend of decreasing signal relative to previously published results[129] concerning CdSe/CdS QDs CD signal in relation to CdS shell thickness though in our study we did not find the same complex trend, as we observed the monotone decrease of the CD intensity with the shell thickness.

In addition, our results also clearly demonstrate that synthetic conditions such as annealing time have a strong impact both on the induced CD signal and luminescence, resulting in an increase in PL QY due to the decrease in crystal defects. We also found that increased annealing time led to a reduction of optical activity, which can be explained by the loss of crystal defects which have been initially associated with optical activity in QDs.

In summary, we are convinced that these fundamental studies are very important for the further development and use of these QDs for various sensing applications, in which both chirality and PL properties can be applied effectively to produce a class of chiral fluorescent nanoprobes. Therefore, this work lays the foundations for the further understanding of the optimal effective methodology and design conditions to realise chiroptically active luminescent QD assays.

4 Chapter 4: The Influence of Cysteine Concentration and Binding Modes on CdSe/CdS QD Induced Optical Activity

4.1 Introduction

Chiroptically active quantum dots (QDs) – fluorescent semiconductor nanocrystals with tuneable optical properties – have been intensively studied in last two decades[44,138] since they were first synthesised in 2007[47]. Chiral QDs have several potential applications [44,57,138–140] such as: biological sensors[41–43,70,79,111,141–144], anticounterfeiting material[145,146], as well as in photonic[45,124,147,148] and in spin-polarized devices[62,115,149].

Optical activity can be induced in QDs by capping them with chiral ligands via post-synthetic phase-transfer ligand exchange[44,48,150–155,49,57,63,103,125,128–130]. For this purpose, after QD hot injection synthesis in organic medium, the initial hydrophobic ligands are exchanged by chiral hydrophilic ligands[63,103,143,150]. The QDs thus synthesised exhibit optical activity in their intrinsic absorption region, unlike ligand molecules which usually absorb light only in UV region[103,150].

The origin of induced chirality can be explained by the following mechanisms: 1) chiral distortion of QD surface atoms by chiral ligands[47,120,126,151]; 2) enantiomeric enrichment of intrinsic chiral defects formed in QDs during the synthesis[48] or 3) hybridization of electron levels of QD and chiral ligand molecules, which leads to splitting of QD hole-electron level to two sublevels absorbing circular polarized light differently[72,127,129,130,150,156,157].

Besides, the shape of QD CD spectra as well as the magnitude of induced CD bands depend on many factors, such as: the material and size of the QD core[49,129], the QD shape and anisotropy[44,48,63,65,103,154,158,159], material and thickness of the shell[129,150,151] and the chemical composition and coordination modes of the ligand[128,153,155,160]. Recently it was shown that chiral ligand concentration also can influence QD induced CD intensity[154,161]. However, no systematic study able to explain this phenomenon has been carried out so far. Besides, as it was observed in the present work, CD intensity can be changed dramatically depending on ligand concentration, up to one order of magnitude, and the dependence is non-linear.

One of the potential causes of this phenomenon can be the changing of ligand binding mode with the concentration. Indeed, it was previously reported that chiral ligand coordination on QD surface can dramatically change CD spectra, even invert it[58,128,153,155,162], and molecules containing several functional groups can chelate metal ions differently depending on ligand/metal ion ratio.

In this chapter we report the systematic investigation of the interrelation between L-cysteine (L-Cys) concentration, coordination mode and CdSe/CdS QD CD intensity. L-Cys QDs we obtained by ligand exchange of organic ligands of QDs synthesised by SILAR hot injection method for L-Cys.

We believe that this investigation is of the great interest from both fundamental and practical point of view. It will give a possibility to find the optimal ligand concentration for maximal CD response, which will allow to increase in signal-to-noise ratio for CD spectroscopy applications, can help to improve electron-transfer kinetics of chiral QDs, that is important for spintronic devices, and etc. Moreover, a lot of works in last few years are devoted to the investigation of influence of different factors on the CD signal intensity, but the ligand concentration and ratio ligand/QD and ligand/QD surface were not taken into account. In this case obtained data can be incorrect, for example, when QDs with different size are compared. Considering of the ligand concentration influence will allow to obtain more accurate results.

4.2 Results and Discussion

4.2.1 The influence of Cys concentration on CdSe/CdS core/shell QD optical activity

CdSe/CdS QDs were synthesized by standard hot injection technique [150]. The quantum dots have been characterized by UV–vis, photoluminescent, fluorescence lifetime and CD spectroscopy and transmission electron microscopy (TEM). The diameter of the QDs was 5.2 ± 0.8 nm, and the thickness of the CdS shell was 1.2 nm, which corresponds to the 5 monolayers of CdS. Then subsequently original hydrophobic ligands (TOPO, oleic acid, oleylamine) of QDs were replaced by L- and D-Cys using phase transfer procedure described in[41]. Briefly, 75 µL of a Cys solution in methanol (from 0.018 to 0.27 M depending on the required final concentration) was added to the 750 µL of QD

chloroform solution (12 µM), shaken, and left for 2 min to allow Cys to replace the hydrophobic ligands. Next, 1,5 mL of an aqueous 0.01 M KOH solution was added and the Cys functionalised QDs were transferred to the aqueous phase. As a result, QDs obtained chiroptical activity which was reflected in the appearance ofmirror-imaged CD signals in the region of intrinsic QD absorbance including excitonic area (Figure 4-1).
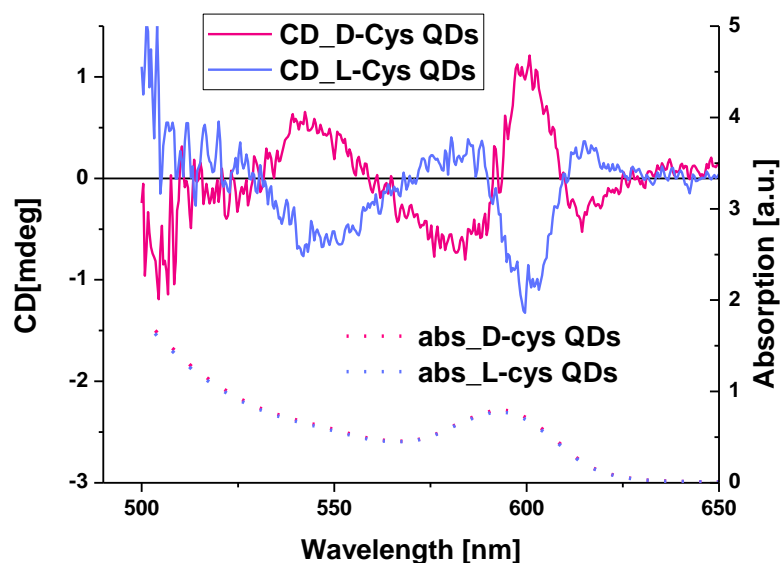
Figure 4-1. CD (solid lines) and UV-Vis (dotted lines) spectra of D-cysteine (red) and L-cysteine (blue) functionalized CdSe/CdS QDs. Cysteine concentration is 0.42 mg/ml.

To study the influence of Cys concentration on QD chiroptical response intensity, ligand exchange procedure was performed with different amounts of Cys ligand (from 0.1 to 1.6 mg/ml in final working solution). It was not technically possible to carry out the procedure with higher amount of Cys due to limited solubility of Cys in methanol. Thus, an extra amount of Cys were added to the aqueous solutions of Cys-QDs to obtain the Cys concentration of 4.7 and 11.6 mg/ml. As the example, several G-factor spectra of L-Cys functionalised QDs after phase transfer with different amount of Cys are illustrated in Figure 4-2, A. G-factor was used instead of CD signal to avoid the QD concentration influence. The G-factor is defined as $G = \Delta\varepsilon/\varepsilon = (A_L - A_R)/A$, where A_L and A_R are the absorbance of circularly polarized left-handed and right-handed light, respectively, and A is the absorbance of unpolarised light.

It can be seen that G-factor intensity changed with the Cys concentration in a non-linear way. The dependence of the G-factor intensity of the maximum peak corresponding to the QD excitonic region on Cys concentration is shown in Figure 4-2, B. As expected initially G-factor intensity increased with Cys concentration. However, after certain critical Cys concentration, QD G-factor intensity reached a maximum and started to decrease. This effect was unusual and required additional investigations.

a)   b)
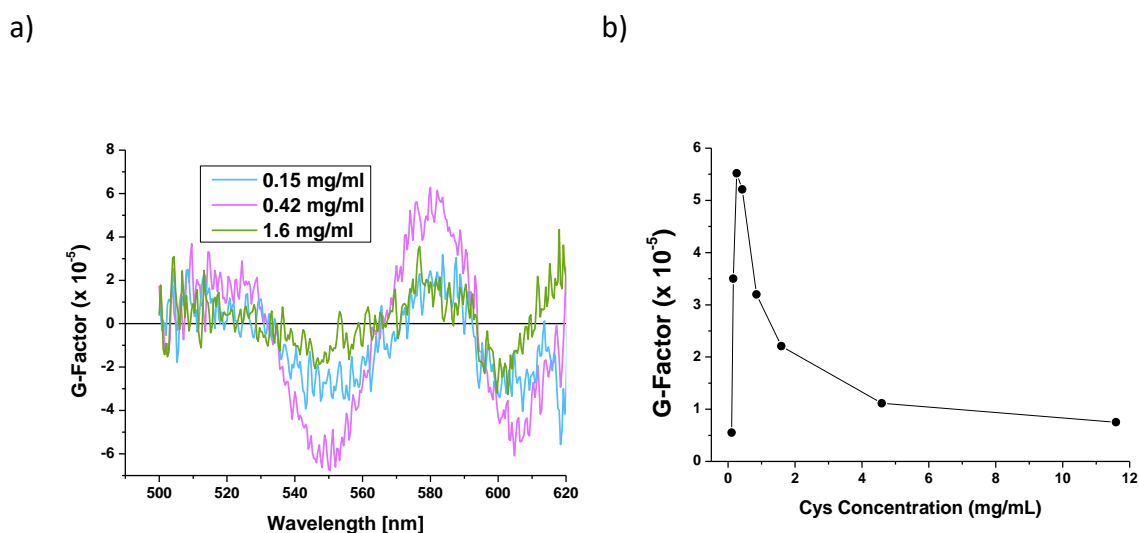
Figure 4-2. (A) G-factor graphs of L-cysteine functionalized CdSe/CdS QDs with varying Cys concentration: 0.42 (pink); 0.85 (blue) and 1.6 (green) mg/ml. (B) Dependence of the G-factor in the excitonic region of L-Cys CdSe/CdS QDs on Cys concentration.

4.2.2 Determination of the ligand binding mode on the QD surface

The most likely reason for the G-factor reduction is due to the change of Cys binding mode with Cd^{2+} ions on the QD surface with increasing of amount of the Cys in the solution. Previously it was shown that QD CD spectra shape strongly depend on coordination mode of chiral ligand on QDs surface[58,128,153,155,162], but the dependence of intensity of QD CD signals on the concentration of chiral ligand has never been studied.

Cys ligand has three functional groups: thiol, carboxylate, and amino groups. Potentially all of them can be coordinated to Cd^{2+} ions on the QD surface, but thiol group has the strongest affinity to Cd^{2+} ions. Thus, cysteine can coordinate to QD with all three groups (tridentate); with combination of SH and NH_2 groups (SH-NH_2 bidentate) or SH and

79

COOH groups (SH-COOH bidentate); and SH group only (monodentate). The possible Cys binding modes are presented in Figure 4-3.

It was shown previously on aqueous complexes of metal ions with Cys that ligand binding mode depends on the ratio between the components. For example, in[163] Cys was coordinated with Pb^{2+} ions by three groups in 1:1 complexes and as bidentate in 2:1 complexes. Thus the concentration of Cys can influence its binding mode and therefore G-Factor intensity of QDs.
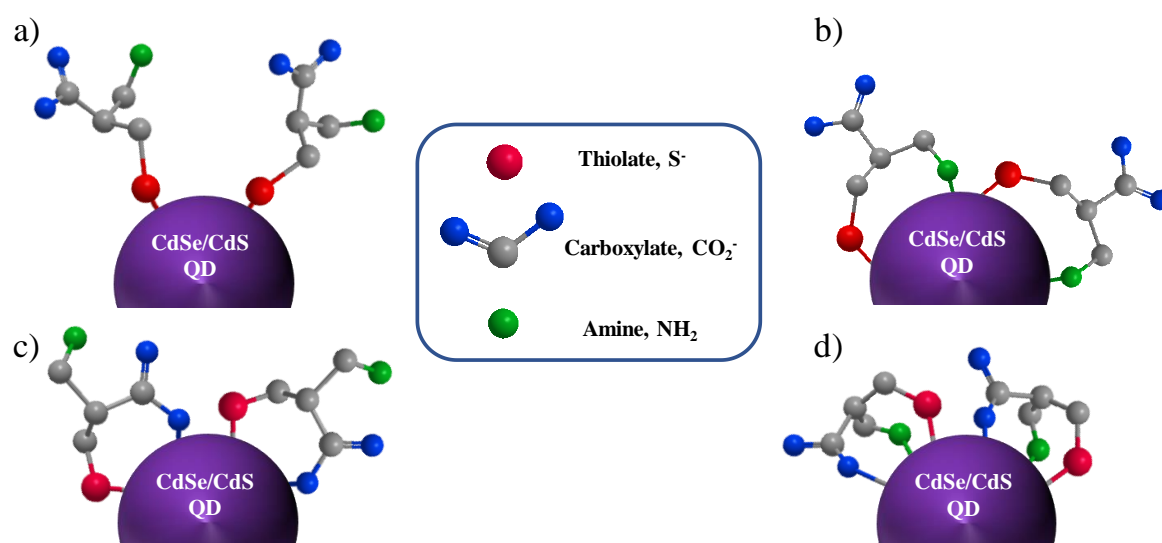
Figure 4-3. Scheme of the possible Cys binding modes on the QD surface. (A) SH-monodentate, (B) SH-NH₂ bidentate, (C) SH-COOH bidentate and (D) tridentate.

4.2.3   Investigation of binding modes by NMR

To investigate how Cys concentration influence the binding mode of cysteine on CdSe/CdS QD surface, ^1H and ^{13}C NMR spectroscopy analysis of two L-Cys QD solutions was performed: 1) solution with "low" Cys concentration (approx. 0.2 mg/ml), at which G-factor increased, and 2) "high" Cys concentration (20 mg/ml) corresponding to maximally decreased G-factor. The way of preparation of the solutions is described below. After phase transfer QDs still have some amount of residue hydrophobic molecules on the surface. In order to remove those molecules, the QDs were purified after phase transfer by washing with excess cysteine (20 mg/mL). Total removing of the hydrophobic ligands

is confirmed by FTIR spectra (see section 4.2.4). To obtain a sample with a low amount of Cys the excess cysteine was removed by washing of QDs 2 times with 10x volume of KOH solution with pH 13 to obtain Cys concentration approx. 0.2 mg/ml. High Cys concentration solution pH was adjusted to 13 by addition of concentrated KOH solution. All Cys-QD solutions for NMR analysis were prepared and measured under Ar atmosphere to avoid Cys oxidation.

Cysteine contains 3 carbon atoms, which NMR peaks for free molecule are(Figure 4-4): C^1 – carbon atom of the carboxylic group; C^2 and C^3 – carbon atoms bound to NH_2 and SH groups – with the peak positions 179, 59 and 29 ppm respectively (Figure 4, insert A, green spectrum).

At low concentrations (Figure 4-4, insert B, pink spectrum), only one set of Cys peaks (different from that of the free molecule) can be observed, proving that almost all cysteine molecules are bonded to the QD surface. Besides, the 3 signals present a significant shift in position (from 179 to 168 ppm for the carboxylic C^1,[164] and from 59 ppm to 72 ppm for the aminated C^2 and from 29 to 62 ppm for the thiolated C^3 [165]) suggesting that a low concentrations Cys is bound in a tridentate mode. Athigh Cys concentration (Figure 4-4,blue spectrum) the ^{13}C NMR spectrum presents three sets of peaks: i) The first one with 3 intense signals corresponding to free Cys; ii) The second one with 3 weak peaks colocalising with the low concentration ones; and iii) the third one where C^1 stayed almost in the same position, but C^2 and C^3 shifted from 59 ppm to 55 ppm and from 29 to 44 ppm respectively, similar to the shifts reported for a NH_2-SH bidentate bound mode[166].
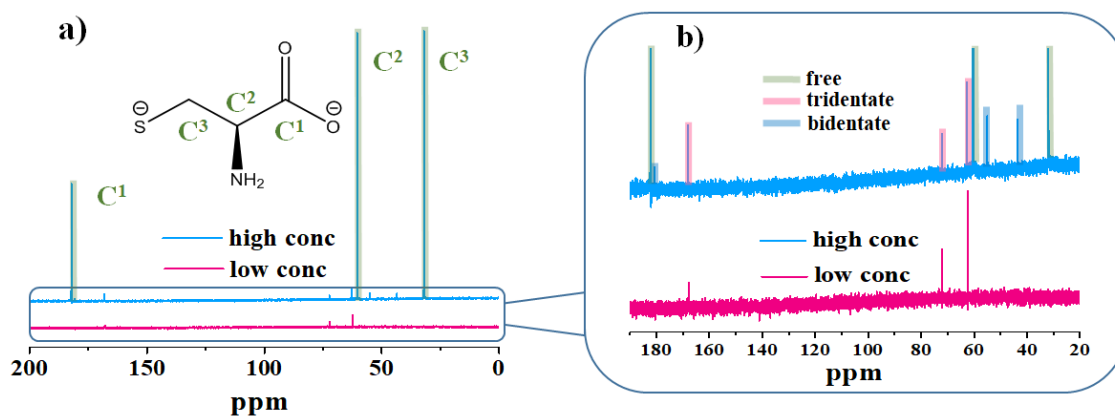
Figure 4-4. a) ^{13}C NMR spectra of QDs with high (blue) and low (red) Cys concentration at pH 13; b) up scaled ^{13}C NMR spectra of QDs with high and low Cys concentration (peaks of bound cysteine).

It is well known that the pH affects the charge of the functional groups and therefore the molecular environment and the NMR spectra. To stabilize the QDs suspension a basic pH is required. The ^{1}H NMRspectrumoffree Cys at pH 13 is shown in figure 5 (green spectrum): 1) Hc at 3.45 ppm, Ha at 2.70 ppm and Hb at 2.95 ppm. The carboxylic and thiol groups are deprotonated at pH 13, so there is no HNMR signal arising from protons on these groups.

^{1}H NMR spectra is consistent with the data obtain by ^{13}C NMR. Atlow concentration all Cys is bound to the QDs surface, and only one set of peaks corresponding to the tridentate[163] union of the molecules is observed from the NMR spectrum. As can be seen in Figure *4-5* (pink spectrum), all peaks are downfield shifted compared to free Cys (Ha, Hb and Hc shifted from 2.70, 2.95 and 3.45 ppm to 3.42, 3.50 and 3.63 respectively).
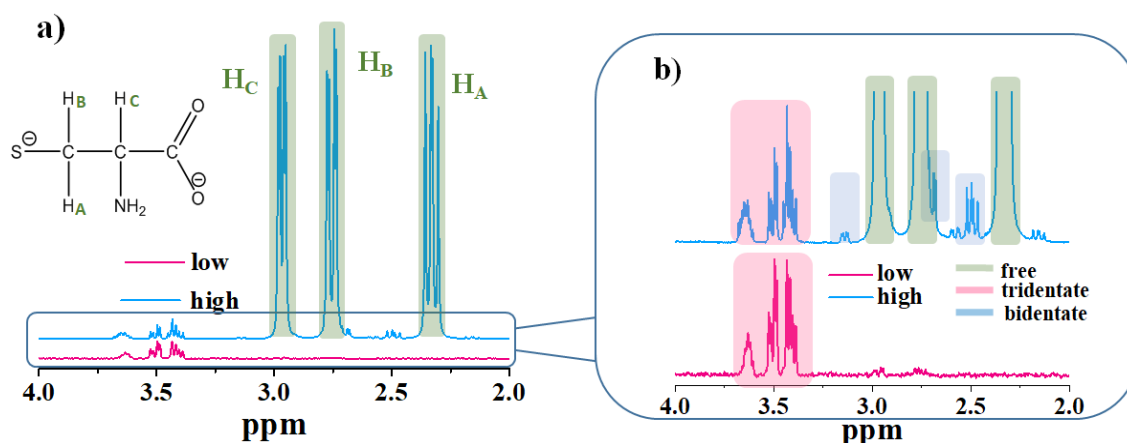
Figure 4-5. a) ^{1}H NMR spectra of QDs with high (blue) and low (red) Cys concentration at pH 13; b) up scaled ^{1}H NMR spectra of QDs with high and low Cys concentration (peaks of bound cysteine).

At high concentration of Cys three sets of ^{1}H NMR peaks were also observed (Figure 4-5, blue spectrum): i) the first one corresponds with the free Cys; ii) the second one has the same peaks as the spectrum recordedat low Cys concentration (tridentate mode); the third one corresponds to the bidentate form. In the case of the bidentate mode Hb peak is shifted downfield, which corresponds to thiol group binding to Cd^{2+}. Hc peak is almost at the same position, hence the carboxylic group is most likely free.

Cys molecule has three staggered rotamers as the result of rotation along the C^2-C^3 axis: trans-rotamer, where carboxyl and thiol groups are in trans position to each other, and two gauche-rotamer configurations: g and h (Figure 4-6).
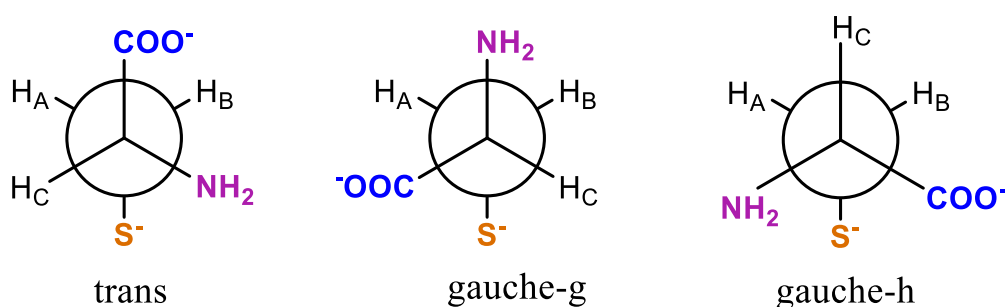
Figure 4-6. Newman projection of the 3 rotamers of Cys

In[163] it was shown that in alkaline conditions, when COOH and SH groups of free Cys are deprotonated and negatively charged, trans-rotamer is prevalent according to the

NMR data. When Cys is bound to the QD with all three functional groups (tridentate) the NMR spectra corresponds to gauche-h-rotamer, i.e. all three groups are situated at one side of the molecule, which facilitates tridentate Cys binding. When Cys is bound in SH-NH_2-bidentate mode, both conformation (rotamers) are present in solution, but trans-rotamer is prevalent. When Cys binds to QDs, trans-rotamer can be even more preferable because of stearic factor.
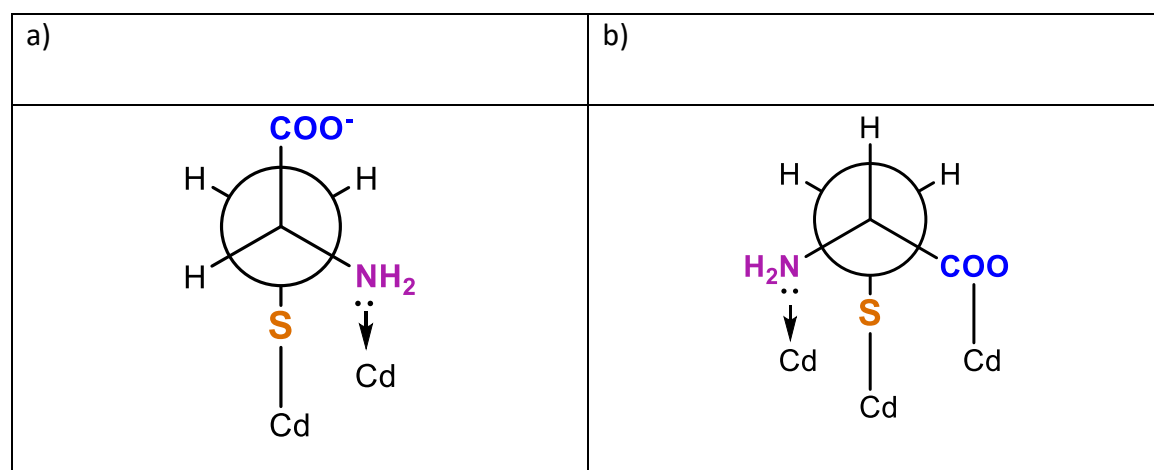
Figure 4-7. a) SH-NH_2-bidentate and b) tridentate coordination configurations of Cys on QD surface.

It has been previously shown[58,128] that one type of enantiomer of a chiral molecule can bind to the QD surface in different ways. For example, Acetyl-L-Cys can bind by SH and COOH groups or SH and Ac groups depending on synthesis conditions[52]). Sometimes, these bound molecules exhibit nearly mirror-image configuration on the QD surface which gives rise to inverted CD spectra. The results were confirmed by theoretical calculations[128]. In our study SH-NH_2-bidentate and tridentate coordination configurations of Cys also appear to be nearly diastereomers of each other (Figure 4-7) and can cause the origin of the opposite CD signals. Thus at high Cys concentrations, when the amount of bidentate bound molecules increased, CD due to tridentate bound Cys is compensated by bidentate Cys resulting in reduced CD signal.

4.2.4 Investigation of Cys binding modes by FTIR

To determine the binding mode of the amino group, which was not obvious from NMR analysis, we also performed FTIR analysis of our samples. To prepare the samples

for our FTIR studies, Cys-stabilized QDs were precipitated from aqueous solutions with high and low Cys concentrations using acetone and subsequently dried. It is important to note that samples did not contain water, which has a very broad and intense peak in the 3000-3750 cm^{-1} regionthatoverlaps with the asymmetrical stretching vibration peaks of the amino group. Cys-QDs spectra are provided in Figure 4-8 for comparison with QDs functionalized with initial organic ligands (mostly oleylamine) and with pure Cys.
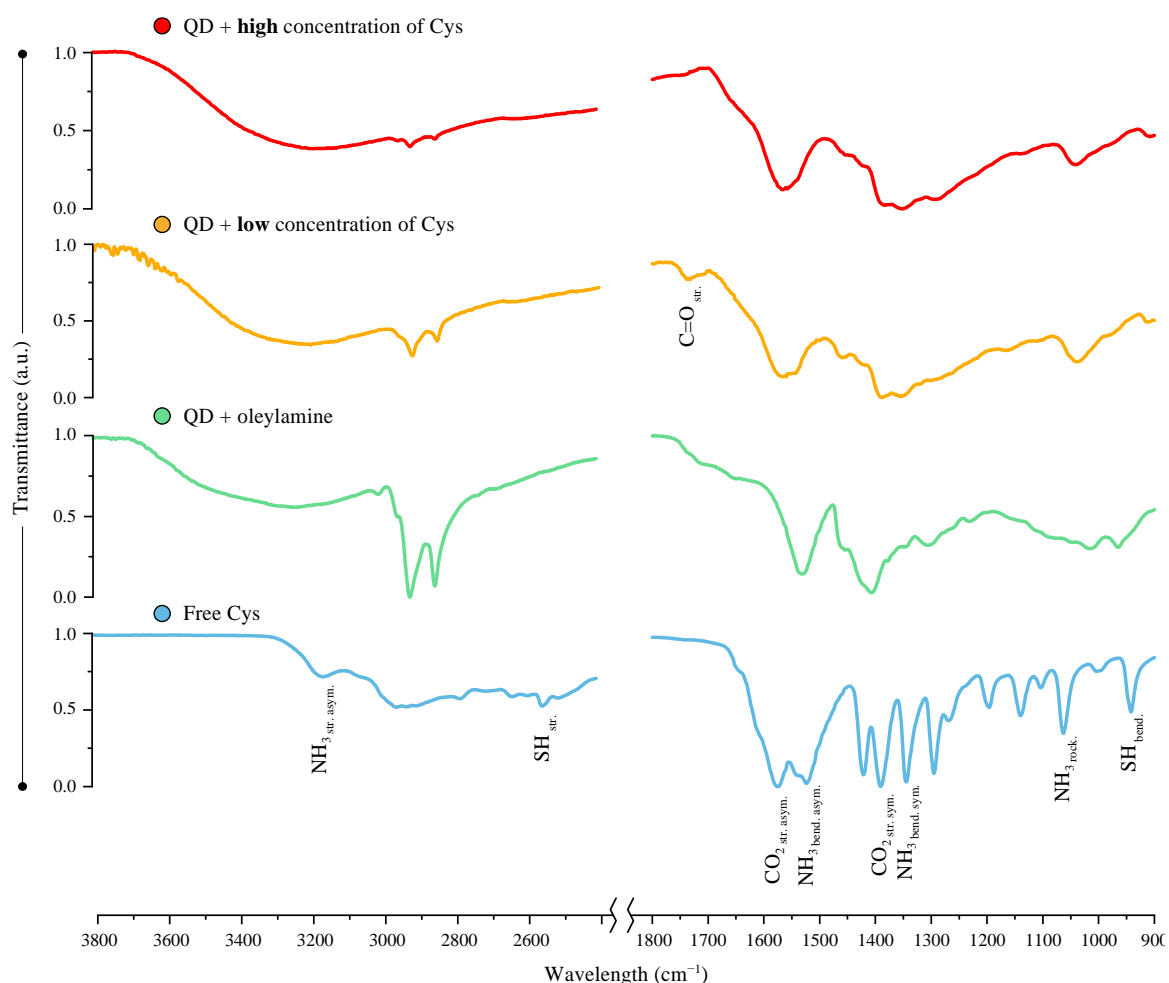
Figure 4-8. FTIR spectra of QDs precipitated from aqueous solutions with a high and low Cys concentration, QDs with organic ligands – mostly oleylamine, and free cysteine.

The S$^-$ group of free Cys has two peaks at 2550 and 942 cm^{-1} corresponding to its stretching and bending modes, respectively. Both peaks are absent on the spectra of Cys-QDs. The NH$_2$ group of free Cys has a peak associated with asymmetrical stretching vibrations at 3165 cm^{-1}, which is significantly broadened when NH$_2$ is bound to the QD surface. This broadening can be observed in the spectra of QDs with oleylamine and QDs

with Cys, both at high and low concentrations, confirming that the amino group is coordinated with the QD surface. Pure Cys has a zwitterionic form with a deprotonated carboxylic group (COO$^-$) and a protonated amino group (NH$_3^+$). The free negatively charged carboxylic group has asymmetric and symmetric stretching vibration peaks at 1575 and 1391 cm^{-1}, respectively. The appearance of a carbonyl stretching mode peak at 1735 cm^{-1} on the FTIR spectra of QDs with a low Cys concentration indicates the binding of the COO$^-$ group. QDs with a high amount of Cys ligands display a smaller peak at this area, indicating that part of the COO$^-$ groups are free. This is in full agreement with the NMR data.

4.2.5 Computational studies of Cys binding modes.

DFT calculation are perforemd by prof. Max García-Melchor Eric Mates-Torres.

Based on the experimental observations presented above, a likely explanation for the change in the coordination of the adsorbed Cys ligands upon increase of Cys concentration is the emergence of ligand-ligand interactions. To confirm this, we conducted a thorough investigation by means of periodic DFT calculations (see the Materials and Methods section for details) in order to elucidate the binding modes of Cys molecules on the QD surface at different concentrations. Following an exhaustive iterative coverage analysis, we selected five theoretical models featuring 1 to 5 Cys molecules adsorbed on a *p* (2×2) supercell of a CdS (0001) surface with the aim to reproduce low, intermediate and high coverage limits, respectively. For each surface coverage, we then considered all possible combinations of binding modes, rendering a total of 67 different structures. The results obtained for the most energetically favorable adsorptions are summarized in Figure 4-9, which also displays the binding modes adopted by each of the ligands per unit cell.
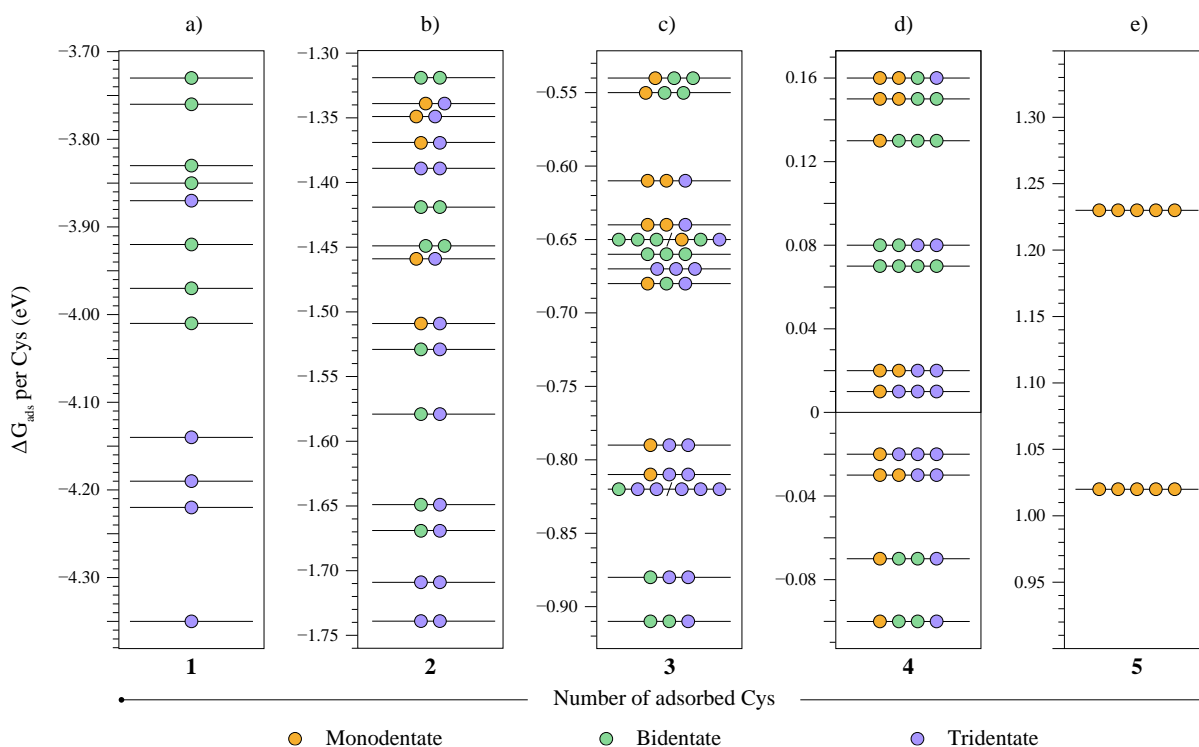
Figure 4-9. Calculated adsorption Gibbs energies, ΔG_{ads}, for the (a) low, (b-c) intermediate, and (d-e) high coverage models with 1 to 5 Cys molecules per unit cell. Each line represents a different configuration of the ligands within a given coverage. Monodentate, bidentate, and tridentate Cys binding modes are represented as orange, green and purple circles, respectively. Grey areas indicate endergonic configurations, and therefore, these are predicted to be unlikely. We note that in (c) there are 2 sets of configurations that possess the same ΔG_{ads} value up to the second decimal digit; these are represented on the same line and separated by a slash.

The analysis of the most stable configurations of the low coverage model (Figure 4-9a) revealed that Cys ligands are predominantly bound to the QD surface in a tridentate conformation with the S^-, COO^- and NH_2 groups coordinated to surface Cd^{2+} ions, in agreement with experiments. As can be seen in Figure 4-9b, the addition of a second ligand did not affect the Cys binding mode in the lowest energy configuration. However, DFT calculations predict the emergence of a relatively stable configuration (only 70 meV higher in energy with respect to the lowest energy configuration) in which one of the Cys ligands becomes bidentate through the S^- and NH_2 groups, while the other one remained coordinated in a tridentate mode. This new configuration points towards a decrease in the prevalence of the tridentate mode at higher Cys coverages, again in line with

experimental observations. This was indeed observed upon the addition of the third and fourth Cys ligands in the intermediate and high coverage models depicted in Figure 4-9c,d. In both cases, the bidentate conformation was found to predominate in the most stable configurations, where even a monodentate Cys was predicted to coexist on the surface covered with four ligands. An inclusion of a fifth Cys molecule was revealed to be energetically unfeasible based on the endergonic ΔG_{ads} values obtained for the models depicted in Figure 4-9e.

The lowest energy structures from the coverages including 1 to 4 Cys ligands are represented in Figure 4-10, alongside 2-dimensional (2D) plots of the charge density differences between the ligands and the QD surface. In these plots, warmer (orange and red) and colder (turquoise and blue) colors indicate a decrease and increase, respectively, in the charge density difference across the interaction plane. Hence, functional groups which lay on higher or lower charge density difference regions are predicted to interact with the QD surface. This allows to confirm the binding mode of each adsorbed Cys molecule based on the number of functional groups laying on these regions.
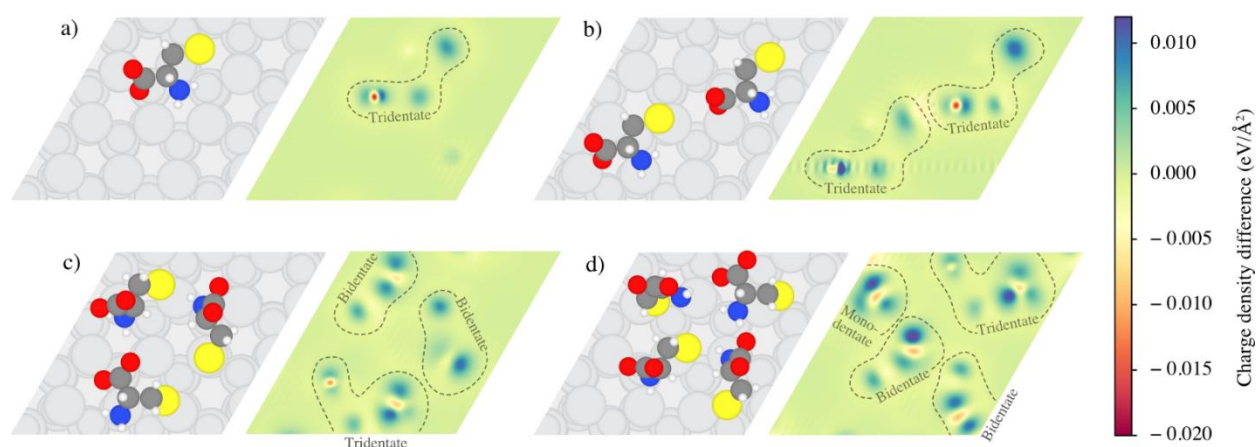
Figure 4-10. Optimized structures of the most stable configurations with a predicted exergonic adsorption for the (a) low, (b-c) intermediate, and (d) high coverage models featuring 1 to 4 Cys, alongside a 2D plot of the charge density difference across the interaction plane. Atom color code: C (grey), H (white), N (blue), O (red), and S (yellow).

To understand the change in the Cys binding mode observed from tridentate to bidentate and monodentate at high ligand concentrations, we subsequently analyzed the intermolecular non-covalent interactions (NCI) on QD surfaces terminated with 2 to 5 Cys

molecules (see Methods section for details) – the low coverage model with 1 Cys per unit cell was not considered as ligands in periodic images are too far apart to interact non-covalently. Importantly, the methodology employed herein allows for the semiquantitative analysis of these interactions by identifying the regions in which the atomic clouds of the Cys molecules overlap. In short, since the electron density in these regions is maximum, the reduced density gradient tends to zero. Hence, by plotting the reduced density gradient as a function of the density multiplied by the sign of the second eigenvalue of the Hessian matrix (λ_2, which effectively distinguishes if the interaction is attractive [negative] or repulsive [positive]), a series of peaks are obtained which can be attributed to each NCI and its attractive or repulsive behavior, as described elsewhere[167,168]. Attractive interactions include hydrogen bonding, dipole-dipole and London dispersion interactions, while very weak interactions correspond to long-range van der Waals interactions; repulsive interactions mainly encompass steric effects.

The NCI analysis of the high coverage model with 4 Cys per unit cell is displayed in Figure 4-11. According to this representation, the three strongest attractive interactions correspond to the hydrogen bonding between the NH_2 group and COO^- or S^-. Interestingly, these attractive interactions offset the steric clashes between Cys molecules, making this configuration stable with a ΔG_{ads} per Cys of *ca.* –0.10 eV (Figure 4-9d). The ability of Cys molecules to create such strong attractive interactions is, however, hindered upon addition of a fifth Cys (high coverage, Figure 4-9e), which derives in weaker attractive interactions and stronger steric clashes leading to the unfavorable adsorption of further Cys ligands.
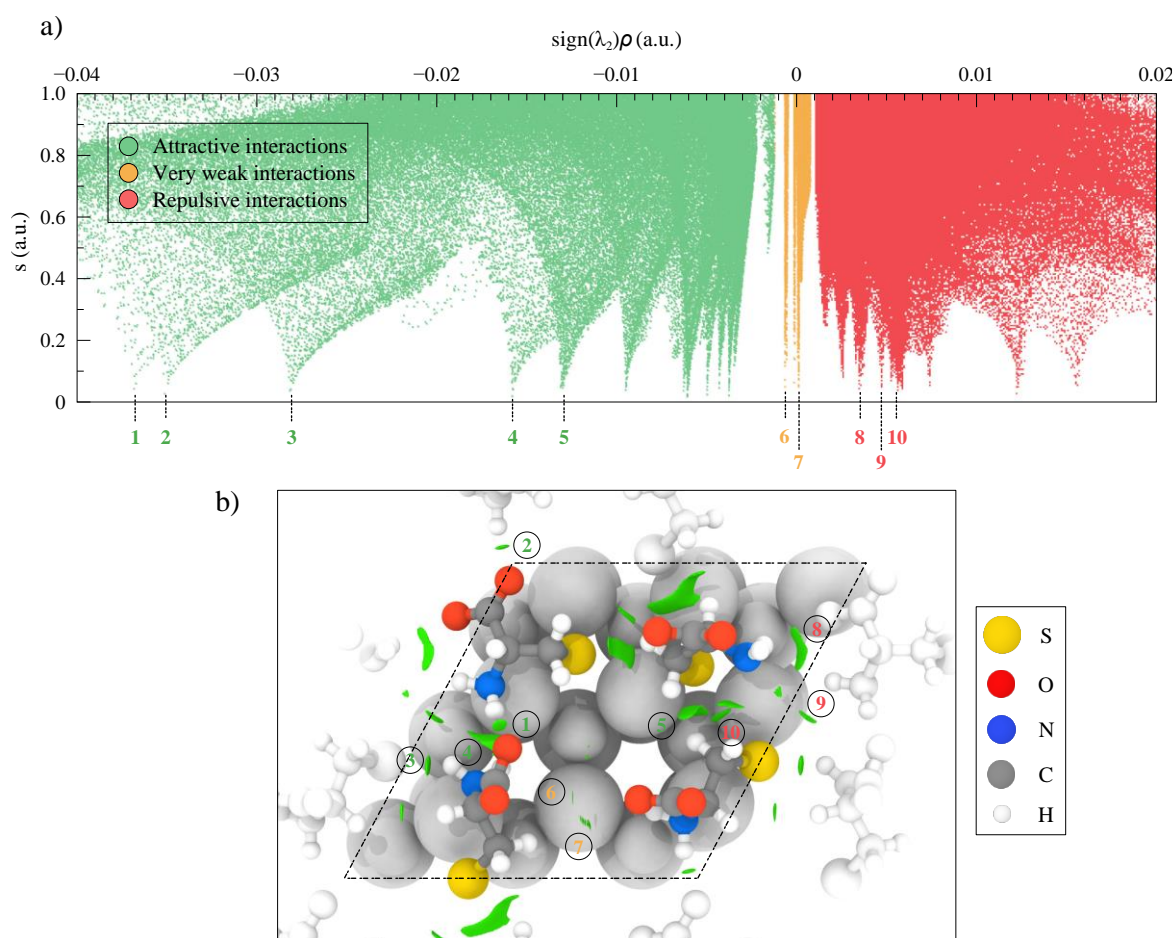
Figure 4-11. a) Plot of the reduced electron density gradient as a function of the electron density multiplied by the sign of the second eigenvalue of the Hessian matrix, which effectively quantifies the non-covalent interactions between the adsorbed Cys ligands. b) Representation of the intermolecular non-covalent interactions inside a unit cell, displayed as a green isosurface with an isovalue of 0.45 e⁻/(a.u.)³. The ten most relevant interactions are labelled in both the reduced density gradient plot and the representation of the non-covalent interactions. Atoms of Cys ligands from neighboring unit cells are colored in white, while Cd and S atoms from the QD surface are colored in light grey for clarity.

Overall, DFT calculations clearly show that, at low concentrations, Cys molecules are predominantly adsorbed on the Cd^{2+} ions of the QD surface in a tridentate mode via the S^-, NH_2 and COO^- groups. However, this trend in coordination is altered as the Cys concentration increases. Particularly, the high coverage models predict the prevalence of

bidentate Cys ligands bound *via* the S⁻ and NH$_2$ groups, with the possibility of ligands present in a monodentate coordination *via* the S⁻ moiety. These results are in good agreement with the experimental peaks observed in the NMR and FTIR spectra at low and high Cys concentrations, showing the same trend in the coordination change with concentration.

4.3 Conclusions

Thus, the influence of Cys concentration on QD CD signal intensity was investigated in details. For this purpose, spherical CdSe/CdS QDs were used. It was shown that QD CD signal intensity increased with Cys concentration at the beginning, then reached a maximum and decreased at high Cys concentrations. FTIR and NMR analyses showed that Cys had different binding configuration on the QD surface at different concentrations. At high concentrations Cys most likely bound to QD surface with thiol and amino groups, while at low concentrations Cys bound to Cd^{2+} ions with all 3 functional groups.

It can be suggested that Cys bound to QDs by three groups and SH-NH$_2$-bidentate Cys have diasterioisomeric coordination configurations on QD surface and give rise to the opposite CD signals. At high concentration of Cys, at which large amount of Cys has bidentate binding mode, CD signal can decrease as a result of superposition of these opposite CD signals.

Since the chirality plays a key role in so many chemical and biological systems, the results obtained in the present work are of real interest from both fundamental and practical point of view and should contribute to the development of potential applications of optically active nanocrystals, involving optical chiral sensing, detection of various enantiomeric species, enantiospecific separation, chiral catalysis, chiral memory and bio-sensing.

5 Chapter 5. Enantioselective cell uptake and cytotoxicity of optically active NPs in A549 cells

5.1 Introduction

Chirality plays a crucial role in chemistry, pharmacology, biology, and medicine, as most of the organic molecules comprising living organisms are chiral, such as amino acids, carbohydrates, proteins, DNA, etc.[169] The area of chirality related research in nanoscience is rapidly expanding, due to the numerous potential applications of optically active nanoparticles (NPs)[6,44,47,79].

QDs can be used in cell biology for many applications, the main of which is fluorescent cell imaging[75]. As it was mentioned in the Introduction (Chapter 1), QDs have much higher photo stability, broader absorption and narrower emission with higher PL QY than most of the organic dyes[170]. Besides, QDs can be used as cell dyes for fluorescence-activated cell sorting (FACS) with the use of flow cytometry analysis[171]; for multicolour optical coding of cells[172] and for cell microarrays[173]. Biosensors for cell microenvironment analysis also can be designed based on QD, such as FRET-QDs sensors[174], or antibody-targeted QDs[175]. Moreover, QDs can be used as energy donor for photosensitisers in PDT and as drug delivery agent[87].

For this purposes, QDs are often functionalised by chiral molecules, such as antibodies or other delivery agents; photosensitiser or other drugs[1]. Chiral QDs can also interact with chiral components in the cell media before reaching the desired target or microorganism. The chiral molecule can induce the optical activity in QDs, and QDs can also dramatically influence the properties of chiral molecules, including their biological activity. Therefore, it is of great interest to investigate the interaction of QDs with cells in the context of chirality.

As chirality plays a very important role in cell biology, it is expected that chiral properties of QDs may influence their ability to interact with biomolecules and thereby modulate a range of vital processes in living cells. It has been recently shown that NPs capped with opposite enantiomers of chiral ligands demonstrate different biological activity, including cytotoxicity within living cells[41,43,81].

Recently, this has been demonstrated for glutathione-coated CdTe QDs[43] with cell toxicity attributed in part to the chirality of the glutathione coating, with D-glutathione-capped CdTe QDs, the non-biologically active form of glutathione, showing lower cytotoxicity than L-glutathione coated CdTe QDs. Despite the fact that chiral NPs are widely investigated, there are only a few reports devoted to their interaction with living cells and this area of research is still underexplored. The aim of this part of our work is to investigate the biological behavior of chiroptically active quantum nanostructures in selected cancer cell lines for potential Nano medicine related applications.

5.2 Results and discussion

5.2.1 Preparation and characterisation of chiroptically active CdSe/CdS DiRs and TPs

Dots in Rods (DiRs) and tetrapods (TPs) were synthesized using previously published procedures[38] by first preparing either wurtzite (for DiRs) or zinc blende CdSe (for TPs) nanocrystals. Wurtzite seeds were produced by hot injection into a solution of cadmium, octadecylphosphonic acid, propylphosphonic acid, trioctylphosphine and trioctylphosphine oxide. Less common cubic zinc blende CdSe cores were prepared using a combination of cadmium myristate and selenium in ODE. These seeds are subsequently reacted with a solution of sulphur and cadmium to selectively direct growth of CdS along the direction of the arms.

TEM images of NPs presented in Figure 5-1 have shown that all the NPs are highly crystalline and monodisperse. The average size of the CdSe/CdS, DiRs and TPs is 5 x 40 nm and 6 x 35 nm (each TP arm) respectively.
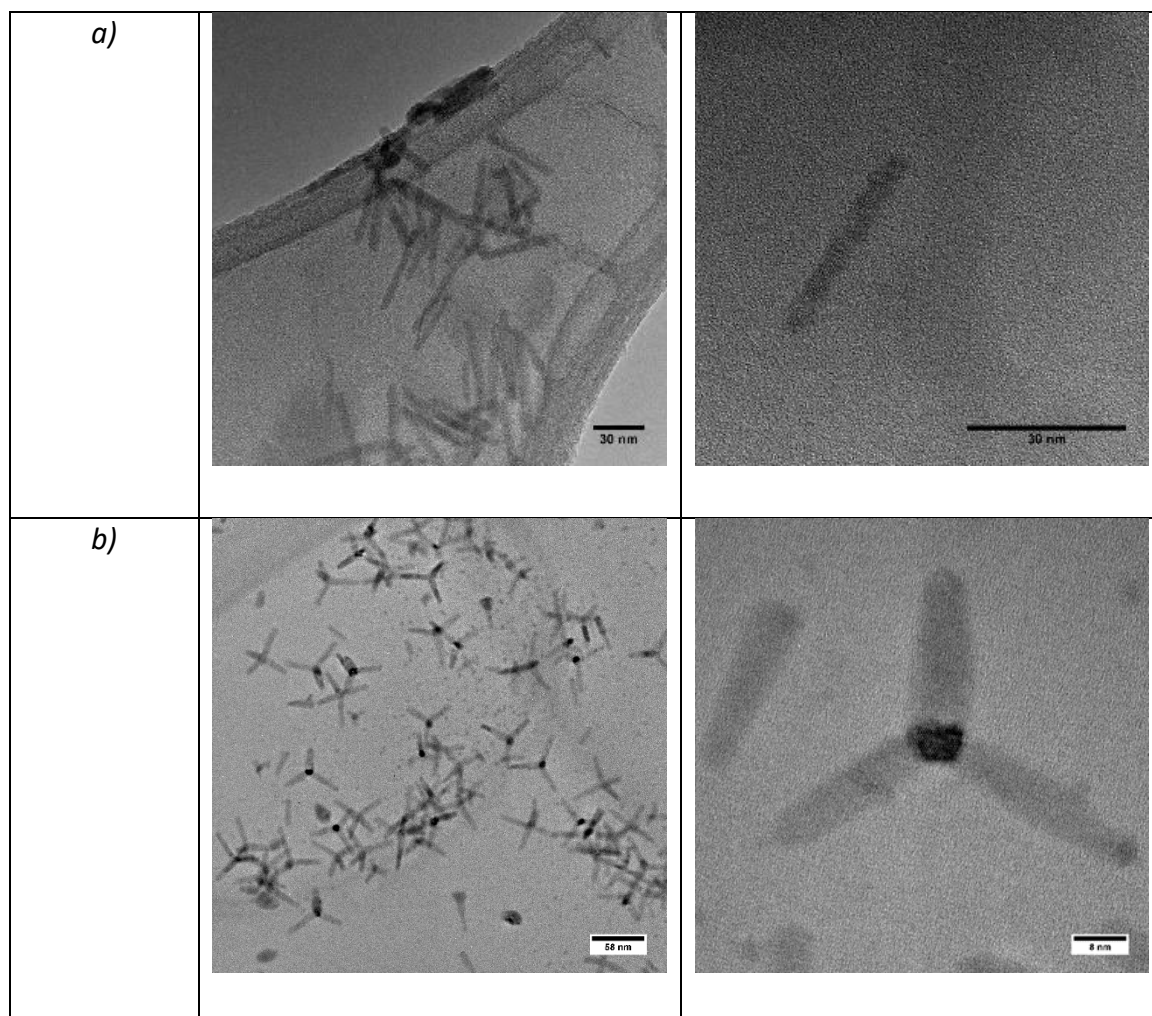
Figure 5-1. TEM images of A) CdSe/CdS Dots in Rods and B) CdSe/CdS Dots in Tetrapods.

After the synthesis of the NPs, optical activity was induced by exchanging the original achiral organic ligands with D- and L-Cys ligands[176]. To achieve this, the chloroform solutions of QDs have been treated with methanol solutions of D- or L- Cys and then the precipitates were extracted with aqueous solutions of KOH. UV Vis, PL and CD spectra of the NPs before and after the ligand exchange are presented in Figure 5-2. After the ligand exchange, the positions and shapes of the NP absorption and PL bands remained unchanged. PL QY decreased after the ligand exchange for all types of NPs, but were identical for L- and D-Cys enantiomers.

The CD spectroscopic data, as seen in Figure 5-2, further confirm that after the phase transfer L- and D-Cys NPs displayed mirror image CD signals in the region of

94

excitonic CdSe core absorption. The QDs with organic ligands on the surface in chloroform did not exhibit a CD signal (data not shown). The CD spectra of the D- and L-Cys NPs provide evidence of a successful ligand exchange and the formation of the enantiomeric D- and L-forms of NPs with induced chirality.

DiR
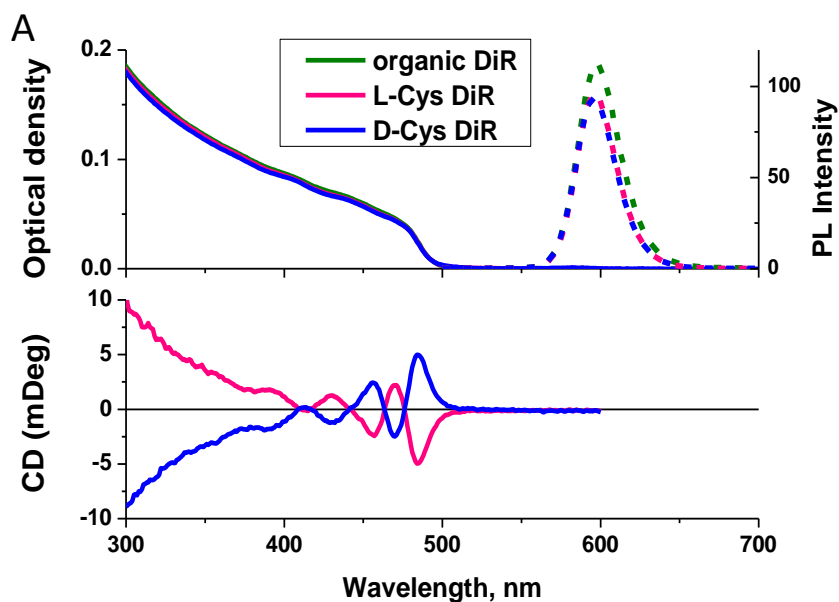
TP
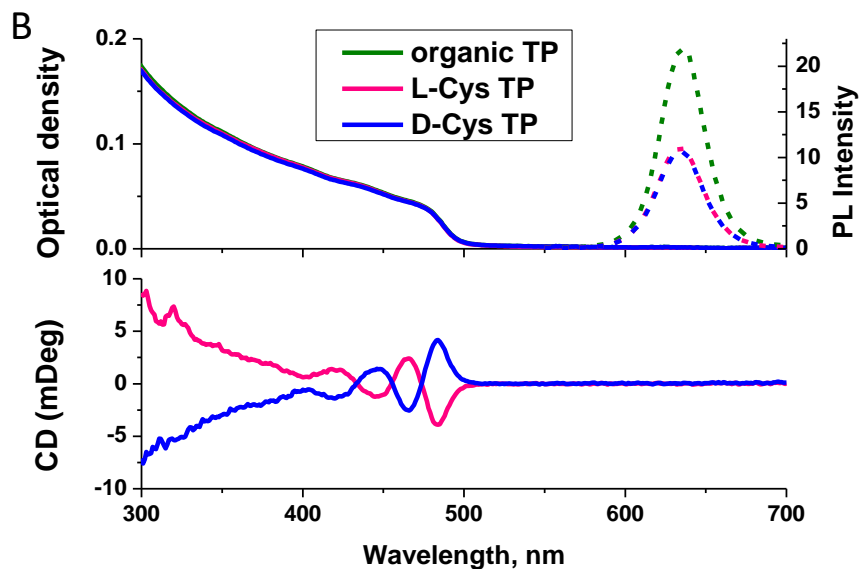
Figure 5-2. UV–Vis, PL and CD spectra of DiRs (A) and TPs (B) in chloroform (green curve) and in aqueous solution with L- and D-Cys ligands (red and blue curves respectively)

5.2.2 Preparation and characterisation of chiroptically active ZnS-based QDs

ZnS:Mn QDs were synthesized according to a previously reported method[23]. The synthesis involves heating up zinc chloride with 4% of manganese chloride and elemental sulphur to high temperatures in the presence of the co-ordinating solvent dibenzylamine. Representative HR TEM image of ZnS:Mn QDs are displayed in Figure 5-3. It shows that the QDs have an approximately spherical shape and are monodisperse with a high degree of crystallinity. The average size of the QDs was determined to be 5.3±0.7 nm.
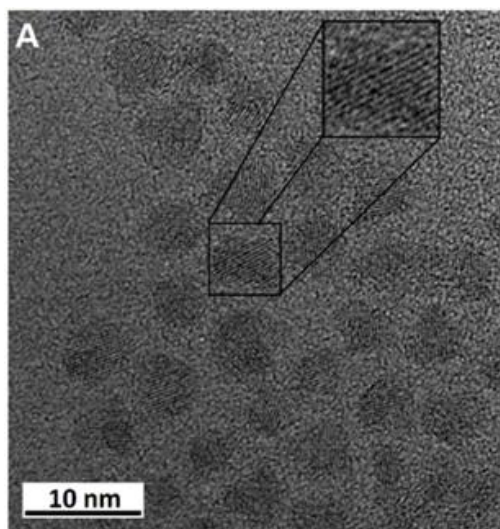
Figure 5-3. TEM images of ZnS:Mn QDs. The insert shows HR TEM image of QDs.

After the synthesis of the QDs, optical activity was induced by exchange of the original oleylamine ligands with D- and L-Cys ligands similarly to the procedure described above[177]. It has been demonstrated before that the ligand exchange method used in this work does not influence either the size or morphology of the QDs[176]. Absorption and PL spectra of the QDs before and after the ligand exchange are presented in Figure 5-4. The edge of the first exciton absorption band was located at 300 nm approximately. The maximum of the QDs phosphorescence peak was located at 585 nm. The phosphorescence of ZnS:Mn QDs occurs as a result of energy transfer from the ZnS host to dopant Mn^{2+} ions[23]. The position of the QDs PL band maximum corresponded to that of Mn^{2+} ions[23].

After the ligand exchange, the positions and shapes of theQDs absorption and PL bands remained unchanged. A comparativeanalysis of the fluorescent properties of theoleylamine QDs and D−/L-Cys QDs has shown that the PLquantum yield of QDs slightly decreased after the ligandexchange from 35% to 29% but was identical both for D−/L-Cys QDs.
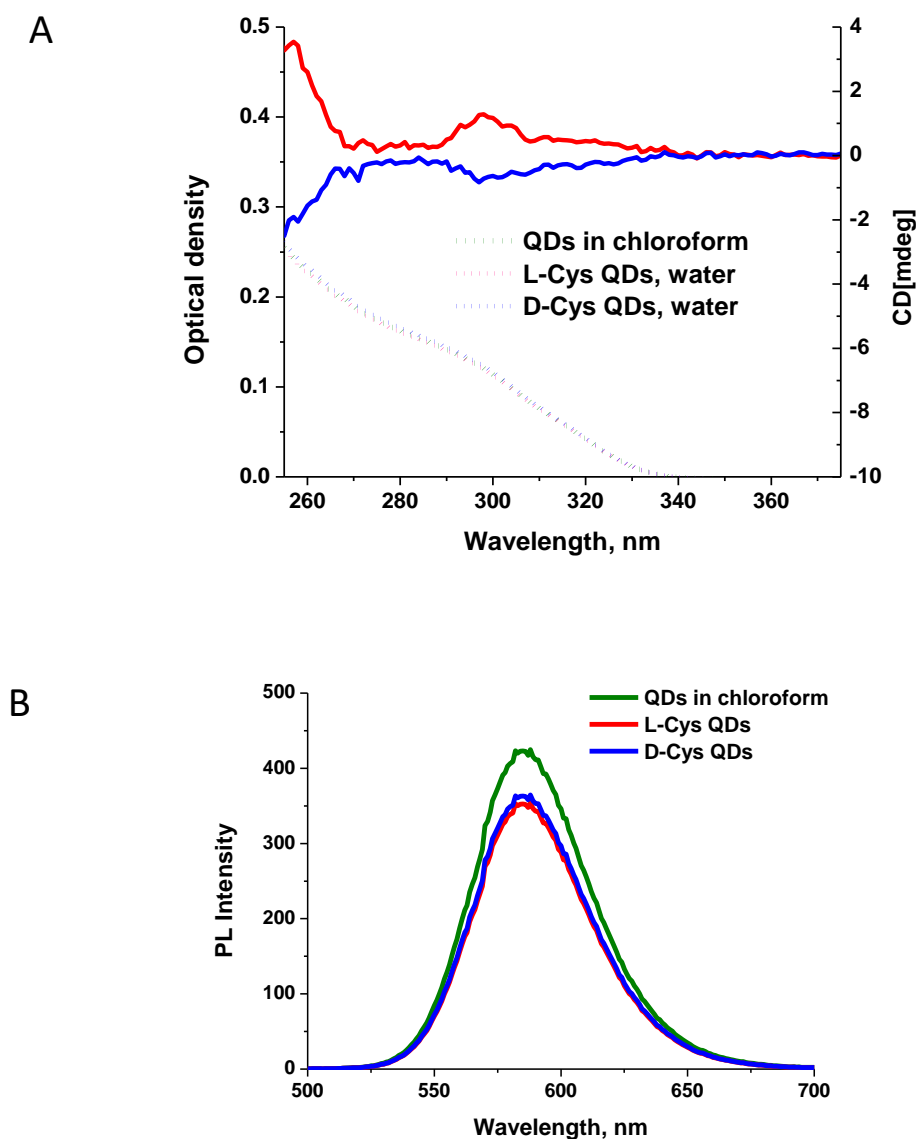
Figure 5-4. Optical properties of oleylamine QDs before (in chloroform, black curve) and after ligand exchange with L- and D-Cys (in water, red and blue curves, respectively): (A) UV–vis and CD spectra, (B) PL spectra. QDs concentration was 3 μM in samples for CD measurements and 0.3 μM in samples for UV–vis and PL measurements

The CD spectra of L-Cys and D-Cys QDs in aqueous solution are presented in Figure 2A. D- and L-Cys QDs were optically active and exhibited pronounced opposite CD signals in the spectral regions of the QDs exciton absorption (255–340 nm) and chiral ligand absorption (255–270 nm). Oleylamine QDs in chloroform did not exhibit a CD signal (data not shown). Induction of optical activity in the spectral region of QDs exciton absorption after the ligand exchange can be attributed to hybridization of the QDs valence band states with the HOMO/LUMO orbitals of the chiral D- and L-Cys ligands[49]. The CD spectra of the D- and L-Cys-QDs provide evidence of successful oleylamine-to-cysteine ligand exchange and the formation of the enantiomeric D- and L-forms of optically active QDs.

5.2.3 Post-phase transfer purification of QDs

During phase transfer, oleylamine did not completely exchange for Cys ligands. Part of the surfactant still remained on the QDs after the procedure. This was confirmed by FTIR analysis (Figure 5-5, A): peaks 2840 and 2920 cm^{-1} correspond to asymmetrical and symmetrical stretch CH_2 bound vibration of oleylamine hydrocarbon tail. The designed purification procedure allows the removal of the remaining oleylamine. For this purpose, the excess of Cys was added to the QD solution to completely replace the organic residues, and then the solution was mixed with the same volume of chloroform to allow the oleylamine to transfer back to organic phase (Figure 5-5, B). This purification is important, in particular for further biological uses as oleylamine is toxic for cells and can induce associated variability in the results of biological tests.
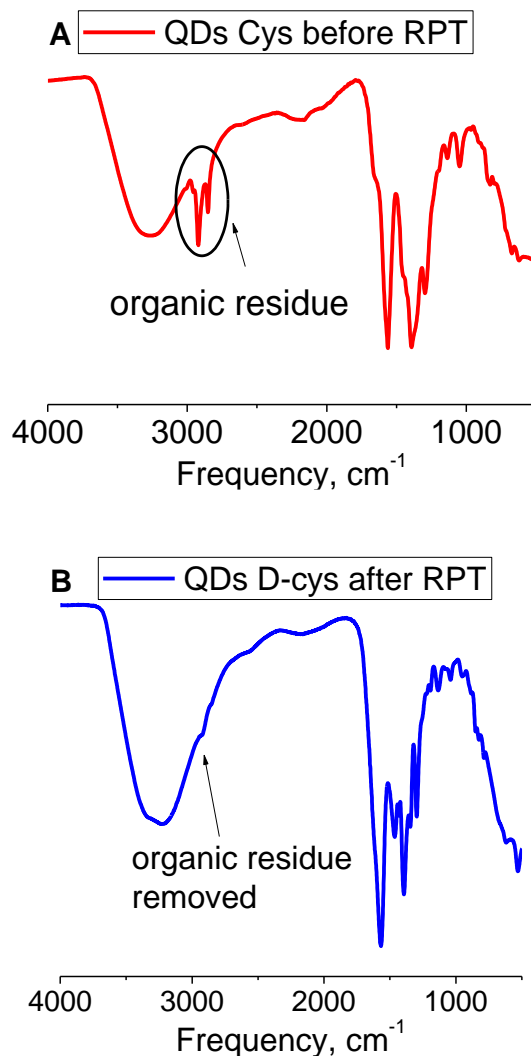
Figure 5-5. FTIR of D-Cys capped 5 shell QDs A: before purification (RPT), B: after RPT.

5.2.4 NP aggregation in biological media

It has been previously shown that cysteine stabilised NPs have a tendency to aggregate in biological media[1]. This phenomenon is explained by the fact that in media with high salt concentration, ions can interact with charged groups of Cys on the NP surface and decrease NP charge, allowing the NPs to come into close contact with each other and agglomerate. Adsorption of proteins on the NPs surfaces may prevent aggregation of NPs and render them stable in biological media.

Bovine serum albumin (BSA) is the most abundant protein in fetal bovine serum (FBS), which is often used for cell culturing. In the present study, BSA were used to prevent the aggregation of NPs in the cell culture medium. For this purpose, QDs were incubated

with BSA. Then L–/D-Cys QDs and L–/D-Cys BSA-QDs were added to culturing medium (DMEM) containing 10% FBS. DLS data of QDs, presented in Figure 5-6, were recorded the next day to establish the aggregation of the QDs.

It was observed that the D- and L-Cys QDs without BSA formed clusters with an average hydrodynamic radius of 70±9 nm and 58±11 nm respectively, whilst the BSA-QD remained monodispersed with an average hydrodynamic diameter of 7±1 nm for both L- and D-Cys QDs. Notably, BSA-QDs revealed PL QY of 29%, which is equal to L–/D-Cys QDs PL QY. This indicates that the adsorption of BSA on ZnS:Mn QDs surface does not significantly change the PL QY of QDs. Further experiments on the NPs within living cells were therefore carried out using L-/D-Cys-BSA NPs.

a)

b)
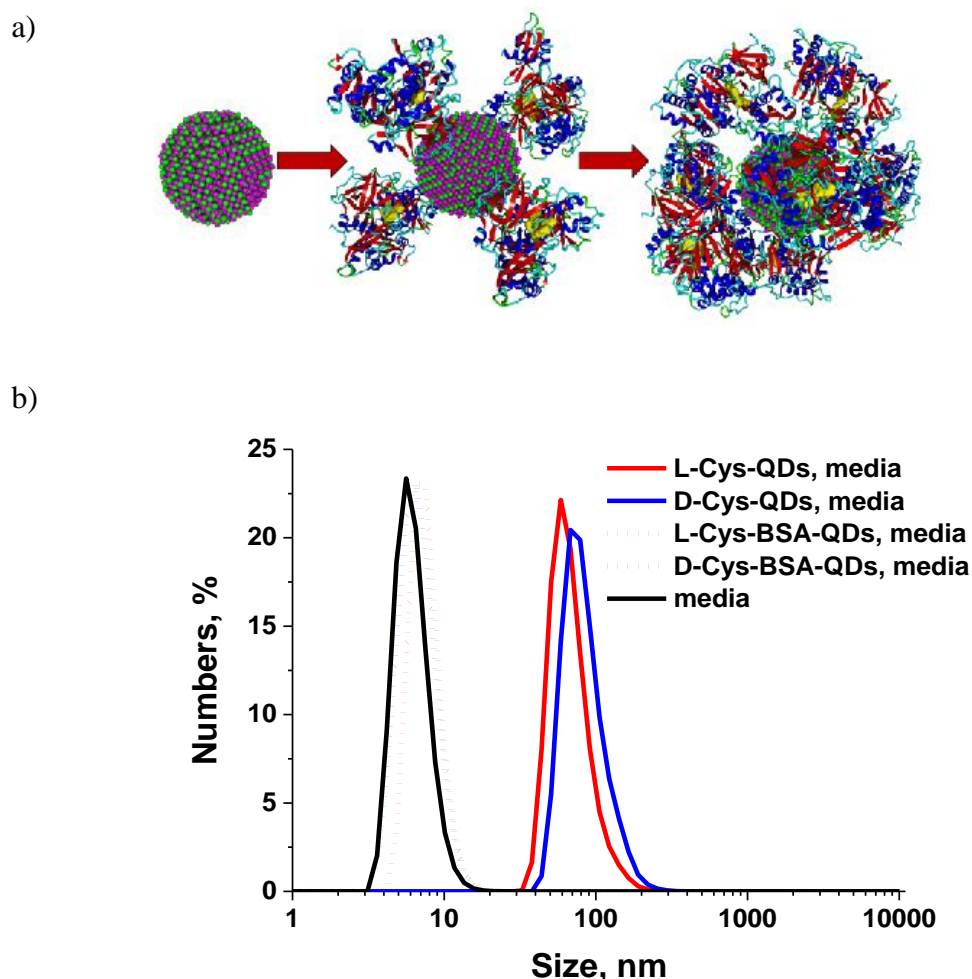
Figure 5-6. A) Scheme of protein corona formation and B) DLS spectra of QDs in biological media (DMEM) containing 10% of FBS.

5.2.5 The influence of biological media on NPs induced chirality

Biological media contain a lot of chiral components, such as amino-acids, carbohydrates and proteins. All these substances can potentially be adsorbed onto the NP surface and influence the induced chirality of the NPs.

CdSe/CdS DiRs were used to investigate the influence of the medium on NP chirality. DiRs have quite large induced CD signal at the wavelength where medium absorbs nearly no light. They also have a large surface area that allows the adsorption of a large amount of material. These properties make DiRs an appropriate object to investigate the optical activity of NPs in biological medium.

CD spectra of DiRs after ligand exchange with L- and D-Cys are presented in Figure 5-7, a. CD signals of L- and D-Cys DiRs were mirror-images and had intensity in the exciton region equal to approximately 2 mDeg. Since BSA was used to stabilize NPs in the medium, it was necessary to determine the influence of BSA on NP chirality. For this purpose, DiRs were incubated with BSA overnight. This resulted in CD signal enhancement of almost two times both for L- and D-Cys DiRs (Figure 5-7, b). Most likely, this can be explained by the decreasing of the amount of Cys molecules on the DiR surface as a result of displacing Cys with BSA. As it was shown in the previous chapter, the intensity of the induced CD signal of NPs is inversely proportional to number of Cys molecules on the NP surface (See 4.2.1). However, additional experiments need to be carried out to fully understand this effect.

Then, the BSA-DiRs were incubated overnight with biological medium (Figure 5-7, c). In the medium, the CD signal of L- and D-Cys BSA-DiRs changed asymmetrically. The CD signal of L-Cys BSA-DiRs decreased by a factor of 2 and returns to approximately the same magnitude as it was in water. The decrease of the D-Cys-BSA-DiR CD signal was approximately 6-fold.

The media contains a lot of different L-amino-acids, but L-Cys has the largest affinity to thiophilic Cd-containing NPs among other amino-acids because it contains a thiol-group. L-Cys can be adsorbed on the DiR surface and it can change the CD signals of L- and

D-Cys DiRs unequally. When L-Cys was adsorbed on the L-Cys BSA-DiRs, the amount of L-Cys molecules on DiR surface increased, and CD signal, being inversely proportional to the number of Cys molecules, decreased. When L-Cys was adsorbed on D-Cys DiRs, L-Cys counteracted the induced CD signal of D-Cys, in such a way decreasing it.

A) water
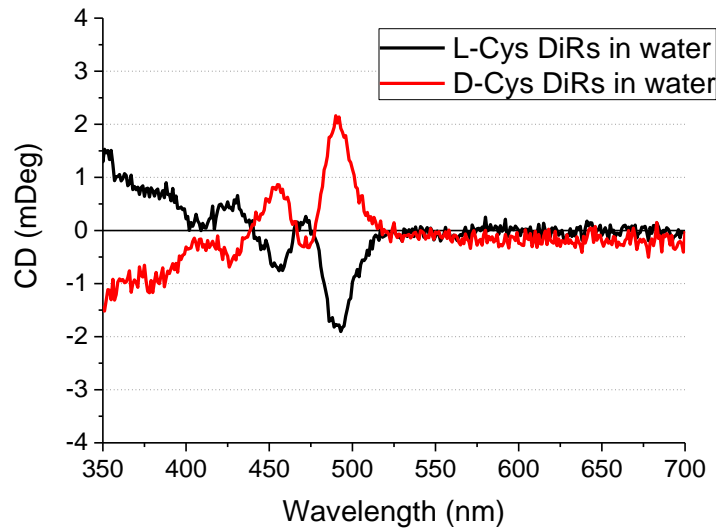
B) BSA
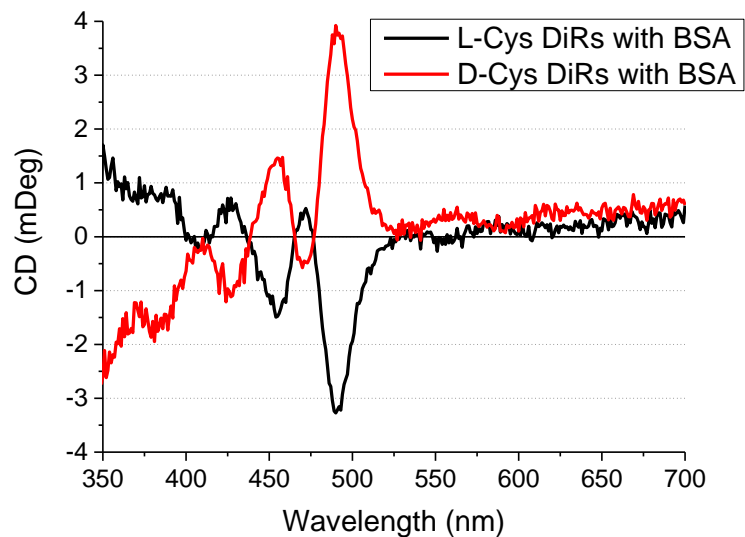
C)   **DMEM**

medium
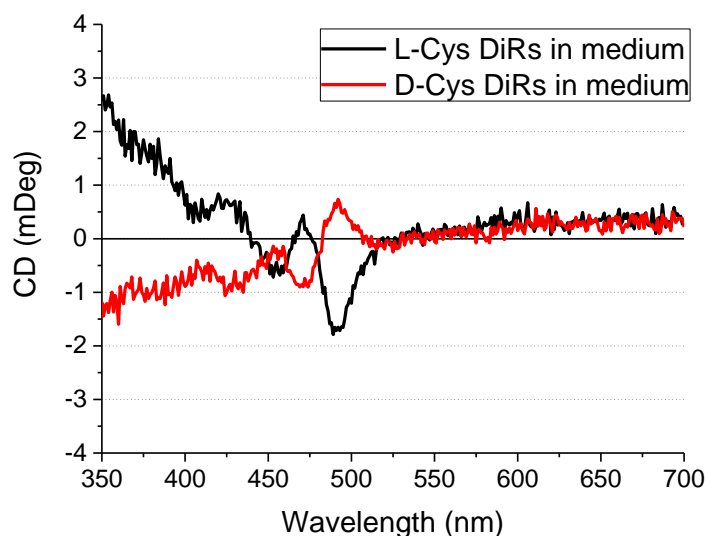
D) Extra L-Cys
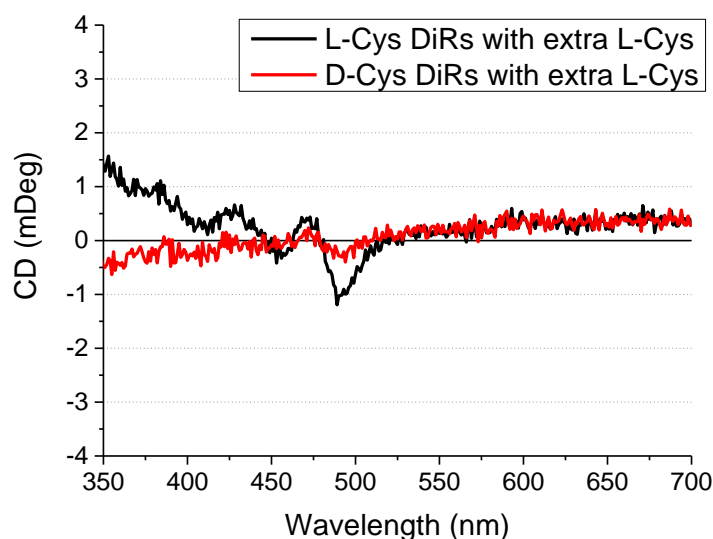
Figure 5-7. CD spectra of L- and D-Cys DiRs in water (A), in water with BSA (B), in DMEM medium (C) and in water with extra 40 µg L-Cys, which is correspond to L-Cys content in DMEM medium (D).

To verify this suggestion, the same amount of L-Cys that is contained in DMEM media was added to L- and D-Cys BSA-DiR solutions. The result can be seen in Figure 5-7, d. The CD signal of L-Cys BSA-DiR significantly decreased, while D-Cys BSA-DiR CD signal almost disappeared. The observed trend was the same as in the medium, but more pronounced, likely because in the medium a smaller amount of L-Cys was adsorbed on the DiR surface, since the DiR binding sites were occupied by other medium components.

Thus, it can be concluded that different changes of the L- and D-Cys DiR CD signal can be partially caused by L-Cys adsorption from medium.

5.2.6 Fluorescence properties of L- and D-Cys QDs in the incubation medium

The cell incubation with QDs was performed in RPMI-1640 medium containing 10% bovine serum. This medium contains large amounts of chiral components, which potentially may enantioselectivelly interact with L- and D-Cys QDs and consequently hamper their cellular uptake. In order to examine possible enantioselective patterns in the incubation medium we have compared the fluorescence properties of L- and D-Cys QDs in RPMI-1640 with 10% of serum and in water. Analysis of the fluorescence spectra (*Figure 5-8*, A) reveals no difference in the intensity and spectral position of the fluorescence bands for both L- and D-Cys QDs in the medium. The PL quantum yield of L- and D-Cys QDs was also the same in the medium and was noteworthy increased compared with that in water. The increase in the PL quantum yield of QDs observed in the medium can be explained by the passivation of the QD surface with proteins and other bio compounds.
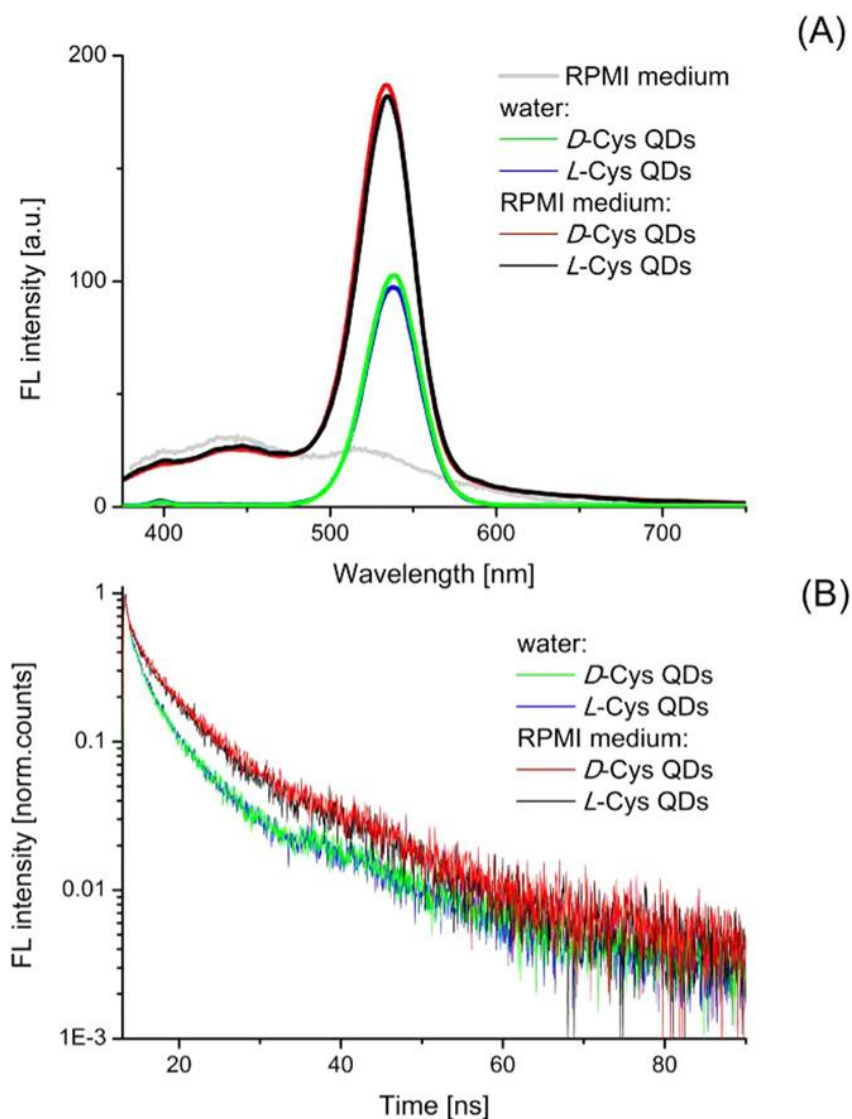
Figure 5-8. Fluorescence spectra (A) and fluorescence lifetime decay curves (B) of L- and D-Cys QDs with identical concentration (1 µmol / L) in water and in RPMI-1640 medium containing 10% of bovine serum. The excitation wavelength is 350 nm.

QD fluorescence lifetimes in water and in the incubation medium were analysed also. Fluorescence decay curves of L- and D-Cys QDs in water and in RPMI-1640 medium containing 10% of bovine serum are presented in *Figure 5-8*, B. As can be seen, the fluorescence decays of L- and D-Cys QDs in the incubation medium are practically identical to each other. Thus, L- and D-Cys QDs do not demonstrate any evidence of enantioselective optical behaviour in the incubation medium, which can have an effect on luminescent properties of chiral QDs.

5.2.7 The influence of NP chirality on the interaction with living cells

PL spectra of QDs inside cells

Fluorescence spectra of chiral QDs inside the cells are presented in *Figure 5-9*. Cells were incubated with 1 µmol/L of D- and L-Cys CdSe/ZnS QDs for 24 h. It can be seen that the localization of QDs in the endocytic vesicles leads to a red shift of the QD fluorescence band with respect to its position in aqueous solution. This may be caused by dot-to-dot energy transfer[137]in cell vesicles where relatively high local QD concentrations are achieved. However, the fluorescence band positions and bandwidths of D- and L-Cys QDs in the vesicles are almost the same, indicating an absence of enantioselective effects on their PL spectra.
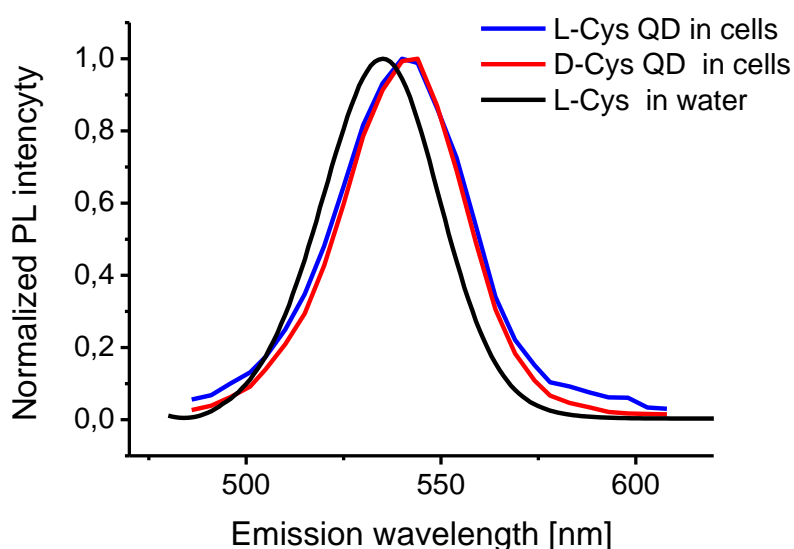
Figure 5-9. Fluorescence spectra of D- and L-Cys QDs in cells (red and blue lines, respectively) and in water (black line). The QD concentration in incubation medium is 1 µmol/L.

Fluorescence-Lifetime Imaging Microscopy of QDs inside cells

Fluorescence-Lifetime Imaging Microscopy (FLIM) images of cells, incubated with 1 μmol/L of D- and L-Cys CdSe/ZnS QDs for 24 h, presented in **Figure 5-10** A and B, show bright spots corresponding to QDs inside the vesicles.

As shown in **Figure 5-10** D, the fluorescence decays associated with the intracellular QDs are significantly longer than those of QDs in aqueous solution, and three-exponential functions better describe the QD fluorescence decay in vesicles (*Table 5-1*). The increase of the fluorescence lifetime and the appearance of the third component in the fluorescence decays together with the red shift of the intracellular fluorescence band (**Figure 5-9**) are a sign of dot-to-dot energy transfer[137] in the vesicles. However, it is important to note that the fluorescence lifetimes of D- and L-Cys QDs in the vesicles are practically the same (see also *Table 5-1*) for all incubation times used. This fact indicates the absence of enantioselective fluorescence quenching upon QD incorporation into the cells and enables the use of PL intensity to estimate the chiral CdSe/ZnS QD relative concentration inside the cells.
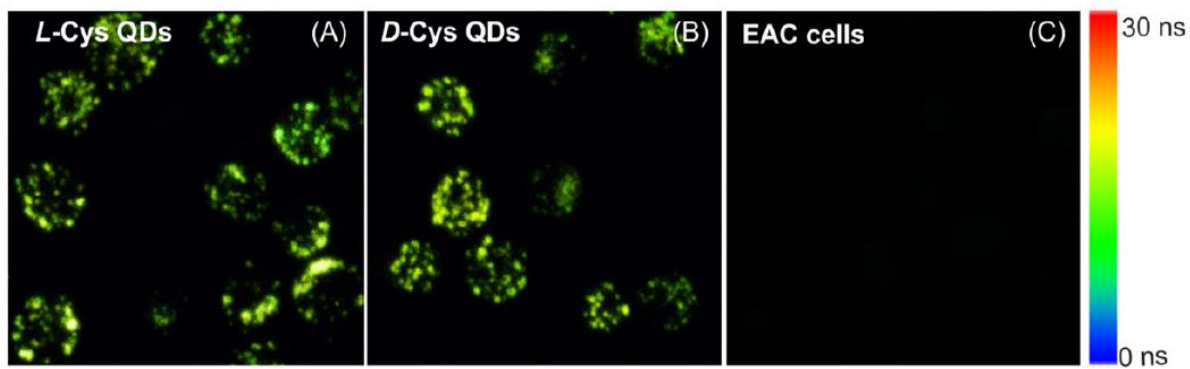
Figure 5-10. FLIM images of cells incubated with L-Cys QDs (A) and D-Cys QDs (B) after 24 h of incubation. The QD concentration in the incubation medium is 1 µmol /L. (C) FLIM image of the cells. (D) Fluorescence lifetime decay curves for TOPO-QDs in chloroform solution, as well as for D- and L- Cys QDs in aqueous solution and in the cells.

Sample	Medium	$\tau_1/\tau_2/\tau_3$ [ns]	$\langle\tau\rangle$ [ns]
TOPO-QDs	chloroform solution	20/5/-	18.0
L-Cys QDs	aqueous solution	14/4/-	10.5
	RPMI-1640 (with bovine embryonic serum)	19/3/-	13.0
	Cells	20/9/3	15.0
D-Cys QDs	aqueous solution	14/4/-	10.5
	RPMI-1640 (with bovine embryonic serum)	19/3/-	13.0
	Cells	21/10/4	16.0

Table 5-1. Fluorescence lifetime characteristics of TOPO-capped and cysteine-capped CdSe/ZnS QDs.

5.2.8 Cell uptake of chiral CdSe/CdS TPs and DiRs

In order to study the chiral NP cellular accumulation, A549 cells were incubated with D- or L-Cys NPs. Fluorescence intensity of the chiral NPs inside cells was assessed by analysis of the PL images obtained after 24 h of incubation with NPs. Average PL intensity per cell were calculated using ImageJ software. Incubation of A549 cells with NPs coated by BSA molecules was carried out in 96-well plates in DMEM containing 10% of FBS and 5 µg/ml gentamicin at 37 °C, 5% CO_2, 90% relative humidity for 24 h. NP concentration was 40 µg/ml.

The fluorescence images of the cells after 24 h of incubation with QDs presented in *Figure 5-11* clearly confirm the intracellular uptake and accumulation of the chiral QDs into the cells, showing their characteristic fluorescent labelling. The bright fluorescent spots observed within the cells reflects the intracellular distribution of NPs, most likely, due to their endosomal localization.
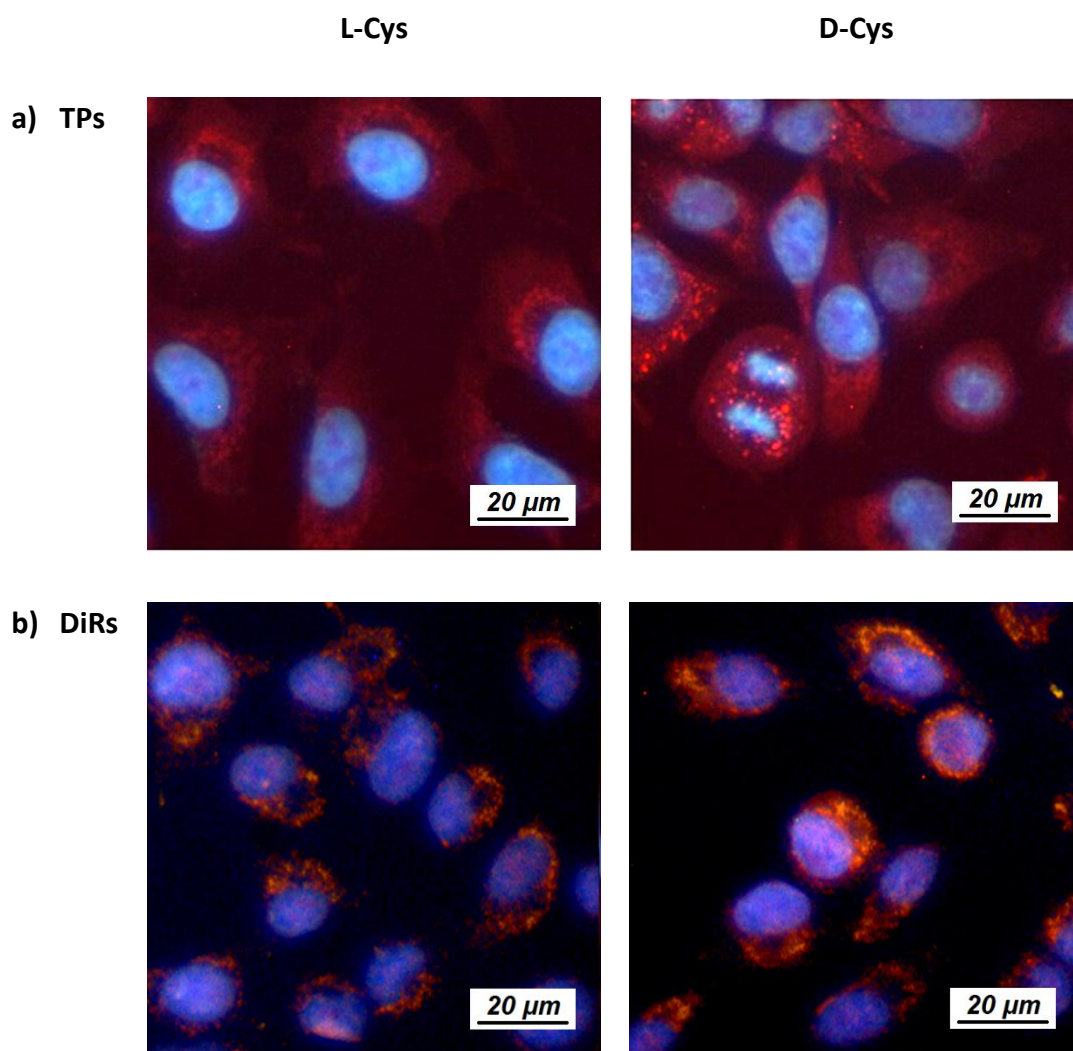
Figure 5-11. PL images of A549 cells incubated with L- and D-Cys TP (A) and with L- and D-Cys DiR (B) after 24 h of incubation. The concentration of NP was 40 µg / mL.

It can be seen that the intensity of the fluorescence of D-Cys TPs is much higher than that of L-Cys TPs, which is evidence of more efficient cellular uptake of D-Cys TPs comparing to L-Cys TPs. While for DiRs, the difference in PL and cellular uptake is not so obvious. It is previously unreported phenomenon requiring more investigations.

5.2.9 Cytotoxicity of chiral CdSe/CdS TPs and DiRs

Cytotoxicity of L- and D-Cys-capped NPs was determined using the HCS assay. For these purposes A549cells were incubated with NPs coated with BSA for 24 h in a 96-well plate in DMEM with 10% FBS and 5 µg/ml gentamicin at 37ºC and 5% CO_2. NP concentration varied from 10 to 80 mg/mL. The results of cytotoxicity test are represented

110

in Figure 5-12. It can clearly be seen that D-Cys enantiomer is more toxic than the L-Cys one for both TPs and DiRs. Notably, the difference in the toxicity between L- and D-Cys NPs is more considerable for TPs than for DiRs, which can be explain most likely by the higher difference in cell uptake, as it was mentioned above.
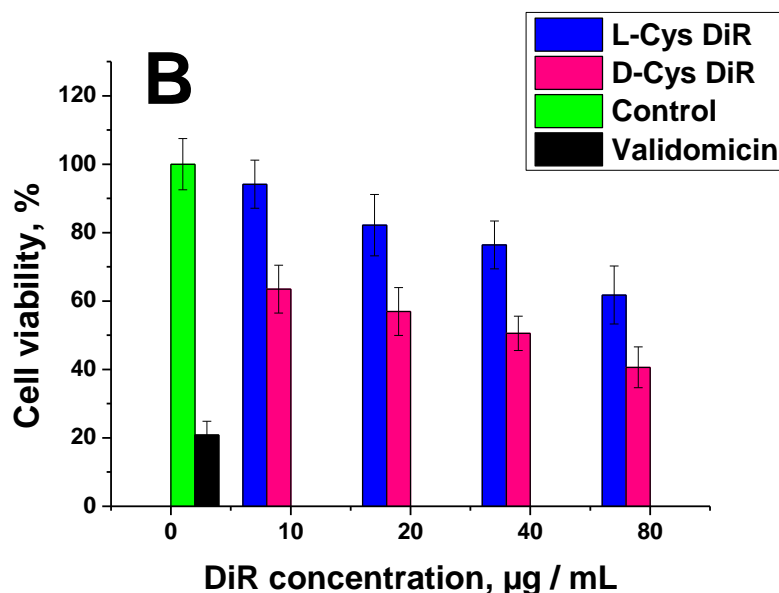
Figure 5-12. A549 cell viability after incubation with chiral TPs (A) and DiRs (B) for 24 h versus NP concentration, represented as the percentage of viable cells obtained by High Content Screening analysis.

5.2.10 Cytotoxicity of chiral ZnS:Mn QDs

To compare the biological activity of L-Cys and D-Cys ZnS: Mn QDs, we studied their toxicity in A549 cell line. It was anticipated that the overall cytotoxicity of the ZnS:Mn QDs would be significantly lower compared to that of cadmium-based QDs[19–22]. Nonetheless, ZnS-based QDs still exhibited cytotoxicity, which was dose-dependent. A wide range of NPs, even consisting of nontoxic elements, revealed nanocytotoxicity[2,178,179]. As the size of a particle decreases, its surface area increases, as well as the ratio of structural defects per surface area. The defects can function as reactive sites, which can catalyse reactive oxygen species (ROS) generation. This could lead to oxidative stress and cell damage[2]. The presence of residual toxic organic ligands from the initial synthesis medium has also been associated with the cytotoxic nature of QDs[3].

For the cytotoxicity assays, the L-/D-Cys BSA-QDs were mixed with DMEM media containing 10% FBS, added to the A549 cell culture and incubated for 24 hours. The QD concentration ranged from 0.8 to 6 mg/mL.
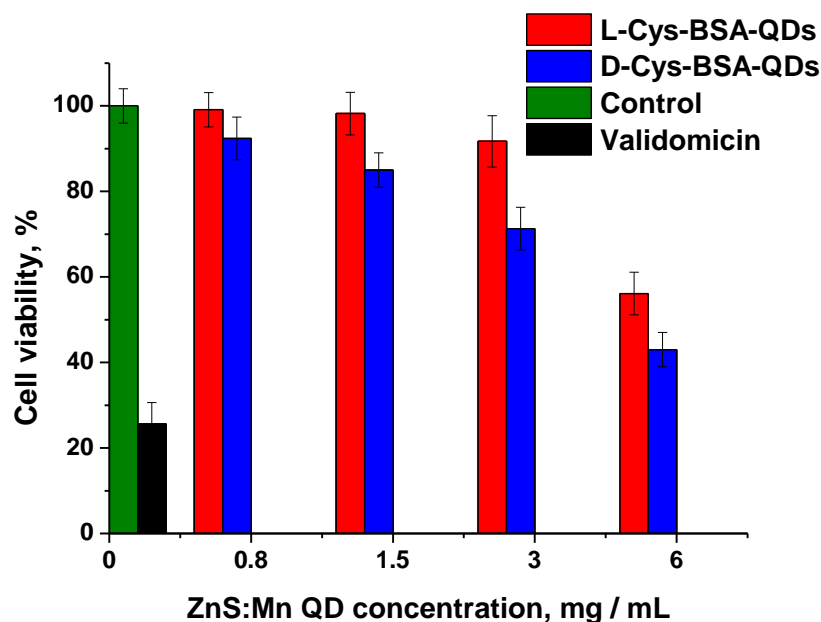
Figure 5-13. Histogram with cell viability data of A549 cells incubated with chiral QDs for 24 h at 37ºC. 100 µM Valinomycin was used for a positive control.

Cell viability was quantified by HCS analysis and the results are shown in Figure 5-13. It can be seen that viability level for A549 cells incubated with L–/D-Cys BSA-QDs was higher than 80% in the range of the QDs concentration up to 3 mg/ml. This is in good agreement with literature data[22,23], where toxicity of ZnS:Mn QDs also did not exceed 80% for the same cell line and range of QD concentrations. The toxicity of Cd-based QDs develops at ~0.01 mg/ml, which is 2-fold higher[20,22]. For example, cell viability of A549 cells[22]and LNCaP cells[20] incubated with CdS and CdTe QDs, respectively, was about 50% and 60% at the QDs concentration of 0.02 mg/ml.

Furthermore, the studies of the two optically active forms have shown that D-Cys-QDs demonstrated higher cytotoxicity for the entire range of QDs concentrations (0.8-6 mg/ml) compared to that of the L-Cys-QDs, with a maximum difference of ~20%. This result is in line with the work of Zhang et al.[81], in which D-glutathione Au NCs were more

toxic for GES-1 cells than L-glutathione Au NCs with a difference of ~40% at the maximum concentration.

Pure L- and D-Cys did not show cytotoxicity at the range of the concentrations used in our studies (up to 0.33 mg / mL). Similar data has also been reported by Zhang et al.[81] for pure L- and D-glutathione. This difference in cytotoxicity can be explained by the following effects. First, L-Cys and D-Cys QDs can exhibit enantioselective cellular uptake[41]. This means that the concentration of QDs inside the cells and the corresponding cytotoxicity will be different. Second, L-Cys and D-Cys-QDs can induce different mechanisms of cytotoxicity, such as level of ROS generation, apoptosis, or autophagy[43,81]. Further investigation of the precise mechanism of different QDs cytotoxicity in living cells is a continuing area of interest for our research.

Thus, we demonstrated that L-Cys and D-Cys-QDs had mirror-image CD spectra in the region of intrinsic QDs absorption and identical UV–Vis and PL spectra. However, most importantly, we found that the chirality of the ligands played a crucial role in the biological interaction with living cells. We found that the incubation with L-Cys NPs resulted in a higher A549 cell viability than with D-Cys NPs. Identification of this chirality-dependent cytotoxicity of NPs provides an important insight into the design of more biocompatible surface coatings.

5.2.11 Determination of the mechanism of QD uptake by laser scanning confocal microscopy

QDs can be internalized in cells by passive and active transport. Passive uptake is accomplished by simple diffusion, while active transport is energy-dependent and mediated by receptors on the cell membrane. In active transport cells absorb QDs by the inward budding of the plasma membrane (invagination) and form vesicles containing the absorbed NPs.

CdSe/CdS QDs were tested for active and passive cellular uptake mechanisms by inhibiting energy-dependent uptake with sodium azide. Then, we performed laser scanning confocal microscopy (LSCM) imaging of cells with QDs after 6 h of incubation Figure 5-14. The QDs are indeed internalized within cells as they appear at the same level

113

as cells and nuclei in orthogonal views. Vesicles filled with QDs all over the cell volume can be clearly seen on the image.
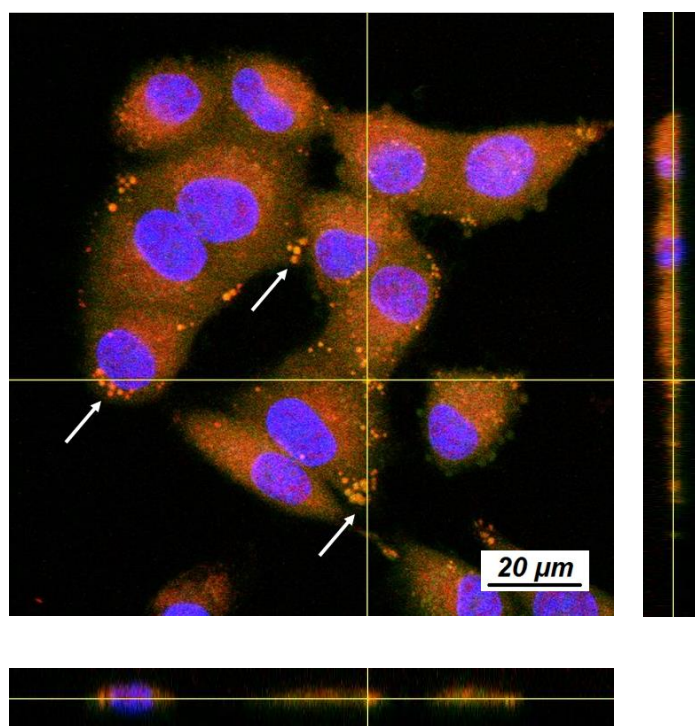
Figure 5-14. LSCM images and orthogonal views of CdSe/CdS QDs (1×10^{-7} M) capped with D-Cys with stained lysosomes (orange, pointed with arrows) and nuclei (blue) after 6 hrs in A549 cells

No considerable quenching of QDs was observed after sodium azide addition in QDs aqueous solutions, thus results are quantitatively comparable. The mean fluorescence signals per cell obtained using LSCM imaging for active and passive uptake of L- and D-Cys are shown in Figure 5-15. Active cell uptake of D-Cys capped CdSe/CdS QDs into cells appears 1.5 times higher than for L-Cys capped QDs. While passive uptake is approximately the same within the measurement accuracy.
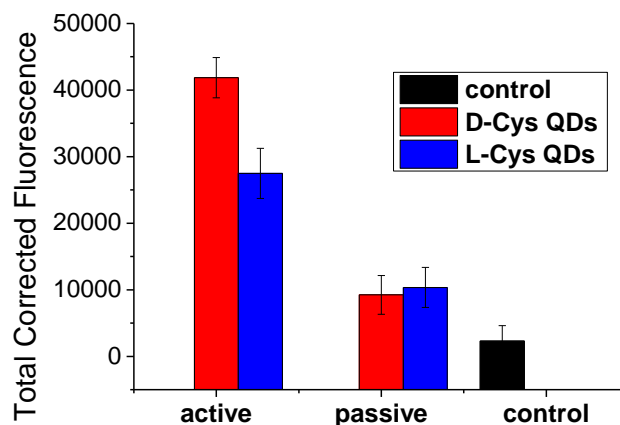
Figure 5-15. Total corrected fluorescence of QDs within A549 cells capped with L- and D-Cys at 1×10⁻⁷ M concentrations in medium after 6 h incubation, calculated based on LSCM data

5.2.12 Determination of the mechanism of uptake by flow cytometry

Flow cytometry can distinguish particle populations by fluorescence intensities and size *via* forward and side light scatter. Forward light scatter gives information about the size of the cells, whilst the side light scatter gives information about the shape and internal complexity, as well as fluorescence. Only QDs internalized within cells are detectable by the machine. We used a laser with a wavelength of 585 ± 40 nm which is within the excitonic fluorescence region of QDs, where tissue auto-fluorescence is not significant. The mean fluorescence signals per cell of QDs within A549 cells capped with L- and D-Cys at $6.7×10^{-8}$ M concentrations calculated based on flowcytometry data is shown in Figure 5-16. The variation in passive uptake of L- and D-Cys capped CdSe/CdS QDs was again below the levels of statistical significance. However, the active uptake of D-Cys into cells was approx. 1.5 times higher than for L-Cys QDs at the region of peak count for fluorescence intensity. Thus, flow cytometry confirms the results obtained with LSCM.
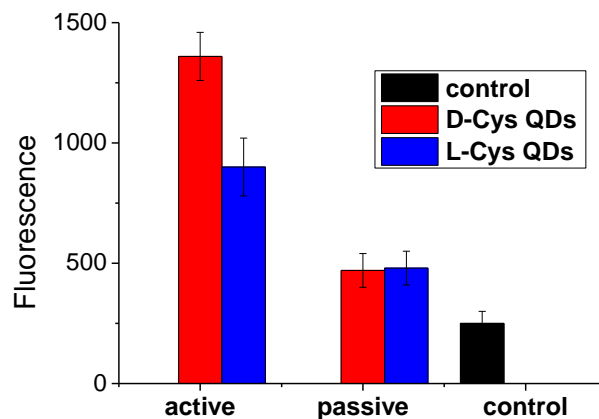
Figure 5-16. Fluorescence of QDs within A549 cells capped with L- and D-Cys at 6.7×10^{-8} M concentrations in medium after 6 h incubation calculated based on flow cytometry data.

Thus, there is possibly a different active mechanism of uptake for D-Cys CdSe/CdS QDs, which is as expected as D-Cys QDs could potentially interact better with L-enantiomeric transporters, receptors or molecules found in cells and media than L-Cys QDs. Therefore, possible active mechanisms of cellular uptake should be investigated for L- and D-Cys capped QDs in greater detail in future.

5.3 Conclusions

Thus, the influence of the chirality of fluorescent semiconductor NPs with different shape on their cellular uptake and cytotoxicity has been investigated. We demonstrated that L-Cys and D-Cys NPs had mirror-image CD spectra in the region of intrinsic QDs absorption and identical UV–Vis and PL spectra, as well as PL lifetime. However, most importantly, we found that the chirality of the ligands played a crucial role in the biological interaction with living cells. We found that the incubation with D-Cys NPs resulted in a higher cytotoxicity and cell accumulation than with L-Cys NPs. This clearly demonstrates an enantiomeric recognition of chiral nanoparticles by living cells. We believe that this finding may lay the groundwork for novel approaches to controlling the biological properties and behaviour of man-made chiral nanomaterials in living cells.

6   Chapter 6. Complexes of Photosensitizer chlorin e6 and QDs for PDT

6.1   Introduction

Due to their remarkable optical, electrical, chemical, and mechanical properties nanomaterials are being used increasingly in biomedical applications including drug delivery, biological imaging and therapeutic purposes[2]. One of the important tasks of modern nanotechnology is the development of new nanomaterials and systems, which would significantly enhance the effects of organic drug molecules traditionally applied in biomedicine.

Photodynamic therapy (PDT) is a promising and delicate method of cancer treatment, which is based on the ability of the photosensitizer molecules to selectively target tumour tissue and transfer photoexcitation energy to surrounding oxygen species generating extremely reactive singlet oxygen to destroy cancer cells[84,86].

Various nanomaterials have been investigated as potential delivery and excitation agents for photosensitizer molecules used in PDT[85]. Semiconductor quantum dots (QDs) are promising for such applications because of their small size and unique size-dependent optical properties. Due to three dimensional quantum confinement, they possess broad absorption, high emission quantum yield, and narrow size-tuneable emission[108]. Therefore, QDs are superior donors in fluorescence resonance energy transfer (FRET) processes in complexes with photosensitizers, as they enhance the molecular excitation efficiency. QDs can be also effectively excited with two-photon[93,180,181] and x-ray irradiation[182,183]. In complexes with QDs an increased generation of singlet oxygen by photosensitizers can be realized via an effective energy transfer from QDs to photosensitizer molecules. In addition, QDs could potentially act as delivery agents for photosensitizer molecules[184]. Therefore, since their discovery, semiconductor QDs have drawn significant attention as potential energy donors in complexes with photosensitizers[87,97,99]. Previous studies have demonstrated the possibility for effective energy transfer in various QD-photosensitizer donor–acceptor systems[185–187]. The efficiency of singlet oxygen generation in many QD-photosensitizer complexes was shown to be enhanced when compared with free photosensitizers[90,92]. The aim of this part of our

work is to investigate interactions between the chiral photosensitizer chlorin e6 and selected QDs for potential PDT applications.

Since the first observation of induced chirality in the excitonic transitions of CdS quantum dots (QDs) capped with chiral penicillamine ligand[188], a lot of effort has been made to investigate the dependence of NC induced chirality on a variety of factors, such as NC size, composition, shape, shell thickness and surface stabilizers type[49,61,126,127,129,130,189]. At the same time, there are no systematic studies of the effects of semiconductor nanocrystals on optical activity of surface molecules, nevertheless such studies are crucial since chiroptical properties of molecules can be significantly changed near a NC's surface. Indeed, it has been theoretically predicted by Govorov et al.[72] that a nonchiral planar molecule can become optically active when it forms a complex and couples via dipole and multipole Coulomb interactions with achiral NC. Balaz et al.[49] experimentally demonstrated that a QD's optical activity can be acquired as a result of hybridization of the ligand HOMO with the QD valence band states. It has also been reported that the optical activity of chiral molecules can be altered in the presence of nonchiral CdSe/ZnS QDs[82]. Moreover, penicillamine molecules attached to the surface of CdS QDs, display a reversed circular dichroism (CD) signal compared to that of free molecules[188]. Such reversal of CD signals after molecule adsorption onto the QD surface has been also reported for glutathione molecules and CdTe QDs[190].

Potentially the change in optical activity of a molecule can be accompanied by a transformation of its spatial configuration and functional properties. This is crucial when applying HyNSs for particular applications, since the functionality of free and NC surface bond molecules can significantly differ. Therefore, studying NC influence on the chiral properties of organic molecules in an organic molecule/nanocrystal HyNSs is of great interest from a fundamental and applied point of view.

Chiral non-fluorescent molecules traditionally used as NC stabilizers (e.g. cysteine, penicillamine, glutathione etc.) absorb in the UV range of the spectrum, which makes it difficult to study their optical properties in HyNSs since semiconductor nanoparticles characteristically possess high absorption coefficients in the UV region. At the same time, there are chiral functional molecules (e.g. chlorin e6), which have absorption bands in the

visible region where QDs do not absorb, and thus can be used to study the influence of semiconductor nanocrystals on chiroptical properties of molecules.

We have investigated for the first time the distance-dependent influence of the semiconductor nanocrystal core on optical activity of chiral organic molecule. For this purpose, hybrid nanostructures based on chiral organic dye, chlorin e6, and various semiconductor nanocrystals (core/shell CdSe/CdS quantum dots, CdSe/CdS dot-in-rods) were produced and investigated via CD spectroscopy. It has been found that chlorin e6 optical activity increases when chlorin e6 bound with nanocrystal, and this phenomenon depends on CdSe quantum dot shell thickness. It has been found that the optical activity of an organic molecule exhibits a pronounced dependence on the distance between the NC core and the molecule, namely, decreasing the distance between the NC core and molecule leading to increase in the optical activity of the molecule. We believe that this work should contribute to both fundamental research and potential applications of optically active nanocrystals.

6.2 Results and Discussion

6.2.1 NC shell thickness influence on optical activity of chiral molecule Ce6

In order to produce HyNSs with different distance between the NC core and Ce6, HyNSs were formed based on QDs with various shell thickness and CdSe/CdS DiRs. We used the same CdSe QDs with 0, 1, 3, 4 and 5 CdS monolayers that were described in Chapter**3**: samples S0, S1, S3, S4 and S5, respectively. CdSe/CdS DiRs used in this study, were synthesized according to the procedure described in Section 2.4.2.

CdSe/CdS DiRs are a type of nanostructures composed of a spherical CdSe core, in which an exciton is localized, embedded inside a rod-like CdS shell (see Figure 6-1 B). As it was demonstrated by Banin et al.[191], CdS rod can be considered as a large rigid spacer between the CdSe core and an organic molecule at the surface. The same idea was proposed by Artemyev to demonstrate the reduced FRET efficiency in complexes of CdS Nano rods and dye molecules as compared to that of spherical CdSe/ZnS quantum dots

based complexes[192]. Thus, using core/shell nanoparticles of rod shape it is possible to investigate HyNSs where the distance between the NC core and Ce6 is large. In contrast to core/shell QDs of spherical shape, shell thickness of rode-like CdSe/CdS DiRs is anisotropic and varies with different directions. Therefore, the distance between the DiR core and organic molecule can be considered as a range from the thinnest and the thickest CdS shell parts, and statistically larger than that in spherical QDs case. The sketch of Ce6/NC HyNSs with different distance between NC core and Ce6 presented in Figure 6-1. Figure 6-2 represents the CD and absorption spectra of Ce6/NC HyNSs in comparison with that of free Ce6 of the same concentration. As it can be seen, the g-factor of Ce6 in the lowest electronic transition decreases with increasing the distance between NC core and Ce6. And for HyNSs based on samples S4, S5 and DiRs, Ce6 optical activity is the same as for free Ce6. Figure 6-3 demonstrates Ce6 g-factors at the lowest electronic transition of Ce6 as a part of Ce6/NC HyNSs.
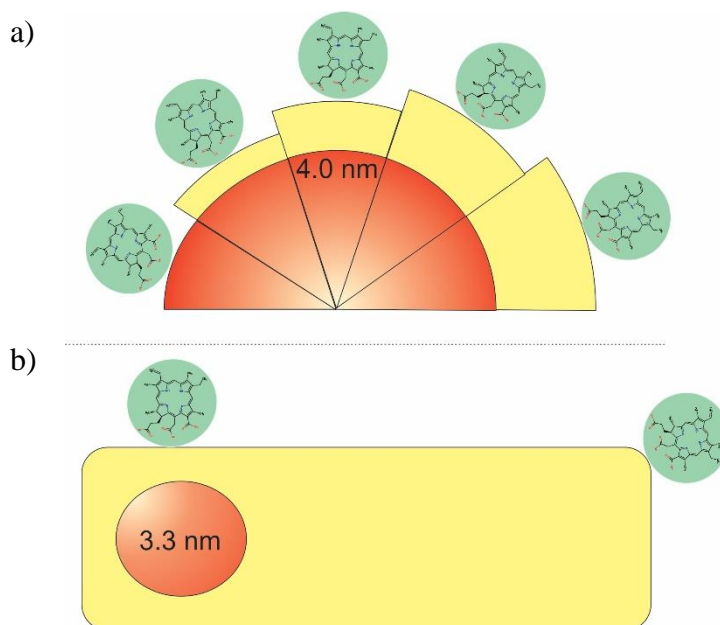
Figure 6-1. Sketch of Ce6/NC HyNSs with different distance between NC core and Ce6. HyNSs based on (A) core/shell CdSe/CdS QDs and (B) CdSe/CdS DiRs.
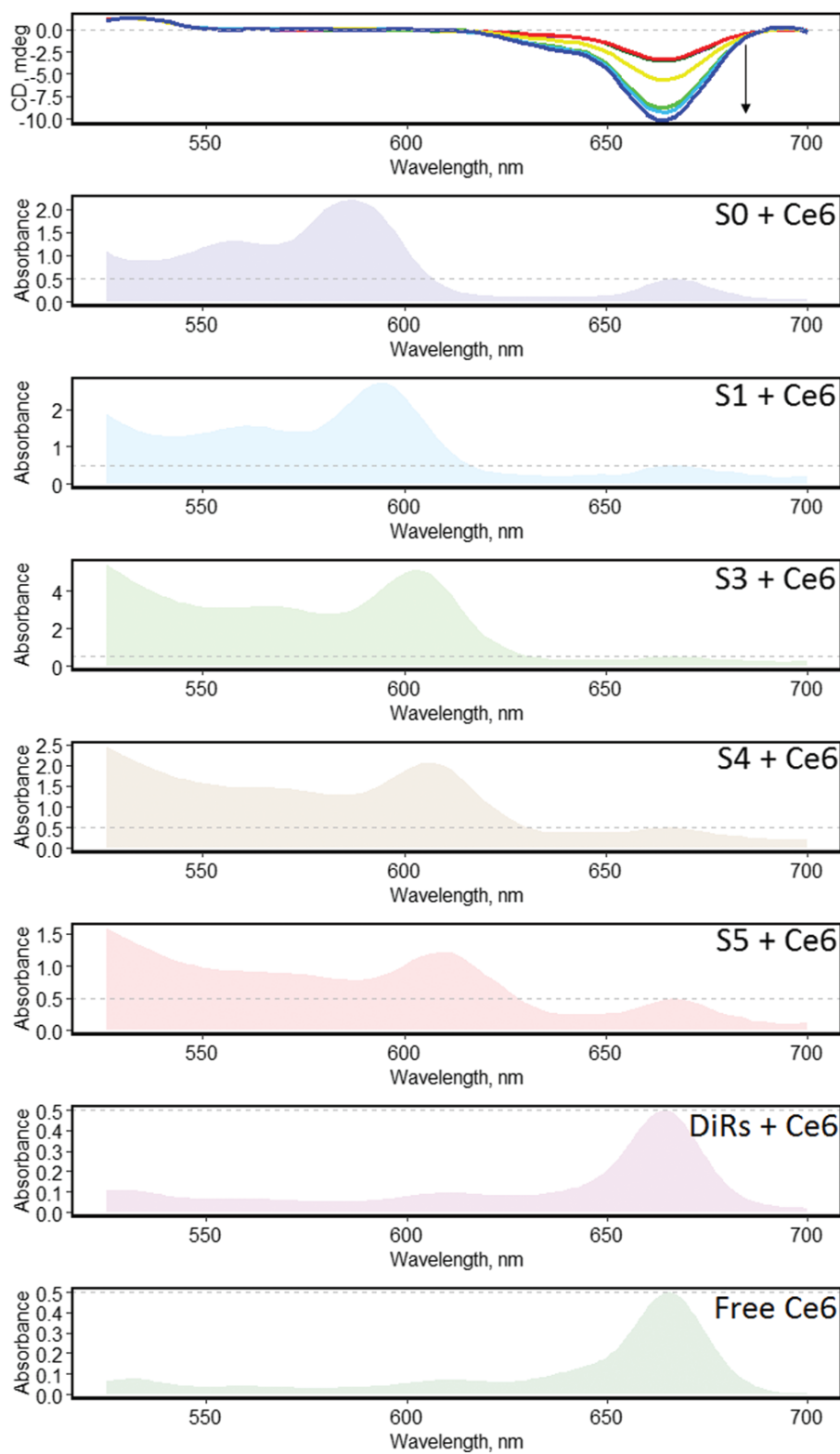
Figure 6-2. Absorption and CD spectra of free Ce6 and Ce6/NC HyNSs.
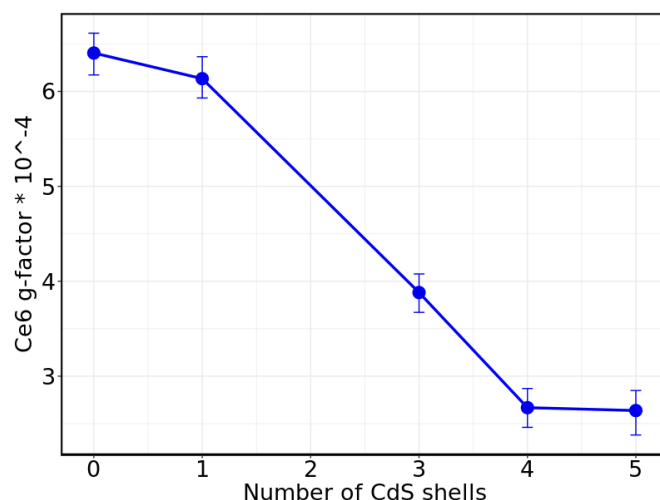
Figure 6-3. G-factors at the lowest electronic transition of Ce6 in Ce6/NC HyNSs with different distance between NC core and Ce6.

As was established earlier[129], including our recent report[176], an increase in the shell thickness of a semiconductor nanocrystal leads to a decrease in its optical activity in the region of the exciton transition. This phenomenon can be explained by hybridization between the QD valence band states and the ligand HOMO. Increasing trend of Ce6 optical activity with decreasing distance between Ce6 and NC core is in a good accordance with these results and support the hybridization theory.

6.2.2 Spectroscopic studies of electrostatic complexes of the ZnSe/ZnS QDs and Ce6.

In this study we proposed to create non-conjugated complexes of the ZnSe/ZnS QDs and Ce6 molecules through electrostatic interaction between positive QDs surface ligands and negative Ce6 functional groups. Optical properties of the pure ZnSe/ZnS QDs and Ce6 solutions are presented in Figure 6-4 A. The lowest excitonic transition $1S_{3/2h} - 1Se$ for ZnSe/ZnS QDs is located at 410 nm (3.02 eV). Size of the QDs derived from tight-binding calculations is 4.3 nm[105].

Due to position of the energy levels of QDs in near UV region donor (QDs) PL overlaps very well with strong Soret band of the acceptor (Ce6) providing excellent facilities for the effective FRET.

122
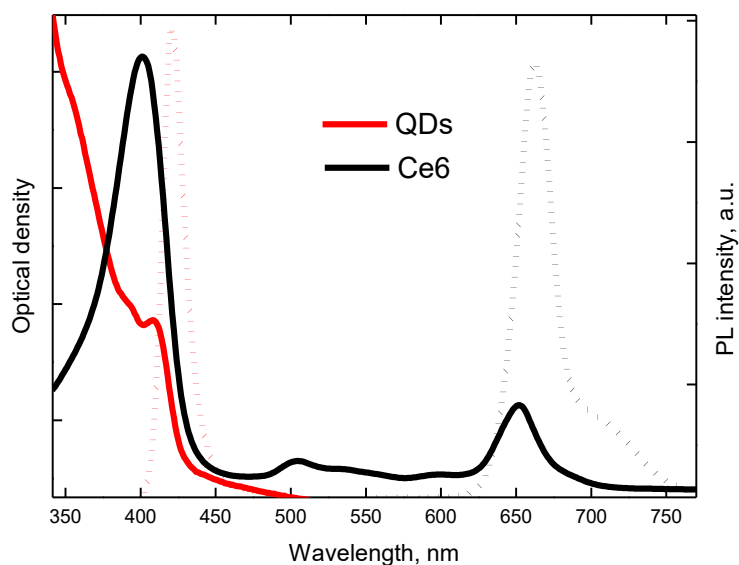
Figure 6-4. UV-VIS (solid line) and PL spectra (short dot line) of the aqueous solutions of pure ZnSe/ZnS QDs and Ce6.

After adding Ce6 with varied concentrations to QDs solution ($C_{QD} = 1\mu M$) changes in positions of the Ce6 absorption bands (*Figure 6-5* A) were remarked. Characteristic Ce6 Q(I) band demonstrates a bathochromic shift to 662 nm while Q(IV) demonstrates hypsochromic shift of the of ≈20 nm, and also a change in the bandwidth of the Soret band at ~400 nm was observed. Similar changes of Ce6 absorption spectrum were obtained in complexes with CdSe/ZnS QDs[88]. It is worthy of note that position of the Ce6 absorption bands changed at once after first addition to QDs and remained unchanged throughout following additions.

In order to understand complex formation process, we investigated QDs PL quenching with increasing Ce6 concentration in solution. *Figure 6-5* B shows that additions of Ce6 to QDs solution lead to strong quenching of the QDs PL.
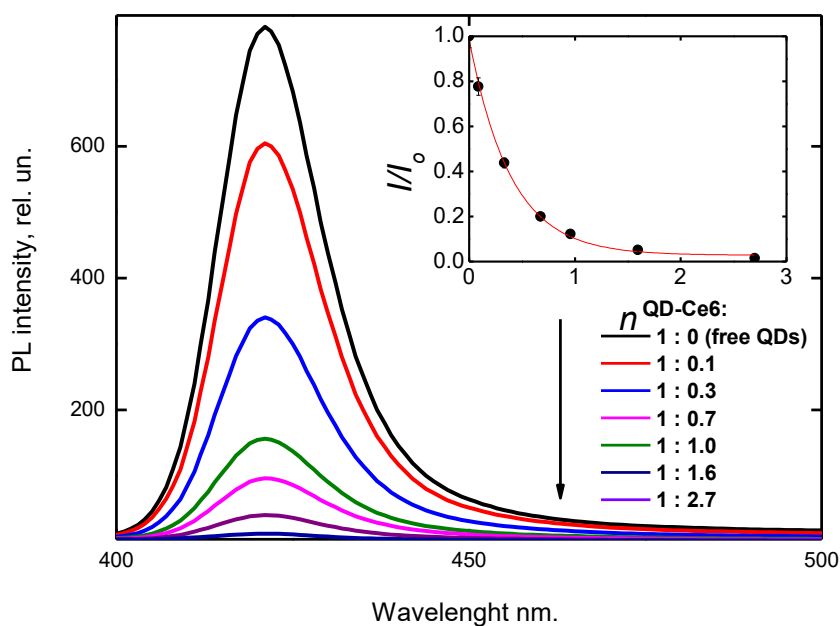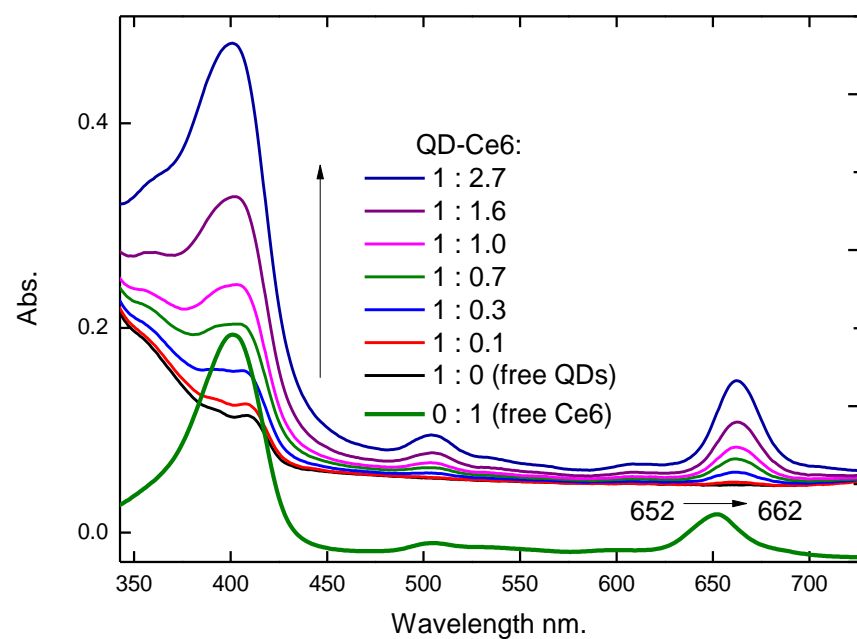
Figure 6-5. UV-VIS (a) and PL spectra under 360 nm excitation (b) of the QD-Ce6 mixture with different molar concentration ratio n_{QD}:n_{Ce6} compared with UV-VIS and PL spectra of free QD and Ce6. Insert in (b) shows the dependence of normalized PL intensity of QDs (I/I0) on n in mixture solutions. The experimental data (dots) is fitted by function y = 0.97·exp(-2.56·n)+0.03.

Maximum possible number of Ce6 molecules per one QD (i.e. the binding sites for solubilize molecules) is approximately 120 for ZnSe/ZnS QDs with core diameter 4.3 nm[180]. The surface area of the QDs with the diameter 4.3 nm is 78.5 nm². The lattice parameters of ZnS wirtzite structure are a = 0.3577 and c = 0.6088 nm. The averaged area of one lattice unit is 0.2177 nm². Each lattice unit contains 4 Zn atoms and each Zn atom is sheared between 4 unit. Thus, apoximately 360 Zn atoms are on the surface of ZnSe/ZnS QDs with core diameter 4.3 nm. The molecule of Ce6 contains 3 carboxilic groups, each of which can bind on Zn atom. Thus, the surface of QD contains approximately 120 binding sites for Ce6.

Ce6 molecules are distributed between QDs by the Poisson law. Poisson distributin can be applied if the events (bindin of the Ce6 molecule) occur independently of each other, i.e. the binding of one Ce6 molecule does not influence the binding of another molecule. As QDs contains approximately 360 surface atom and contates up to 360 positively charged cysteamine molecules, the binding of one Ce6 molecule does not significantly chage the charge of the QD surface. And Ce6 binding events can be considered as independent. In this case we can express probability that x Ce6 molecules interact with one QD, by Poisson distribution[181]:

$$P(t, x) = e^{-t} \frac{t^x}{x!}$$

Equation 6-1. Poisson distribution, where t is the average number of quenching molecules interacting with QD, defined by equation:

$$t = \frac{C_{Ce6}}{AC_{QD}} = \frac{n}{A}$$

Equation 6-2, where A is the part of QDs interacting with Ce6 molecules $0 \leq A \leq 1$ and $n = C_{Ce6}/C_{QD}$ is the molar concentration ratio between the components.

At the same time, it was found that PL decay of QD (14 ns and 4 ns) remained unchanged after Ce6 additions to the QDs solution. This indicates that PL of the only free

QDs is observed in the mixture solution and that an interaction of the QD even with one Ce6 molecule lead to complete quenching of this QD. Consequently, we can equate *x* to zero and express relative intensity of QD PL by equation:

$$\frac{I}{I_0} = Ae^{-nt+(1-A)}$$

Equation 6-3

Function *y = 0.97·exp(-2.56·n)+0.03* (see insert in the *Figure 6-5* B) achieved from experimental data indicates that nearly all QDs are interacted with Ce6 molecules and that addition of one Ce6 molecule lead to quenching of in average ~ 2.6 QDs. Taking into account the working range of the Ce6 concentrations of ~ $10^{-8} - 10^{-6}$ M these findings directly signify that QDs quenching is statistic and that QDs-Ce6 complexes with intracomplex energy transfer are formed in the mixture solution.

To confirm the presence of the effective intracomplex energy transfer we analyzed PL excitation (PLE) spectra of the complexes. *Figure 6-6* demonstrates PLE spectrum of Ce6 in complex with QDs compared with Ce6 and QDs absorption spectra. The contribution of donor (QDs) absorption to Ce6 PLE spectra, which can be easily seen in the spectral range 300 – 370 nm, is decisive evidence of the presence of the energy

transfer from QDs to Ce6.
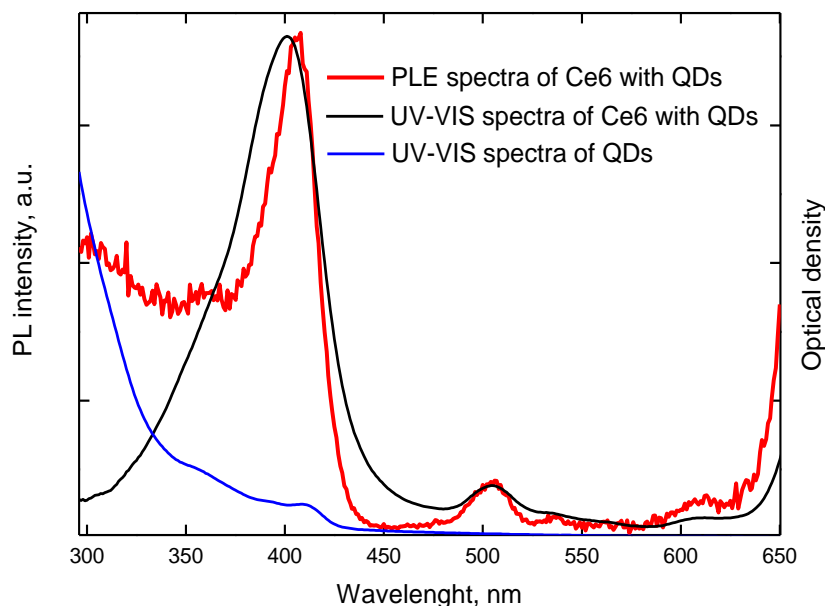
Figure 6-6. PLE spectra of QDs-Ce6 at the wavelengths 680 nm and UV-VIS spectra of QDs-Ce6 and pure QDs solution.

Then we analyzed Ce6 PL in complexes. For the correct evaluation of the sensitized Ce6 PL we perform PL excitation using two different wavelengths. We choose wavelength of 505 nm for direct excitation of the Ce6 (in this wavelength QDs absorption is negligible) and wavelength of 405 nm where simultaneous QDs and Ce6 absorption is provided.

It was uncovered that Ce6 PL intensity does not increase proportionally to the growth of the Ce6 concentration in the solution (*Figure 6-7* A). The reduction of Ce6 PL intensity was evaluated by comparison of the QY of the free Ce6 (F_0) and the QY of Ce6 within the complexes with QDs (F), which was experimentally measured with direct excitation of the Ce6. *Figure 6-7* B shows the dramatic fall of Ce6 PL quantum yield with n increasing. Quite similar data of the reduction of the QY of Ce6 when supported on QDs[88] was reported. Unfortunately, origin of this reduction is not well understood or explained and in simplistic terms can be attributed to Ce6 aggregation on the QDs surface.

Nevertheless, it was found that sensitized Ce6 PL makes a significant contribution in apparent PL of Ce6. Data of the sensitized Ce6 PL (*Figure 6-7* A) was obtained from

standard procedure of the subtracting the contribution due to direct excitation of the acceptor. Hereafter we use this data to estimate energy transfer efficiency.
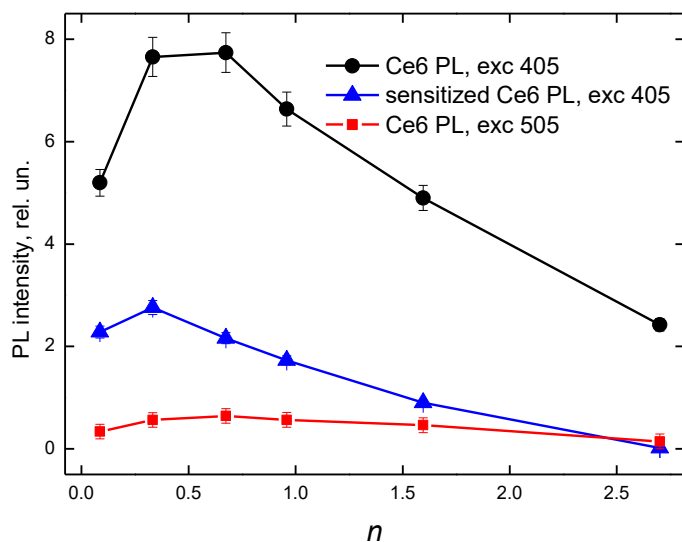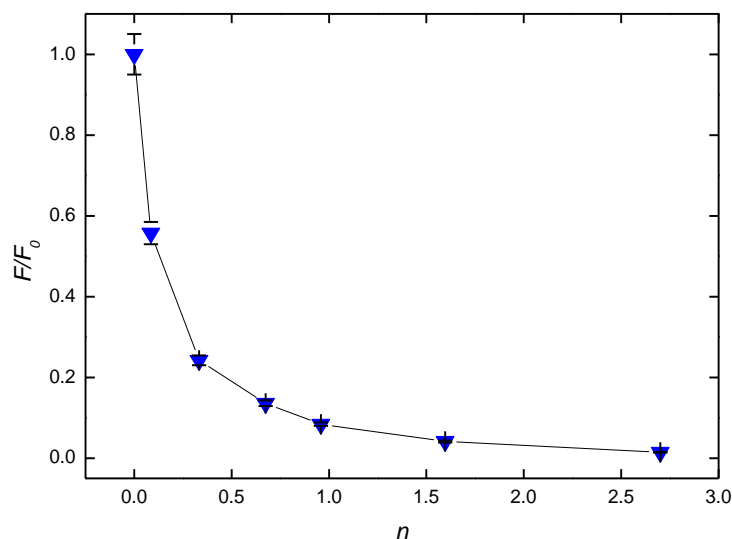
Figure 6-7. PL data of QD-Ce6. (a) Ce6 PL intensities in QD-Ce6 complexes versus n: recorded Ce6 PL values under 405 nm excitation (black curve), values of the sensitized Ce6 PL after subtraction the contribution due to direct Ce6 excitation (blue curve) and values of recorded Ce6 PL under direct excitation 505 nm (red curve). (b) Dependency of relative Ce6 PL quantum yield F/F_0 in the QD QD-Ce6 complexes on n.

The FRET efficiency for the donor-acceptor pair can be evaluated using the well-known Forster formalism as:

$$Q_{FRET} = \frac{R_0^6}{R_0^6 + R^6},$$

Equation 6-4, where R is the distance between donor and acceptor of energy. R0 is the critical radius, i.e. the distance between donor and acceptor at which FRET probability is equal to probability of spontaneous deactivation of excited state of donor that can be expressed as follows:

$$R_0^6 = \frac{9000 \cdot \ln 10 \cdot \Phi^2 \cdot QY_{0D} I}{128 \cdot \pi^5 \cdot n^4 \cdot N}$$

$$I = \int I_D^N(v) \cdot \varepsilon_A(v) \cdot v^{-4} \cdot dv$$

,

Equation 6-5, where QY0D is the quantum yield of PL of donor energy at the absence of acceptor; $\Phi^2 = \frac{2}{3}$ is the orientation factor; I is overlapping integral, $I_D^N(v)$ is the normalized PL spectrum of donor energy ($\int I_D^N(v)dv = 1$); $\varepsilon_A(v)$ is the extinction of acceptor; v is the wavenumber; n is the refractive index; N is Avogadro's number.

But in the case of QDs-tetrapirrole molecules interaction, occurrence of the additional channels of the nonradiative deactivation of the exited state of the donor may take place[88]. So *Equation 6-4* can be rather utilized for estimation of the maximum possible rate of FRET for separated donor-acceptor pair.

The FRET efficiency can be measured experimentally and is defined as ratio between acceptor PL quantum yields in the presence and in the absence of the donor:

$$\beta = \frac{F_D}{F}$$

Equation 6-6.

For more correct evaluation we took into account changes in Ce6 PL quantum yield and modified Eq. 6 as ratio between quantum yield of sensitized PL of the Ce6 molecules complexed with QDs to quantum yield of PL of molecules exited with direct

photoexcitation. Sensitized Ce6 PL quantum yield was found as ration between sensitized

Ce6 PL I_{Ce6}^{sens} (*Figure 6-7* A, blue curve) to optical density of the QDs D_{QD} at the wavelength of the sensitized PL excitation.

We also utilized $(1-\dfrac{I}{I_0})$ from Eq. 3 considering that it has physical meaning as a part of QDs bond to complex with Ce6 molecules:

$$\beta = \frac{(I_{Ce6}^{sens} / D_{QD})}{(I_{Ce6}^{direct} / D_{Ce6}^{direct}) \cdot (1-\dfrac{I}{I_0})},$$

Equation 6-7

Table 6-1 shows calculated Forster radius R_0, overlapping integral I, and FRET efficiency Q_{FRET} and β for ZnSe/ZnS-Ce6 pair. We suppose that the distance between donor and acceptor R is approximately equal to the dot radius, taking into account a size of QDs (2.15 nm), a thickness of ZnS shell (0.3 nm) and a length of solubilizer molecules (0.1 nm).

Distance between donor and acceptor R, nm	Forster radius R_0, nm	Overlapping integral I, $M^{-1}cm^4$	Q_{FRET}, %	β, %
2.55	12.7	$1.09 \cdot 10^{-11}$	99	65

Table 6-1. FRET characteristics for ZnSe/ZnS QDs-Ce6 donor-acceptor pair.

ZnSe/ZnS-Ce6 complexes for PDT

There are only few studies that perform PDT efficacy tests on QD-photosensitizer complexes against cancer cells. For example, complexes of CdSe/ZnS QDs with Rose Bengal[93] showed cytotoxic effect in HeLa cells. The hybrid photosensitizer CdTe-methylene blue was tested against HepG2 and HeLa cancerous cells[94]. CdSe/CdS/ZnS-

aluminium phthalocyanine conjugates demonstrated improved photodynamic reactions in destroying human nasopharyngeal carcinoma cells[95]. However, the toxicity of cadmium-based QDs limits the in vivo applications of these complexes. Less toxic InP/ZnS QDs were conjugated to chlorin e6 but the conjugates showed almost the same PDT efficacy against the MDA-MB-231 breast cancer cell line as Ce6 alone[98].

The data of the energy transfer efficiency show sufficiently high potential of the ZnSe/ZnS-Ce6 complexes for PDT so we next perform *ex-vivo* studies using an Ehrlich ascites carcinoma cells, extracted from mouse. Cells were incubated with Ce6, QDs, and QDs-Ce6 for 2 hours and then irradiated with a 405 nm laser at a power density of 40 mW/cm^2 for 10 min (light dose = 24 J/cm^2). In this test we kept QDs concentration constant $C_{QD} = 0.5\mu M$ and varied concentration of free Ce6 and Ce6 in complexes. The trypan blue assay was carried out to determine the cell viabilities.
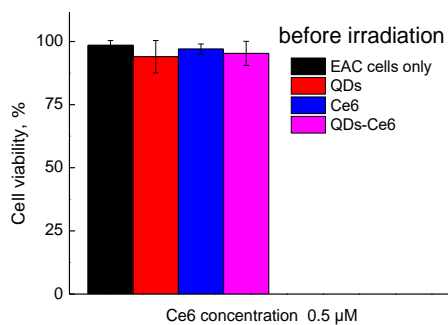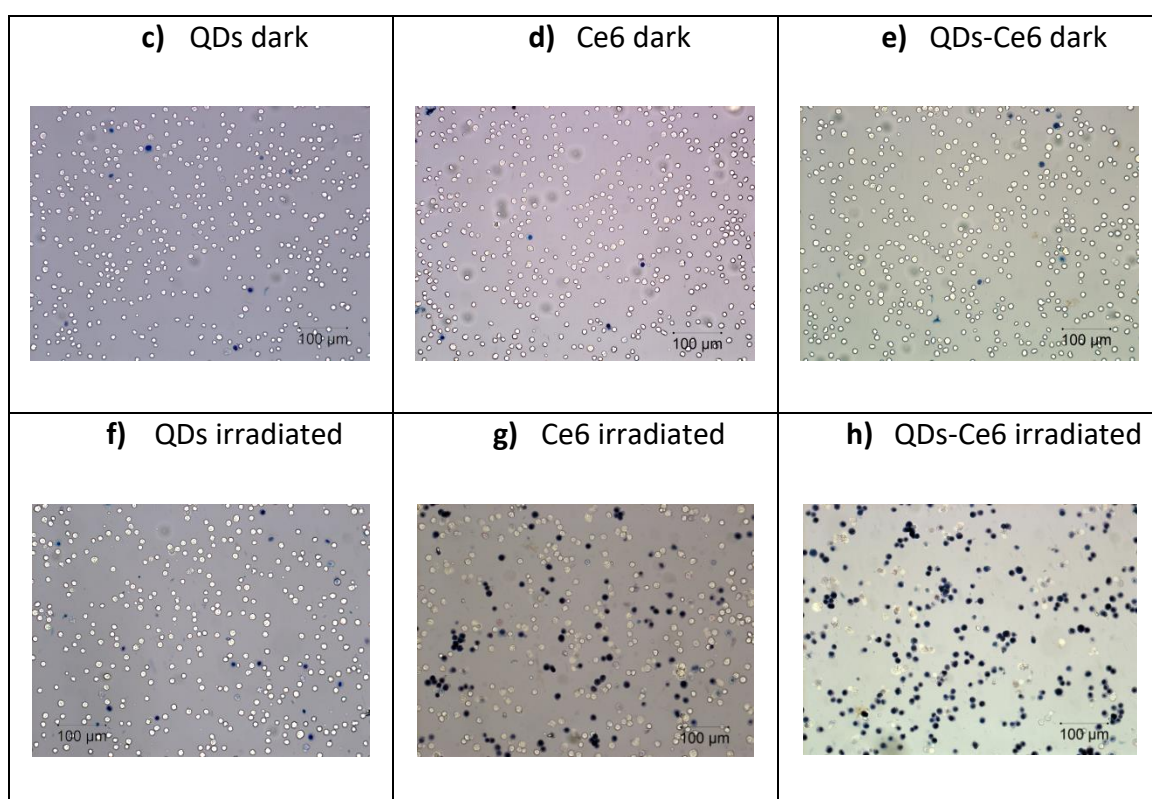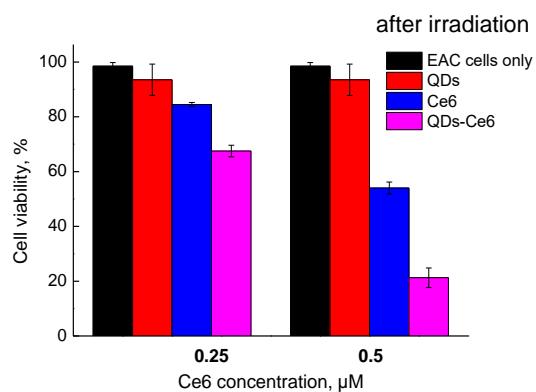
Figure 6-8. Ex-vivo photodynamic cancer cell destruction. (a-b) Cell viability data represented as percentage of viable cells obtained from the trypan blue assay of AEC cells after various treatments. Cells treated with QDs, Ce6 and the QD-Ce6 complexes without (a) and with (b) irradiation by the 405 nm laser (40 mW/cm², 10 min). Error bars were based on SD of five parallel samples. Transmitted light microscopy images of trypan blue stained AEC cells incubated with QDs (c, f), Ce6 (d, g) or QD-Ce6 (e, h) with and without laser irradiation. The QDs and Ce6 concentration was 0.5 µM in c-h.

It was found that without irradiation Ce6, QDs, and QDs-Ce6 complexes do not exhibit essential dark toxicity to ACE cells (*Figure 6-8* A). After the irradiation QDs-Ce6 complexes show remarkably higher cells destruction effect compared with that of free Ce6. ZnSe/ZnS QDs did not show phototoxity at the used concentration under light irradiation.

Improved photodynamic cancer cell killing efficiency with QDs-Ce6 complexes might be owned to two unrelated reasons: the increased cellular uptake of Ce6 delivered by QDs and strong enhancement of the singlet oxygen generation by FRET.

At the first approach we assume that enhancement of PDT effect is primary associated with intracomplex FRET from QDs to Ce6 molecules. To check this hypothesis, we perform PDT test using wavelength of light irradiation corresponding to the direct excitation of Ce6. For this 660 nm diode with power density 0.2 W/cm^2 (time of exposure 7 min, light dose 85 J/cm^2) was utilized. To provide similar conditions for PDT treatment with 405/660 nm exposure we match light dose of 660 nm irradiation of to provide the same data of cells viabilities for pure Ce6. For this we take into account that Ce6 absorption at the 405 nm wavelengths is significantly higher than that at the 660 nm.
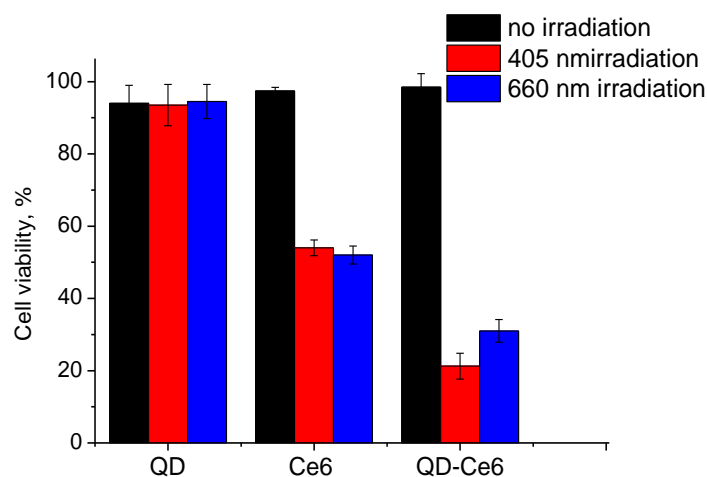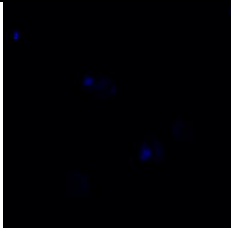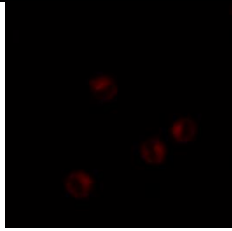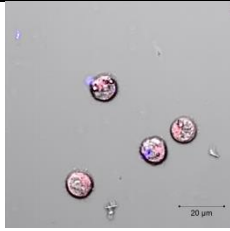
Figure 6-9. Cell viability data of EAC cells incubated with QD-Ce6, free Ce6, or QDs respectively at Ce6 and QDs concentration of 0.5 µM in every sample. Black, red and blue bars represent samples without any light exposure, with 405 nm (24 J/cm^2) and
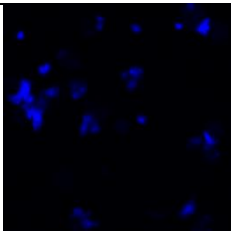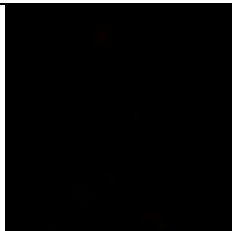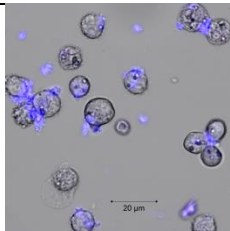
We find that combined utilization of QDs and Ce6 lead to enhancement of PDT effect even with direct Ce6 excitation at 660 nm. This strongly indicates that intracellular Ce6 concentration was higher when cells were incubated with QD-Ce6 compared with that with free Ce6. But the difference between cells viabilities for cells with Ce6 or QD-Ce6 with 660 nm exposure was less than that with 405 nm exposure. Based on these results we canpresume that FRET from QDs to Ce6 may take place within cells.

On the next step we compared QDs, Ce6 and QD-Ce6 cellular uptake behaviors. EAC cells were incubated with QDs-Ce6 complexes or free Ce6 and QDs at the same Ce6 and QDs concentrations (0.5 µM) for 1, 2 and 7h at 37 C and then imaged under a confocal fluorescence microscope. The emission was collected from two spectral regions corresponding to QDs emission peak (410-460 nm) and Ce6 emission peak (630-730 nm). *Figure 6-10* shows the PL confocal images of the living cells incubated with Ce6, QD and Ce6-QDs.

	QD-Ce6			

		Channel 1	Channel 2	PMT
2 hours	QDs			
	Ce6			
	QD-Ce6			

		Channel 1	Channel 2	PMT
7 hours	QDs			
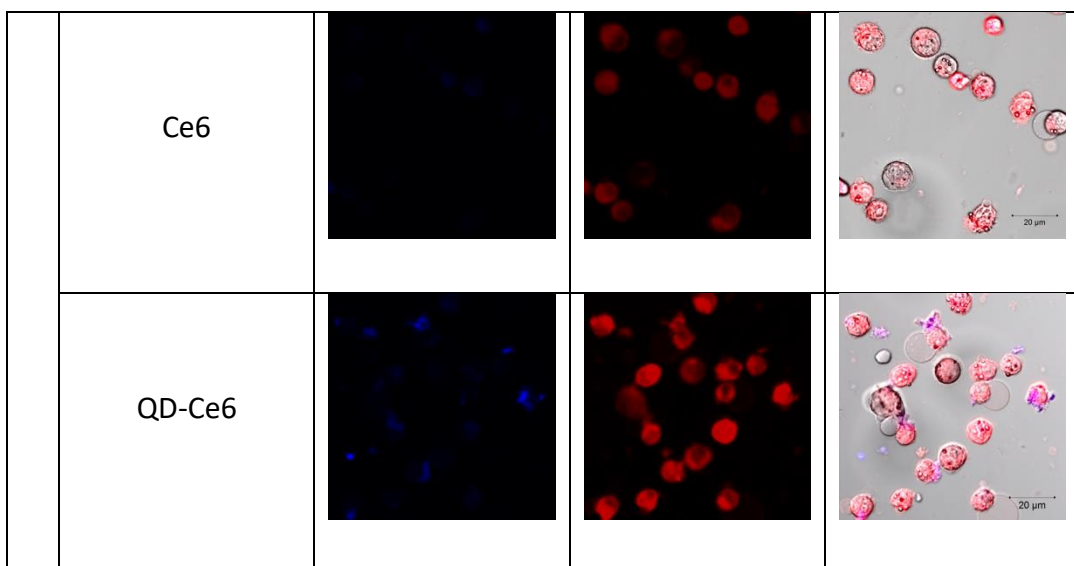
Figure 6-10. Cellular uptake of QDs, Ce6 and QDs-Ce6. (a) Confocal PL images of cells incubated with QDs (upper row), free Ce6 (second row), and QDs-Ce6 (bottom row) after different periods of incubation (1, 2, and 7 h). Channel 1 is correspondied to QDs emission peak (410-460 nm) and Channel 2 is corresponded to Ce6 emission peak (630-730 nm). Images in separate PL channel were taken under identical instrumental setting.
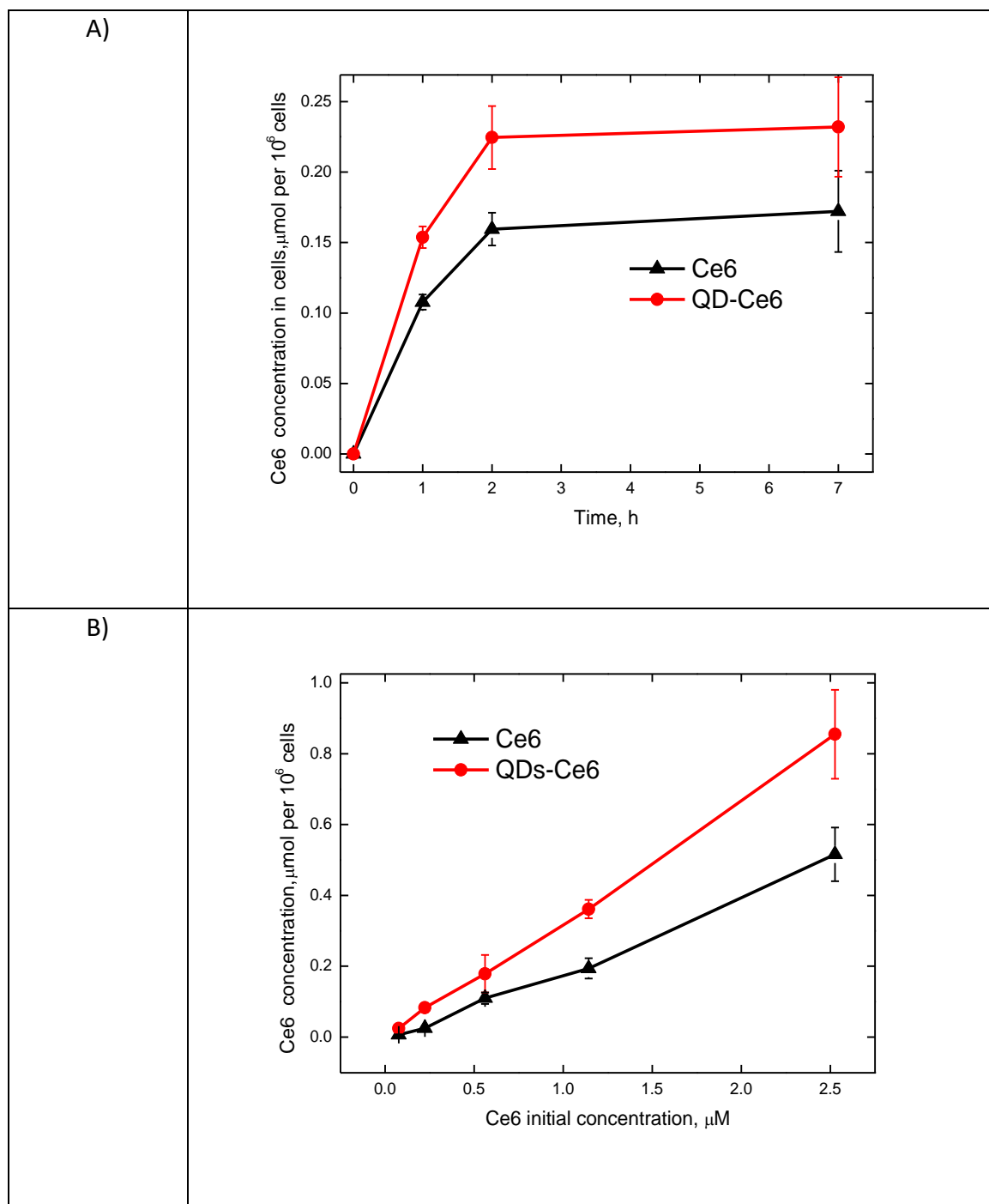
Figure 6-11. (a) Estimated values of Ce6 concentration in cells after different periods of incubation (0.5, 1, 2, 4 and 7 h). (c) Estimated values of Ce6 concentration in cells depending from initial Ce6 concentration. Initial concentrations of QDs (in a-c) and Ce6 (in a-b) were 0.5 µM. Error bars were based on SD of triplicate samples.

The intracellular PL in all channels increased over time. It is known from previous studies that QDs cellular uptake and intracellular localization somewhat depend on the size, shape, surface modification, and cell type. Our results show that ZnSe/ZnS QDs with

cysteamine modified surface do not show highly efficient targeting of the EAC cells but some PL signals localized in cells area can be observed. It also should be mentioned that PL intensity for cells incubated with free QDs is a shade more than that in cells incubated with QD-Ce6. This may be caused by QDs PL quenching as a result of FRET to Ce6 molecules.

The cells incubated with QDs-Ce6 showed stronger Ce6 PL inside cells, despite the PL quenching of Ce6 attached on QDs.

We presuppose that QDs can act as a delivery agent. To qualitatively evaluate Ce6 cell uptake we study a concentration level of Ce6 in cells. For this we measured Ce6 optical density in Soret band in supernatant after cells incubation. Ce6 concentration in cells can be estimated as a remainder after substation of Ce6 concentration in supernatant from Ce6 initial concentration before incubation. Results are shown in *Figure 6-11*. The amount of Ce6 delivered into cells by QD-Ce6 was found to be twofold higher than that of free Ce6. We speculate that the significantly enhanced Ce6 delivery may likely be due to the efficient cell entry of QDs by endocytosis[77] that shuttles Ce6 into cells, while free Ce6 has less effective intracellular cross membrane diffusion ability.

6.2.3 Complexes of Photosensitizer and CdSe/Zns QDs Passivated with BSA: Optical Properties and Intra-Complex Energy Transfer

One of the main problems of many QD-tetrapyrrole complexes is the appearance of new non-radiative energy deactivation channels in QDs as well as tetrapyrrole aggregation in the complexes[193]. Both of these processes considerably reduce the intracomplex energy transfer efficiency and decrease tetrapyrrole singlet oxygen generation. The passivation of QD surface with proteins can partially eliminate the non-radiative channels of energy relaxation and enhance QD luminescence quantum yield (QY)[194]. In our study we use bovine serum albumin (BSA) for the QD passivation. The serum albumin is the most abundant protein in the blood serum. One of the main

functions of this protein is the transportation of hydrophobic substances to the tissues. In particular, serum albumin delivers photosensitizer molecules to the cancer cells during photodynamic therapy. Binding of tetrapyrroles with serum albumin allows to stabilize tetrapyrroles and to reduce their possible aggregation[195], thereby enables to increase singlet oxygen generation efficiency. Moreover, serum albumin can also serve as a linker between QDs and tetrapyrroles.

In this work we have studied the formation conditions and photo physical properties of complexes between Ce6 and CdSe/ZnS QDs, linked by BSA.It was shown, that the passivation of QDs with BSA resulted in significant increase of QD luminescence quantum yield. It has been found thatthe complexes between QDs, passivated by BSA, and chlorin e6 demonstrated effective photoexcitation energy transfer from QDs to chlorin e6 molecules. It was also demonstrated that chlorin e6 was in complexes in monomeric molecular form.

Optical properties of the initial components

For the efficient Förster resonance energy transfer (FRET) it is necessary to have significant overlap between donor PL and acceptor UV/Vis absorption spectra (Figure 6-12). As can be seen in Figure 6-12 , UV/Vis absorption and PL bands of BSA, determined by tryptophan[196], are located in UV region with the absorption maximum at 280 nm and PL maximum at 349 nm[197]. Ce6 have pronounced absorption bands in the visible spectrum region: Soret band at 401 nm and Q bands including Q (IV) band at 503 nm and Q (I) band at 654 nm. PL band of Ce6 locate in red region at 662 nm. Spectra of QDs have excitonic absorption band at 517 nm, and 2.5 nm CdSe core diameter calculated according to[102]. The maximum of QD excitonic PL band is located at 540 nm.

The analysis of the spectra in Figure 6-12 shows that QD PL band, excited at 460 nm, overlapped quite well with Ce6 Q-bands at the region of 500-550 nm, which fulfilled the condition for FRET from QDs to Ce6. Also it can be seen that BSA PL band, excited at 290 nm, had considerable overlap with both QD and Ce6 UV/Vis absorption spectra. Consequently, FRET from BSA to QDs[197] as well as to Ce6[195] was possible on condition that

PL was excited at the BSA absorption region. To exclude energy transfer from BSA we used PL excitation wavelengths located at the region where BSA does not absorb light[197]. At the same time, BSA significantly affected QD and Ce6 optical properties, as it will be considered in details below.
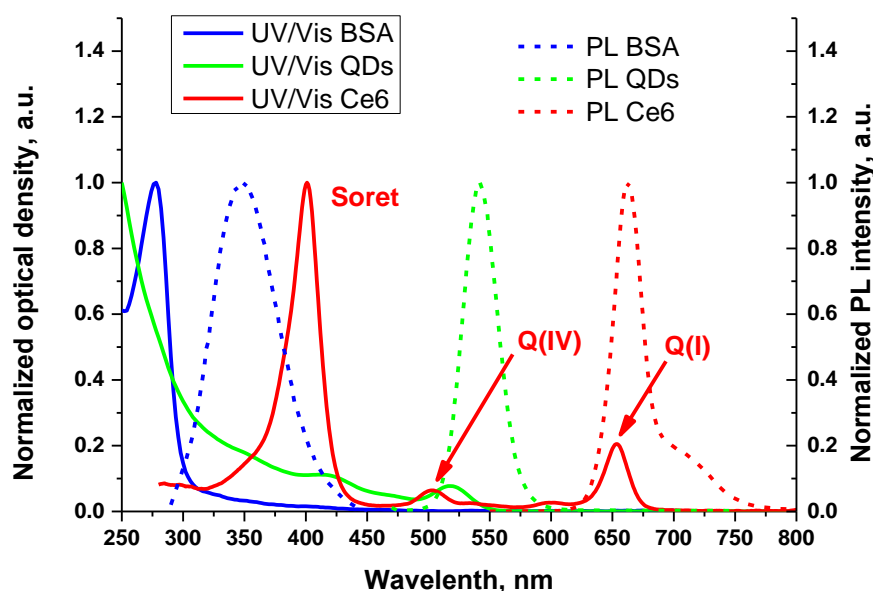
Figure 6-12. Normalized PL (dotted lines) and UV-Vis absorption spectra (solid lines) of BSA, QD and Ce6 aqueoussolutions at pH=8. The excitation wavelengths for BSA, QD and Ce6 PL were 290 nm, 460 nm and 640 nm respectively.

BSA Influence on optical properties of QD and Ce6

To investigate QD-Ce6 complexes with BSA as a linker, initially it was necessary to study the influence of BSA on optical properties of QDs and Ce6.

For this purpose, UV/Vis absorption and PL spectra of aqueous solutions of QDs, Ce6 and their mixtures, containing different amount of BSA, were analyzed.

The additions of BSA to QD solutions resulted in a significant increase of QD PL intensity while QD absorption spectra remained unchanged after every addition (Figure 6-13). This can be explained by the enhancement of PL quantum yield of QDs with an increase of BSA concentration. At the maximum BSA:QD ratio used in this work, which is

equal to 30:1, the QD PL quantum yield increased by approximately 3.5 times. That is the evidence of QDs and BSA interaction. It is well known, that BSA adsorbs on the QD surface by hydrophobic and electrostatic forces[197] and by coordination of BSA thiol groups with Zn atoms on QD surface. As it was mentioned above, BSA did not have a significant absorption at the PL excitation wavelength 460 nm (see Figure 6-12). Consequently, the increasing of QD PL intensity is not being caused by FRET from BSA to QD and can be explained by QD surface passivation with BSA. That can significantly enlarge the efficiency of intracomplex energy transfer from QDs to Ce6, because, as it is well known, FRET rises with an increase of donor PL quantum yield[88].
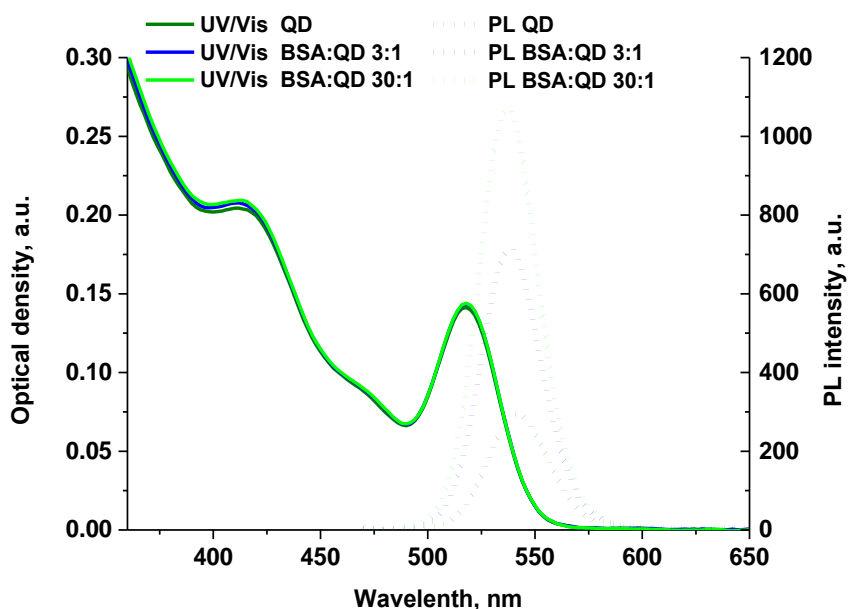
Figure 6-13. PL (dotted lines) and UV/Vis absorption spectra (solid lines) of QD aqueous solution and BSA-QD mixtures with the BSA:QD ratios equaled to 3:1 and 30:1. The PL excitation wavelength was 460 nm.

Next, we examined the influence of BSA binding on optical properties of Ce6. For this purpose, BSA was added to Ce6 solution in PBS. BSA:Ce6 ratio was 15:1 to achieve the excess of BSA in solution for complete binding of Ce6. The addition of BSA resulted in significant changes in optical properties of Ce6, as can be seen from UV/Vis absorption spectra (a) and PL spectra (b) of pure Ce6 and BSA-Ce6 mixture in *Figure 6-14*. It is clear that in the mixtures with BSA Ce6 Soret band was shifted from 401 to 408 nm and Q (I)

band was shifted from 654 to 660 nm. The spectra in *Figure 6-14* B show that Ce6 PL band maximum changed from 662 to 665 nm. Such changes of the optical properties of Ce6 in the mixtures with BSA proved the binding of Ce6 with BSA and in agreement with the results in other publications where binding of Ce6 to BSA was accompanied by similar bathochromic shift of Ce6 absorption and PL bands[195]. Binding of Ce6 with BSA most likely occurred at the specific BSA binding sites by hydrophobic and van der Waals interactions[195].

As mentioned above, the possible aggregation of Ce6 molecules in complexes with QDs is one of the reason of energy transfer efficiency drop in QD-Ce6 complexes[88]. In present study using PL and circular dichroism (CD) spectroscopy we have shown that Ce6 bound to BSA did not aggregate. One of the evidence of that was the location of Ce6 Q (I) band. For example, in the case of the dimerization of Ce6 the Q (I) band maximum shifts to 640 nm[198], that did not occur in our system. Similar data were previously reported[198].

a)
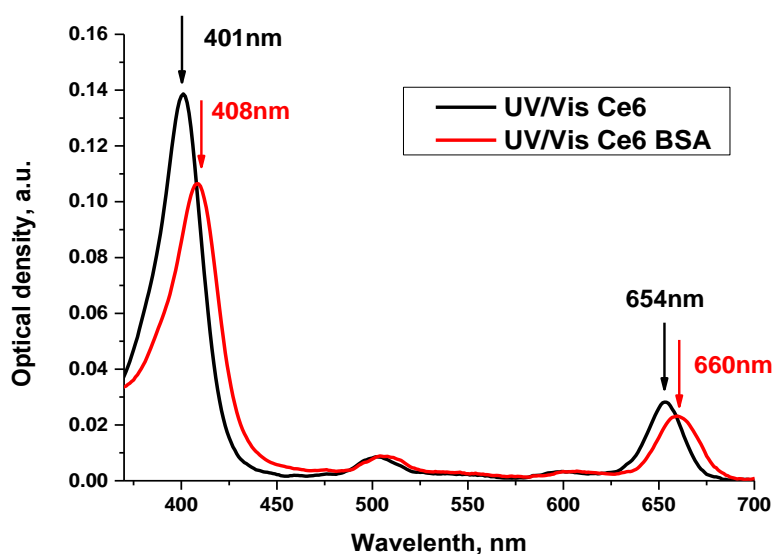
b)
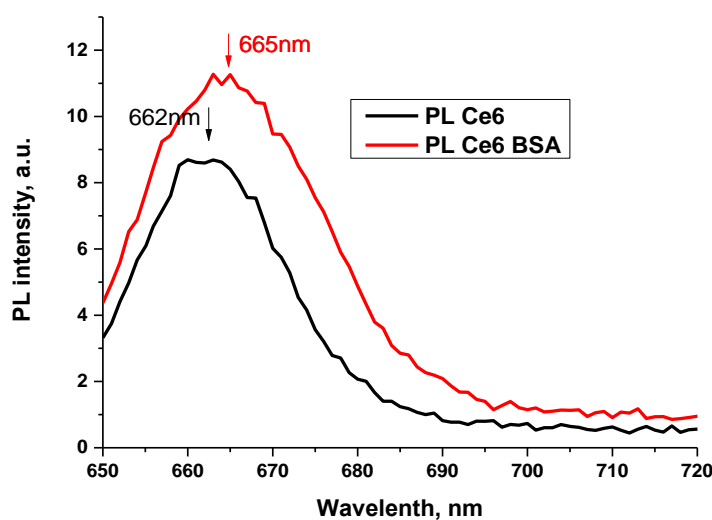
Figure 6-14. UV/Vis absorption spectra (a) and PL spectra (b) of pure Ce6 and BSA-Ce6 mixture with the BSA:Ce6 ratio of 15:1 in PBS. BSA was taken in excess to provide the binding of the most part of the Ce6 molecules. The PL excitation wavelength was 460 nm.

The absence of Ce6 aggregation was evidenced by circular dichroism (CD) spectra of Ce6 in the mixtures with BSA (Figure 6-15). As it was shown in the previous research[199], CD spectra with one minimum in the region of Q (I) band are typical for tetrapyrroles in monomeric form. Whereas CD signals of the aggregated tetrapyrroles split to positive and

negative CD components, crossing zero near the absorption maximum. We registered CD spectra of BSA-Ce6 mixtures with BSA:Ce6 ratio of 1:0.5; 1:3; 1:5 and 1:10. All CD spectra of Ce6-BSA mixtures had minimum at the wavelength 655 nm, corresponding to Ce6 Q (I) absorption band. CD signal corresponding to Ce6 Q I band of BSA-Ce6 mixtures did not split at all concentrations, i.e. Ce6 was in monomeric form.
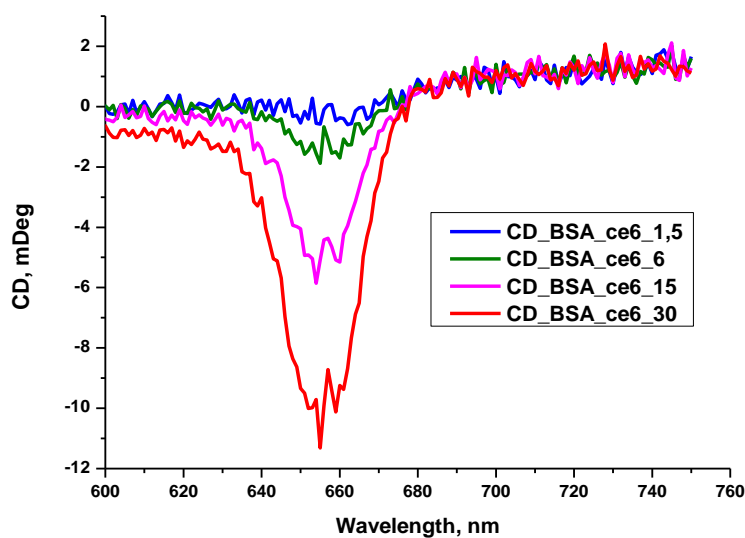
Figure 6-15 Circular dichroism spectra of the mixtures of Ce6 and BSA in PBS. BSA concentration is 3 μM; Ce6 concentrations are 1,5; 9; 15 and 30 μM.

Thereby, it can be concluded that BSA can prevent possible aggregation of Ce6 and enlarge FRET efficiency in QD-Ce6 complexes.

The Influence of BSA on optical properties of the QD and Ce6 mixtures

In order to demonstrate the possibility of QD-Ce6 complex formation with BSA as the linker we used QDs that did not reveal the evidence of interaction with Ce6 without BSA. The QDs were capped with cysteine ligands, that are negatively charged in aqueous solution at pH=7.4. The electrostatic repulsion between QDs and negatively charged Ce6 molecules, bearing 3 carboxylic groups, prevents the complex formation.

To analyze the interaction of Ce6 with QDs capped with cysteine in the absence of BSA the PL spectra of QD-Ce6 mixtures were registered. It was demonstrated that neither

PL quenching of QDs (donor) nor sensibilization of Ce6 (acceptor) PL were observed (data not shown). Thereby, no experimental evidence of the formation of complexes with energy transfer was obtained at the component concentrations used in this work.

After that we investigated the behavior of mixtures of QDs and Ce6 in the presence of BSA. For this purpose the QD were mixed with different amount of BSA and incubated for 12 hours at 4°C. Then Ce6 was added the mixtures. The concentrations of QDs and Ce6 were constant, equaled to 1 µmol/L. BSA:QD ratio was varied from 1: 1 to 30:1.

Figure 6-16 displays UV/Vis absorption spectra of QD and Ce6 solutions and mixtures of BSA-QD-Ce6 with ratio BSA:QD:Ce6 equaled 3:1:1 and 30:1:1, as examples. It is clear that BSA did not influence QD absorption spectrum. While Ce6 absorption spectra changed after BSA additions, testifying that Ce6 bound to BSA. As it can be seen in *Figure 6-16*, bathochromic shift of Ce6 Q (I) absorption band enhanced with the increase of BSA concentration, i.e. the amount of bound Ce6 increased.
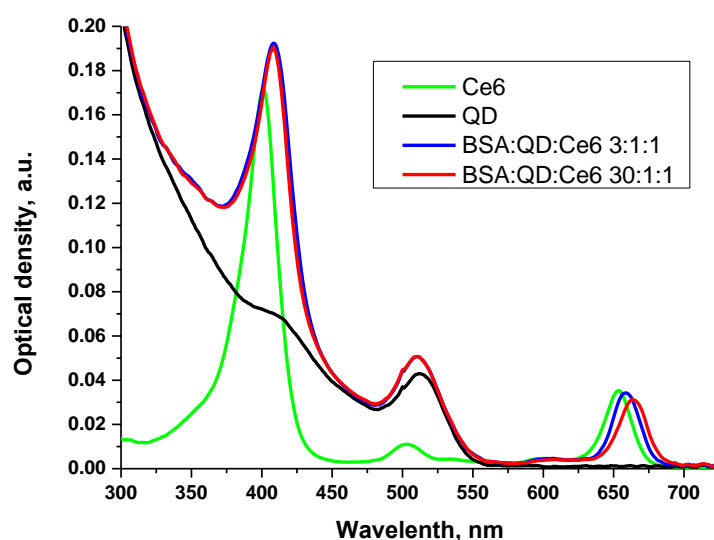
Figure 6-16. UV/Vis absorption spectra of QD and Ce6 solutions and mixtures of BSA-QD-Ce6 with ratio BSA:QD:Ce6 equalled 3:1: 1 and 30:1: 1 in PBS.

146

Then PL of QD and Ce6 mixtures in the presence of BSA was investigated. PL was excited by 460 nm light, at region where QDs had significant extinction coefficient, and by 640 nm, where QDs didn't absorb the light, in order to compare sensitized Ce6 PL caused by FRET with the intrinsic Ce6 PL.

Figure 6-17 shows the influence of BSA on sensitizedand intrinsic Ce6 PL in QD and Ce6 mixtures. Normalized sensitizedPL of Ce6 was calculated by the following formula:

$$I_{ns} = \frac{I^{460} - I_0^{460}}{I_0^{460}}$$

Equation 6-8, where I^{460} is Ce6 PL intensity in the presence of BSA, excited at 460 nm, And I_0^{460} is initial Ce6 PL intensity in the absence of BSA, excited at 460 nm. For the convenience of comparison the same calculation was performed for intrinsic Ce6 PL, excited at 640 nm I_{ni}.

As can be seen from the graphs in Figure 6-17, BSA did not have significant influence on intrinsic Ce6 PL intensity, because of PL quantum yield of Ce6 did not changed. It also demonstrated (Figure 6-17) that in the presence of BSA a sensitized Ce6 PL appeared, meaning that FRET from QD to Ce6 occurred. Consequently, the complexes of QDs and Ce6 with BSA as a linker were formed.
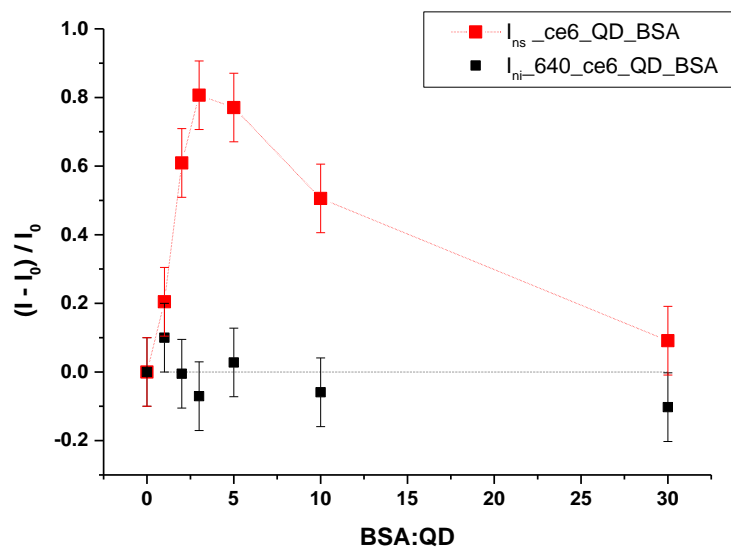
Figure 6-17. Dependence of relative Ce6 PL variation in QDs, BSA and Ce6 mixtures on BSA:QD ratio. Ce6:QD ratio was 1:1. BSA:QD ratio was variated from 1:1 to 30:1. The excitation wavelength were 460 and 640 nm.

Besides, sensitized Ce6 PL primarily rose with increase of BSA concentration, reaching the maximum at BSA:QD ratio of 3:1, and then decreased. We assume, that this decrease of sensitized Ce6 PL was caused by the increase of the relative portion of free BSA, not bound to QDs, with the augmentation of BSA:QD ratio. Thus, at small concentration, BSA was mostly adsorbed on QD surface, and major part of Ce6 binding to BSA appeared to be in complexes with QDs. With the increase of BSA concentration the relative portion of free BSA increased, and Ce6, being distributed among free and adsorbed BSA, was mostly bound to free BSA. In other words, at lager BSA concentration relatively less amount of Ce6 molecules were bound to BSA, adsorbed on the QDs, then at smaller BSA concentration. That means that the amount of QD–Ce6 complexes decreased with increase of BSA concentration.

It can be concluded that BSA:QD ratio of 3:1 is optimal for complex formation in this system at the working concentration. In our future work we are going to estimate the intracomplex FRET efficiency from QDs to Ce6 in the systems with optimal BSA:QD ratio of 3:1 and determine the influence of Ce6 concentration on FRET efficiency.

6.3 Conclusions

Thus in this work we have investigated the distance dependent influence of the nanocrystal core on optical activity of a chiral organic molecule, chlorin e6. Hybrid nanostructures based on chiral organic dye, chlorin e6, and various semiconductor nanocrystals (core/shell CdSe/CdS quantum dots, CdSe/CdS dot-in-rods) were produced. It has been found that chlorin e6 optical activity increases when chlorin e6 bound with nanocrystal, and this phenomenon depends on NC shell thickness. It has been found that the optical activity of an organic molecule exhibits a pronounced dependence on the distance between the NC core and the molecule, namely, decreasing the distance between the NC core and molecule leading to increase in the optical activity of the molecule. We believe that these results are of great interest for both fundamental research and potential applications of optically active hybrid Nano complexes of QDs with Ce6 for PDT.

We have demonstrated that Cd-free ZnSe/ZnS QDs can serve as a successful delivery agent and photosensitizer of chlorin e6 in PDT against the Erlich acsite carcinoma cell culture. We applied steady-state and transient spectroscopic optical techniques to show the formation of aqueous solutions of the QD–Ce6 complexes with efficient QD to Ce6 intracomplex photoexcitation energy transfer. By using confocal luminescence microscopy and the trypan blue assay of EAC cells we have shown that QD–Ce6 complexes demonstrate dramatically improved photodynamic cancer cell killing efficiency due to synergistic effect of photoexcitation energy transfer from QD to Ce6 and the increased cellular uptake of Ce6 delivered by QDs.

In the second part of the work we have investigated the optical properties of complexes of QDs and chlorin e6 with BSA as a linker. It was demonstrated that BSA significantly improved the optical properties of complexes. BSA passivated the QD surface and in such a way enhanced QD PL quantum yield. In addition, BSA prevented the possible aggregation of Ce6 on QD surface. Thus, we have clearly demonstrated that BSA can significantly enhance the energy transfer efficiency of QD Ce6 complexes. To test these complexes on cells for PDT is one of the aim of our future work.

We expect that similar QD systems should be promising for further investigation in combination with other conventional therapeutic agents in human cancer theranostic and potentially in other emerging Nano medicine areas.

7 Conclusions and Future work

7.1 Conclusions

Thus, we have developed a range of new chiral quantum dot based materials of different shapes and investigated their biological behaviour*in vitro.* In particular, we have investigated how the CdS shell thickness and ligand concentrations influence CdSe/CdS QD induced optical activity; tested the biological activity of semiconductor fluorescent NPs capped with chiral ligands on leaving cells; investigated the influence of QDs on optical activity of chiral molecule of Ce6 and studied FRET and PTD efficiency of complexes of QDs with Ce6.

Our investigations have shown the subtle relationship between PL and CD signals in chiral ligand induced chiroptically active CdSe/CdS QDs. We have found that it is paramount to optimise the thickness of the CdS layer on a CdSe/CdS QD so as to produce luminophores with a strong CD response and effective PL following ligand exchange. We also observed the same trend of decreasing signal relative to previously published results[129] concerning CdSe/CdS QDs CD signal in relation to CdS shell thickness though in our study we did not find the same complex trend, instead we observed monotone decrease dependence of CD with shell thickness.

In addition, our results also clearly demonstrated that synthetic conditions such as annealing time have a strong impact both on the induced CD signal and luminescence, resulting in an increase in PL QY due to the decrease in crystal defects. We also found that increased annealing time led to a reduction of optical activity, which can be explained by the loss of crystal defects which have been initially associated with optical activity in QDs.

We have also shown that QD CD signal intensity depend on ligand concentration and binding mode: CD intensity increased with ligand concentration at the beginning, then reached a maximum and decreased at high Cys concentrations. FTIR and NMR analysis enabled us to demonstrate that Cys had different binding configuration on the QD surface at different concentrations. At high concentrations Cys most likely bound to QD surface with thiol and amino groups, while at low concentrations Cys bound to Cd^{2+} ions with all 3 functional groups.

It can be suggested that Cys bound to QDs by three groups and SH-NH$_2$-bidentate Cys have diasterioisomeric coordination configurations on QD surface and give rise to the opposite CD signals. We believe that at high concentration of Cys, at which large amount of Cys has bidentate binding mode, CD signal can decrease as a result of superposition of these opposite CD signals.

We have investigated the influence of the chirality of fluorescent semiconductor NPs with different shape on their cellular uptake and cytotoxicity. We demonstrated that L-Cys and D-Cys NPs had mirror-image CD spectra in the region of intrinsic QDs absorption and identical UV–Vis and PL spectra, as well as PL lifetime. However, most importantly, we found that the chirality of the ligands played a crucial role in the biological interaction with living cells. We have clearly demonstrated that the incubation with D-Cys NPs resulted in a higher cytotoxicity and cell accumulation than with L-Cys NPs. This evidently proves an enantiomeric recognition of chiral nanoparticles by living cells.

We have investigated the distancedependent influence of the nanocrystal core on optical activity of a chiral organic molecule, chlorin e6 in hybrid nanostructures based on chiral photosensisiser chlorin e6, and various semiconductor nanocrystals (core/shell CdSe/CdS quantum dots, CdSe/CdS dot-in-rods). It was found that chlorin e6 optical activity increases when chlorin e6 bound with nanocrystal, and this phenomenon depends on NC shell thickness. It was revealed that the optical activity of an organic molecule exhibits a pronounced dependence on the distance between the NC core and the molecule, namely, decreasing the distance between the NC core and molecule leading to increase in the optical activity of the molecule.

We have also demonstrated that Cd-free ZnSe/ZnS QDs can serve as a successful delivery agent and photosensitizer of chlorin e6 in PDT against the Erlich acsite carcinoma cell culture. We applied steady-state and transient spectroscopic optical techniques to show the formation of aqueous solutions of the QD–Ce6 complexes with efficient QD to Ce6 intra-complex photoexcitation energy transfer. By using confocal luminescence microscopy and the trypan blue assay of EAC cells we have shown that QD–Ce6 complexes demonstrate dramatically improved photodynamic cancer cell killing efficiency due to the

synergistic effect of photoexcitation energy transfer from QD to Ce6 and the increased cellular uptake of Ce6 delivered by QDs.

Finally, we have investigated the optical properties of complexes of QDs and chlorin e6 with BSA as a linker. It was demonstrated that BSA significantly improved the optical properties of complexes. BSA passivated the QD surface and in such a way enhanced QD PL quantum yield. In addition, BSA prevented the possible aggregation of Ce6 on QD surface. Thus, we have clearly shown that BSA can significantly enhance the energy transfer efficiency of QD Ce6 complexes. To test these complexes in cancer cells for PDT is one of the aim of our future work.

Since the chirality plays a key role in so many chemical and biological systems, the results obtained in the present work are of significant interest from both fundamental and practical point of view and expected to contribute to the further development of potential applications of optically active nanocrystals, involving optical chiral sensing, detection of various enantiomeric species, enantiospecific separation, chiral catalysis, chiral memory and bio sensing. We believe that these findings may also lay the groundwork for novel approaches to controlling the biological properties and behaviour of man-made chiral nanomaterials in living cells.

7.2   Future work

In the present research we have shown that active mechanism of cell uptake is responsible for enantioselective NPs accumulation. QDs can be internalized in cells through several pathways involving endocytosis receptors and transporters, which could be sensitive to the chirality of nanoparticles. Thus one of our future aims is to determine what is the difference between L- and D-Cys covered NP cell internalization pathways.

We have also demonstrated that BSA significantly improved the optical properties of complexes, passivating the QD surface and in such a way that it enhanced QD PL quantum yield. In addition, BSA prevented the possible aggregation of Ce6 on QD surface

and thus improve the energy transfer efficiency of QD Ce6 complexes. We are planning to test the QD complexes with Ce6 linked by BSA in selected cancer cells for PDT.

In addition, we have performed some preliminary studies which are described in detail below and we would like to continue these investigations in the future.

7.2.1 Investigation of the influence of Cys concentration and pH on CdSe/CdS NB chiral response intensity

We have investigated the influence of cysteine concentration of CD signal intensity of CdSe/CdS spherical QDs. It is of the great interest to study the same effect in the NPs with anisotropic shape. We have performed some preliminary studies of the influence of cysteine concentration on chiral respond intensity of Nano balalaikas (NBs), novel NPs first synthesised in our laboratory (see TEM in Figure 7-1). Unlike with spherical QDs we studied the CD signal intensity lies in the CdS shell absorption region.
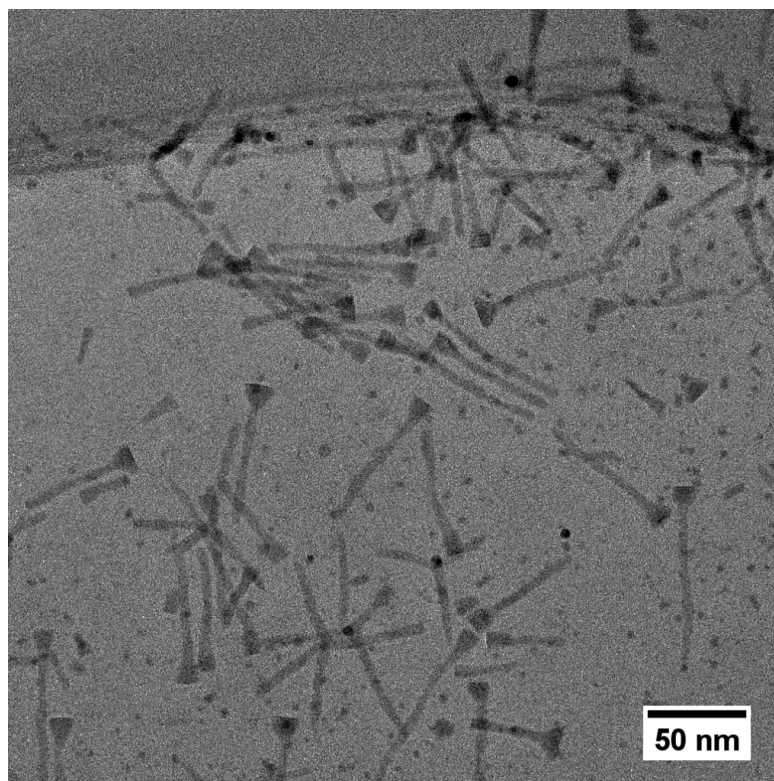
Figure 7-1. TEM images of NBs.

Our preliminary feasibility studies of the influence of Cys concentration on NP CD signal intensity after the ligand exchange procedure were performed with different amount of L-Cys varied from 0.1 to 1.7 mg/ml. The preliminary results are shown in Figure 7-2, A. G-factor was used instead of CD signal to avoid the NP concentration influence. At this concentration range G-factor intensity increased with Cys concentration.

Then an extra amount of Cys was added to the aqueous solution of NBs to obtain the Cys concentration of 11.6, 21.6 and 31.6 mg/ml (Figure 7-2, B). At Cys high concentration NB g-factor decreased with every Cys addition. Consequently, when decreasing the Cys concentration in solution the intensity of the NPs` chiral response increased at the low Cys concentration, then reached a maximum and began to decrease again (Figure 7-2, C).

155
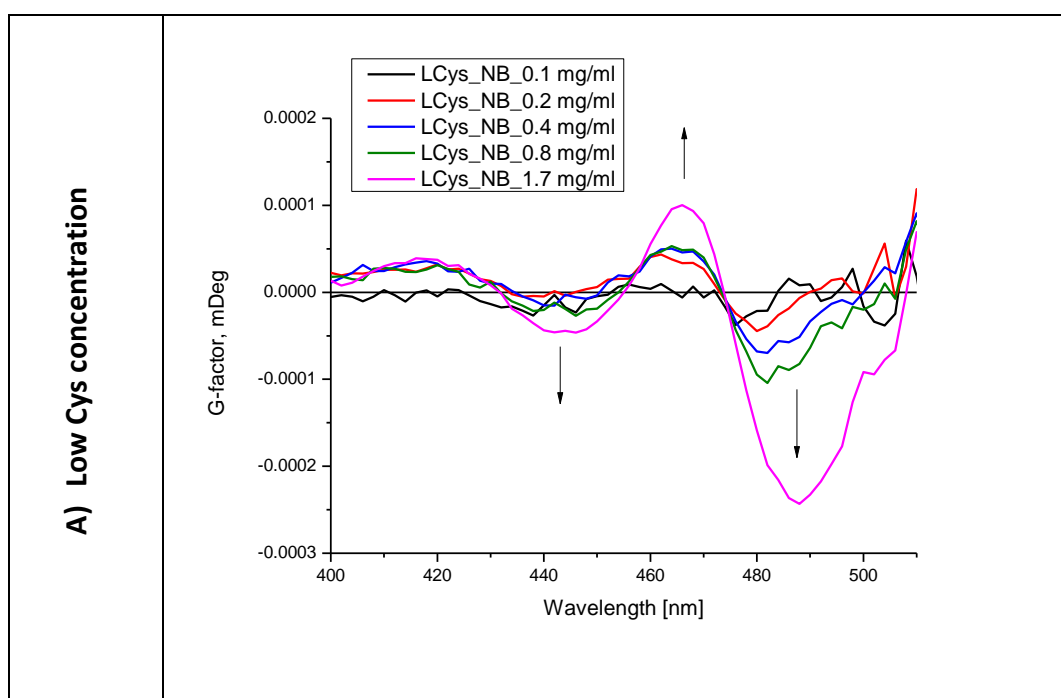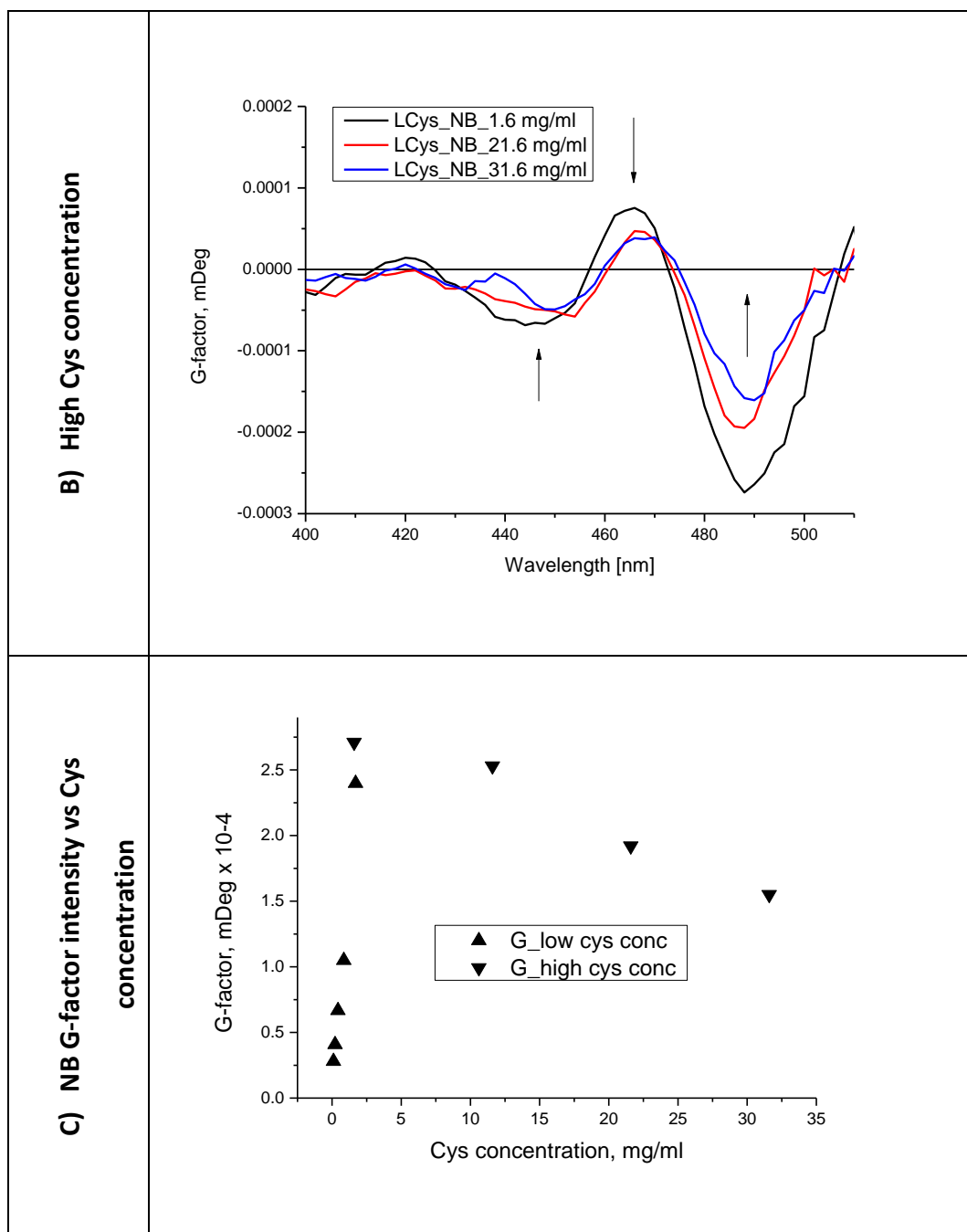
Figure 7-2 The influence of Cys concentration on QD g-factor intensity: G-Factor spectra of L-Cys-NBs aqueous solutions with the L-Cys concentration a) 0.1-1.7 mg/ml and b) 1.6-31.6 mg/ml. c) The dependence of NB G-factor intensity on L-Cys concentration.

A similar result was also obtained on spherical QDs (Figure 7-3), where initially a positive correlation was detected with increasing cysteine concentration until a limiting concentration was reached and the QD G-Factor intensity began to fall. But falling of G-factor began at much lower Cys concentration comparing to NBs.
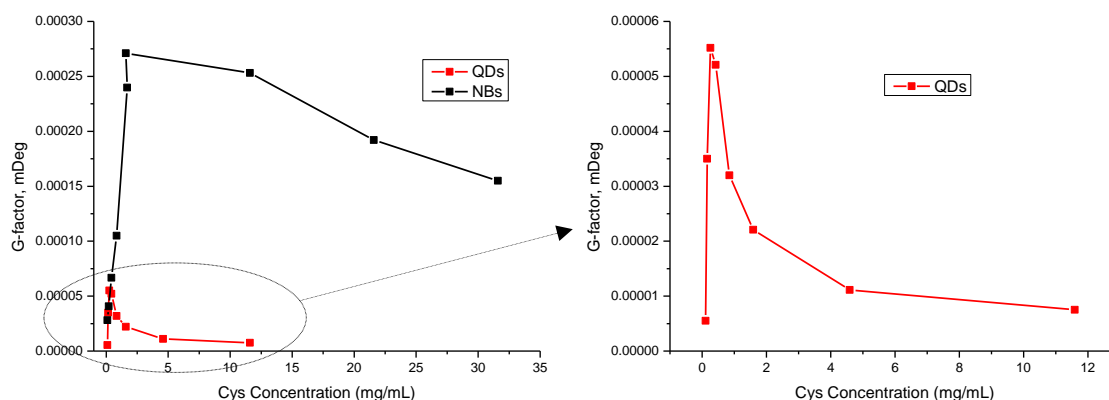
Figure 7-3The dependence of CdSe/CdS NB and spherical *QD G-Factor on Cys*
concentration.

We have also shown that chiral response almost did not change at the pH range of 8.5 - 11.3 (See Figure 7-4), which means that influence of Cys concentration doesn't associate with pH. It worth noting that CD signal drop at the high Cys concentration was reversible (Figure 7-5), which indicates that CD signal decrease was not a result of NP surface destruction.

The decreasing of NP chiral response at high Cys concentration can be caused by pH changes since Cys at large concentration shifted pH of the solution from ≈11 to ≈9. To study if pH influence g-factor of NPs the spectra were registered at different pH (Figure 7-4). NP G-Factor was almost the same at different pH.
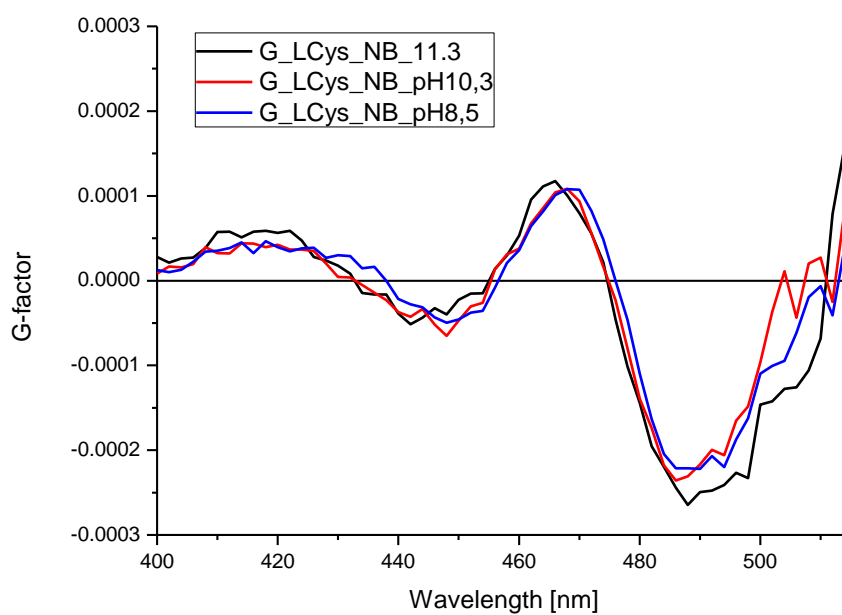
Figure 7-4 NB G-factor spectra at the different pH

Finally, to study if the changes of CD signal was reversible, the excess Cys was washed away with KOH solution using concentrators 2 times. G-factor spectra were registered after each step (Figure 7-5).
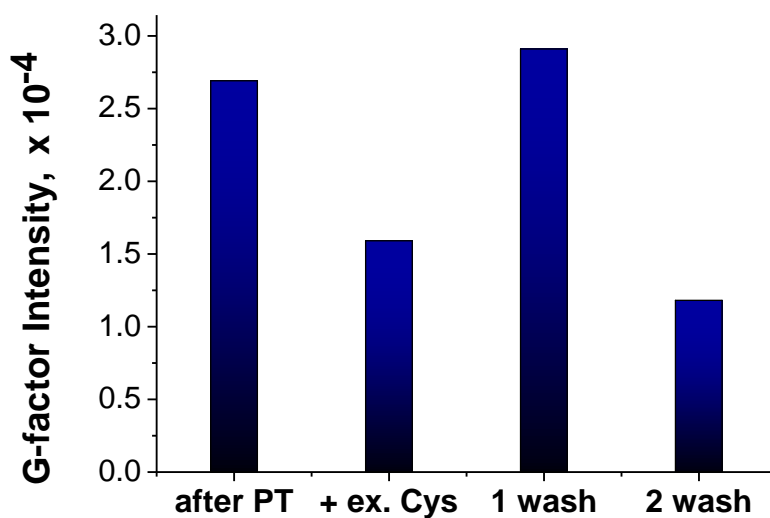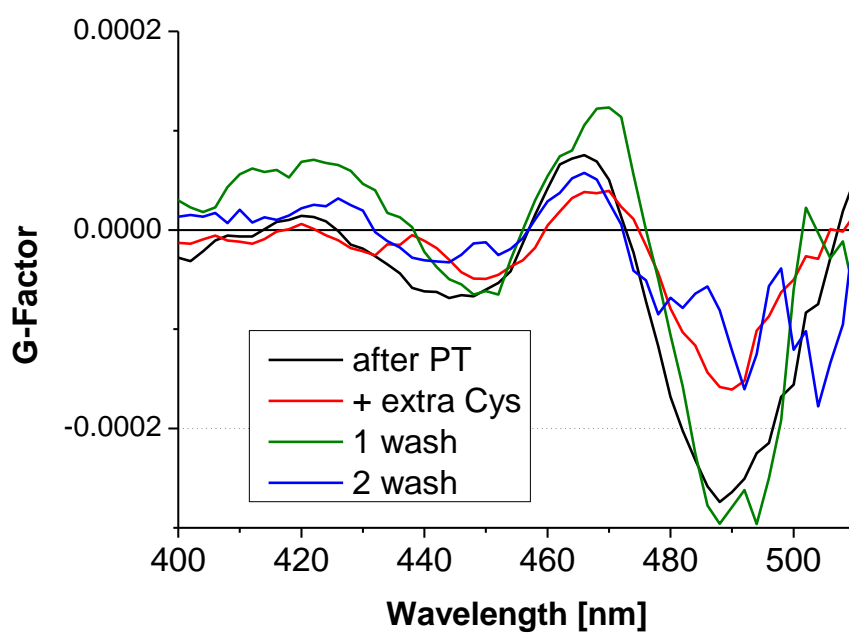
Figure 7-5 NB g-factor spectra after removing the excess of Cys.

G-factor decreased after addition of 30 mg/ml Cys, then increased again after 1st washing (probably, because excess of Cys was washed away) and decreased again after 2nd washing (probably, because Cys concentration became too low). It should be mentioned that G-Factor intensity of spherical CdSe/CdS QDs was measured in the region of CdSe core exciton adsorption region and G-Factor of NBs was measured in the region of CdS shell absorption. It was quite problematic to measure the concentration

159

dependence of G-Factor on NBs at the CdSe core region, because due to the small size of core compared to the shell, the CD signal from the core was very low in spite of G-Factor from the core being an order of magnitude greater than from the shell (Figure 7-6).
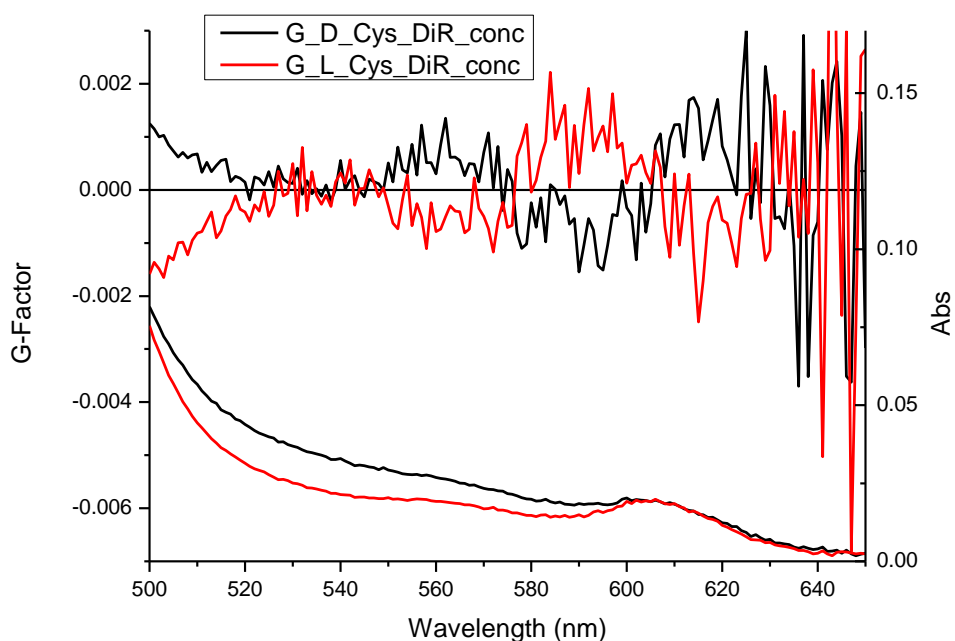
*Figure 7-6 G-*Factor spectra of L- and D-Cys *CdSe/CdS* Dots in Rodsin the exciton region*.

Thus, in our preliminary studies we have shown that CD signal intensity initially increases and then start to decrease after reaching a maximum. The similar effect was observed on spherical QDs. However, in the case of NBs the maximum was reached at much higher concentrations. This phenomenon is not fully understood and additional studies will be required in the future in order to complete this work and explain the behaviour of nanostructures.

8 References.

(1)   Conde, J.; Dias, J. T.; Grazú, V.; Moros, M.; Baptista, P. V; de la Fuente, J. M. Revisiting 30 Years of Biofunctionalization and Surface Chemistry of Inorganic Nanoparticles for Nanomedicine. *Front. Chem.* **2014**, *2*, 48.

(2)   Volkov, Y. Quantum Dots in Nanomedicine: Recent Trends, Advances and Unresolved Issues. *Biochem. Biophys. Res. Commun.* **2015**, *468* (3), 419–427.

(3)   Resch-Genger, U.; Grabolle, M.; Cavaliere-Jaricot, S.; Nitschke, R.; Nann, T. Quantum Dots versus Organic Dyes as Fluorescent Labels. *Nat. Methods* **2008**, *5*, 763.

(4)   Linkov, P.; Krivenkov, V.; Nabiev, I.; Samokhvalov, P. High Quantum Yield CdSe/ZnS/CdS/ZnS Multishell Quantum Dots for Biosensing and Optoelectronic Applications. *Mater. Today Proc.* **2016**, *3* (2), 104–108.

(5)   Baker, D. R.; Kamat, P. V. Tuning the Emission of CdSe Quantum Dots by Controlled Trap Enhancement. *Langmuir* **2010**, *26* (13), 11272–11276.

(6)   Medintz, I. L.; Uyeda, H. T.; Goldman, E. R.; Mattoussi, H. Quantum Dot Bioconjugates for Imaging, Labelling and Sensing. *Nat. Mater.* **2005**, *4* (6), 435–446.

(7)   Brus, L. E. Electron–Electron and Electron-hole Interactions in Small Semiconductor Crystallites: The Size Dependence of the Lowest Excited Electronic State. *J. Chem. Phys.* **1984**, *80* (9), 4403–4409.

(8)   Peng, Z. A.; Peng, X. Formation of High-Quality CdTe, CdSe, and CdS Nanocrystals Using CdO as Precursor. *J. Am. Chem. Soc.* **2001**, *123* (1), 183–184.

(9)   Byun, H.-J.; Lee, J. C.; Yang, H. Solvothermal Synthesis of InP Quantum Dots and Their Enhanced Luminescent Efficiency by Post-Synthetic Treatments. *J. Colloid Interface Sci.* **2011**, *355* (1), 35–41.

(10)   Li, T.-L.; Teng, H. Solution Synthesis of High-Quality CuInS2 Quantum Dots as Sensitizers for TiO2 Photoelectrodes. *J. Mater. Chem.* **2010**, *20* (18), 3656–3664.

(11)   Wang, Q.; Pan, D.; Jiang, S.; Ji, X.; An, L.; Jiang, B. *Luminescent CdSe and CdSe/CdS Core-Shell Nanocrystals Synthesized via a Combination of Solvothermal and Two-Phase Thermal Routes*; 2006; Vol. 118.

(12)   Gerbec, J. A.; Magana, D.; Washington, A.; Strouse, G. F. Microwave-Enhanced Reaction Rates for Nanoparticle Synthesis. *J. Am. Chem. Soc.* **2005**, *127* (45), 15791–

15800.

(13)   Ge, X.; Ni, Y.; Zhang, Z. A Novel Route to Prepare Cadmium Sulfide Nano-Rods. *Radiat. Phys. Chem.* **2002**, *64* (3), 223–227.

(14)   Ni, Y.; Ge, X.; Liu, H.; Xu, X.; Zhang, Z. γ-Irradiation Preparation of CdS Nano-Particles and Their Formation Mechanism in Non-Water System. *Radiat. Phys. Chem.* **2001**, *61* (1), 61–64.

(15)   Murray, C. B.; Norris, D. J.; Bawendi, M. G. Synthesis and Characterization of Nearly Monodisperse CdE (E = Sulfur, Selenium, Tellurium) Semiconductor Nanocrystallites. *J. Am. Chem. Soc.* **1993**, *115* (19), 8706–8715.

(16)   Sinatra, L.; PAN, J.; Bakr, O. *Methods of Synthesizing Monodisperse Colloidal Quantum Dots*; 2017; Vol. 12.

(17)   Sugimoto, T. Preparation of Monodispersed Colloidal Particles. *Adv. Colloid Interface Sci.* **1987**, *28*, 65–108.

(18)   Gallagher, S. A.; Moloney, M. P.; Wojdyla, M.; Quinn, S. J.; Kelly, J. M.; Gun'ko, Y. K. Synthesis and Spectroscopic Studies of Chiral CdSe Quantum Dots. *J. Mater. Chem.* **2010**, *20* (38), 8350–8355.

(19)   Chen, N.; He, Y.; Su, Y.; Li, X.; Huang, Q.; Wang, H.; Zhang, X.; Tai, R.; Fan, C. The Cytotoxicity of Cadmium-Based Quantum Dots. *Biomaterials* **2012**, *33* (5), 1238–1244.

(20)   Su, Y.; Hu, M.; Fan, C.; He, Y.; Li, Q.; Li, W.; Wang, L.; Shen, P.; Huang, Q. The Cytotoxicity of CdTe Quantum Dots and the Relative Contributions from Released Cadmium Ions and Nanoparticle Properties. *Biomaterials* **2010**, *31* (18), 4829–4834.

(21)   Geszke, M.; Murias, M.; Balan, L.; Medjahdi, G.; Korczynski, J.; Moritz, M.; Lulek, J.; Schneider, R. Folic Acid-Conjugated Core/Shell ZnS:Mn/ZnS Quantum Dots as Targeted Probes for Two Photon Fluorescence Imaging of Cancer Cells. *Acta Biomater.* **2011**, *7* (3), 1327–1338.

(22)   Manzoor, K.; Johny, S.; Thomas, D.; Setua, S.; Menon, D.; Nair, S. Bio-Conjugated Luminescent Quantum Dots of Doped ZnS: A Cyto-Friendly System for Targeted Cancer Imaging. *Nanotechnology* **2009**, *20* (6), 65102.

(23)   Yu, J. H.; Kwon, S.-H.; Petrášek, Z.; Park, O. K.; Jun, S. W.; Shin, K.; Choi, M.; Park, Y. Il; Park, K.; Na, H. Bin; et al. High-Resolution Three-Photon Biomedical Imaging

Using Doped ZnS Nanocrystals. *Nat. Mater.* **2013**, *12*, 359.

(24)   Reiss, P.; Protière, M.; Li, L. Core/Shell Semiconductor Nanocrystals. *Small* **2009**, *5* (2), 154–168.

(25)   Talapin, D. V; Koeppe, R.; Götzinger, S.; Kornowski, A.; Lupton, J. M.; Rogach, A. L.; Benson, O.; Feldmann, J.; Weller, H. Highly Emissive Colloidal CdSe/CdS Heterostructures of Mixed Dimensionality. *Nano Lett.* **2003**, *3* (12), 1677–1681.

(26)   Carbone, L.; Nobile, C.; De Giorgi, M.; Sala, F. Della; Morello, G.; Pompa, P.; Hytch, M.; Snoeck, E.; Fiore, A.; Franchini, I. R.; et al. Synthesis and Micrometer-Scale Assembly of Colloidal CdSe/CdS Nanorods Prepared by a Seeded Growth Approach. *Nano Lett.* **2007**, *7* (10), 2942–2950.

(27)   Reiss, P.; Bleuse, J.; Pron, A. Highly Luminescent CdSe/ZnSe Core/Shell Nanocrystals of Low Size Dispersion. *Nano Lett.* **2002**, *2* (7), 781–784.

(28)   Song, K.-K.; Lee, S. Highly Luminescent (ZnSe)ZnS Core-Shell Quantum Dots for Blue to UV Emission: Synthesis and Characterization. *Curr. Appl. Phys.* **2001**, *1* (2), 169–173.

(29)   Haubold, S.; Haase, M.; Kornowski, A.; Weller, H. Strongly Luminescent InP/ZnS Core–Shell Nanoparticles. *ChemPhysChem* **2001**, *2* (5), 331–334.

(30)   Du, F.; Zhang, H.; Du, X.; Zhu, J.; Zhong, X. Controllable Synthesis and Optical Properties of CdS/CdSe Hetero-Nanostructures with Various Dimensionalities. *Mater. Chem. Phys.* **2010**, *121* (1), 118–124.

(31)   Shen, H.; Yuan, H.; Niu, J. Z.; Xu, S.; Zhou, C.; Ma, L.; Li, L. S. Phosphine-Free Synthesis of High-Quality Reverse Type-I ZnSe/CdSe Core with CdS/CdxZn1 −xS/ZnS Multishell Nanocrystals and Their Application for Detection of Human Hepatitis B Surface Antigen. *Nanotechnology* **2011**, *22* (37), 375602.

(32)   Wang, S.; Wang, L.-W. Exciton Dissociation in CdSe/CdTe Heterostructure Nanorods. *J. Phys. Chem. Lett.* **2011**, *2* (1), 1–6.

(33)   Lo, S. S.; Khan, Y.; Jones, M.; Scholes, G. D. Temperature and Solvent Dependence of CdSe/CdTe Heterostructure Nanorod Spectra. *J. Chem. Phys.* **2009**, *131* (8), 84714.

(34)   Huber, D.; Withers, N.; Osinski, M.; Gonzales, G.; Alas, G.; Sandoval, A.; Minetos, C.; Ivanov, S.; A. Smolakov, G.; Senthil, A. *Synthesis and Characterization of Colloidal ZnTe Nanocrystals and ZnTe/ZnSe Quantum Dots*; 2018.

(35) Talapin, D. V; Mekis, I.; Götzinger, S.; Kornowski, A.; Benson, O.; Weller, H. CdSe/CdS/ZnS and CdSe/ZnSe/ZnS Core–Shell–Shell Nanocrystals. *J. Phys. Chem. B* **2004**, *108* (49), 18826–18831.

(36) Green, M.; Williamson, P.; Samalova, M.; Davis, J.; Brovelli, S.; Dobson, P.; Cacialli, F. Synthesis of Type II/Type I CdTe/CdS/ZnS Quantum Dots and Their Use in Cellular Imaging. *J. Mater. Chem.* **2009**, *19* (44), 8341–8346.

(37) Li, J. J.; Wang, Y. A.; Guo, W.; Keay, J. C.; Mishima, T. D.; Johnson, M. B.; Peng, X. Large-Scale Synthesis of Nearly Monodisperse CdSe/CdS Core/Shell Nanocrystals Using Air-Stable Reagents via Successive Ion Layer Adsorption and Reaction. *J. Am. Chem. Soc.* **2003**, *125* (41), 12567–12575.

(38) Talapin, D. V; Nelson, J. H.; Shevchenko, E. V; Aloni, S.; Sadtler, B.; Alivisatos, A. P. Seeded Growth of Highly Luminescent CdSe/CdS Nanoheterostructures with Rod and Tetrapod Morphologies. *Nano Lett.* **2007**, *7* (10), 2951–2959.

(39) Teitelboim, A.; Meir, N.; Kazes, M.; Oron, D. Colloidal Double Quantum Dots. *Acc. Chem. Res.* **2016**, *49* (5), 902–910.

(40) Berova, N.; Bari, L. Di; Pescitelli, G. Application of Electronic Circular Dichroism in Configurational and Conformational Analysis of Organic Compounds. *Chem. Soc. Rev.* **2007**, *36* (6), 914–931.

(41) Martynenko, I. V.; Kuznetsova, V. A.; Litvinov, I. K.; Orlova, A. O.; Maslov, V. G.; Fedorov, A. V.; Dubavik, A.; Purcell-Milton, F.; Gun'ko, Y. K.; Baranov, A. V. Enantioselective Cellular Uptake of Chiral Semiconductor Nanocrystals. *Nanotechnology* **2016**, *27* (7).

(42) Han, C.; Li, H. Chiral Recognition of Amino Acids Based on Cyclodextrin-Capped Quantum Dots. *Small* **2008**, *4* (9), 1344–1350.

(43) Li, Y.; Zhou, Y.; Wang, H.-Y.; Perrett, S.; Zhao, Y.; Tang, Z.; Nie, G. Chirality of Glutathione Surface Coating Affects the Cytotoxicity of Quantum Dots. *Angew. Chemie Int. Ed.* **2011**, *50* (26), 5860–5864.

(44) Milton, F. P.; Govan, J.; Mukhina, M. V; Gun'ko, Y. K. The Chiral Nano-World: Chiroptically Active Quantum Nanostructures. *Nanoscale Horiz.* **2016**, *1* (1), 14–26.

(45) Yeom, J.; Yeom, B.; Chan, H.; Smith, K. W.; Dominguez-Medina, S.; Bahng, J. H.; Zhao, G.; Chang, W.-S.; Chang, S.-J.; Chuvilin, A.; et al. Chiral Templating of Self-Assembling Nanostructures by Circularly Polarized Light. *Nat. Mater.* **2014**, *14*, 66.

(46) Kuzyk, A.; Schreiber, R.; Fan, Z.; Pardatscher, G.; Roller, E.-M.; Högele, A.; Simmel, F. C.; Govorov, A. O.; Liedl, T. DNA-Based Self-Assembly of Chiral Plasmonic Nanostructures with Tailored Optical Response. *Nature* **2012**, *483*, 311.

(47) Moloney, M. P.; Gun'ko, Y. K.; Kelly, J. M. Chiral Highly Luminescent CdS Quantum Dots. *Chem. Commun.* **2007**, No. 38, 3900–3902.

(48) Mukhina, M. V; Maslov, V. G.; Baranov, A. V; Fedorov, A. V; Orlova, A. O.; Purcell-Milton, F.; Govan, J.; Gun'ko, Y. K. Intrinsic Chirality of CdSe/ZnS Quantum Dots and Quantum Rods. *Nano Lett.* **2015**, *15* (5), 2844–2851.

(49) Tohgha, U.; Deol, K. K.; Porter, A. G.; Bartko, S. G.; Choi, J. K.; Leonard, B. M.; Varga, K.; Kubelka, J.; Muller, G.; Balaz, M. Ligand Induced Circular Dichroism and Circularly Polarized Luminescence in CdSe Quantum Dots. *ACS Nano* **2013**, *7* (12), 11094–11102.

(50) Melnikau, D.; Savateeva, D.; Gaponik, N.; Govorov, A. O.; Rakovich, Y. P. Chiroptical Activity in Colloidal Quantum Dots Coated with Achiral Ligands. *Opt. Express* **2016**, *24* (2), A65–A73.

(51) Kim, J.; Lee, J.; Kim, W. Y.; Kim, H.; Lee, S.; Lee, H. C.; Lee, Y. S.; Seo, M.; Kim, S. Y. Induction and Control of Supramolecular Chirality by Light in Self-Assembled Helical Nanostructures. *Nat. Commun.* **2015**, *6*, 6959.

(52) Kawasaki, T.; Araki, Y.; Hatase, K.; Suzuki, K.; Matsumoto, A.; Yokoi, T.; Kubota, Y.; Tatsumi, T.; Soai, K. Helical Mesoporous Silica as an Inorganic Heterogeneous Chiral Trigger for Asymmetric Autocatalysis with Amplification of Enantiomeric Excess. *Chem. Commun.* **2015**, *51* (42), 8742–8744.

(53) Kobayashi, S.; Hamasaki, N.; Suzuki, M.; Kimura, M.; Shirai, H.; Hanabusa, K. Preparation of Helical Transition-Metal Oxide Tubes Using Organogelators as Structure-Directing Agents. *J. Am. Chem. Soc.* **2002**, *124* (23), 6550–6551.

(54) Delclos, T.; Aimé, C.; Pouget, E.; Brizard, A.; Huc, I.; Delville, M.-H.; Oda, R. Individualized Silica Nanohelices and Nanotubes: Tuning Inorganic Nanostructures Using Lipidic Self-Assemblies. *Nano Lett.* **2008**, *8* (7), 1929–1935.

(55) Liu, S.; Han, L.; Duan, Y.; Asahina, S.; Terasaki, O.; Cao, Y.; Liu, B.; Ma, L.; Zhang, J.; Che, S. Synthesis of Chiral TiO2 Nanofibre with Electron Transition-Based Optical Activity. *Nat. Commun.* **2012**, *3*, 1215.

(56) Jin, R.-H.; Yao, D.-D.; Levi, R. (Tamoto). Biomimetic Synthesis of Shaped and Chiral

Silica Entities Templated by Organic Objective Materials. *Chem. – A Eur. J.* **2014**, *20* (24), 7196–7214.

(57)   Ben-Moshe, A.; Maoz, B. M.; Govorov, A. O.; Markovich, G. Chirality and Chiroptical Effects in Inorganic Nanocrystal Systems with Plasmon and Exciton Resonances. *Chem. Soc. Rev.* **2013**, *42* (16), 7028–7041.

(58)   Kuno, J.; Imamura, Y.; Katouda, M.; Tashiro, M.; Kawai, T.; Nakashima, T. *Inversion of Optical Activity in the Synthesis of Mercury Sulfide Nanoparticles: Role of Ligand Coordination*; 2018.

(59)   Horvath, J. D.; Koritnik, A.; Kamakoti, P.; Sholl, D. S.; Gellman, A. J. Enantioselective Separation on a Naturally Chiral Surface. *J. Am. Chem. Soc.* **2004**, *126* (45), 14988–14994.

(60)   Sedghamiz, T.; Bahrami, M.; Ghatee, M. H. Enantiospecific Adsorption of Propranolol Enantiomers on Naturally Chiral Copper Surface: A Molecular Dynamics Simulation Investigation. *Chem. Phys.* **2017**, *487*, 48–58.

(61)   Moloney, M. P.; Govan, J.; Loudon, A.; Mukhina, M.; Gun'ko, Y. K. Preparation of Chiral Quantum Dots. *Nat Protoc* **2015**, *10* (4), 558–573.

(62)   Bloom, B. P.; Graff, B. M.; Ghosh, S.; Beratan, D. N.; Waldeck, D. H. Chirality Control of Electron Transfer in Quantum Dot Assemblies. *J. Am. Chem. Soc.* **2017**, *139* (26), 9038–9043.

(63)   Moloney, M. P.; Govan, J.; Loudon, A.; Mukhina, M.; Gun'ko, Y. K. Preparation of Chiral Quantum Dots. *Nat. Protoc.* **2015**, *10*, 558.

(64)   Moloney, M.; Gallagher, S.; Gun'ko, Y. *Chiral CdTe Quantum Dots*; 2009; Vol. 1241.

(65)   Govan, J. E.; Jan, E.; Querejeta, A.; Kotov, N. A.; Gun'ko, Y. K. Chiral Luminescent CdS Nano-Tetrapods. *Chem. Commun.* **2010**, *46* (33), 6072–6074.

(66)   Schaaff, T. G.; Whetten, R. L. Giant Gold−Glutathione Cluster Compounds: Intense Optical Activity in Metal-Based Transitions. *J. Phys. Chem. B* **2000**, *104* (12), 2630–2641.

(67)   Yao, H.; Miki, K.; Nishida, N.; Sasaki, A.; Kimura, K. Large Optical Activity of Gold Nanocluster Enantiomers Induced by a Pair of Optically Active Penicillamines. *J. Am. Chem. Soc.* **2005**, *127* (44), 15536–15543.

(68)   Gautier, C.; Bürgi, T. Chiral Gold Nanoparticles. *ChemPhysChem* **2009**, *10* (3), 483–492.

(69)   Gautier, C.; Bürgi, T. Chiral N-Isobutyryl-Cysteine Protected Gold Nanoparticles: Preparation, Size Selection, and Optical Activity in the UV–vis and Infrared. *J. Am. Chem. Soc.* **2006**, *128* (34), 11079–11087.

(70)   Xia, Y.; Zhou, Y.; Tang, Z. Chiral Inorganic Nanoparticles: Origin, Optical Properties and Bioapplications. *Nanoscale* **2011**, *3* (4), 1374–1382.

(71)   Fan, Z.; Govorov, A. O. Plasmonic Circular Dichroism of Chiral Metal Nanoparticle Assemblies. *Nano Lett.* **2010**, *10* (7), 2580–2587.

(72)   Govorov, A. O.; Fan, Z.; Hernandez, P.; Slocik, J. M.; Naik, R. R. Theory of Circular Dichroism of Nanomaterials Comprising Chiral Molecules and Nanocrystals: Plasmon Enhancement, Dipole Interactions, and Dielectric Effects. *Nano Lett.* **2010**, *10* (4), 1374–1382.

(73)   Wong, J. I.; Mishra, N.; Xing, G.; Li, M.; Chakrabortty, S.; Sum, T. C.; Shi, Y.; Chan, Y.; Yang, H. Y. Dual Wavelength Electroluminescence from CdSe/CdS Tetrapods. *ACS Nano* **2014**, *8* (3), 2873–2879.

(74)   Mukhina, M. V; Baimuratov, A. S.; Rukhlenko, I. D.; Maslov, V. G.; Purcell Milton, F.; Gun'ko, Y. K.; Baranov, A. V; Fedorov, A. V. Circular Dichroism of Electric-Field-Oriented CdSe/CdS Quantum Dots-in-Rods. *ACS Nano* **2016**, *10* (9), 8904–8909.

(75)   Michalet, X.; Pinaud, F. F.; Bentolila, L. A.; Tsay, J. M.; Doose, S.; Li, J. J.; Sundaresan, G.; Wu, A. M.; Gambhir, S. S.; Weiss, S. Quantum Dots for Live Cells, in Vivo Imaging, and Diagnostics. *Science (80-.).* **2005**, *307* (5709), 538 LP – 544.

(76)   Chern, M.; Kays, J. C.; Bhuckory, S.; Dennis, A. M. Sensing with Photoluminescent Semiconductor Quantum Dots. *Methods Appl. Fluoresc.* **2019**, *7* (1), 12005.

(77)   Mattoussi, H.; Palui, G.; Na, H. Bin. Luminescent Quantum Dots as Platforms for Probing in Vitro and in Vivo Biological Processes. *Adv. Drug Deliv. Rev.* **2012**, *64* (2), 138–166.

(78)   Howes, P. D.; Chandrawati, R.; Stevens, M. M. Colloidal Nanoparticles as Advanced Biological Sensors. *Science (80-.).* **2014**, *346* (6205), 1247390.

(79)   Delgado-Pérez, T.; Bouchet, L. M.; de la Guardia, M.; Galian, R. E.; Pérez-Prieto, J. Sensing Chiral Drugs by Using CdSe/ZnS Nanoparticles Capped with N-Acetyl-L-Cysteine Methyl Ester. *Chem. – A Eur. J.* **2013**, *19* (33), 11068–11076.

(80)   Freeman, R.; Finder, T.; Bahshi, L.; Willner, I. β-Cyclodextrin-Modified CdSe/ZnS Quantum Dots for Sensing and Chiroselective Analysis. *Nano Lett.* **2009**, *9* (5),

2073–2076.

(81)   Zhang, C.; Zhou, Z.; Zhi, X.; Ma, Y.; Wang, K.; Wang, Y.; Zhang, Y.; Fu, H.; Jin, W.; Pan, F.; et al. Insights into the Distinguishing Stress-Induced Cytotoxicity of Chiral Gold Nanoclusters and the Relationship with GSTP1. *Theranostics* **2015**, *5* (2), 134–149.

(82)   Kundelev, E. V; Orlova, A. O.; Maslov, V. G.; Baranov, A. V; Fedorov, A. V. Circular Dichroism Spectroscopy of Complexes of Semiconductor Quantum Dots with Chlorin E6. In *Proc.SPIE*; 2016; Vol. 9884.

(83)   Visheratina, A. K.; Martynenko, I. V; Orlova, A. O.; Maslov, V. G.; Baranov, A. V; Fedorov J. and Deckert, V., A. V. E. D.-B. Energy Transfer Efficiency in Quantum Dot/Chlorin E6 Complexes. In *Clinical and Biomedical Spectroscopy and Imaging IV*; SPIE Proceedings; Optical Society of America: Munich, 2015; Vol. 9537, p 95372C.

(84)   Dougherty, T. J.; Gomer, C. J.; Henderson, B. W.; Jori, G.; Kessel, D.; Korbelik, M.; Moan, J.; Peng, Q. Photodynamic Therapy. *JNCI J. Natl. Cancer Inst.* **1998**, *90* (12), 889–905.

(85)   Thakor, A. S.; Gambhir, S. S. Nanooncology: The Future of Cancer Diagnosis and Therapy. *CA. Cancer J. Clin.* **2013**, *63* (6), 395–418.

(86)   Sharman, W. M.; Allen, C. M.; van Lier, J. E. Photodynamic Therapeutics: Basic Principles and Clinical Applications. *Drug Discov. Today* **1999**, *4* (11), 507–517.

(87)   Biju, V.; Mundayoor, S.; Omkumar, R. V; Anas, A.; Ishikawa, M. Bioconjugated Quantum Dots for Cancer Research: Present Status, Prospects and Remaining Issues. *Biotechnol. Adv.* **2010**, *28* (2), 199–213.

(88)   Martynenko, I.; Visheratina, A.; Kuznetsova, V.; Orlova, A.; Maslov, V.; Fedorov, A.; Baranov, A. Quantum Dot-Tetrapyrrole Complexes as Photodynamic Therapy Agents. In *Optics InfoBase Conference Papers*; 2014.

(89)   Tsay, J. M.; Trzoss, M.; Shi, L.; Kong, X.; Selke, M.; Jung, M. E.; Weiss, S. Singlet Oxygen Production by Peptide-Coated Quantum Dot–Photosensitizer Conjugates. *J. Am. Chem. Soc.* **2007**, *129* (21), 6865–6871.

(90)   Ma, J.; Chen, J.-Y.; Idowu, M.; Nyokong, T. Generation of Singlet Oxygen via the Composites of Water-Soluble Thiol-Capped CdTe Quantum DotsSulfonated Aluminum Phthalocyanines. *J. Phys. Chem. B* **2008**, *112* (15), 4465–4469.

(91)   Ishii, K. Functional Singlet Oxygen Generators Based on Phthalocyanines. *Coord.*

Chem. Rev. **2012**, *256* (15), 1556–1568.

(92) Duong, H. D.; Rhee, J. Il. Singlet Oxygen Production by Fluorescence Resonance Energy Transfer (FRET) from Green and Orange CdSe/ZnS QDs to Protoporphyrin IX (PpIX). *Chem. Phys. Lett.* **2011**, *501* (4), 496–501.

(93) Fowley, C.; Nomikou, N.; McHale, A. P.; McCarron, P. A.; McCaughan, B.; Callan, J. F. Water Soluble Quantum Dots as Hydrophilic Carriers and Two-Photon Excited Energy Donors in Photodynamic Therapy. *J. Mater. Chem.* **2012**, *22* (13), 6456–6462.

(94) Rakovich, A.; Savateeva, D.; Rakovich, T.; Donegan, J. F.; Rakovich, Y. P.; Kelly, V.; Lesnyak, V.; Eychmüller, A. CdTe Quantum Dot/Dye Hybrid System as Photosensitizer for Photodynamic Therapy. *Nanoscale Res. Lett.* **2010**, *5* (4), 753.

(95) Li, L.; Zhao, J.-F.; Won, N.; Jin, H.; Kim, S.; Chen, J.-Y. Quantum Dot-Aluminum Phthalocyanine Conjugates Perform Photodynamic Reactions to Kill Cancer Cells via Fluorescence Resonance Energy Transfer. *Nanoscale Res. Lett.* **2012**, *7* (1), 386.

(96) Chan, A. L.; Juarez, M.; Allen, R.; Volz, W.; Albertson, T. Pharmacokinetics and Clinical Effects of Mono-l-Aspartyl Chlorin E6 (NPe6) Photodynamic Therapy in Adult Patients with Primary or Secondary Cancer of the Skin and Mucosal Surfaces. *Photodermatol. Photoimmunol. Photomed.* **2005**, *21* (2), 72–78.

(97) Yaghini, E.; Seifalian, A. M.; MacRobert, A. J. Quantum Dots and Their Potential Biomedical Applications in Photosensitization for Photodynamic Therapy. *Nanomedicine* **2009**, *4* (3), 353–363.

(98) Charron, G.; Stuchinskaya, T.; Edwards, D. R.; Russell, D. A.; Nann, T. Insights into the Mechanism of Quantum Dot-Sensitized Singlet Oxygen Production for Photodynamic Therapy. *J. Phys. Chem. C* **2012**, *116* (16), 9334–9342.

(99) Samia, A. C. S.; Dayal, S.; Burda, C. Quantum Dot-Based Energy Transfer: Perspectives and Potential for Applications in Photodynamic Therapy. *Photochem. Photobiol.* **2006**, *82* (3), 617–625.

(100) Chen, Y.; Vela, J.; Htoon, H.; Casson, J. L.; Werder, D. J.; Bussian, D. A.; Klimov, V. I.; Hollingsworth, J. A. "Giant" Multishell CdSe Nanocrystal Quantum Dots with Suppressed Blinking. *J. Am. Chem. Soc.* **2008**, *130* (15), 5026–5027.

(101) Mahler, B.; Spinicelli, P.; Buil, S.; Quelin, X.; Hermier, J.-P.; Dubertret, B. Towards Non-Blinking Colloidal Quantum Dots. *Nat. Mater.* **2008**, *7*, 659.

(102) Yu, W. W.; Qu, L.; Guo, W.; Peng, X. Experimental Determination of the Extinction Coefficient of CdTe, CdSe, and CdS Nanocrystals. *Chem. Mater.* **2003**, *15* (14), 2854–2860.

(103) Mukhina, M. V; Maslov, V. G.; Korsakov, I. V; Purcell Milton, F.; Loudon, A.; Baranov, A. V; Fedorov, A. V; Gun'ko, Y. K. Optically Active II-VI Semiconductor Nanocrystals via Chiral Phase Transfer. *MRS Proc.* **2015**, *1793*, 27–33.

(104) McCloy, R. A.; Rogers, S.; Caldon, C. E.; Lorca, T.; Castro, A.; Burgess, A. Partial Inhibition of Cdk1 in G2 Phase Overrides the SAC and Decouples Mitotic Events. *Cell Cycle* **2014**, *13* (9), 1400–1412.

(105) Chen, H.-S.; Lo, B.; Hwang, J.-Y.; Chang, G.-Y.; Chen, C.-M.; Tasi, S.-J.; Wang, S.-J. J. Colloidal ZnSe, ZnSe/ZnS, and ZnSe/ZnSeS Quantum Dots Synthesized from ZnO. *J. Phys. Chem. B* **2004**, *108* (44), 17119–17123.

(106) Kramer, I. J.; Sargent, E. H. Colloidal Quantum Dot Photovoltaics: A Path Forward. *ACS Nano* **2011**, *5* (11), 8506–8514.

(107) Shields, A. J. Semiconductor Quantum Light Sources. *Nat. Photonics* **2007**, *1*, 215.

(108) Towe, E.; Pan, D. Semiconductor Quantum-Dot Nanostructures: Their Application in a New Class of Infrared Photodetectors. *IEEE J. Sel. Top. Quantum Electron.* **2000**, *6* (3), 408–421.

(109) Purcell-Milton, F.; Gun'ko, Y. K. Quantum Dots for Luminescent Solar Concentrators. *J. Mater. Chem.* **2012**, *22* (33), 16687–16697.

(110) Chan, Y.; Steckel, J. S.; Snee, P. T.; Caruge, J.-M.; Hodgkiss, J. M.; Nocera, D. G.; Bawendi, M. G. Blue Semiconductor Nanocrystal Laser. *Appl. Phys. Lett.* **2005**, *86* (7), 73102.

(111) Visheratina, A. K.; Purcell-Milton, F.; Serrano-García, R.; Kuznetsova, V. A.; Orlova, A. O.; Fedorov, A. V.; Baranov, A. V.; Gun'ko, Y. K. Chiral Recognition of Optically Active $CoFe_2O_4$ magnetic Nanoparticles by CdSe/CdS Quantum Dots Stabilised with Chiral Ligands. *J. Mater. Chem. C* **2017**, *5* (7).

(112) Mukhina, M. V; Korsakov, I. V; Maslov, V. G.; Purcell-Milton, F.; Govan, J.; Baranov, A. V; Fedorov, A. V; Gun'ko, Y. K. Molecular Recognition of Biomolecules by Chiral CdSe Quantum Dots. *Sci. Rep.* **2016**, *6*, 24177.

(113) Shah, E.; Soni, H. P. Inducing Chirality on ZnS Nanoparticles for Asymmetric Aldol Condensation Reactions. *RSC Adv.* **2013**, *3* (38), 17453–17461.

(114) Rukhlenko, I. D.; Tepliakov, N. V; Baimuratov, A. S.; Andronaki, S. A.; Gun'ko, Y. K.; Baranov, A. V; Fedorov, A. V. Completely Chiral Optical Force for Enantioseparation. *Sci. Rep.* **2016**, *6*, 36884.

(115) Bloom, B. P.; Kiran, V.; Varade, V.; Naaman, R.; Waldeck, D. H. Spin Selective Charge Transport through Cysteine Capped CdSe Quantum Dots. *Nano Lett.* **2016**, *16* (7), 4583–4589.

(116) Lobanov, S. V; Weiss, T.; Gippius, N. A.; Tikhodeev, S. G.; Kulakovskii, V. D.; Konishi, K.; Kuwata-Gonokami, M. Polarization Control of Quantum Dot Emission by Chiral Photonic Crystal Slabs. *Opt. Lett.* **2015**, *40* (7), 1528–1531.

(117) Konishi, K.; Nomura, M.; Kumagai, N.; Iwamoto, S.; Arakawa, Y.; Kuwata-Gonokami, M. Circularly Polarized Light Emission from Semiconductor Planar Chiral Nanostructures. *Phys. Rev. Lett.* **2011**, *106* (5), 57402.

(118) Ben-Moshe, A.; Govorov, A. O.; Markovich, G. Enantioselective Synthesis of Intrinsically Chiral Mercury Sulfide Nanocrystals. *Angew. Chemie Int. Ed.* **2013**, *52* (4), 1275–1279.

(119) Baimuratov, A. S.; Rukhlenko, I. D.; Gun'ko, Y. K.; Baranov, A. V; Fedorov, A. V. Dislocation-Induced Chirality of Semiconductor Nanocrystals. *Nano Lett.* **2015**, *15* (3), 1710–1715.

(120) Elliott, S. D.; Moloney, M. P.; Gun'ko, Y. K. Chiral Shells and Achiral Cores in CdS Quantum Dots. *Nano Lett.* **2008**, *8* (8), 2452–2457.

(121) Nakashima, T.; Kobayashi, Y.; Kawai, T. Optical Activity and Chiral Memory of Thiol-Capped CdTe Nanocrystals. *J. Am. Chem. Soc.* **2009**, *131* (30), 10342–10343.

(122) Zhou, R.; Wei, K.-Y.; Zhao, J.-S.; Jiang, Y.-B. Alternative Chiral Thiols for Preparation of Chiral CdS Quantum Dots Covered Immediately by Achiral Thiols. *Chem. Commun.* **2011**, *47* (22), 6362–6364.

(123) Zhou, Y.; Marson, R. L.; van Anders, G.; Zhu, J.; Ma, G.; Ercius, P.; Sun, K.; Yeom, B.; Glotzer, S. C.; Kotov, N. A. Biomimetic Hierarchical Assembly of Helical Supraparticles from Chiral Nanoparticles. *ACS Nano* **2016**, *10* (3), 3248–3256.

(124) Zhu, Z.; Guo, J.; Liu, W.; Li, Z.; Han, B.; Zhang, W.; Tang, Z. Controllable Optical Activity of Gold Nanorod and Chiral Quantum Dot Assemblies. *Angew. Chemie Int. Ed.* **2013**, *52* (51), 13571–13575.

(125) Tohgha, U.; Varga, K.; Balaz, M. Achiral CdSe Quantum Dots Exhibit Optical Activity

in the Visible Region upon Post-Synthetic Ligand Exchange with d- or l-Cysteine. *Chem. Commun.* **2013**, *49* (18), 1844–1846.

(126) Zhou, Y.; Yang, M.; Sun, K.; Tang, Z.; Kotov, N. A. Similar Topological Origin of Chiral Centers in Organic and Nanoscale Inorganic Structures: Effect of Stabilizer Chirality on Optical Isomerism and Growth of CdTe Nanocrystals. *J. Am. Chem. Soc.* **2010**, *132* (17), 6006–6013.

(127) Zhou, Y.; Zhu, Z.; Huang, W.; Liu, W.; Wu, S.; Liu, X.; Gao, Y.; Zhang, W.; Tang, Z. *Optical Coupling Between Chiral Biomolecules and Semiconductor Nanoparticles: Size-Dependent Circular Dichroism Absorption*; 2011; Vol. 50.

(128) Choi, J. K.; Haynie, B. E.; Tohgha, U.; Pap, L.; Elliott, K. W.; Leonard, B. M.; Dzyuba, S. V; Varga, K.; Kubelka, J.; Balaz, M. Chirality Inversion of CdSe and CdS Quantum Dots without Changing the Stereochemistry of the Capping Ligand. *ACS Nano* **2016**, *10* (3), 3809–3815.

(129) Ben-Moshe, A.; Teitelboim, A.; Oron, D.; Markovich, G. Probing the Interaction of Quantum Dots with Chiral Capping Molecules Using Circular Dichroism Spectroscopy. *Nano Lett.* **2016**, *16* (12), 7467–7473.

(130) Ben Moshe, A.; Szwarcman, D.; Markovich, G. Size Dependence of Chiroptical Activity in Colloidal Quantum Dots. *ACS Nano* **2011**, *5* (11), 9034–9043.

(131) Wuister, S. F.; de Mello Donegá, C.; Meijerink, A. Influence of Thiol Capping on the Exciton Luminescence and Decay Kinetics of CdTe and CdSe Quantum Dots. *J. Phys. Chem. B* **2004**, *108* (45), 17393–17397.

(132) Liang, Y.; Thorne, J. E.; Parkinson, B. A. Controlling the Electronic Coupling between CdSe Quantum Dots and Thiol Capping Ligands via PH and Ligand Selection. *Langmuir* **2012**, *28* (30), 11072–11077.

(133) Chen, O.; Zhao, J.; Chauhan, V. P.; Cui, J.; Wong, C.; Harris, D. K.; Wei, H.; Han, H.-S.; Fukumura, D.; Jain, R. K.; et al. Compact High-Quality CdSe–CdS Core–Shell Nanocrystals with Narrow Emission Linewidths and Suppressed Blinking. *Nat. Mater.* **2013**, *12*, 445.

(134) Ristov, M.; Sinadinovski, G.; Grozdanov, I.; MITRESKI, M. *Chemical Deposition of TIN(II) Sulphide Thin Films*; 1989; Vol. 173.

(135) Pal, B. N.; Ghosh, Y.; Brovelli, S.; Laocharoensuk, R.; Klimov, V. I.; Hollingsworth, J. A.; Htoon, H. 'Giant' CdSe/CdS Core/Shell Nanocrystal Quantum Dots As Efficient

Electroluminescent Materials: Strong Influence of Shell Thickness on Light-Emitting Diode Performance. *Nano Lett.* **2012**, *12* (1), 331–336.

(136) Peterson, M. D.; Cass, L. C.; Harris, R. D.; Edme, K.; Sung, K.; Weiss, E. A. The Role of Ligands in Determining the Exciton Relaxation Dynamics in Semiconductor Quantum Dots. *Annu. Rev. Phys. Chem.* **2014**, *65* (1), 317–339.

(137) Kruchinin, S.; Fedorov, A.; Baranov, A.; Perova, T.; Berwick, K. *Resonant Energy Transfer in Quantum Dots: Frequency-Domain Luminescent Spectroscopy*; 2008; Vol. 78.

(138) Ma, W.; Xu, L.; de Moura, A. F.; Wu, X.; Kuang, H.; Xu, C.; Kotov, N. A. Chiral Inorganic Nanostructures. *Chem. Rev.* **2017**, *117* (12), 8041–8093.

(139) Govan, J.; Gun'ko, Y. K. Recent Progress in Chiral Inorganic Nanostructures. In *Nanoscience: Volume 3*; The Royal Society of Chemistry, 2016; Vol. 3, pp 1–30.

(140) Kumar, J.; Thomas, K. G.; Liz-Marzán, L. M. Nanoscale Chirality in Metal and Semiconductor Nanoparticles. *Chem. Commun.* **2016**, *52* (85), 12555–12569.

(141) Carrillo-Carrión, C.; Cárdenas, S.; Simonet, B. M.; Valcárcel, M. Selective Quantification of Carnitine Enantiomers Using Chiral Cysteine-Capped CdSe(ZnS) Quantum Dots. *Anal. Chem.* **2009**, *81* (12), 4730–4733.

(142) Ghasemi, F.; Hormozi-Nezhad, M. R.; Mahmoudi, M. Time-Resolved Visual Chiral Discrimination of Cysteine Using Unmodified CdTe Quantum Dots. *Sci. Rep.* **2017**, *7* (1), 890.

(143) Kuznetsova, V. A.; Visheratina, A. K.; Ryan, A.; Martynenko, I. V; Loudon, A.; Maguire, C. M.; Purcell-Milton, F.; Orlova, A. O.; Baranov, A. V; Fedorov, A. V; et al. Enantioselective Cytotoxicity of ZnS:Mn Quantum Dots in A549 Cells. *Chirality* **2017**, *29* (8), 403–408.

(144) Zhu, F.; Li, X.; Li, Y.; Yan, M.; Liu, S. Enantioselective Circular Dichroism Sensing of Cysteine and Glutathione with Gold Nanorods. *Anal. Chem.* **2015**, *87* (1), 357–361.

(145) Hou, X.; Ke, C.; Bruns, C. J.; McGonigal, P. R.; Pettman, R. B.; Stoddart, J. F. Tunable Solid-State Fluorescent Materials for Supramolecular Encryption. *Nat. Commun.* **2015**, *6*, 6884.

(146) Li, W.-S.; Shen, Y.; Chen, Z.-J.; Cui, Q.; Li, S.-S.; Chen, L.-J. Demonstration of Patterned Polymer-Stabilized Cholesteric Liquid Crystal Textures for Anti-Counterfeiting Two-Dimensional Barcodes. *Appl. Opt.* **2017**, *56* (3), 601–606.

(147) Nguyen, T.-D.; Hamad, W. Y.; MacLachlan, M. J. CdS Quantum Dots Encapsulated in Chiral Nematic Mesoporous Silica: New Iridescent and Luminescent Materials. *Adv. Funct. Mater.* **2014**, *24* (6), 777{\textendash}783.

(148) Hu, T.; Isaacoff, B. P.; Bahng, J. H.; Hao, C.; Zhou, Y.; Zhu, J.; Li, X.; Wang, Z.; Liu, S.; Xu, C.; et al. Self-Organization of Plasmonic and Excitonic Nanoparticles into Resonant Chiral Supraparticle Assemblies. *Nano Lett.* **2014**, *14* (12), 6799–6810.

(149) Naaman, R.; Waldeck, D. H. Spintronics and Chirality: Spin Selectivity in Electron Transport Through Chiral Molecules. *Annu. Rev. Phys. Chem.* **2015**, *66* (1), 263–281.

(150) Purcell-Milton, F.; Visheratina, A. K.; Kuznetsova, V. A.; Ryan, A.; Orlova, A. O.; Gun'ko, Y. K. Impact of Shell Thickness on Photoluminescence and Optical Activity in Chiral CdSe/CdS Core/Shell Quantum Dots. *ACS Nano* **2017**, acsnano.7b04199.

(151) Martynenko, I. V.; Baimuratov, A. S.; Osipova, V. A.; Kuznetsova, V. A.; Purcell-Milton, F.; Rukhlenko, I. D.; Fedorov, A. V.; Gun'Ko, Y. K.; Resch-Genger, U.; Baranov, A. V. Excitation Energy Dependence of the Photoluminescence Quantum Yield of Core/Shell CdSe/CdS Quantum Dots and Correlation with Circular Dichroism. *Chem. Mater.* **2018**, *30* (2).

(152) Ben Moshe, A.; Markovich, G.; Tang Tang, Z. Optically Active and Chiral Semiconductor Nanocrystals. In *Chiral Nanomaterials: Preparation, Properties and Applications*; 2017; pp 85–98.

(153) Varga, K.; Tannir, S.; Haynie, B. E.; Leonard, B. M.; Dzyuba, S. V; Kubelka, J.; Balaz, M. CdSe Quantum Dots Functionalized with Chiral, Thiol-Free Carboxylic Acids: Unraveling Structural Requirements for Ligand-Induced Chirality. *ACS Nano* **2017**, *11* (10), 9846–9853.

(154) Cheng, J.; Hao, J.; Liu, H.; Li, J.; Li, J.; Zhu, X.; Lin, X.; Wang, K.; He, T. Optically Active CdSe-Dot/CdS-Rod Nanocrystals with Induced Chirality and Circularly Polarized Luminescence. *ACS Nano* **2018**, *12* (6), 5341–5350.

(155) Puri, M.; Ferry, V. E. Circular Dichroism of CdSe Nanocrystals Bound by Chiral Carboxylic Acids. *ACS Nano* **2017**, *11* (12), 12240–12246.

(156) Tsay, J. M.; Doose, S.; Pinaud, F.; Weiss, S. Enhancing the Photoluminescence of Peptide-Coated Nanocrystals with Shell Composition and UV Irradiation. *J. Phys. Chem. B* **2005**, *109* (5), 1669–1674.

(157) Harris, R. D.; Amin, V. A.; Lau, B.; Weiss, E. A. Role of Interligand Coupling in

Determining the Interfacial Electronic Structure of Colloidal CdS Quantum Dots. *ACS Nano* **2016**, *10* (1), 1395–1403.

(158) Mukhina, M. V; Maslov, V. G.; Baranov, A. V; Artemyev, M. V; Orlova, A. O.; Fedorov, A. V. Anisotropy of Optical Transitions in Ordered Ensemble of CdSe Quantum Rods. *Opt. Lett.* **2013**, *38* (17), 3426–3428.

(159) Gao, X.; Zhang, X.; Deng, K.; Han, B.; Zhao, L.; Wu, M.; Shi, L.; Lv, J.; Tang, Z. Excitonic Circular Dichroism of Chiral Quantum Rods. *J. Am. Chem. Soc.* **2017**, *139* (25), 8734–8739.

(160) Frederick, M. T.; Amin, V. A.; Swenson, N. K.; Ho, A. Y.; Weiss, E. A. Control of Exciton Confinement in Quantum Dot–Organic Complexes through Energetic Alignment of Interfacial Orbitals. *Nano Lett.* **2013**, *13* (1), 287–292.

(161) Li, T.; Park, H. G.; Lee, H.-S.; Choi, S.-H. Circular Dichroism Study of Chiral Biomolecules Conjugated with Silver Nanoparticles. *Nanotechnology* **2004**, *15* (10), S660–S663.

(162) Gautier, C.; Bürgi, T. Chiral Inversion of Gold Nanoparticles. *J. Am. Chem. Soc.* **2008**, *130* (22), 7077–7084.

(163) Kane-Maguire, L. A. P.; Riley, P. J. HIGH FIELD NMR STUDY OF THE BINDING OF LEAD(II) TO CYSTEINE AND GLUTATHIONE. *J. Coord. Chem.* **1993**, *28* (2), 105–120.

(164) Cistola, D.; M Small, D.; Hamilton, J. *Ionization Behavior of Aqueous Short-Chain Carboxylic Acids: A Carbon-I3 NMR Study*; 1982; Vol. 23.

(165) Abraham, A.; Mihaliuk, E.; Kumar, B.; Legleiter, J.; Gullion, T. Solid-State NMR Study of Cysteine on Gold Nanoparticles. *J. Phys. Chem. C* **2010**, *114* (42), 18109–18114.

(166) Akbarzadeh, M.; Moosavi-Movahedi, Z.; Shockravi, A.; Jafari, R.; Nazari, K.; Sheibani, N.; Moosavi-Movahedi, A. A. Metallo-Vesicular Catalysis: A Mixture of Vesicular Cysteine/Iron Mediates Oxidative PH Switchable Catalysis. *J. Mol. Catal. A Chem.* **2016**, *424*, 181–193.

(167) Contreras-García, J.; Boto, R.; Izquierdo-Ruiz, F.; Reva, I.; Woller, T.; Alonso, M. A Benchmark for the Non-Covalent Interaction (NCI) Index Or… Is It Really All in the Geometry? *Theor. Chem. Acc.* **2016**, *135*.

(168) Johnson, E. R.; Keinan, S.; Mori-Sánchez, P.; Contreras-García, J.; Cohen, A. J.; Yang, W. Revealing Noncovalent Interactions. *J. Am. Chem. Soc.* **2010**, *132* (18), 6498–6506.

(169) Zhang, M.; Qing, G.; Sun, T. Chiral Biointerface Materials. *Chem. Soc. Rev.* **2012**, *41* (5), 1972–1984.

(170) Smith, A. M.; Nie, S. Chemical Analysis and Cellular Imaging with Quantum Dots. *Analyst* **2004**, *129* (8), 672–677.

(171) Abrams, B.; Dubrovsky, T. *Quantum Dots in Flow Cytometry*; 2007; Vol. 374.

(172) Lee, H.; Kim, C.; Lee, D.; Park, J. H.; Searson, P. C.; Lee, K. H. Optical Coding of Fusion Genes Using Multicolor Quantum Dots for Prostate Cancer Diagnosis. *Int. J. Nanomedicine* **2017**, *12*, 4397–4407.

(173) Hong, H. J.; Koom, W. S.; Koh, W.-G. Cell Microarray Technologies for High-Throughput Cell-Based Biosensors. *Sensors (Basel).* **2017**, *17* (6), 1293.

(174) Shamirian, A.; Ghai, A.; Snee, P. T. QD-Based FRET Probes at a Glance. *Sensors (Basel).* **2015**, *15* (6), 13028–13051.

(175) Francis, J. E.; Mason, D.; Lévy, R. Evaluation of Quantum Dot Conjugated Antibodies for Immunofluorescent Labelling of Cellular Targets. *Beilstein J. Nanotechnol.* **2017**, *8*, 1238–1249.

(176) Purcell-Milton, F.; Visheratina, A. K.; Kuznetsova, V. A.; Ryan, A.; Orlova, A. O.; Gun'ko, Y. K. Impact of Shell Thickness on Photoluminescence and Optical Activity in Chiral CdSe/CdS Core/Shell Quantum Dots. *ACS Nano* **2017**.

(177) Kuznetsova, V. A.; Visheratina, A. K.; Ryan, A.; Martynenko, I. V.; Loudon, A.; Maguire, C. M.; Purcell-Milton, F.; Orlova, A. O.; Baranov, A. V.; Fedorov, A. V.; et al. Enantioselective Cytotoxicity of ZnS:Mn Quantum Dots in A549 Cells. *Chirality* **2017**.

(178) Lewinski, N.; Colvin, V.; Drezek, R. Cytotoxicity of Nanoparticles. *Small* **2008**, *4* (1), 26–49.

(179) Nel, A.; Xia, T.; Mädler, L.; Li, N. Toxic Potential of Materials at the Nanolevel. *Science (80-.).* **2006**, *311* (5761), 622 LP – 627.

(180) Wen, Y.; Song, W.; An, L.; Liu, Y.; Wang, Y.; Yang, Y. Activation of Porphyrin Photosensitizers by Semiconductor Quantum Dots via Two-Photon Excitation. *Appl. Phys. Lett.* **2009**, *95* (14), 143702.

(181) Qi, Z.-D.; Li, D.-W.; Jiang, P.; Jiang, F.-L.; Li, Y.-S.; Liu, Y.; Wong, W.-K.; Cheah, K.-W. Biocompatible CdSe Quantum Dot-Based Photosensitizer under Two-Photon Excitation for Photodynamic Therapy. *J. Mater. Chem.* **2011**, *21* (8), 2455–2458.

(182) Padilha, L. A.; Bae, W. K.; Klimov, V. I.; Pietryga, J. M.; Schaller, R. D. Response of Semiconductor Nanocrystals to Extremely Energetic Excitation. *Nano Lett.* **2013**, *13* (3), 925–932.

(183) Lawrence, W. G.; Thacker, S.; Palamakumbura, S.; Riley, K. J.; Nagarkar, V. V. Quantum Dot-Organic Polymer Composite Materials for Radiation Detection and Imaging. *IEEE Trans. Nucl. Sci.* **2012**, *59* (1), 215–221.

(184) Probst, C. E.; Zrazhevskiy, P.; Bagalkot, V.; Gao, X. Quantum Dots as a Platform for Nanoparticle Drug Delivery Vehicle Design. *Adv. Drug Deliv. Rev.* **2013**, *65* (5), 703–718.

(185) Thomas, A.; Nair, P. V; George Thomas, K. InP Quantum Dots: An Environmentally Friendly Material with Resonance Energy Transfer Requisites. *J. Phys. Chem. C* **2014**, *118* (7), 3838–3845.

(186) Clapp, A. R.; Medintz, I. L.; Mauro, J. M.; Fisher, B. R.; Bawendi, M. G.; Mattoussi, H. Fluorescence Resonance Energy Transfer Between Quantum Dot Donors and Dye-Labeled Protein Acceptors. *J. Am. Chem. Soc.* **2004**, *126* (1), 301–310.

(187) Dworak, L.; Matylitsky, V. V; Ren, T.; Basché, T.; Wachtveitl, J. Acceptor Concentration Dependence of Förster Resonance Energy Transfer Dynamics in Dye–Quantum Dot Complexes. *J. Phys. Chem. C* **2014**, *118* (8), 4396–4402.

(188) Moloney, M. P.; Gun'ko, Y. K.; Kelly, J. M. Chiral Highly Luminescent CdS Quantum Dots. *Chem. Commun. (Camb).* **2007**, *7345* (38), 3900–3902.

(189) Mukhina, M. V.; Maslov, V. G.; Korsakov, I. V.; Milton, F. P.; Loudon, A.; Baranov, A. V.; Fedorov, A. V.; Gunko, Y. K. Optically Active II-VI Semiconductor Nanocrystals via Chiral Phase Transfer. In *Materials Research Society Symposium Proceedings*; 2015; Vol. 1793.

(190) Li, Y.; Zhou, Y.; Wang, H. Y.; Perrett, S.; Zhao, Y.; Tang, Z.; Nie, G. Chirality of Glutathione Surface Coating Affects the Cytotoxicity of Quantum Dots. *Angew. Chemie - Int. Ed.* **2011**, *50* (26), 5860–5864.

(191) Halivni, S.; Sitt, A.; Hadar, I.; Banin, U. Effect of Nanoparticle Dimensionality on Fluorescence Resonance Energy Transfer in Nanoparticle-Dye Conjugated Systems. *ACS Nano* **2012**, *6* (3), 2758–2765.

(192) Artemyev, M. Resonance Energy Transfer in Conjugates of Semiconductor Nanocrystals and Organic Dye Molecules. *J. Nanophotonics* **2012**, *6* (1), 061705.

(193) Martynenko, I. V; Orlova, A. O.; Maslov, V. G.; Baranov, A. V; Fedorov, A. V; Artemyev, M. Energy Transfer in Complexes of Water-Soluble Quantum Dots and Chlorin E6 Molecules in Different Environments. *Beilstein J. Nanotechnol.* **2013**, *4*, 895–902.

(194) Zhang, B.; Wang, X.; Liu, F.; Cheng, Y.; Shi, D. Effective Reduction of Nonspecific Binding by Surface Engineering of Quantum Dots with Bovine Serum Albumin for Cell-Targeted Imaging. *Langmuir* **2012**, *28* (48), 16605–16613.

(195) Chin, W. W. L.; Praveen, T.; Heng, P. W. S.; Olivo, M. Effect of Polyvinylpyrrolidone on the Interaction of Chlorin E6 with Plasma Proteins and Its Subcellular Localization. *Eur. J. Pharm. Biopharm.* **2010**, *76* (2), 245–252.

(196) Bai, Z.; Liu, Y.; Zhang, P.; Guo, J.; Ma, Y.; Yun, X.; Zhao, X.; Zhong, R.; Zhang, F. Fluorescence Resonance Energy Transfer between Bovine Serum Albumin and Fluoresceinamine. *Luminescence* **2016**, *31* (3), 688–693.

(197) Qisui, W.; Xiaolei, Z.; Xiaolan, Z.; Tingting, F.; Pengfei, L.; Peng, L.; Xinmin, M.; Li, X. Interaction of Different Thiol-Capped CdTe Quantum Dots with Bovine Serum Albumin. *J. Lumin.* **2012**, *132* (7), 1695–1700.

(198) Mojzisova, H.; Bonneau, S.; Vever-Bizet, C.; Brault, D. The PH-Dependent Distribution of the Photosensitizer Chlorin E6 among Plasma Proteins and Membranes: A Physico-Chemical Approach. *Biochim. Biophys. Acta - Biomembr.* **2007**, *1768* (2), 366–374.

(199) Houssier, C.; Sauer, K. Circular Dichroism and Magnetic Circular Dichroism of the Chlorophyll and Protochlorophyll Pigments. *J. Am. Chem. Soc.* **1970**, *92* (4), 779–791.

9   List of Publications

1.   Vera A Kuznetsova, Eric Mates-Torres, Nadezda Prochukhan, Madeline Marcastel, Finn Purcell-Milton, John O'Brien, Anastasia K Visheratina, Marina Martínez Carmona, Yulia Gromova, Max Garcia-Melchor, Yurii K Gun'ko. The Effect of Chiral Ligand Concentration and Binding Mode on Chiroptical Activity of CdSe/CdS Quantum Dots. ACS nano, 2019, 13, 11, 13560-13572.

2.   Kuznetsova, V. A.; Visheratina, A. K.; Ryan, A.; Martynenko, I. V.; Loudon, A.; Maguire, C. M.; Purcell-Milton, F.; Orlova, A. O.; Baranov, A. V.; Fedorov, A. V.; et al. Enantioselective Cytotoxicity of ZnS:Mn Quantum Dots in A549 Cells. Chirality 2017.

3.   Kuznetsova, V.; Orlova, A.; Martynenko, I.; Kundelev, E.; Maslov, V.; Fedorov, A.; Baranov, A.; Gun'ko, Y. Complexes of Photosensitizer and CdSe/ZnS Quantum Dots Passivated with BSA: Optical Properties and Intracomplex Energy Transfer. In Proceedings of SPIE - The International Society for Optical Engineering; 2016; Vol. 9887, p 988738.

4.   Kuznetsova, V. A.; Almjasheva, O. V.; Gusarov, V. V. Influence of Microwave and Ultrasonic Treatment on the Formation of CoFe2O4 under Hydrothermal Conditions. Glas. Phys. Chem. 2009.

5.   Purcell-Milton, F.; Visheratina, A. K.; Kuznetsova, V. A.; Ryan, A.; Orlova, A. O.; Gun'ko, Y. K. Impact of Shell Thickness on Photoluminescence and Optical Activity in Chiral CdSe/CdS Core/Shell Quantum Dots. ACS Nano 2017.

6.   Elena V Ushakova, Sergei A Cherevkov, Vera A Kuznetsova, Alexander V Baranov. Lead-Free Perovskites for Lighting and Lasing Applications: A Minireview. Materials, 2019, 12(23), 3845

7.   Visheratina, A. K.; Loudon, A.; Kuznetsova, V. A.; Orlova, A. O.; Gun'ko, Y. K.; Baranov, A. V; Fedorov, A. V. Water-Soluble Conjugates of ZnS:Mn Quantum Dots with Chlorin E6 for Photodynamic Therapy. Opt. Spectrosc. 2018, 125 (1), 94–98.

8.   Gromova, Y. A.; Maslov, V. G.; Baranov, M. A.; Serrano-García, R.; Kuznetsova, V. A.; Purcell-Milton, F.; Gun'ko, Y. K.; Baranov, A. V; Fedorov, A. V. Magnetic and Optical Properties of Isolated and Aggregated CoFe2O4 Superparamagnetic Nanoparticles Studied by MCD Spectroscopy. J. Phys. Chem. C 2018, 122 (21), 11491–11497.

9.   Martynenko, I. V.; Baimuratov, A. S.; Osipova, V. A.; Kuznetsova, V. A.; Purcell-Milton, F.; Rukhlenko, I. D.; Fedorov, A. V.; Gun'Ko, Y. K.; Resch-Genger, U.; Baranov, A. V. Excitation Energy Dependence of the Photoluminescence Quantum Yield of Core/Shell CdSe/CdS Quantum Dots and Correlation with Circular Dichroism. Chem. Mater. 2018, 30 (2).

10.   Visheratina, A. K.; Orlova, A. O.; Purcell-Milton, F.; Kuznetsova, V. A.; Visheratin, A. A.; Kundelev, E. V.; Maslov, V. G.; Baranov, A. V.; Fedorov, A. V.; Gun'Ko, Y. K. Influence of CdSe and CdSe/CdS Nanocrystals on the Optical Activity of Chiral Organic Molecules. J. Mater. Chem. C 2018, 6 (7).

11.   Visheratina, A. K.; Purcell-Milton, F.; Serrano-García, R.; Kuznetsova, V. A.; Orlova, A. O.; Fedorov, A. V.; Baranov, A. V.; Gun'ko, Y. K. Chiral Recognition of Optically Active CoFe2O4 magnetic Nanoparticles by CdSe/CdS Quantum Dots Stabilised with Chiral Ligands. J. Mater. Chem. C 2017, 5 (7).

12.   Martynenko, I. V.; Kuznetsova, V. A.; Litvinov, I. K.; Orlova, A. O.; Maslov, V. G.; Fedorov, A. V.; Dubavik, A.; Purcell-Milton, F.; Gun'ko, Y. K.; Baranov, A. V. Enantioselective Cellular Uptake of Chiral Semiconductor Nanocrystals. Nanotechnology 2016, 27 (7).

13.   Martynenko, I.; Visheratina, A.; Kuznetsova, V.; Orlova, A.; Maslov, V.; Fedorov, A.; Baranov, A. Quantum Dot-Tetrapyrrole Complexes as Photodynamic Therapy Agents. In Progress in Biomedical Optics and Imaging - Proceedings of SPIE; 2015; Vol. 9537.

14.   Martynenko, I. V; Kuznetsova, V. A.; Orlova, A. O.; Kanaev, P. A.; Maslov, V. G.; Loudon, A.; Zaharov, V.; Parfenov, P.; Gun'ko, Y. K.; Baranov, A. V; et al. Chlorin E6– ZnSe/ZnS Quantum Dots Based System as Reagent for Photodynamic Therapy. Nanotechnology 2015, 26 (5), 55102.

15.   Martynenko, I.; Kuznetsova, V.; Orlova, A.; Kanaev, P.; Gromova, Y.; Maslov, V.; Baranov, A.; Fedorov, A. ZnSe/ZnS Quantum Dots - Photosensitizer Complexes: Optical Properties and Cancer Cell Photodynamic Destruction Effect. In Proceedings of SPIE - The International Society for Optical Engineering; 2014; Vol. 9126.

16.   Visheratina, A.; Kuznetsova, V.; Purcell-Milton, F.; Orlova, A.; Fedorov, A.; Baranov, A.; Gun'ko, Y. Optically active hybrid nanostructures based on semiconductor quantum dots and chiral molecules for biomedicine. Imaginenano. 2018.

17.	Gromova, Y. A.; Maslov, V. G.; Baranov, M. A.; Andreeva O.; Serrano-García, R.; Kuznetsova, V. A.; Purcell-Milton, F.; Gun'ko, Y. K.; Baranov, A. V; Fedorov, A. V. Magnetic circular dichroism spectroscopy as a probe for the investigation of aggregation, structure and magnetization of CoFe2O4 nanoparticles. Book of Abstracts Smart nanosystems for translation medicine. 2017. 20.

18.	Martynenko, I. V.; Kuznetsova, V. A.; Orlova, A. O.; Maslov, V. G.; Fedorov, A. V.; Gun'ko, Y. K.; Baranov, A. V. Chiral Semiconductor Nanocrystals: Photoluminescence Properties Within Living Cells. Nanocon. 2014.